Synthesis and characterisation of novel lithium containing metal sulphide phases

Thesis submitted in accordance with the requirements of the University of Liverpool for the degree of Doctor in Philosophy by Bernhard Theodor Leube.

January 2020

Supervised by

Professor M. J. Rosseinsky FRS

Dr J. B. Claridge

Abstract

This thesis is focused on the discovery and characterisation of novel lithium containing metal sulphide phases. Exploratory solid state synthesis was carried out in previously underexplored phase fields to find new crystalline phases, that could potentially be used as solid lithium electrolytes. In-depth characterisation was conducted on several new materials to gain understanding of structural and electrochemical properties. In future this knowledge might be used in the design of novel materials.

Chapter 1 gives a brief introduction to rechargeable lithium batteries, the limitations of current technology, the concept of ionic conduction in solids and prominent materials which have been studied in respect to solid state lithium ion conductivity.

The second chapter focuses on the fundamentals of the experimental and analytical techniques used for this work. In particular powder diffraction and AC-impedance spectroscopy were applied to investigate compositional phase fields and characterise new materials.

The first set of new materials is introduced in chapter 3. For the first time the concept of high entropy stabilised rock salts was applied in the discovery of sulphide based rock salts. The most promising material as lithium conductor, $LiBiMgCaS_4$, was studied by SXRD and NPD techniques to create a structural model. $LiBiMgCaS_4$ crystallises in the rock-salt structure with fully disordered cation sites. AC-impedance spectroscopy and solid state NMR showed that the lithium ion mobility is negligible.

More promising was the exploratory synthesis in the Li_5AlS_4-Li_4GeS_4-Li_3PS_4 phase field, described in chapter 4. A novel crystallographic phase, $Li_{4.4}Al_{0.4}Ge_{0.6}S_4$, was discovered and structurally studied. The structure of the material is based on a hexagonal close packed sulphur sublattice with a layered arrangement of the cations. Both cations, Al^{3+} and Ge^{4+}, could be substituted for isovalent cations, expanding the structural family to $Li_{4.4}M_{0.4}M'_{0.6}S_4$ (M= Al^{3+}, Ga^{3+}, In^{3+} and M'= (Si^{4+}), Ge^{4+}, Sn^{4+}). The total lithium conductivity σ_{tot} in this family of materials ranges from 10^{-6} S cm^{-1} to 10^{-4} S cm^{-1}, which is a significant improvement over structurally related Li_5AlS_4 (σ_{tot}= 9.7 x 10^{-9} S cm^{-1}). These findings could be understood on the distinct interplay of the occupied lithium sites and disordered vacancies. The stability of $Li_{4.4}M_{0.4}M'_{0.6}S_4$ against lithium metal decreases with increasing position in the periodic table, which is related to the higher red-ox potential of the larger homologues.

Finally, work in the $LiS_{0.5}$-ZnS-SiS_2 phase field is presented in chapter 5. Surprisingly a new low temperature (LT) Argyrodite was found: $Li_{14}ZnSi_2S_{12}$, the first sulphide based lithium containing argyrodite without pnictogens, which is not quenched from high temperature. Its isotypical homologue $Li_{14}MgSi_2S_{12}$ was obtained after substitution of Zn^{2+} for Mg^{2+}. These two materials crystallise in a large tetragonal unit cell (space group: $I\bar{4}m2$) at ambient temperature and undergo a phase transition to a cubic structure upon heating to ~423 K. The structures of the LT polymorphs could not be fully solved, but structural models were developed for the high temperature (HT) phases. The HT phases crystallise in the argyrodite structure type, with a large degree of disorder on a shared Li/M^{2+} site and an additional Li site. Both phases showed low lithium (σ_{tot}~10^{-7} -10^{-8} S cm^{-1}) and low electronic conductivity. Both materials are very instable against lithium metal. The degradation reactions at the Li|$Li_{14}ZnSi_2S_{12}$ interface leads to bulk degradation and subsequent rapid cell failure. The tetragonal-cubic transition temperature could be reduced significantly *via* aliovalent substitution on the Si^{4+} site with P^{5+}. The resultant $Li_{13}M^{2+}SiPS_{12}$ phases crystallise in the cubic structure at room temperature.

Acknowledgements

It's been an exciting adventure and scientific challenge to work in the research group of Professor Rosseinsky. I would like to thank Professor Rosseinsky for the opportunity to join and do a PhD in his group. His guidance, mentoring and provision of resources were crucial to the project. I received invaluable everyday support in planning, executing and evaluating my experiments by an amazing team of supervisors/advisors, in particular Dr J. B. Claridge, Dr L. Daniels, Dr M. Gaultois and Dr M. Pitcher. Arriving in Liverpool, my understanding of theory, methods and application of solid state chemistry was negligible. There is a significant number of people who helped me to stuff my head with all the necessary basics (and sometimes slightly more advanced skills). Thank you for teaching, listening to my problems and answering my questions! I would like to thank Richard Feetham, Dr Hongjun Niu and Dr Marco Zanella for their ever-patient support in maintaining and fixing all the instruments and running the labs so smoothly.

It would be a lie pretending that all my time in Liverpool was fully filled with study, research and work. The occasional cup of tea, doughnut, game of football or pint of ale were paramount to sustain a healthy work-life balance. Luckily enough there were always colleagues and friends at hand to indulge in these pleasures together. It's been delightful to spend time with you!

Großvater, ich hoffe, dass diese Arbeit neben Urgroßvaters, deiner und Vaters Werken einen Platz im Regal finden wird.

Contents

1 Introduction

This introductory chapter aims to give the reader a brief tour of the world of lithium ion batteries. Initially the basics and limitations of current lithium ion battery technology will be discussed and the idea of all-solid state batteries as the way forward will be introduced. The fundamental models of ionic movement in solids will then be presented, which can help to understand the structural requirements of a solid state electrolyte. Finally, the most important classes of solid state conductors will be examined and the necessity of this work established.

1.1 Lithium-ion battery technology

Modern society relies on the ubiquitous availability of electrical energy on a temporal and a local dimension. The provision of this simple requirement is challenged by two key developments: the change of modes in energy production towards renewable energies and the increased usage of electricity in mobile devices. Both trends require bespoke solutions for energy conversion and storage and will not be met by one technology alone: The drive towards renewable energy requires technologies which store energy on a large scale for extended periods when wind or solar power are not available. In contrast mobile devices depend on the availability of safe and small-scale storage devices with high volumetric and gravimetric energy density. Rechargeable lithium ion battery technology has emerged as a prominent solution to store electrical energy for portable devices and is being used increasingly in electric cars.

Conventional lithium ion battery design is based on three components: the two electrodes (anode and cathode) and the separating electrolyte. The energy is stored by the potential difference of the anode material compared to the cathode material. Upon application of an external voltage lithium ions are extracted from the cathode, transported through the electrolyte and inserted in the anode material which results in charging of the battery. During discharge the lithium ions migrate into the cathode material, with the electrons flowing through an external circuit, thus providing energy to a device connected in this circuit, as shown in Figure 1. The separating electrolyte is a key component as it must have both a high

lithium ion mobility to facilitate the transport of lithium ions and must be electrically insulating to prevent electrical shorting of the cell.

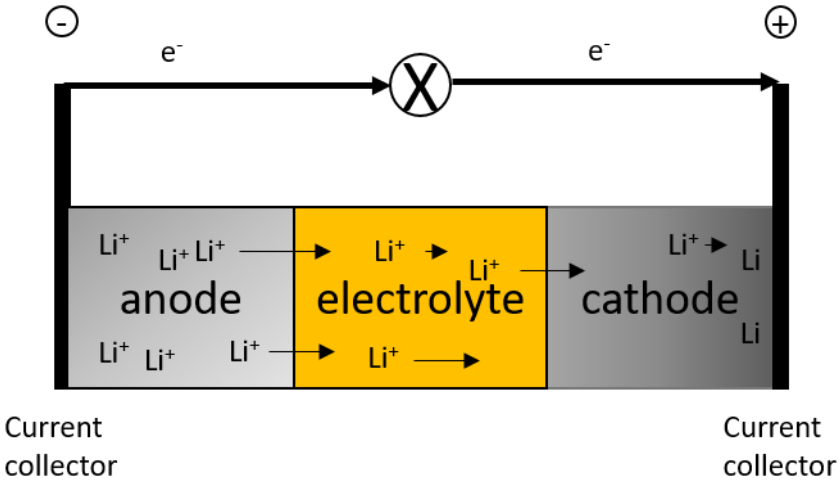

Figure 1: Schematic of a lithium ion battery during discharge. Lithium ions migrate through the electrolyte from the anode to the cathode, while electrons flow through the external electrical circuit providing energy to device X.

This cell architecture has been used and optimised for the last 30 years. Increasingly potent electrode materials and processing techniques have pushed the volumetric and gravimetric energy densities up to 770 Wh l^{-1} and 260 Wh kg^{-1} respectively.[1] But due to intrinsic limitations of materials and processing techniques, the limit of energy densities will soon be reached (~800 Wh l^{-1} and ~420 Wh kg^{-1} respectively). Additionally, safety concerns have arisen, as conventional lithium ion battery technology relies on the use of liquid electrolytes such as $LiPF_6$ in organic solvents. These solvents are highly flammable which, when combined with the large amount of chemical energy stored in the electrodes, is not ideal.

1.2 All solid-state batteries

One of the most promising solutions to overcome the gridlocks on the limits in energy density and safety concerns is substituting the liquid electrolyte for a solid electrolyte (SE) material. It is believed that solid-state battery technology has the potential to increase the energy density by 250 %.[2]

However, while substituting the liquid electrolyte for a solid electrolyte might directly improve safety aspects, it does not automatically guarantee higher energy densities. Only if the electrolytes are also stable enough to withstand high voltage electrode materials, *e.g.* lithium metal as an anode, can significant improvements regarding volumetric and gravimetric energy densities be expected.[1]

Although counterintuitive, crystalline phases are known to give rise to very high ionic mobility up to 10^{-2} S cm^{-1} which is in the order of magnitude of solvent based electrolytes. During the 1980's in particular solid silver conductors were investigated and ionic conductivities of exemplarily 2.15 x 10^{-2} S cm^{-1} for Ag_7SiS_5Br and 5.97 x 10^{-2} S cm^{-1} in Ag_7SnS_5I were reported.[3] The rigidity of a crystalline framework can give rise to very flat energy landscapes for the movement of ions in solids. The fundamentals of ionic movement in solids and conditions for high mobility are presented in the following chapter.

1.2.1 Ion conduction mechanism in solids

Several models for ionic conduction in solids have been proposed based on differing degrees of sophistication. Simple ionic movement can be understood on the basis of the classic diffusion model, here referred to as direct-hopping mechanism:[4] individual ions hop from one lattice site to an adjacent vacant site, as schematically depicted in Figure 2(a). Alongside the geometrical considerations of the crystal structure, the ionic conductivity (σ) is dependent on the ion concentration (n), the charge of the mobile ion (q) and the mobility of the ion (μ):

$$\sigma = n\, q\, \mu \quad (1)$$

The mobility μ usually follows an Arrhenius type activation process:

$$\mu \propto \exp\left(-\frac{E_a}{k_B T}\right) \quad (2)$$

with the activation energy E_a, the Boltzmann factor k_B and the temperature T. These two equations lead to the following conditions for significant ionic conduction in solid materials:[5]

(a) High concentration of the mobile ion n
(b) High concentration of vacant sites available for the mobile ions to migrate into
(c) The occupied and empty sites should be of similar potential energy with low activation barrier E_a for migration
(d) Corresponding to the activation energy: highly polarizable anion frameworks are believed to reduce the activation barrier E_a
(e) Existence of 3 dimensional percolated pathways for long range ion conduction.

This simple picture of individual ion diffusion does not consider correlated diffusion of multiple ions, which is described by the "concerted" or "collective" mechanism. It is assumed that in materials with high carrier concentration, lattices sites of high energy are partially occupied as a result of all low energy sites being fully filled. As cations on high energy sites

start to migrate into neighbouring sites, the activation barrier for the migration of an ion in a low energy site is reduced due to the strong Coulomb interaction among mobile cations (Figure 2(b)).[6]

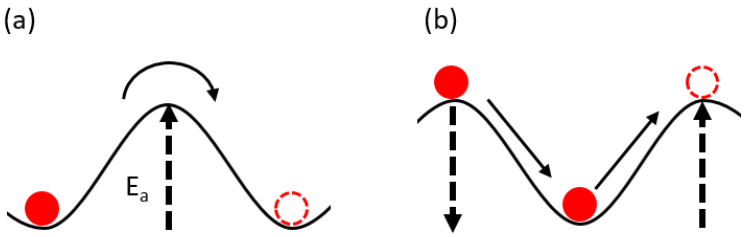

Figure 2: (a) Direct-hopping mechanism of charge carriers in solids with indicated height of activation barrier E_a. (b) Concerted ion migration, resulting in lower energy barriers.

Several factors affect the ion conductivity in solid electrolytes. Ideally the presence of three dimensional percolating diffusion pathways results in macroscopic lithium diffusion. These percolation pathways are dependent on the interplay of mobile carrier ions and vacant sites into which the ions might migrate. It is possible to change ion-to-vacancy-ratio in a given crystal structure by aliovalent doping which is common a mechanism to optimise ionic conductivity in solid state materials.[6] In general pathways consisting of face-sharing coordination polyhedra are favoured compared to pathways with edge-sharing polyhedra, as the bottleneck of carrier diffusion is larger in the former.[7] As such, the anion sublattice arrangement and the corresponding availability of polyhedral sites has been proposed to have a significant impact on activation barriers to ionic mobility. Computational studies show that materials with bcc (body centred cubic) related anion frameworks have lower activation barriers than materials with fcc (face centred cubic) or hcp (hexagonal close packed) anion frameworks.[7] In the bcc lattice cations can hop from one tetrahedral site to a face-sharing tetrahedral site with comparatively low barriers. In contrast in fcc and hcp lattices, two tetrahedral sites are connected *via* an octahedral site with higher activation barrier. Figure 3 shows exemplarily the migration of a tetrahedrally coordinated lithium cation and the corresponding energy path in a bcc (panel a) and a fcc (panel b) sublattice.

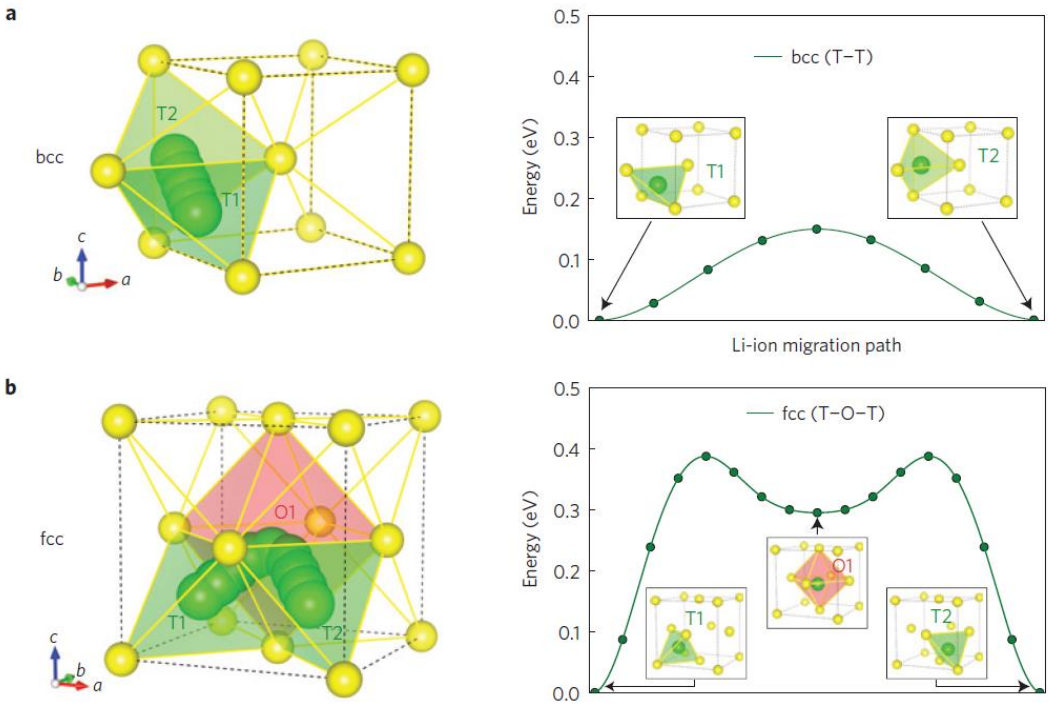

Figure 3: Migration path (left) and calculated energy path (right) of a tetrahedrally coordinated lithium cation in body centred cubic (bcc) (a) and face centred cubic (fcc) (b) sulphur sublattices. From Nat. Mater. ***2015,*** *14, 1026-1032. Reprinted with permission from Nature Research.*[7]

The hopping distance between polyhedral sites can be fine-tuned by isovalent doping. Electrolytes that use sulphur as the anion are superior to oxide based materials due to the higher polarizability of the framework.[8] During cation migration these frameworks are more easily displaced with lower energy cost and thus reducing the activation barrier. Correspondingly the best performing lithium ion conductors are primarily based on sulphide sublattices.

1.2.2 Defects in solid state conductors

In a perfect crystal all atoms are at rest on their ideal lattice positions, leaving no defects through which ionic conduction could occur.[5] Due to atomic vibrations at temperatures > 0 K atoms get displaced and defects are formed. Two types of intrinsic point defects can be distinguished:

(a) Schottky defect: an anion-cation pair leaves their lattice site resulting in two vacancies. This type of defect is the principle point defect in alkali halides
(b) Frenkel defect: an ion displaces into a normally empty interstitial site, resulting in a vacancy on its original position. This type o defect is predominant in AgCl.

The Schottky and Frenkel defects are intrinsic to crystalline phases and their concentration is governed by thermodynamic considerations. The formation of point defects is

enthalpically unfavourable but entropically driven. The change in standard free energy $\Delta G°$ is determined by the change in enthalpy $\Delta H°$ and the change in entropy $\Delta S°$ multiplied by the temperature:

$$\Delta G° = \Delta H° - T\Delta S° \quad (3)$$

The number of defects increases with temperature. Additional extrinsic defects can be introduced into a crystalline material by aliovalent doping. NaCl can be doped with $CaCl_2$ leading to the formation of vacant sites *V* on former Na positions according to: $Na_{1-2x}Ca_xV_xCl$.

1.2.3 Electrochemical stability at solid state electrolyte – electrode interface

Solid electrolytes cannot be assessed on the basis of lithium mobility alone. The combination of the electrolyte material with the electrodes leads inherently to the formation of interfaces. The chemistry at these interfaces is crucial to the overall cell performance:

Electrochemical reactions are observed at the electrolyte-electrode interface. These reactions are driven by the thermodynamics of the electrolyte and the electrode material to create new stable interphases.[9] These reactions can be classified as redox decomposition of the electrolyte or as irreversible chemical reactions between electrolyte and electrode. Purely redox decomposition reactions can be reversible regarding the applied voltage. This phenomenon can be exploited in the assembly of a single material batteries. Exemplarily *Han* et al. reported on a solid-state battery using $Li_{10}GeP_2S_{12}$ as cathode, electrolyte and anode material.[10]

More problematic are irreversible chemical oxidation and reduction reactions at the interfaces between the electrolyte and the electrode materials. These reactions lead to material degradation and subsequent formation of chemically distinct interphases. The electrochemical stability windows of electrolytes are determined by their elemental composition. The voltage onset of oxidation reactions is determined by the anion framework and its propensity to be oxidised. Computational studies predict the following order of stability against oxidation:[11-13] $N^{3-}<P^{3-}<H^-<S^{2-}<I^-<O^{2-}<Br^-<Cl^-<F^-$. In contrast, the stability against reduction is governed by the affinity of the electropositive cations to be reduced. Three different types of interfaces have been identified depending on the interfacial transport properties:[14-15]

(a) Thermodynamically stable interface: no reaction between solid electrolyte and electrode material.

(b) Thermodynamically unstable but kinetically stabilised interface: Formation of an interphase which impedes either ionic or electron conduction: The reaction at the interface is blocked and a kinetically stable interface of finite thickness is established. Ideally the interphase would be electrically insulating and ionically conducting. This would result in an additional impedance contribution to the cell but would not impede the functioning of the cell.

(c) Thermodynamically and kinetically unstable interface: Formation of a mixed-conducting interphase. This enables the interphase to grow into the solid electrolyte and can lead eventually to cell failure.

The ideal scenario of interface type (a) is rare and has been reported for the Na-β-Al_2O_3 versus Na metal interface.[16] More common interfaces are of type (b) and (c). A promising strategy to overcome interfacial degradation is to coat the electrode material with a protective material (*e.g.* $LiCoO_2$ coated spray-coated with $Li_4Ti_5O_{12}$ in combination with $Li_{3.25}Ge_{0.25}P_{0.75}S_4$ as the solid electrolyte and Li-In alloy as the counter electrode)[17]. It is believed that the coating smooths the voltage drop at the interface by establishing a buffer in which the Li potential is intermediate between that of the electrode material and the solid electrolyte.[9]

Overall more redox stable electrolytes would enable the use of both higher and lower voltage electrode materials, which can increase the overall energy density of a battery significantly.

1.2.4 Requirement of solid state electrolytes in lithium-ion batteries

The following section will list and discuss criteria which solid-state electrolytes must meet in order to be used in all-solid lithium-ion batteries. Paramount to electrolytes is a sufficiently high Li^+ ion conductivity of $\sigma > 1 \times 10^{-4}$ S cm^{-1},[18] which has been achieved in various classes of crystalline materials. A selection of these materials will be presented in the next section. As discussed above the material needs to be stable against electrode materials or more work needs to be undertaken to artificially protect the interface. Solid electrolytes must also be poor electronic conductors to prevent self-discharge and short circuiting of the electrochemical cell. Apart from these material-intrinsic requirements, the cell stability must be ensured by preventing the formation and growth of metallic dendrites.[19-21] The maintenance of physical contact between the solid electrolyte and the electrode material is crucial in the solid state cell design, as the transport of lithium atoms across the interface relies on contact of solid particles. During cell cycling the electrode volumes can expand and deflate which can lead to the formation of cracks and delamination.[22-23] Finally the material

must meet the final criterion in industrial application: cost. This encompasses methods for easy and effective up-scaling production (*e.g.* solvent based synthesis). Reagents need to be abundant and non-toxic, preferably sourced in regions which do not raise doubts about human-rights abuse, deforestation or war mongering.

1.3 Crystalline solid state cation conductors

The following section introduces briefly the most important crystalline materials, studied in respect to ion conductivity.

1.3.1 NASICON

NASICONs (NA Super Ionic CONductors) are materials based on the stoichiometry $Na_{1+x}M_2P_{3-x}Si_xO_{12}$ (*M* = Ti, Al, Cr, Ga, Fe, Sc, In, Lu, Y, La, Sn, Hf) and often exhibit high ionic conductivity.[24] MO_6 octahedra and $(P/Si)O_4$ tetrahedra form a three dimensional framework structure connected through corner sharing oxygen. This arrangement provides percolating pathways for monovalent-cation diffusion. Monovalent cations can be found on two different sites which form a migration path, limited by the narrowest part, referred to as the bottleneck. A wide range of cation substitution is possible, encompassing a large isostructural family of lithium containing materials. Exemplarily the 3-d framework structure and the lithiated structure of $Li_3Ti_2(PO_4)_3$ are shown in Figure 4. Panel (c) indicates a bottleneck of the diffusion pathway in a NASICON structure.

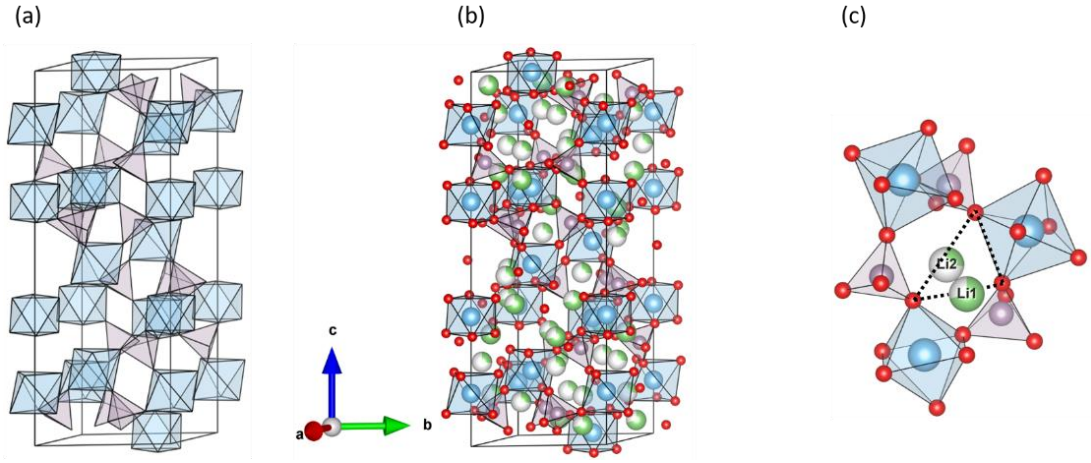

Figure 4: (a) 3-d framework structure of corner shared MO_6 octahedra and MO_4 tetrahedra in NASICON type $Li_3Ti_2(PO_4)_3$. (b) Population of two crystallographic sites by Li^+ in $Li_3Ti_2(PO_4)_3$. (c) bottleneck of Li^+ diffusion pathway (blue: Ti, purple: P, green: Li, red: O).[25]

The best lithium conductor in the NASICON family is aluminium doped lithium titanium phosphate $Li_{1+x}Al_xTi_{2-x}(PO_4)_3$ (LATP). At x= 0.3 a conductivity of 3×10^{-3} S cm^{-1} is achieved, which is three orders of magnitude larger than the undoped parent phase.[26] Bulk LATP is

instable in contact with lithium anodes according to: $LiTi_2(PO_4)_3 + Li \rightarrow Li_2Ti_2(PO_4)_3$.[27] However application of buffer layer such as atomic layer deposited Al_2O_3 or a thin film LiPON (nitrogen doped lithium phosphate glass, general formula: $Li_xPO_yN_z$)[28] can protect the solid state electrolyte.[29-30]

1.3.2 Garnet

Garnets have the general formula $A_3B_2(XO_4)_3$ with eight coordinate cations *A* (Ca^{2+}, Mg^{2+}, Fe^{2+}), six coordinate cations *B* (Al^{3+}, Cr^{3+}, Fe^{3+}, Ga^{3+}) and tetrahedrally coordinated cations *X* (Si^{4+}, Ge^{4+}), crystallizing in cubic space group $Ia\bar{3}d$. Lithium containing garnets with the formula $Li_3Ln_3Te_2O_{12}$ (*Ln*= Y^{3+}, Pr^{3+}, Sm^{3+}-Lu^{3+}) are known, in which lithium occupies the tetrahedral *X* site. Thangadurai *et al.* first reported the lithium rich garnet (stuffed garnet) $Li_5La_3M_2O_{12}$ (*M*= Nb^{5+}, Ta^{5+}) with a conductivity of 10^{-6} S cm^{-1}.[31] The tetrahedral site *X* cannot accommodate all five lithium atoms, therefore further octahedral or trigonal prismatic sites become occupied. More lithium rich garnets are found in the $Li_7La_3Zr_2O_{12}$(LLZO), family, which show lithium ion conductivities up to 10^{-4} S cm^{-1} at room temperature.[32] The full crystal structure of $Li_7La_3Zr_2O_{12}$ is drawn in Figure 5(a). The coordination environments of La^{3+} and Zr^{4+} are shown in panel (b).

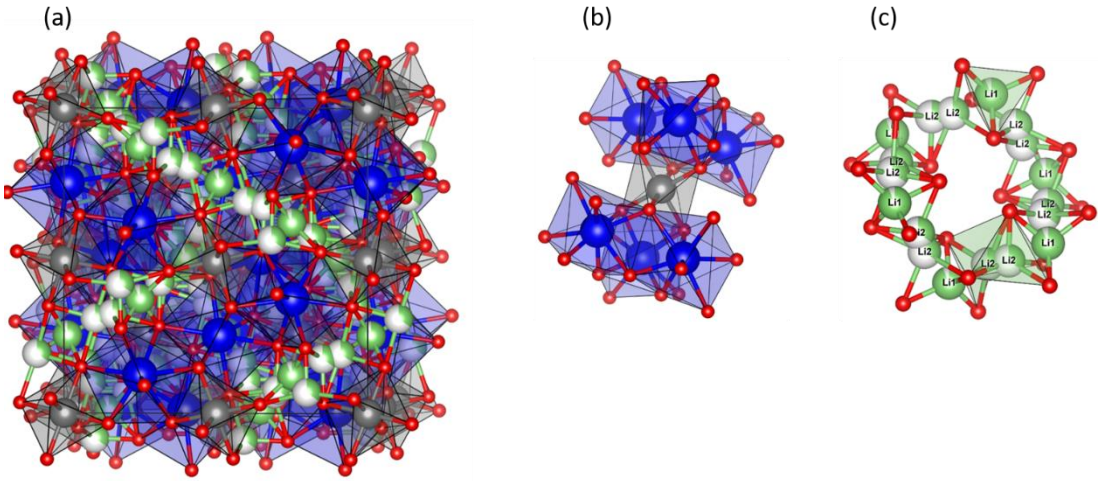

Figure 5: (a) Crystal structure of the fast lithium ionic conductor $Li_7La_3Zr_2O_{12}$ (b) framework structure of LaO_8 and ZrO_6. (c) tetrahedral coordinated lithium (Li1) and partial occupation of the distorted octahedral lithium site (Li2) (blue: La, grey: Zr, green: Li, red: O).[33]

In $Li_7La_3Zr_2O_{12}$ lanthanum and zirconium are eight and six coordinated respectively while lithium is distributed on the tetrahedral 24*d* site (Li1) and the distorted octahedral 96*h* site (this Li2 site is vacant in the ideal garnet structure).[33] Lithium diffusion occurs between the corner sharing octahedral sites (Li2) that are connected by face shared tetrahedral sites (Li1) (compare to Figure 5(c)). The partial occupation of the lithium sites leads to low energetic percolating conduction pathways.

1.3.3 LISICON

The name LIthium Super Ionic CONductor (LISICON) has first been introduced for $Li_{14}Zn(GeO_4)_4$ by Hong.[34] More general LISICONs have the general formula $Li_{3+x}Y_{1-x}X_xO_4$ (*X*= Si, Ge, Ti and *Y*= P, As, V, Cr) and are essentially found on solid solutions between Li_4XO_4 and Li_3YO_4.[35-36] LISICON materials have frameworks which are related to the *γ*-Li_3PO_4 crystal structure, based on a hcp (hexagonal close packed) oxide array.[37] The crystal structure of *γ*-Li_3PO_4 with fully ordered Li^+ ions is depicted in Figure 6(a). It exhibits a low ionic conductivity of ~2 x 10^{-10} S cm^{-1} at 373 K.[38]

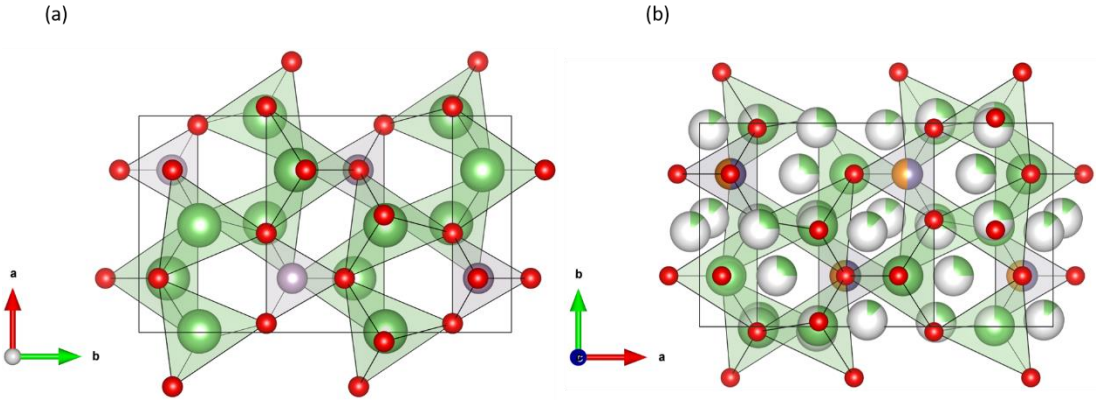

Figure 6: Crystal structures of (a) γ-Li_3PO_4[39] and the LISION $Li_{3.5}Ge_{0.5}V_{0.5}S_4$ (purple: P, green: Li, purple-grey: Ge, orange: V, red: O).[40]

A structurally closely related material, *γ*-$Li_{3.5}Ge_{0.5}V_{0.5}S_4$ is shown in panel (b). Aliovalent doping of Ge into the *γ*-Li_3PO_4 structure type introduces partially occupied interstitial lithium sites. This results in the highest conductivity (σ= 4 x 10^{-5} S cm^{-1} at ambient temperature)[41] so far reported for LISICON related materials, which is too low for application in solid-state batteries.

1.3.4 Thio-LISICON

Significantly improved conductivities could be achieved by development of so called thio-LISICONs introduced by Kanno *et al*.[42-43] Replacement of oxygen in LISICON with more polarizable sulphur anions weakens the Li-anion interaction and leads to reduced activation barriers. A wide range of solid solutions is achievable by aliovalent doping of trivalent or pentavalent cations into Li_4GeS_4 or Li_4SiS_4 according to $Li_zX_{1-x}Y_xS_4$ (*X*= Si, Ge and *Y*= P, Al, Zn, Ga, Sb)[43-45] yielding the highest reported conductivity in $Li_{4-x}Ge_{1-x}P_xS_4$ (x= 0.75, σ= 2.2 x 10^{-3} S cm^{-1}).[46] Besides improved Li^+ mobility, sulphide based materials are more ductile and have lower/negligible grain boundary resistance compared to oxides.[47] In practice this leads to obviation of the need to sinter pellets, rendering the fabrication of solid-state devices more convenient. Further structural discussion of thio-LISICONs will be presented in chapter 4.

1.3.5 $Li_{10}GeP_2S_{12}$ (LGPS)

A breakthrough development was achieved in 2011 by Kanno *et al.* with the discovery of the new $Li_{10}GeP_2S_{12}$ phase (LGPS) with a very high ionic conductivity of 1.2 x 10^{-2} S cm^{-1}.[48] Even though the composition is related to the thio-LISICON family, it features a completely new structure, unrelated to the *γ*-Li_3PO_4 phase. LGPS is based on a bcc (body centred cubic) sulphur sublattice. The material crystallises in the $P4_2/nmc$ space group and features isolated GeS_4 and PS_4 tetrahedra. Four crystallographic distinct Li^+ sites were identified: octahedrally coordinated lithium on the 4*d* site and tetrahedrally coordinated lithium on the 4*c* site, both of which are not believed to participate in lithium diffusion. Instead ionic conduction is facilitated by two tetrahedrally coordinated lithium sites (Li1 on 16*h* and Li3 on 8*f*). These sites are located in tunnels parallel to the *c*-axis that serve as fast transport channels as schematically shown in Figure 7.[49]

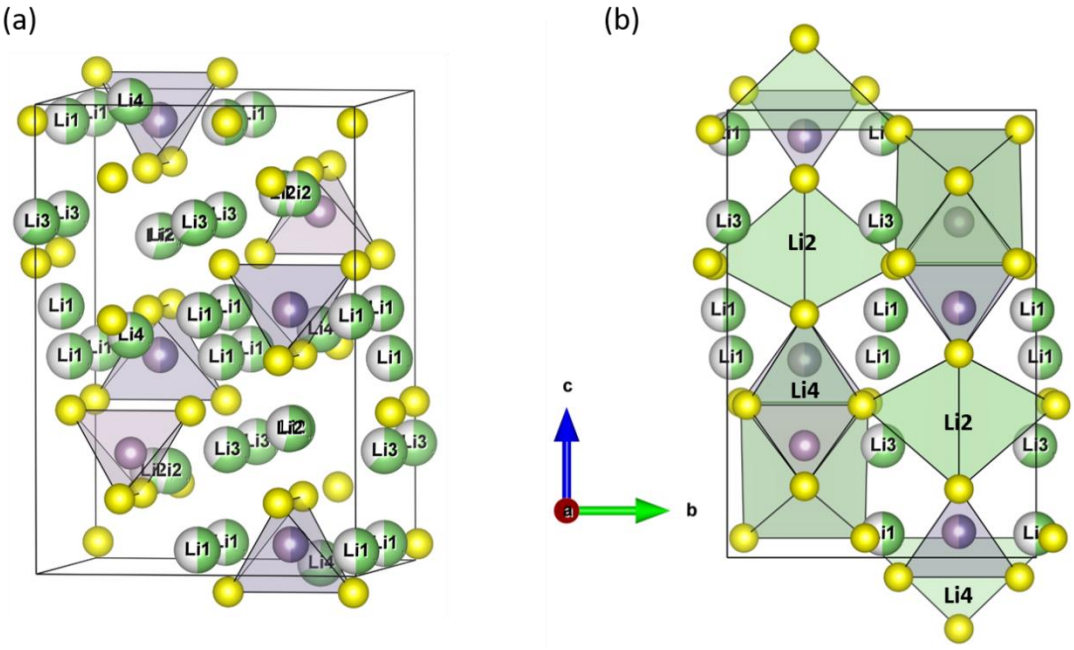

Figure 7: (a) Full structure of $Li_{10}GeP_2S_{12}$ showing the isolated $(Ge/P)S_4$ tetrahedra. (b) Li1 and Li3 distribution, which are believed to be responsible for long range Li^+ transport; Li2 and Li4 are part of the immobile framework (purple: P, grey-purple: Ge, green: Li, yellow: S).

Unfortunately $Li_{10}GeP_2S_{12}$ is limited regarding application in solid-state batteries by the low natural abundance of Ge and the interfacial instability against a lithium metal anode.[50] The LGPS|Li interface is thermodynamically instable towards degradation into Li_2S, Li_3P and $Li_{15}Ge_4$.[51] Isovalent substitution strategies expanded the LGPS structural family to $Li_{10}MP_2S_{12}$ (*M*= Si,[52] Sn[53-54]) which all exhibit very high Li^+ ion mobility. The highest Li^+ conductivity to date is reported for $Li_{9.54}Si_{1.74}P_{1.44}S_{11.7}Cl_{0.3}$ (σ= 2.5x10^{-2} S cm^{-1}) which is a Cl^- doped LGPS member.[55]

1.3.6 Argyrodite

Lithium containing sulphide based argyrodites (*e.g.* Li_7PS_6) have most recently attracted the attention of the solid state community. Aliovalent halogen and cation doping has led to the discovery of superionic conductors $Li_{6+x}M_xP_{1-x}S_5X$ (*M*= Si, Ge; *X*= Br, I) with conductivities up to 1.8 x 10^{-2} S cm^{-1}.[56-57] Argyrodite related materials will be discussed in depth in chapter 5.

1.4 Aim of the thesis

The development of all solid-state battery technology is key to meet the demand for mobile and safe power storage systems with high energy densities. Despite the wide range of explored materials, each material suffers significant drawbacks, rendering it impractical for application in solid-state batteries. The aim of this thesis is the discovery and characterisation of novel materials as solid lithium conductors. Isovalent and aliovalent doping of known materials has proven to be a reliable strategy towards new materials. But the doped materials rarely overcome the intrinsic problem of the material; *e.g.* the impressive improvement of lithium conductivity in phosphorous based argyrodites does not result in a more stable SE|Li interface. In contrast this work is dedicated to exploratory synthesis in underexplored phase fields targeting the identification of novel lithium containing sulphide based crystalline phases. Crystallographic and electrochemical characterisation of the new materials will lead to important insights into structures, ionic mobility and electrochemical stability. Eventually this improved understanding could guide the design and synthesis of new solid electrolyte materials.

1.5 References

1. Janek, J.; Zeier, W. G., A solid future for battery development. *Nat. Energy* **2016,** *1*.
2. Dudney, N. J. A. W., William C; A Nanda, Jagjit, *Handbook of Solid State Batteries*.
3. Laqibi, M.; Cros, B.; Peytavin, S.; Ribes, M., New silver superionic conductors Ag_7XY_5Z (X = Si, Ge, Sn; Y = S, Se; Z = Cl, Br, I)-synthesis and electrical studies. *Solid State Ion.* **1987,** *23* (1), 21-26.
4. Zhang, Z.; Shao, Y.; Lotsch, B.; Hu, Y.-S.; Li, H.; Janek, J.; Nazar, L. F.; Nan, C.-W.; Maier, J.; Armand, M.; Chen, L., New horizons for inorganic solid state ion conductors. *Energy Environ. Sci.* **2018,** *11* (8), 1945-1976.
5. West, A. R., *Basic solid state chemistry*. 2nd ed.; John Wiley & Sons: New York, 1999; p xvi, 480 p.
6. Wang, Q.; Wu, J. F.; Lu, Z.; Ciucci, F.; Pang, W. K.; Guo, X., A New Lithium-Ion Conductor $LiTaSiO_5$: Theoretical Prediction, Materials Synthesis, and Ionic Conductivity. *Adv. Funct. Mater.* **2019**.
7. Wang, Y.; Richards, W. D.; Ong, S. P.; Miara, L. J.; Kim, J. C.; Mo, Y. F.; Ceder, G., Design principles for solid-state lithium superionic conductors. *Nat. Mater.* **2015,** *14* (10), 1026-1032.
8. Lotsch, B. V.; Maier, J., Relevance of solid electrolytes for lithium-based batteries: A realistic view. *J. Electroceram.* **2017,** *38* (2), 128-141.
9. Famprikis, T.; Canepa, P.; Dawson, J. A.; Islam, M. S.; Masquelier, C., Fundamentals of inorganic solid-state electrolytes for batteries. *Nat. Mater.* **2019,** *18* (12), 1278-1291.
10. Han, F.; Gao, T.; Zhu, Y.; Gaskell, K. J.; Wang, C., A Battery Made from a Single Material. *Adv. Mater.* **2015,** *27* (23), 3473-3483.
11. Richards, W. D.; Miara, L. J.; Wang, Y.; Kim, J. C.; Ceder, G., Interface Stability in Solid-State Batteries. *Chem. Mater.* **2016,** *28* (1), 266-273.
12. Zhu, Y.; He, X.; Mo, Y., Origin of Outstanding Stability in the Lithium Solid Electrolyte Materials: Insights from Thermodynamic Analyses Based on First-Principles Calculations. *ACS Appl. Mater. Interfaces* **2015,** *7* (42), 23685-23693.
13. Zhu, Y.; He, X.; Mo, Y., First principles study on electrochemical and chemical stability of solid electrolyte–electrode interfaces in all-solid-state Li-ion batteries. *J. Mater. Chem. A* **2016,** *4* (9), 3253-3266.
14. Wenzel, S.; Sedlmaier, S. J.; Dietrich, C.; Zeier, W. G.; Janek, J., Interfacial reactivity and interphase growth of argyrodite solid electrolytes at lithium metal electrodes. *Solid State Ion.* **2018,** *318*, 102-112.
15. Wenzel, S.; Leichtweiss, T.; Kruger, D.; Sann, J.; Janek, J., Interphase formation on lithium solid electrolytes-An in situ approach to study interfacial reactions by photoelectron spectroscopy. *Solid State Ion.* **2015,** *278*, 98-105.
16. Wenzel, S.; Leichtweiss, T.; Weber, D. A.; Sann, J.; Zeier, W. G.; Janek, J., Interfacial Reactivity Benchmarking of the Sodium Ion Conductors Na_3PS_4 and Sodium β-Alumina for Protected Sodium Metal Anodes and Sodium All-Solid-State Batteries. *ACS Appl. Mater. Interfaces* **2016,** *8* (41), 28216-28224.
17. Ohta, N.; Takada, K.; Zhang, L.; Ma, R.; Osada, M.; Sasaki, T., Enhancement of the High-Rate Capability of Solid-State Lithium Batteries by Nanoscale Interfacial Modification. *Adv. Mater.* **2006,** *18* (17), 2226-2229.
18. Zhao, W.; Yi, J.; He, P.; Zhou, H., Solid-State Electrolytes for Lithium-Ion Batteries: Fundamentals, Challenges and Perspectives. *Electrochem. Energy Rev.* **2019,** *2* (4), 574-605.
19. Bhattacharyya, R.; Key, B.; Chen, H.; Best, A. S.; Hollenkamp, A. F.; Grey, C. P., In situ NMR observation of the formation of metallic lithium microstructures in lithium batteries. *Nat. Mater.* **2010,** *9*, 504.

20. Li, L.; Basu, S.; Wang, Y.; Chen, Z.; Hundekar, P.; Wang, B.; Shi, J.; Shi, Y.; Narayanan, S.; Koratkar, N., Self-heating–induced healing of lithium dendrites. *Science* **2018,** *359* (6383), 1513.
21. Ren, Y.; Shen, Y.; Lin, Y.; Nan, C.-W., Direct observation of lithium dendrites inside garnet-type lithium-ion solid electrolyte. *Electrochem. Commun.* **2015,** *57*, 27-30.
22. Koerver, R.; Zhang, W.; de Biasi, L.; Schweidler, S.; Kondrakov, A. O.; Kolling, S.; Brezesinski, T.; Hartmann, P.; Zeier, W. G.; Janek, J., Chemo-mechanical expansion of lithium electrode materials – on the route to mechanically optimized all-solid-state batteries. *Energy Environ. Sci.* **2018,** *11* (8), 2142-2158.
23. Koerver, R.; Aygün, I.; Leichtweiß, T.; Dietrich, C.; Zhang, W.; Binder, J. O.; Hartmann, P.; Zeier, W. G.; Janek, J., Capacity Fade in Solid-State Batteries: Interphase Formation and Chemomechanical Processes in Nickel-Rich Layered Oxide Cathodes and Lithium Thiophosphate Solid Electrolytes. *Chem. Mater.* **2017,** *29* (13), 5574-5582.
24. Anantharamulu, N.; Rao, K. K.; Rambabu, G.; Kumar, B. V.; Radha, V.; Vithal, M., A wide-ranging review on Nasicon type materials. *J. Mater. Sci.* **2011,** *46* (9), 2821-2837.
25. Arbi, K.; Hoelzel, M.; Kuhn, A.; García-Alvarado, F.; Sanz, J., Local structure and lithium mobility in intercalated $Li_3AlxTi_{2-x}(PO_4)_3$ NASICON type materials: a combined neutron diffraction and NMR study. *Phys. Chem. Chem. Phys.* **2014,** *16* (34), 18397-18405.
26. Aono, H.; Sugimoto, E.; Sadaoka, Y.; Imanaka, N.; Adachi, G. Y., Ionic-Conductivity of the Lithium Titanium Phosphate $(Li_{1+x}Al_xTi_{2-x}(PO_4)_3)$, $(Li_{1+x}Sc_xTi_{2-x}(PO_4)_3)$, $(Li_{1+x}Y_xTi_{2-x}(PO_4)_3)$, $(Li_{1+x}La_xTi_{2-x}(PO_4)_3$ Systems. *J. Electrochem. Soc.* **1989,** *136* (2), 590-591.
27. DeWees, R.; Wang, H., Synthesis and Properties of NaSICON-type LATP and LAGP Solid Electrolytes. *ChemSusChem* **2019,** *12* (16), 3713-3725.
28. Lacivita, V.; Artrith, N.; Ceder, G., Structural and Compositional Factors That Control the Li-Ion Conductivity in LiPON Electrolytes. *Chem. Mater.* **2018,** *30* (20), 7077-7090.
29. Liu, Y.; Sun, Q.; Zhao, Y.; Wang, B.; Kaghazchi, P.; Adair, K. R.; Li, R.; Zhang, C.; Liu, J.; Kuo, L.-Y.; Hu, Y.; Sham, T.-K.; Zhang, L.; Yang, R.; Lu, S.; Song, X.; Sun, X., Stabilizing the Interface of NASICON Solid Electrolyte against Li Metal with Atomic Layer Deposition. *ACS Appl. Mater. Interfaces* **2018,** *10* (37), 31240-31248.
30. Kim, H. S.; Oh, Y.; Kang, K. H.; Kim, J. H.; Kim, J.; Yoon, C. S., Characterization of Sputter-Deposited $LiCoO_2$ Thin Film Grown on NASICON-type Electrolyte for Application in All-Solid-State Rechargeable Lithium Battery. *ACS Appl. Mater. Interfaces* **2017,** *9* (19), 16063-16070.
31. Thangadurai, V.; Kaack, H.; Weppner, W. J. F., Novel fast lithium ion conduction in garnet-type $Li_5La_3M_2O_{12}$ (M = Nb, Ta). *J. Am. Ceram. Soc.* **2003,** *86* (3), 437-440.
32. Murugan, R.; Thangadurai, V.; Weppner, W., Fast lithium ion conduction in garnet-type $Li_7La_3Zr_2O_{12}$. *Angew. Chem., Int. Edit.* **2007,** *46* (41), 7778-7781.
33. Awaka, J.; Takashima, A.; Kataoka, K.; Kijima, N.; Idemoto, Y.; Akimoto, J., Crystal structure of fast lithium-ion-conducting cubic $Li_7La_3Zr_2O_{12}$. *Chem. Lett.* **2010,** *40* (1), 60-62.
34. Hong, H. Y. P., Crystal-Structure and Ionic-Conductivity of $Li_{14}Zn(GeO_4)_4$ and Other New Li^+ Superionic Conductors. *Mater. Res. Bull.* **1978,** *13* (2), 117-124.
35. Robertson, A. D.; West, A. R.; Ritchie, A. G., Review of crystalline lithium-ion conductors suitable for high temperature battery applications. *Solid State Ion.* **1997,** *104* (1), 1-11.
36. Deng, Y.; Eames, C.; Fleutot, B.; David, R.; Chotard, J.-N.; Suard, E.; Masquelier, C.; Islam, M. S., Enhancing the Lithium Ion Conductivity in Lithium Superionic Conductor (LISICON) Solid Electrolytes through a Mixed Polyanion Effect. *ACS Appl. Mater. Interfaces* **2017,** *9* (8), 7050-7058.
37. Knauth, P., Inorganic solid Li ion conductors: An overview. *Solid State Ion.* **2009,** *180* (14), 911-916.

38. Muy, S.; Bachman, J. C.; Chang, H.-H.; Giordano, L.; Maglia, F.; Lupart, S.; Lamp, P.; Zeier, W. G.; Shao-Horn, Y., Lithium Conductivity and Meyer-Neldel Rule in Li_3PO_4–Li_3VO_4–Li_4GeO_4 Lithium Superionic Conductors. *Chem. Mater.* **2018,** *30* (16), 5573-5582.
39. Zemann, J., Die Kristallstruktur von Lithiumphosphat, Li_3PO_4. *Acta Crystallogr.* **1960,** *13* (11), 863-867.
40. Abrahams, I.; Bruce, P. G., Defect clustering in the superionic conductor lithium germanium vanadate. *Acta Cryst. B* **1991,** *47* (5), 696-701.
41. Kuwano, J.; West, A. R., New Li+ ion conductors in the system, Li_4GeO_4-Li_3VO_4. *Mater. Res. Bull.* **1980,** *15* (11), 1661-1667.
42. Kanno, R.; Hata, T.; Kawamoto, Y.; Irie, M., Synthesis of a new lithium ionic conductor, thio-LISICON-lithium germanium sulfide system. *Solid State Ion.* **2000,** *130* (1-2), 97-104.
43. Murayama, M.; Kanno, R.; Irie, M.; Ito, S.; Hata, T.; Sonoyama, N.; Kawamoto, Y., Synthesis of New Lithium Ionic Conductor Thio-LISICON—Lithium Silicon Sulfides System. *J. Solid State Chem.* **2002,** *168* (1), 140-148.
44. Liu, Z.; Fu, W.; Payzant, E. A.; Yu, X.; Wu, Z.; Dudney, N. J.; Kiggans, J.; Hong, K.; Rondinone, A. J.; Liang, C., Anomalous High Ionic Conductivity of Nanoporous β-Li_3PS_4. *J. Am. Chem. Soc.* **2013,** *135* (3), 975-978.
45. Liu, Z.; Huang, F.; Yang, J.; Wang, B.; Sun, J., New lithium ion conductor, thio-LISICON lithium zirconium sulfide system. *Solid State Ion.* **2008,** *179* (27), 1714-1716.
46. Kanno, R.; Murayama, M., Lithium Ionic Conductor Thio-LISICON: The Li_2S-GeS_2-P_2S_5 System. *J. Electrochem. Soc.* **2001,** *148* (7), A742-A746.
47. Sakuda, A.; Hayashi, A.; Tatsumisago, M., Sulfide Solid Electrolyte with Favorable Mechanical Property for All-Solid-State Lithium Battery. *Sci. Rep.* **2013,** *3*, 2261.
48. Kamaya, N.; Homma, K.; Yamakawa, Y.; Hirayama, M.; Kanno, R.; Yonemura, M.; Kamiyama, T.; Kato, Y.; Hama, S.; Kawamoto, K.; Mitsui, A., A lithium superionic conductor. *Nat. Mater.* **2011,** *10* (9), 682-686.
49. Krauskopf, T.; Culver, S. P.; Zeier, W. G., Bottleneck of Diffusion and Inductive Effects in $Li_{10}Ge_{1-x}Sn_xP_2S_{12}$. *Chem. Mater.* **2018,** *30* (5), 1791-1798.
50. Wenzel, S.; Randau, S.; Leichtweiss, T.; Weber, D. A.; Sann, J.; Zeier, W. G.; Janek, J., Direct Observation of the Interfacial Instability of the Fast Ionic Conductor $Li_{10}GeP_2S_{12}$ at the Lithium Metal Anode. *Chem. Mater.* **2016,** *28* (7), 2400-2407.
51. Sang, L. Z.; Haasch, R. T.; Gewirth, A. A.; Nuzzo, R. G., Evolution at the Solid Electrolyte/Gold Electrode Interface during Lithium Deposition and Stripping. *Chem. Mater.* **2017,** *29* (7), 3029-3037.
52. Whiteley, J. M.; Woo, J. H.; Hu, E. Y.; Nam, K. W.; Lee, S. H., Empowering the Lithium Metal Battery through a Silicon-Based Superionic Conductor. *J. Electrochem. Soc.* **2014,** *161* (12), A1812-A1817.
53. Kato, Y.; Saito, R.; Sakano, M.; Mitsui, A.; Hirayama, M.; Kanno, R., Synthesis, structure and lithium ionic conductivity of solid solutions of $Li_{10}(Ge_{1-x}M_x)P_2S_{12}$ (M = Si, Sn). *J. Power Sources* **2014,** *271*, 60-64.
54. Bron, P.; Johansson, S.; Zick, K.; Schmedt auf der Günne, J.; Dehnen, S.; Roling, B., $Li_{10}SnP_2S_{12}$: An Affordable Lithium Superionic Conductor. *J. Am. Chem. Soc.* **2013,** *135* (42), 15694-15697.
55. Kato, Y.; Hori, S.; Saito, T.; Suzuki, K.; Hirayama, M.; Mitsui, A.; Yonemura, M.; Iba, H.; Kanno, R., High-power all-solid-state batteries using sulfide superionic conductors. *Nat. Energy* **2016,** *1*.
56. Kraft, M. A.; Ohno, S.; Zinkevich, T.; Koerver, R.; Culver, S. P.; Fuchs, T.; Senyshyn, A.; Indris, S.; Morgan, B. J.; Zeier, W. G., Inducing High Ionic Conductivity in the Lithium Superionic Argyrodites $Li_{6+x}P_{1-x}Ge_xS_5I$ for All-Solid-State Batteries. *J. Am. Chem. Soc.* **2018,** *140* (47), 16330-16339.

57. Minafra, N.; Culver, S. P.; Krauskopf, T.; Senyshyn, A.; Zeier, W. G., Effect of Si substitution on the structural and transport properties of superionic Li-argyrodites. *J. Mater. Chem. A* **2018,** *6* (2), 645-651.

2 Methods

2.1 The crystalline state

The object of this thesis is the discovery and characterisation of new crystalline phases. Crystalline materials are characterised by long-range ordering of atoms, based on the principles of symmetry, summarised by Bärnighausen as follows:[1]

(a) "In the solid state the arrangement of atoms reveals a pronounced tendency towards the highest possible symmetry"
(b) "Several counteracting factors may prevent the attainment of the highest possible symmetry, but in most cases the deviations from the ideal arrangement are only small, and frequently the observed symmetry reduction even corresponds to the smallest possible step"
(c) "During a solid state reaction which results in one or more products of lower symmetry very often the higher symmetry of the starting material is indirectly preserved by the orientation of domains formed within the crystalline matrix."

The reason for (a) can be understood by consideration of the local energetics of each atom. There is only one energetically most favourable surrounding for an atom of a given species, depending on chemical composition, nature of chemical bonding, electronic configuration, relative sizes of the ions involved, temperature and pressure of the system. All atoms of one species strive to achieve this most favourable configuration, which makes them symmetrically equivalent and results thus in high symmetry of the structure.[2] Therefore (a) promotes the formation of well-ordered crystalline phases *vs* the formation of amorphous phases. The crystalline state of materials is fundamental to this project as it is a prerequisite for analytical techniques based on diffraction, which is the primary technique used in this thesis.

Notion (b) explains why the crystal structures of compositionally similar materials tend to differ only by small deviations due to distortions based on various perturbations, *e.g.* stereochemically active lone electron pairs, Jahn-Teller effect, ordering of atoms in disordered structures, partial vacation of atomic positions.[2] In many cases crystallographic group theory can be applied to investigate the precise relationship of the structures.

Statement (c) is not particularly relevant in the context of this thesis but was included for completeness.

2.2 Solid state reactions

One of the oldest and most used technique for the synthesis of solids, is the direct reaction between solid particles at high temperatures (compared to solvent based reactions) over an extended period of time (compared to solvent based reactions). The main advantages are the relatively easy experimental procedure (grinding and heating) and that there is no need for solvents, catalysts or any by-reagents that must be separated after the reaction. On the other hand, purification of the reaction products is usually very hard/impossible. It is therefore necessary to very carefully optimise the synthetic conditions, *i.e.* determine exact composition, heating temperature *T*, heating time *t*, number of grinding/heating cycles.

Manual grinding facilitates the homogenisation of reactants at the particle level (typically 10^{-6} - 10^{-4} m), which is large compared to the atomic scale at which reactions take place.[3] Subsequently a large amount ion-mixing by diffusion is required to reach the thermodynamic equilibrium and to form the desired product; thus the need for prolonged reaction times at high temperatures, typically approaching 1273K (*i.e.* 1000 °C).

The reaction itself occurs at the interface of two or more particles. The first step is the formation of small product crystallites, called *nucleation*. Nucleation of sufficiently large size (multiple unit cells) is critical to form stable crystallites that do not disintegrate spontaneously. The positive surface energy of the nuclei must be counterbalanced by the negative free energy, associated with the formation of the product. After nucleation the particles must grow until a homogenous material (on the atomic scale) is obtained. Continued growth of the product particles is complicated by the presence of the product material itself; it becomes a barrier between the reactants, which the latter have to pass through. As the product layer grows, the length of the diffusion pathway increases reducing the rate of the reaction. Besides temperature and time, the particle size is a crucial parameter. The smaller the particle, the higher the surface to volume ratio, making both nucleation and diffusion easier and increasing reactivity. Repeated intermediate grinding and subsequent refiring is commonly used, to break up particles and interfaces and enhance kinetics. The addition of materials with a low melting temperature results in flux formation. These can act as transporting agents and are effective in increasing reaction rates, which can help to lower reaction temperatures.

2.2.1 Particularities of reactions conducted during this project

Most materials used during this project are highly air- and moisture-sensitive. Consequently, considerable effort was made to control the atmosphere of reactants and reaction products

by storing and handling all materials under inert gases in dry boxes. Measurements were either performed in dry boxes or air-tight measurement kits. The reactions were carried out using the following general procedure:

- Weighing, mixing and grinding of reagents in glove box
- Placement of mixture in carbon coated quartz tube as powder
- Evacuation and consequent sealing of quartz tube in propane/oxygen flame
- Heating/firing of the reaction mixture
- Opening the reaction vessel in the glove box

Carbon coated tubes can easily be manufactured by rinsing quartz tubes with acetone and subsequent heating in a propane/oxygen flame.

2.3 Crystal lattice and unit cell

Crystalline materials with a long-range ordering of the atoms can best be described by a lattice of repeating unit cells. The lattice is built by elementary parallelepipeds, called unit cells, which are equal in size and content. Once the size and content of one unit cell are established, the structure of the whole crystal can be reconstructed by repeating the unit cell in all three dimensions along the unit cell vectors.[4]

The unit cell can be described by the six lattice parameters: *a*, *b*, *c*, α, β and γ. The lengths of the unit cell edges are represented by *a*, *b* and *c*, while the angles between them are described by α, β and γ.

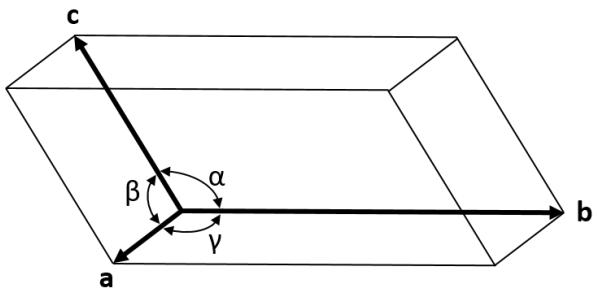

Figure 8: Schematic representation of a unit cell, with cell parameters, a, b, c and the angles α, β and γ.

2.3.1 Miller indices

Sets of crystallographic planes can be constructed and referred to using the notation of Miller indices (*hkl*). Each set of crystallographic planes is parallel to each other and equally spaced, as depicted in Figure 9.

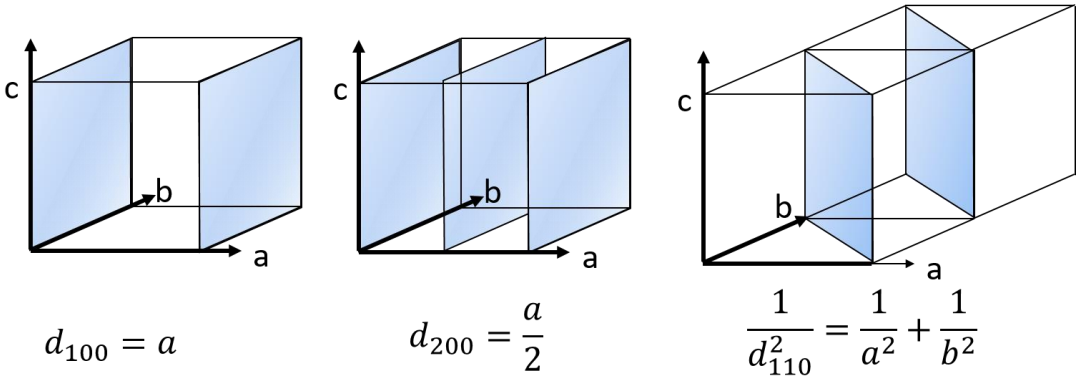

Figure 9: Real space representation of the (100), (200) and (110) planes in a cubic unit cell.

The distances of the planes can be easily calculated and used to determine the unit cell dimensions (see below). Reciprocal space is a construct used to illustrate and understand crystal structures and corresponding diffraction phenomena. A reciprocal lattice can be built orthogonal to the direct lattice, using the three vectors **a***, **b*** and **c***, which satisfy following conditions:[5]

$$\mathbf{a}^*\mathbf{b} = \mathbf{a}^*\mathbf{c} = \mathbf{b}^*\mathbf{a} = \mathbf{b}^*\mathbf{c} = \mathbf{c}^*\mathbf{a} = \mathbf{c}^*\mathbf{b} = 0 \quad (1)$$

$$\mathbf{a}^*\mathbf{a} = \mathbf{b}^*\mathbf{b} = \mathbf{c}^*\mathbf{c} = 1 \quad (2)$$

Importantly the infinite set of lattice planes in direct space is replaced by a single vector in reciprocal space, while the symmetry of the lattice is conserved. The Miller indices can be used to notate directions and label reflections in reciprocal space. The relation between the direct space crystal lattice and the diffraction pattern in reciprocal space is shown in Figure 10.

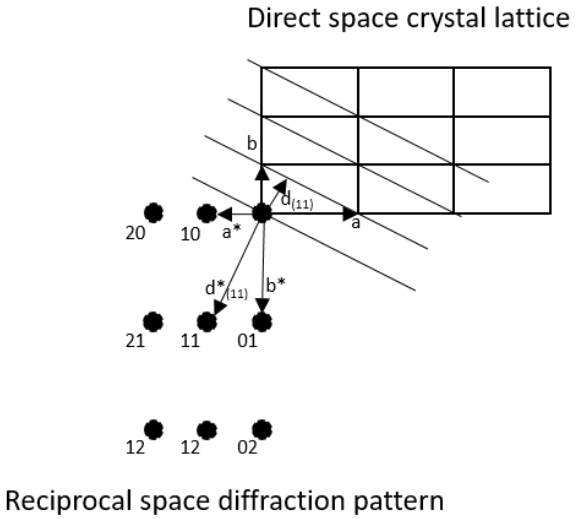

Figure 10: Relationship between direct and reciprocal space.

2.4 Diffraction

2.4.1 Scattering

Scattering describes the interaction of a point object with a wave (*e.g.* electromagnetic wave).[5] The scattering object becomes the source of a new wave, which spreads in all direction. Figure 11 sketches the interaction of an incident wave front with an array of point objects which are the source of new waves.

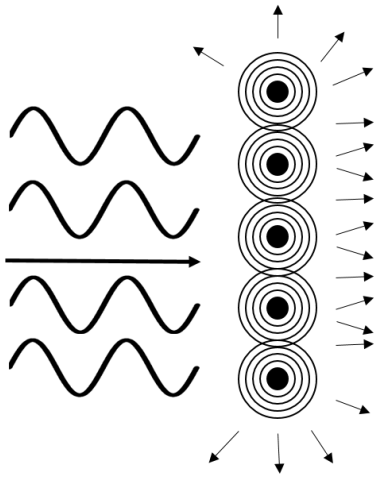

Figure 11: Diffraction of waves at a grating (e.g. water waves, visible light, X-ray radiation, neutron radiation). Every diffracting object (e.g. obstacle, optical slit) acts as a secondary source of spherical radiation.

The result of multiple scattering objects with a wave front, is the formation of multiple waves which can interact with each other, depending on their relative phase difference Δ, the number *n* and the wavelength *λ*.

$$\Delta = n\lambda \quad (3)$$

Two extremes of equation (3) need to be considered: (a) given that *n* is an integer number, the waves are completely in phase, as in shown in Figure 12(a) describing two waves with the same wavelength exemplarily. Constructive interference of the two waves occurs and the amplitude of the resulting wave is the doubled amplitude of the initial waves. (b) for values of *n*= $\frac{1}{2}, \frac{3}{2}$… the two waves are completely out of phase (Figure 12(b)). They cancel each other out, a process called destructive interference. Constructive and deconstructive interference occur only on periodically arrayed point scatterers.

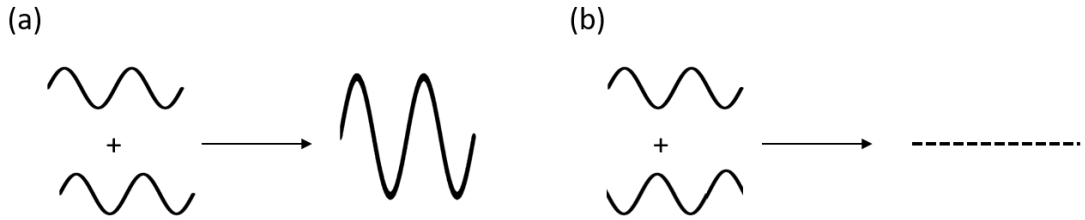

Figure 12 (a) Constructive interference of two waves, which are in phase; (b) deconstructive interference by two waves which are completely out of phase.

2.4.2 Laue equations

The geometry of a lattice with respect to constructive interference leading to diffraction was first given by Max von Laue in form of three equations which must be simultaneously satisfied, for diffraction to occur.

$$a\,(\cos(\psi_1) - cos(\varphi_1) = h\,\lambda \quad (4)$$

$$b\,(\cos(\psi_2) - cos(\varphi_2) = k\,\lambda \quad (5)$$

$$c\,(\cos(\psi_3) - cos(\varphi_3) = l\,\lambda \quad (6)$$

with the unit cell dimension *a*, *b* and *c*, the incident angle ψ, the angle of the diffracted beam φ, the Miller indices *h*, *k*, *l* and the wavelength λ. An illustration is given in Figure 13. The Laue equations state that a periodic lattice produces strong constructive interference peaks only at specific angles, which are dependent on the wavelength λ and the distance between the lattice points, which are given in form of the Miller indices *h*, *k*, *l*.

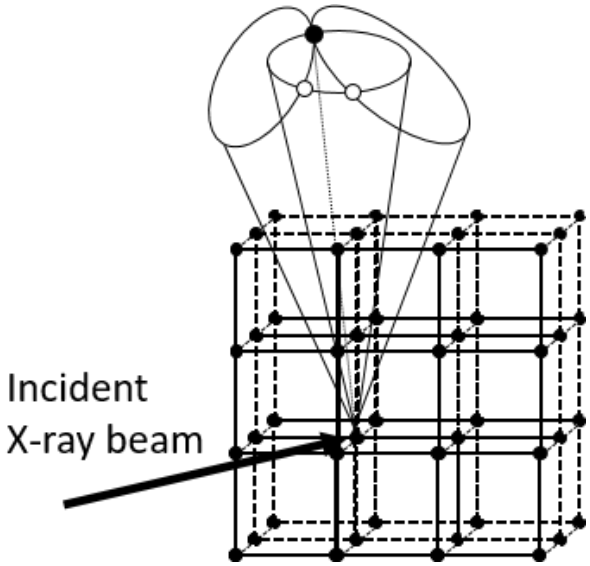

Figure 13: Illustration of the Laue equations. Each of the cones satisfy one of the Laue equations. Where two spheres intersect, two equations are met and weak constructive interference occurs (hollow sphere). All three conditions are met where all three cones overlap (black sphere), strong constructive interference can be expected.

2.4.3 Bragg's law

Bragg's law[6] is a convenient, although not completely rigorous, model to illustrate the relationship between the diffraction angle, wavelength and interplanar spacing *d* in a crystallite. It is assumed that the crystallographic planes act as a series of crystallographic mirrors, which are equidistant and parallel to each other. The incident and reflected waves form an angle θ with the planes. Only at specific θ angles constructive interference can occur. The waves are mirrored on the first and second plane, as illustrated in Figure 14, introducing a phase difference Δ between the pair of waves.

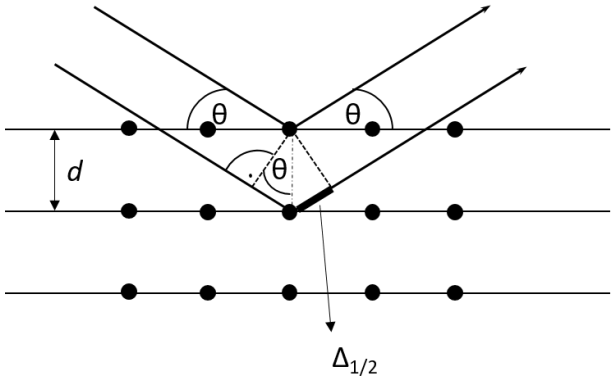

Figure 14: Geometrical interpretation of Bragg's law.

Constructive interference will only occur, when the phase difference Δ between the two waves corresponds to an integer *n* multiplied by the wavelength *λ*

$$\Delta = n\,\lambda \quad (7)$$

The half phase difference $\Delta_{1/2}$ in Figure 14 can be geometrically related to

$$\Delta_{\frac{1}{2}} = \sin(\theta)\,d \quad (8)$$

And the full phase difference Δ:

$$\Delta = 2d\sin(\theta) \quad (9)$$

Equating equations (7) and (9) gives the famous Bragg's law, as the condition for Bragg reflections:

$$2d\sin(\theta) = n\lambda \quad (10)$$

2.4.4 Scattering of X-rays by electrons

Diffraction occurs only when the wavelength and the separation of the lattice points are in the same order of magnitude. The X-ray region of the electromagnetic spectrum, with

wavelength 0.01 nm < λ < 10 nm, is therefore suitable to study the array of atoms, which typically have interatomic distances of 1.5-2.5 Å. In a crystalline material the periodic array of unit cells leads to constructive and deconstructive interferences, which can increase the amplitude of the resulting wave by many orders of magnitude. Each electron in an atom is a point scatterer, as X-rays are electromagnetic waves with an oscillating electric field. The oscillating field exerts a force on the electron, as it is a charged particle, and accelerates and decelerates the electron. Acceleration and deceleration of charged particles results in the emission of electromagnetic radiation, spreading in all directions. The wavelength and amplitude of the emitted wave is equal to the incident wave, resulting in coherent scattering. The following processes occur while X-ray interacts with physical matter:

(a) Coherent scattering: incident wavelength and resulting wavelength are equal
(b) Incoherent scattering: the wavelength of the resulting wave is increased, as energy is lost during the interaction of the photon with core electrons (Compton effect)
(c) Absorption of the X-rays: loss of photon energy due to photoelectric effect of ionization.

The atomic scattering factor (or form factor) is a measure for the X-ray scattering power of each atom and exhibits a dependence on the atomic number *Z* and the direction of scattering with respect to the incident wave. The electrons are radially distributed around the nuclei, which can be schematically sketched as in Figure 15.

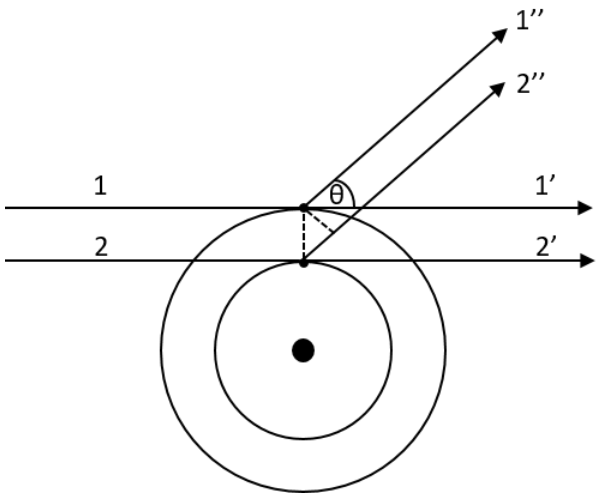

Figure 15: Coherent scattering of X-rays by the radially distributed electrons of an atom. A path difference is introduced, when θ deviates from 0 °, introducing deconstructive interference.

Increase of the phase angle θ leads to the introduction of a path difference and to a gradually decaying amplitude of the scattered beam. The angular dependency of the intensity of the scattered X-ray is given by the Thomson equation:

$$I \propto \frac{1}{2}(1 + \cos^2(2\theta)) \quad (11)$$

Scattering is thus strongest in parallel with the incident beam and weakest at 90 °. As the scattering power of an atom increases with the number of electrons present, powder X-ray diffraction (PXRD) patterns are dominated by the atoms with greater number of electrons. The form factors of atoms are tabulated in the *International Tables for X-ray Crystallography* against (sinθ/λ) to include both the effects of angle and wavelength dependency.[7]

2.5 Structure solution of crystalline materials

Powder patterns are characterized by two principle features:

(a) Position of the reflections → dimensions of unit cell
(b) Intensity of the reflections → contents of unit cell

The Bragg equation relates the distance of the crystallographic planes to the scattering angle 2θ. By measuring the diffraction maxima of a crystalline material in dependence on 2θ one can calculate the interplanar distances *d*. Depending on the geometry of the unit cell the *d* spacing is related to the unit cell dimensions *a*, *b*, *c* and the *hkl* Miller indices of the respective reflection; thus enabling the determination of the unit cell sizes. Exemplarily for a cubic cell:[5]

$$\frac{1}{d_{hkl}} = \sqrt{\frac{h^2 + k^2 + l^2}{a^2}} \quad (12)$$

For an orthorhombic cell:

$$\frac{1}{d_{hkl}} = \sqrt{\frac{h^2}{a^2} + \frac{k^2}{b^2} + \frac{l^2}{c^2}} \quad (13)$$

For a hexagonal cell:

$$\frac{1}{d_{hkl}} = \sqrt{\frac{4}{3a^2}\left(\frac{h^2+hk+k^2}{a^2}\right) + \frac{l^2}{c^2}} \quad (14)$$

The intensity of a reflection with the Miller indices *h*, *k*, *l* (represented by a vector h in three dimensions) is determined by the content of the unit cell, given by a function called structure amplitude **F**(h):

$$\mathbf{F}(\mathrm{h}) = \sum_{j=1}^{n} g^j t^j(s) f^j(s) \exp\left(2\pi i \mathrm{h} \mathrm{x}^j\right) \quad (15)$$

n: total number of atoms

s: $\sin\theta_{hkl}/\lambda$

g^j: occupancy factor of the jth atom

t^j: temperature dependent displacement factor of the jth

$f^j(s)$: atomic scattering factor as a function of $\sin(\theta)/\lambda$

x^j: fractional coordinates of the jth atom

If the dimensions of the unit cell, fractional coordinates, displacement factors and occupancies of the atoms are known, a full PXRD pattern can be calculated.

2.5.1 Relationship between direct and reciprocal space

The Fourier transformation is the tool to relate the structure factor (reciprocal space) to the corresponding electron density ρ (direct space) in the unit cell:

$$\rho_{x,y,z} = \frac{1}{V}\sum_{h=-\infty}^{h=+\infty}\sum_{k=-\infty}^{k=+\infty}\sum_{l=-\infty}^{l=+\infty} F_{hkl}\exp\left[-2\pi i(hx+ky+lz)\right] \quad (16)$$

The diffraction experiment recovers only the absolute structure amplitude $\left|F_{hkl}^{obs}\right|$, while the corresponding information about the phase is lost, leading to the well-known phase problem in crystallography. Compared to single crystal diffraction experiments, PXRD patterns are the one-dimensional projections of a three-dimensional diffraction pattern. This complicates the determination of crystal structures from powder further.

2.5.2 The Rietveld method

Powder diffraction patterns contain a lot of information about the structure of the material (*e.g.* long range ordering, particle size, crystallinity). But due to the phase problem the construction and refinement of structural models are far from trivial. The Rietveld method is an attempt to overcome this problem by using an appropriate starting model (which might be very difficult to find) and refining structural parameters until the calculated pattern matches the observed data as closely as possible. If the model was refined fully, the difference between the calculated and the observed profiles should be close to zero. The Rietveld method minimizes the function Φ between an observed PXRD pattern against a model (calculated) pattern using non-linear least square refinement algorithms (see next section):[8]

$$\Phi = \sum_{i=1}^{n} w_i\left(Y_i^{obs} - Y_i^{calc}\right)^2 \quad (17)$$

With *n* being the total number of data points and w_i the weight assigned to the *i*th data point. Once a suitable starting model is introduced, parameters can be refined whilst keeping other at constant values. When these parameters are refined to a stable minimum, new parameters can be refined sequentially until the difference between the calculated pattern and the observed data points becomes negligible. Correlation of parameters is a serious problem, such as the correlation between wavelength, zero offset and cell parameters, potentially leading to false minima and unphysical models.

2.5.3 Non-linear least square refinement

Linear least-square algorithms are used to calculate the solution of overdetermined systems, *i.e.* the number of simultaneous equations *n* >> number unknown parameters *m*. Each equation is a linear function with respect to the parameters x_1, x_2, …, x_m. The overall aim is to minimise the sum of the squares of the residuals. The set of equations can be represented as:

$$f_1(x_1, x_2, \dots, x_m) = y_1 \quad (18)$$

$$f_2(x_1, x_2, \dots, x_m) = y_2 \quad (19)$$

$$f_m(x_1, x_2, \dots, x_m) = y_m \quad (20)$$

and is more conveniently written in matrix notation

$$\mathbf{Ax} = \mathbf{y} \quad (21)$$

with the design matrix **A**, vector of unknowns **x** and the set of observations **y**

$$\mathbf{A} = \begin{pmatrix} a_{11} & a_{12} & \dots & a_{1m} \\ a_{21} & a_{22} & \dots & a_{2m} \\ \dots & \dots & \dots & \dots \\ a_{n1} & a_{n2} & \dots & a_{nm} \end{pmatrix}; \mathbf{x} = \begin{pmatrix} x_1 \\ x_2 \\ \dots \\ x_m \end{pmatrix}; \ \mathbf{y} = \begin{pmatrix} y_1 \\ y_2 \\ \dots \\ y_m \end{pmatrix} \quad (22)$$

The vector of unknowns **x** can be solved according to the following expression:

$$\mathbf{x} = \left(\mathbf{A^T A}\right)^{-1} (\mathbf{A^T y}) \quad (23)$$

In the case of Rietveld refinement, the set of equations are not linear in respect to each other. But each equation can be expanded in a Taylor series as:

$$\left(\frac{\partial Y}{dx_1}\right) \partial x_1 + \left(\frac{\partial Y}{dx_2}\right) \partial x_2 + \dots + \left(\frac{\partial Y}{dx_m}\right) \partial x_m = Y_o - Y_c \quad (24)$$

which is linear with respect to the shifts δ_i. In matrix notation this is expressed as:

$$\mathbf{A} \cdot \boldsymbol{\delta}\mathbf{x} = \mathbf{y} \quad (25)$$

The full set of equations describes one observation Y_o per row and one parameter m_i per column:

$$\begin{pmatrix} \frac{\partial Y_1}{dx_1} & \frac{\partial Y_1}{dx_2} & \cdots & \frac{\partial Y_1}{dx_m} \\ \frac{\partial Y_2}{dx_1} & \frac{\partial Y_2}{dx_2} & \cdots & \frac{\partial Y_2}{dx_m} \\ \cdots & \cdots & \cdots & \cdots \\ \frac{\partial Y_n}{dx_1} & \frac{\partial Y_n}{dx_2} & \cdots & \frac{\partial Y_n}{dx_m} \end{pmatrix} \begin{pmatrix} \partial x_1 \\ \partial x_2 \\ \cdots \\ \partial x_n \end{pmatrix} = \begin{pmatrix} (Y_o - Y_c)_1 \\ (Y_o - Y_c)_2 \\ \cdots \\ (Y_o - Y_c)_n \end{pmatrix} \quad (26)$$

And can be solved in the exact same way according to

$$\boldsymbol{\partial}\mathbf{x} = \left(\mathbf{A}^{\mathbf{T}}\mathbf{W}\mathbf{A}\right)^{-\mathbf{1}}(\mathbf{A}^{\mathbf{T}}\mathbf{W}\mathbf{y}) \quad (27)$$

The square matrix **W** introduces individual weights w_i for each data point n. The solution to this set of equations describes the shift, which needs to be applied to each parameter x_i in order to minimise the difference between Y_c and Y_o. The Rietveld method is an iterative algorithm, in which an initial set of parameters $\mathbf{x_0}$ is used as a starting point for the refinement. The refined parameters **x** are calculated as:

$$\mathbf{x} = \mathbf{x_0} + \boldsymbol{\partial}\mathbf{x} \quad (28)$$

and then used as the starting set of parameters for a new cycle of refinement until convergence is detected. If the initial set of parameters $\mathbf{x_0}$ is too far off the correct values, convergence can be difficult to achieve, as the non-linear least squares may diverge and become unstable or a false local minimum can be found, as exemplarily shown in Figure 16.

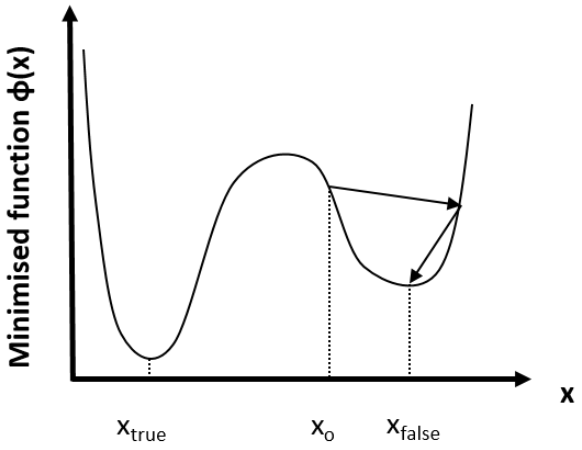

Figure 16: The initial set of parameters x_o are chosen too far away from the correct set of parameters x_{true}, the non-linear least square refinement results in a false minimum.

The standard deviations for each parameter x_i can be calculated according to:

$$\sigma(x_i) = \sqrt{\frac{(\mathbf{A^T W A})^{-1}_{jj} \sum_{i=1}^{n} w_i (y_i)^2}{n-m}}, j = 1, \ldots, m \quad (29)$$

Correlation between two pairs of free least square variables x_i and x_j can be evaluated by considering the correlation coefficients (ρ_{ij}):

$$\rho_{ij} = \frac{\left(\mathbf{A^T W A}\right)^{-1}_{ij}}{\sqrt{(\mathbf{A^T W A})^{-1}_{ii} (\mathbf{A^T W A})^{-1}_{jj}}} \quad (30)$$

A correlation of 1 indicates fully correlated parameters, while $\rho < 0.5$ is associated with little to no correlation. Correlated parameters can make refinements unstable and it is advisable to exclude those from the refinement.

Non-linear least square functions are used in the Rietveld method to minimise the function in respect to the following parameters: background function, sample displacement, peak shape function, unit cell dimension, preferred orientation, scale factors, fractional coordinates of the atoms, occupancy of the individual sites, atomic displacement parameter.[5] As non-linear least-square algorithms are iterative and no fixed endpoints are defined, the progress of the refinement can be assessed by different figures of merit (f.o.m.): the profile residual R_p, the weighted profile residual R_{wp}, or goodness of fit (χ^2). [9]

$$R_P = \sum_{i}^{n} \frac{\left|Y_i^{obs} - Y_i^{calc}\right|}{\sum_i^n Y_i^{obs}} \times 100\ \% \quad (31)$$

$$R_{wp} = \sum_{i}^{n} \left(\frac{w_i (Y_i^{obs} - Y_i^{calc})^2}{\sum_i^n w_i \left(Y_i^{obs}\right)^2} \right)^{\frac{1}{2}} \times 100\,\% \quad (32)$$

$$x^2 = \sum_{i}^{n} \frac{\left(Y_i^{obs} - Y_i^{calc}\right)^2}{n-p} = \left(\frac{R_{wp}}{R_{exp}} \right)^2 \quad (33)$$

The smaller those parameters, the closer the model is related to the observed data. The figures of merit cannot be taken as absolute values to judge the quality of a refinement as they strongly depend on the quality of the data. It can be therefore useful to compare the figures of merit obtained by the Rietveld refinement to the result of a simple profile fit, *e.g.* Pawley fit to make a final assessment:

$$(\text{f. o. m.})_{\text{real}} = \frac{(\text{f. o. m.})_{\text{Riet}}}{(\text{f. o. m.})_{\text{Pawley}}} \quad (34)$$

2.5.4 Indexing

The determination of the unit cell parameters is relatively straight forward for cubic structures. But without previous knowledge of the crystal system, it can be very hard to index a PXRD pattern to the correct unit cell by hand, as multiple solutions are possible. This task is complicated by inaccurate peak position (zero-angle shift, peak broadening, poor crystallinity), potential presence of impurity phases or insufficient signal/noise ratio, to resolve weak reflections. Autoindexing programs like DICVOL or TREOR are used to index patterns from scratch and make suggestions about possible unit cell dimensions and corresponding space groups. But the user still must make a decision which unit cell to use based on systematic absences, figure of merit and/or crystallographic/chemical knowledge about the sample.

Once a satisfactory space group assignment has been achieved, the crystal structure solution can be attempted. If crystallographic models for related phases, parent phases, or structural analogues exist, Rietveld refinement is a powerful tool to refine the model. In the case where the experimenter has no knowledge about the crystal structure, *ab initio* algorithms for the solution of powder diffraction data have been developed, *e.g.* Patterson method, simulated annealing or the charge flipping algorithm. During this work in particular the charge flipping algorithm was used and will be briefly described below.

2.5.5 Charge flipping

The charge flipping algorithm is a dual-space method for *ab initio* determination of an approximate scattering density on a discrete grid. It requires only lattice parameters of the unit cell and reflection intensities as input parameters. The algorithm switches back and forth between direct and reciprocal space, as shown in the Fourier cycle in Figure 17.[10] This cycle includes four principle steps:

(a) Real space modification of the electron density
(b) Fast Fourier transformation to reciprocal space
(c) Reciprocal-space modification of the calculated structure factors
(d) Inverse fast Fourier transformation to recover the electron density

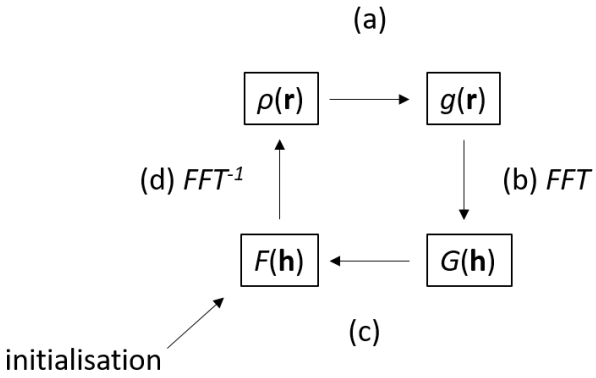

*Figure 17: Schematic representation of switching between direct and reciprocal space, i.e., Fourier cycle; with the the structure factor F(***h**), the electron density *ρ*(**r**), *temporary electron density g*(**r**) *and temporary structure factor G*(**h**)*.*

The charge flipping algorithm is a special way to perform the real space and reciprocal space modifications. Initially a random phase set ($\varphi(\mathbf{h})$) is chosen, which is used to calculate the structure factor $F(\mathbf{h}) = F_{obs}(\mathbf{h})\exp[i\varphi(\mathbf{h})]$.

The electron density $\rho(\mathbf{r})$ is obtained from this initialised structure by inverse fast Fourier transformation. A positive threshold δ is used to partition the electron density ρ into two regions: $\rho = \rho_1 + \rho_2$ with $\rho_1 > \delta$ and $\rho_2 < \delta$. The charge of the low density region ρ_2 is flipped to give the new electron density $g(\mathbf{r})$ with $g = \rho_1 - \rho_2$, which is used to calculate the corresponding structure factors $G(\mathbf{h})$ by Fourier transformation. Structure factors $F(\mathbf{h})$ are calculated from $G(\mathbf{h})$ by combining the phases φ_G with the experimental amplitudes $F_{obs}(\mathbf{h})$. Finally, the electron density $\rho(\mathbf{h})$ is recovered by inverse Fourier transformation and the cycle is repeated until convergence is detected.

2.6 Neutron powder diffraction (NPD)

Neutron powder diffraction (NPD) is a powerful to complement PXRD techniques. Due to the wave-particle duality, a neutron beam can be treated as a wave and diffraction can occur at a periodic array of point scatterers. Neutrons are scattered by the nucleus of an atom, which are point scatterers, compared to the scattering of X-rays by electrons. Therefore, the scattering factor shows no dependence on 2θ. This makes it easier to obtain high resolution data in the small *d* spacing region.

In PXRD analysis it can be challenging to resolve the contributions of light elements to the structure factor $F(\mathbf{h})$, if atoms with significantly higher atomic numbers Z are present. This can be related to the form factor of atoms, which rises monotonously with the atomic number Z (red plot), as shown in Figure 18.

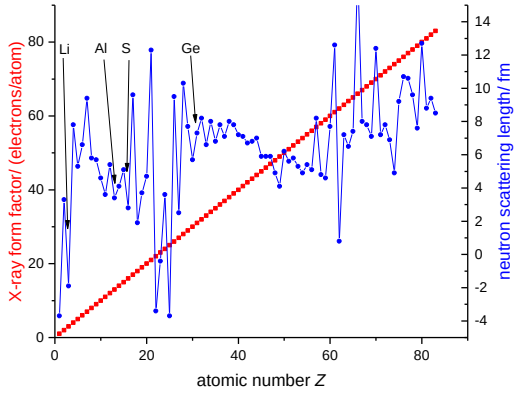

Figure 18: Comparison plots of X-ray form factor and neutron scattering length for the elements as a function of the atomic number Z.[11]

In contrast the neutron scattering lengths show no such dependence on Z. Lithium, titanium, hydrogen and manganese have negative scattering lengths. This helps to unambiguously locate and identify these species in Fourier difference maps in the presence of significantly heavier atoms or atoms with very similar Z. Additionally neutrons, which have a magnetic spin (s = ½), are scattered by magnetic moments, making NPD an invaluable tool for the investigation of magnetic structures and properties.

2.7 Refinement of Powder Diffraction data

It is a non-trivial task to extract as much structural information from a powder diffraction pattern as possible. Initially it must be established which and how many crystalline phases are present in the studied sample. This can be done most easily by matching the recorded pattern against a database of known materials using programs like HighScore Plus.[12] Any

unindexed reflection can be indicative of a new/unknown crystalline phase and indexing of the unit cell is then essential. Once the identity of all phases is established, the individual components of the overall model can be refined using the Rietveld method. Typically, the background is fitted using a Chebyshev polynomial function while the reflections are modelled using a Pseudo Voigt peak shape for laboratory PXRD data or a Pearson VII function for synchrotron SXRD data. The non-ideality of the experimental setup can be adjusted by refining simple axial model parameter and the zero error, when measuring in capillary mode. After these non-structural parameters have been established, the Rietveld method can be applied to refine the structural parameters of interest: lattice parameter, atomic positions, displacement parameters, occupancies, crystallite size.

2.8 AC-impedance

2.8.1 Principle of measurement

Alternating current impedance spectroscopy (AC-impedance spectroscopy) or electrochemical impedance spectroscopy (EIS) is a method to study the electrochemical properties of materials. The general approach is to apply a stimulus (voltage or current) across the sample and measure the response (current or voltage) over a large range of frequencies. Typically, a single-frequency voltage $V(t)$ with the amplitude V_m is applied and the responsive current $I(t)$ with the amplitude I_m and the phase difference θ is recorded.

$$V(t) = V_m \sin(\omega t) \quad (35)$$

$$I(t) = I_m \sin(\omega t + \theta) \quad (36)$$

An electrical field can interact with a solid in two ways, which both result in a current I:

(a) Reorientation of defects with electric dipole moments:
$i = dD/dt$, with D being the electric displacement according to
$D = \varepsilon_0 E + P$, where E is the electric field, ε_0 the permittivity of free space and P the polarization of the dielectric material

(b) Translational motion of charge carriers:
$i = \sigma E$, with σ being a DC (direct current) conductivity

Impedance Z is the ability of a circuit to resist an alternating current and is related to the voltage V and the current I by Ohm's law:

$$Z(t) = \frac{V(t)}{I(t)} = \frac{V_0 \sin(\omega t)}{I_0 \sin(\omega t + \theta)} = Z_0 \frac{\sin(\omega t)}{\sin(\omega t + \theta)} \quad (37)$$

Responses of resistor *R*, capacitance *C* and inductance *L* in a circuit can be calculated as:[13]

$$V(t) = RI(t) \quad (38)$$

$$I(t) = \frac{dV(t)}{dt}C \quad (39)$$

$$V(t) = \frac{dI(t)}{dt}L \quad (40)$$

The combination of many such elements results in very complex problems in the time domain. Fourier transformations simplify these problems in the frequency domain, where *i* is the imaginary number (i^2 = -1):

$$I(i\omega) = C \cdot \omega \cdot i \cdot V(i\omega) \quad (41)$$

$$I(i\omega) = \frac{V(i\omega)}{L \cdot \omega \cdot i} \quad (42)$$

Using the complex quantity *Z(iω)* as the "impedance function", Ohm's law can be reformulated in the frequency domain to

$$Z(i\omega) = \frac{V(i\omega)}{I(i\omega)} \quad (43)$$

where the resistance is expressed by $Z_{resistor} = R$, the capacitance is expressed by the complex function $Z(i\omega) = 1/(Ci\omega)$ and the inductance is $Z(i\omega) = L\, i\omega$. For this Ohm's law relationship, the impedance of a system can be calculated using the rules used for multiple resistors.

Impedance is a more general concept than resistance, as it takes phase differences into account and can be represented in a complex plane with the Euler's relationship,

$$Z(\omega) = |Z| \exp(i\theta) = |Z|(\cos\theta + i\, sin\theta) = Z' + iZ'' \quad (44)$$

This expression can conveniently be plotted in a complex plane plot, with the phase difference θ represented as the angle between *Z'* and *Z''* (Figure 19). It can be noted that the system is time-invariant, but frequency-dependent (*ω*).

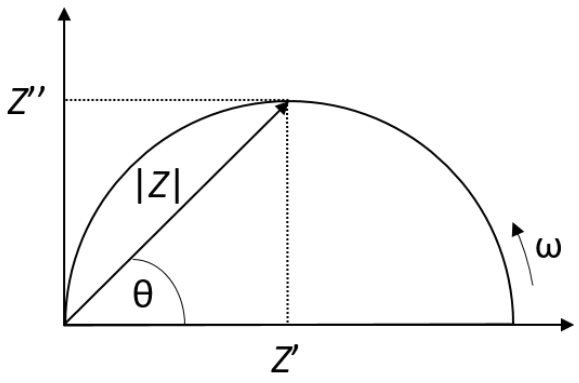

Figure 19: Representation of the impedance Z in a complex plane plot using polar coordinates.

The modulus $|Z|$ is the magnitude of the vectoral sum of *Z'* and *Z''*.

$$|Z| = [(Z')^2 + (Z'')^2]^{\frac{1}{2}} \quad (45)$$

Z' is the real part of the impedance and is also called resistance *R*. For purely resistive behaviour of the circuit, the phase difference is zero and the impedance is completely described by the real resistance *R* with the imaginary part *Z''* equal to zero. Consequently, the impedance is frequency-independent. For systems which are not purely resistive but also comprise capacitance and inductance related elements, *Z'* and *Z''* are variable functions of the frequency *ω*. The imaginary part *Z'* (also called reactance *X*) is the sum of inductive reactance, X_L and capacitive reactance, X_C:

$$Z'' = X = X_L + X_C = \omega \cdot L - \frac{1}{\omega \cdot C} \quad (46)$$

2.8.2 Modelling AC-impedance data using equivalent circuit elements

Data obtained by AC-experiments are typically modelled by using combinations of ideal elements (resistors *R*, capacitors *C*, inductors *I*) in an equivalent circuit. These elements can be combined in parallel or series to emulate the measured physical responses. Careful interpretation of the equivalent circuits enables the assignment of physical properties to the elements. Simple RC elements (combination of a resistor with a capacitor in parallel) are adequate to describe electrochemical responses of materials (*e.g.* bulk conductivity, grain boundary contributions, electrode polarization). Each RC element is characterised by a relaxation time or time constant *τ* and can be related to a distinct physical response.

$$\tau = RC = 1/\omega_{max} \quad (47)$$

In practice the capacitance values of the RC elements are calculated and then related to physical phenomena. Table 1 gives an overview of typical capacitance values and physical interpretations.

Table 1: Capacitance values and typical corresponding phenomena.[14]

Capacitance/ F	Phenomenon responsible
10^{-12}	Bulk
10^{-11}	Minor, second phase
$10^{-11} – 10^{-8}$	Grain boundary
$10^{-10} – 10^{-9}$	Bulk ferroelectric
$10^{-9} – 10^{-7}$	Surface layer
$10^{-7} – 10^{-5}$	Sample-electrode interface
10^{-4}	Electrochemical reactions

Typically, more than one RC element in an equivalent circuit must be used to explain the measured data. The brickwork model of a ceramic (Figure 20) is instructive to estimate the capacitance values. An ideal parallel capacitor with area *A*, the distance between the plates *l* and a permittivity ε' has a capacitance *C*:

$$C = \frac{\varepsilon' \varepsilon_0 A}{l} \quad (48)$$

with ε_0 (8.854 x 10^{-12} Fm^{-1}) as the permittivity of free space. The brickwork model describes the origin of different responses in a ceramic.[15] A ceramic consists of conducting “bricks” (grains, bulk response), which are surrounded by resistive “mortar” (corresponding to the grain boundary response).

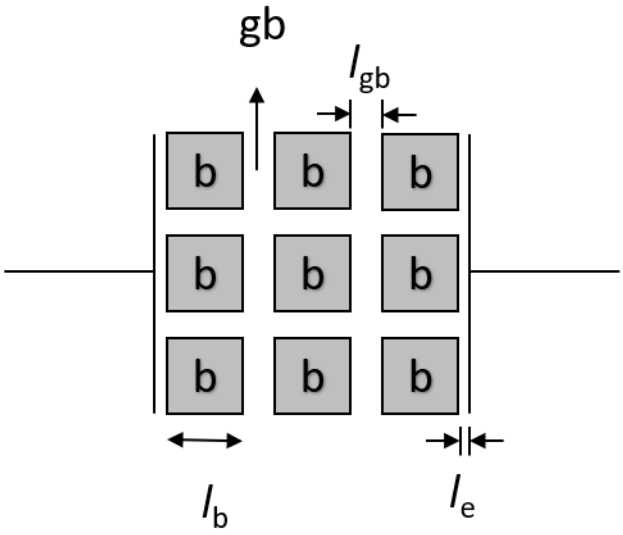

Figure 20: Brickwork model of a ceramic. The material consists of multiple bulk grains with a length l_b, grain boundaries of the thickness l_{gb} and grain-electrode distance of l_e.

A simulated AC-impedance spectrum of an idealized solid electrolyte with contributions from the bulk, the grain boundary and the ceramic-electrode interface is shown in Figure 21 (bulk resistance R_b: 20 kΩ, bulk capacitance C_b: 10^{-13} F, grain boundary resistance R_{gb}: 40 kΩ, grain boundary capacitance C_{gb}: 10^{-10} F, ceramci-electrode interface capacitance C_e). Clearly a spike at low frequencies and two semicircles can be distinguished which are associated with two different RC elements and a resistive element R. The resistance values of the RC elements can be established by reading the low frequency intercept of the respective semicircle with the x-axis. Capacitance values of 10^{-13} F and 10^{-10} F are obtained by evaluation of ω_{max}. Hence the two arcs could easily be assigned to bulk and grain boundaries respectively. The ceramic-electrode response is a spike, which is due to the polarization of the interface. This spike is commonly modelled by simple capacitors or constant phase elements (CPEs).

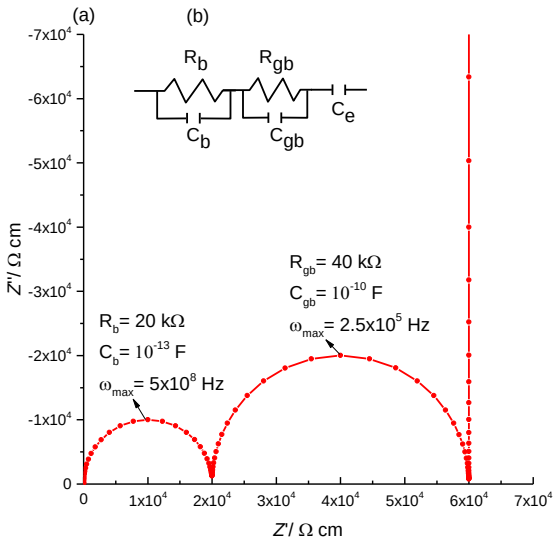

Figure 21: Simulated AC-impedance spectrum of two RC elements and a capacitor C in series.

Difficulties arise in the non-ideal behaviour of ceramics. The mathematical model treats each element as point elements. Actual responses in the real world exhibit always some degree of capacitance and inductance, because of their finite dimensions and distribution in space. Ceramics are characterised by inhomogeneous surfaces, surface defects, local charge distribution, adsorbed species and variable stoichiometries. Thus, the experiment gathers data over a certain range around a mean. This leads to a depression of the semicircle. Constant phase elements (CPE) are used to consider these irregularities of relaxation times by mixing elements from the ideal capacitor and the ideal resistor. They are treated mathematically in the following way:

$$Z_{CPE} = \frac{1}{Q_0(i\omega)^n} \quad (49)$$

Q_0 relates to $1/|Z|$ at ω=1, n describes the mixing of the ideal capacitor (n= 1) and the ideal resistor (n= 0).

Modelling of AC-impedance data with equivalent circuits does not lead to unambiguous results. In particular the use of CPEs with similar capacitance values can result in over-interpretation of data. As exemplified in Figure 22(a) the data of a depressed semicircle can be modelled using two RC elements with similar capacitance values in series (equivalent circuit (b)). But the same response can be modelled using equivalent circuit (c). Both equivalent circuits (b) and (c) result in the same set of data.

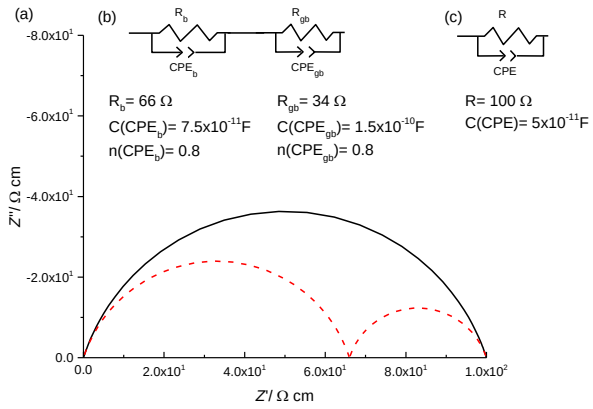

Figure 22: (a) The same set of data (single depressed semicircle) is calculated by using either the combination of two RC elements (b) or a single RC element (c). The response of the two individual RC circuits in (b) is plotted as red dashes.

It is therefore not sufficient to model the data to any equivalent circuit. An in depth understanding of the physical characteristics is essential to evaluate impedance data correctly.

2.8.3 Arrhenius behaviour of conductivity – activation energy

Ionic conductivity is a process, which can be described by reaction kinetics theory. A mobile ionic species must overcome an activation barrier, in order to jump from one interstitial minimum to the next minimum. The higher the temperature of the system the more energy each ion has and the more probable are hopping events. This temperature-dependent behaviour of conductivity can be linked to the activation barrier by the Arrhenius equation:

$$\sigma = A \exp\left(-\frac{E_a}{k_B T}\right) \quad (50)$$

with A as the the pre-exponential constant and k_B as the Boltzmann constant.

Rearrangement of the equation gives:

$$\ln(\sigma) = A + \left(-\frac{E_a}{k_B T}\right) \quad (51)$$

By plotting ln(σ) against 1/T one can obtain the activation barrier E_a, as the gradient of the regression fit. For solid electrolytes typically log(σ) is plotted against 1000/T.

2.9 DC polarization experiment

Solids can allow the flow of charge either by the movement of ions σ_{ion} and/or by electrical current σ_{elec} (electrons and holes). Solids can be classed to be either ionic, electronic or mixed

conductors. The transference number t_{elec} is a measurement of the electrical contribution to the overall conductivity σ_T and can be determined by a DC polarization experiment.

$$t_{elec} = \frac{\sigma_{elec}}{\sigma_T} = \frac{I_{elec}}{I_T} \quad (52)$$

Typically, the faces of the cylindrical pellet are covered with an ion-blocking electrode and a constant DC potential is applied; the resultant current is monitored as a function of time. The current versus time plots for an ideal ionic conductor and a mixed conductor are shown in Figure 23.

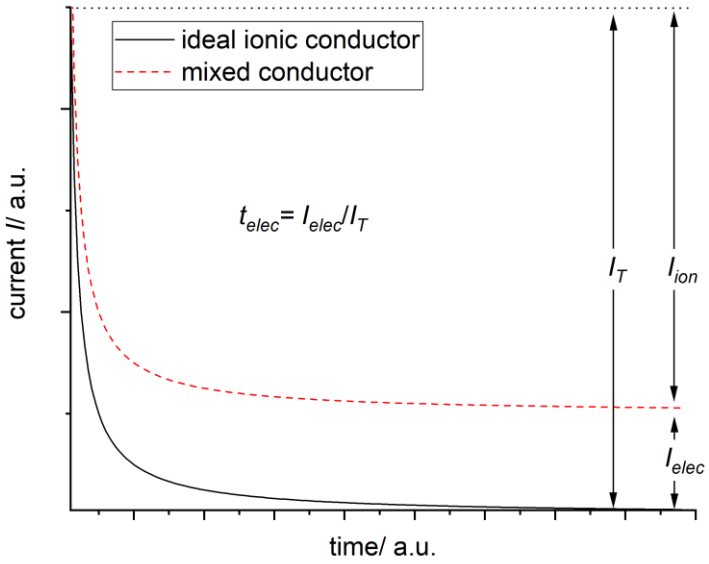

Figure 23: Schematic current versus time plot of a DC polarization experiment comparing an ideal ionic conductor (black) with a mixed conductor (red).

It is assumed that the initial peak current is due to a combination of ionic and electronic response and represents the total conductivity σ_T of the sample. This peak decreases rapidly with time due to polarization of the mobile ions across the pellet which impedes ionic movement and only electronic contributions to the conductivity is measurable. In an ideal ionic conductor, the electronic contribution is zero and thus the current approaches zero with time. In case of a residual current ≠ 0, the residual current is the electronic conductivity σ_{elec}. The transference number t_{elec} can easily be calculated by forming a ratio between the residual conductivity σ_{elec} and the total conductivity σ_T.[16]

During this project DC polarization experiments were conducted on pellets with a silver paste electrode. It was assumed that the silver electrode is completely Li^+ ion blocking, although it

is known that silver and lithium can form an alloy. Thus the results of these experiments have to treated with caution.

2.10 Differential scanning calorimetry

Differential scanning calorimetry (DSC) is a method to investigate endo- and exothermic phase transitions. In a DSC experiment the heat flow difference between the sample and a reference cell is measured as a function of temperature. Events such as phase transitions result in a change of heat flow between the sample and surrounding environment as they either emit energy (exothermic event) or require an input of energy (endothermic event) from the surroundings. This resultant heat flow difference between the sample and the reference cell is recorded and plotted against temperature.

2.11 References

1. Bärnighausen, H., Group-subgroup relations between space groups: a useful tool in crystal chemistry. *MATCH* **1980,** *9*, 139-175.
2. Müller, U., *Symmetry relationships between crystal structures : applications of crystallographic group theory in crystal chemistry*. 1st ed.; Oxford University Press: Oxford, 2013; p xvi, 332 p.
3. West, A. R., *Basic solid state chemistry*. 2nd ed.; John Wiley & Sons: New York, 1999; p xvi, 480 p.
4. Müller, U., *Inorganic Structural Chemistry*. John Wiley & Sons: 2007; Vol. 25.
5. Pecharsky, V. K.; Zavalij, P. Y., *Fundamentals of powder diffraction and structural characterization of materials*. 2nd ed.; Springer: New York, 2009; p xxiii, 741 p.
6. Bragg, W. H.; Bragg, W. L., The reflection of X-rays by crystals. *Proceedings of the Royal Society of London. Series A, Containing Papers of a Mathematical and Physical Character* **1913,** *88* (605), 428-438.
7. Crystallography, I. U. o., *International Tables for X-ray Crystallography*. Kynock Press: 1952.
8. Dinnebier, R. E.; Leineweber, A.; Evans, J. S., *Rietveld refinement: practical powder diffraction pattern analysis using TOPAS*. Walter de Gruyter GmbH & Co KG: 2018.
9. Young, R. A., *The rietveld method*. International union of crystallography: 1993; Vol. 5.
10. Oszlanyi, G.; Suto, A., The charge flipping algorithm. *Acta Crystallogr A* **2008,** *64*, 123-134.
11. Sears, V. F., Neutron scattering lengths and cross sections. *Neutron News* **1992,** *3* (3), 26-37.
12. Degen, T.; Sadki, M.; Bron, E.; König, U.; Nénert, G., The HighScore suite. *Powder Diffr.* **2014,** *29* (S2), S13-S18.
13. Orazem, M. E.; Tribollet, B., *Electrochemical Impedance Spectroscopy*. John Wiley & Sons, Inc.: 2008.
14. Irvine, J.; Sinclair, D.; West, A., Electroceramics: Characterization by Impedance Spectroscopy. *Adv. Mater.* **1990,** *2*, 132-138.
15. Kidner, N. J.; Perry, N. H.; Mason, T. O.; Garboczi, E. J., The brick layer model revisited: introducing the nano-grain composite model. *J. Am. Ceram. Soc.* **2008,** *91* (6), 1733-1746.
16. Agrawal, R. C., dc Polarisation: An experimental tool in the study of ionic conductors. *Indian J. Pure Appl. Phys.* **1999,** *37*, 294-301.

3 Metal sulphide based high-entropy stabilised rock salts

3.1 Introduction

A chemical reaction will proceed spontaneously and result in a stable phase, if the Gibbs free energy Δ*G* of the reaction is < 0. The Gibbs free energy Δ*G* is defined by the equilibrium constant *K*, the temperature *T* and the gas constant *R*:

$$\Delta G = -RT\ln K \qquad (1)$$

and further reformulated as

$$\Delta G = \Delta H - T\Delta S \qquad (2)$$

where Δ*H* describes the change in enthalpy, *T* the temperature and Δ*S* the change in entropy of the system. The concept of entropy stabilized phase formation[1] capitalises on the fact, that phase formation is dependent on the fine balance between the change of enthalpy and temperature dependent change of entropy during a reaction. At 0 K the entropy of a perfect crystal is zero and therefore the outcome of the reaction is completely dependent on the change of enthalpy Δ*H*.[2] With increasing finite temperature the change of entropy Δ*S* becomes more and more influential, until phase formation is governed by the entropic term at high temperatures. The reaction temperature *T* and the change of entropy Δ*S* are two variables accessible to experimental chemists. The configurational entropy S_{conf} of a system can be modified by manipulation of the composition (entropy of mixing). A system with *N* different species and the fractional composition x_i ($\sum_{i=1}^{N} = x_i$) has configurational entropy of:[3]

$$S_{conf} = -k_{\mathrm{B}} \sum_{i=1}^{N} x_i \ln(x_i) \qquad (3)$$

This relationship describes how configurational entropy is increased when more distinct ions are present. The entropic contribution Δ*S* to the Gibbs free energy Δ*G* at elevated temperatures becomes more significant the more different species are present (assuming no significant differences occur in the change of enthalpy Δ*H* due to different bonding interactions).

By quenching reaction mixtures of a multitude of different elements from elevated temperatures one can isolate phases which are enthalpically unstable at ambient temperature (but kinetically stable). This concept has successfully been exploited in the discovery of the high-entropy alloy family (HEA).[4-6] Exemplarily the high entropy alloy of equimolar CrMnFeCoNi crystallises in a single face-centred cubic (fcc) crystal structure even

though the individual metals exhibit different crystal structures: Cr and Fe crystallise with the body-centred cubic structure (bcc), Ni with a face-centred cubic (fcc), Co with a hexagonal close-packed (hcp) structure and Mn with the complex *A*12 structure.[5]

Rost *et al.* applied this concept of HEAs (materials with a multitude of distinct elements and quenching the reactions from elevated temperatures) to oxides and extensively investigated the formation of high entropy oxides crystallising with the rock salt structure (HERS, space group: $Fm\bar{3}m$).[3] The relationship between phase formation and quenching temperature T_{qu} and compositional variation were studied. It was shown that configurational disorder promotes the formation of new phase-pure oxide-based rock salt materials, which should normally not form solid solutions. A minimum of five different cations in equimolar amounts and typical quenching temperatures of T_{qu} > 1173 K were necessary to gain enough configurational entropy to drive single phase formation, whereas slow cooling the same reactions to ambient temperatures resulted in poly-phase mixtures. In 2016 Bérardan *et al.* reported on superionic lithium conductivity in high entropy oxides.[7] They investigated phase formation and ionic conductivity in the $(MgCoNiCuZn)_{1-2x}Ga_xLi_xO$ field. Samples with x= 0.33 were reported to show ionic conductivity of 1 x 10^{-3} S cm^{-1}.

The report of high ionic conductivity in $(MgCoNiCuZn)_{1-2x}Ga_xLi_xO$ inspired the following work: The formation and ionic conductivity of sulphur-based entropy stabilised rock salts is investigated. The exchange of O^{2-} for S^{2-} is reported to reduce the activation barrier E_a of lithium diffusion due the higher polarizability of S^{2-} *vs* O^{2-}.[8] Synthesis of lithium containing sulphide based HERS might result in even higher lithium mobility in the materials.

1.2 Experimental

Reagents. Magnesium sulphide (MgS) was synthesised from $MgSO_4$. An alumina boat filled with $MgSO_4$ was placed in a quartz tube and heated to 1023 K for 6 h under a stream of CS_2 vapour. The reaction product was analysed by PXRD and found to be 97.5 wt % MgS with a minor MgO impurity (2.5 wt %). PXRD analysis of commercially available MgS did not show improved purity of the reagent.

All other sulphides were used as commercially supplied: MnS (Alfa Aesar, 99.9 %), ZnS (Sigma-Aldrich, 99.99 %), CdS (Sigma-Aldrich, 99.995 %), CaS (Alfa Aesar, 99.9 %), SrS (Alfa Aesar, 99.9 %), PbS (Sigma-Aldrich, 99.9 %), BaS (Sigma-Aldrich, 99.9 %), Y_2S_3 (Alfa Aesar, 99.9 %) Li_2S (Alfa Aeasar, 99.9 %) and Bi_2S_3 (Alfa Aesar, 99.9 %).

Synthesis. All sample/reagent/product handling was carried out in a drybox under a helium atmosphere (O_2 < 3 ppm). Powders with appropriate stoichiometric ratios were mixed, ground and placed in alumina crucibles, which then were placed in quartz tubes. The tubes were sealed under static vacuum (p= 1 x 10^{-4} mbar) and heated to the desired temperature typically for 17 h. The samples were quenched in an ice bath from high temperature. PXRD patterns were collected on powder samples sealed under helium atmosphere in borosilicate capillaries using a Bruker D8 Advance diffractometer with monochromated molybdenum source ($K\alpha_1$, λ= 0.7093 Å).

Compositional analysis. The composition of $LiBiMgCaS_4$ was determined by measurement of the lithium, bismuth, magnesium and calcium contents by ICP-OES (Agilent 5110 SVDV). $LiBiMgCaS_4$ (24 mg) was dissolved in 13 mL concentrated HCl (~ 37 %), which was consequently made up to 100 mL with deionised H_2O.

AC-impedance spectroscopy. $LiBiMgCaS_4$ (~80 mg) was pelletized by hand (pellet diameter: 5 mm; p~ 2.5 MPa) and subsequently densified using a cold isostatic press (CIP) (p~ 200 MPa) with achieved densities of ~85 %. The pellets were painted with Koartan 4129 gold paste and heated to 423 K in a quartz tube under dynamic vacuum. Temperature dependent AC-impedance measurements were performed from 303 to 398 K under a flow of Argon gas. A Solartron 1296 dielectric interface with the Solartron 1255B frequency analyser was used. A sinusoidal amplitude of 300 mV was employed in the frequency range 1 MHz to 100 mHz. The data was evaluated with the ZView2 software package.[9]

Solid state NMR experiments. All NMR experiments have been conducted by Kenneth K. Inglis in the research group of Dr. F. Blanc at the University of Liverpool. The procedures for line narrowing experiments are published in Chem. Mater. **2018,** 30, 7183-7200: [10]

Variable temperature ^{7}Li NMR experiments were recorded on a 4 mm HXY MAS probe in double resonance mode (between 110 K – 400 K) and a 4 mm HX High Temperature MAS Probe (above room temperature), both on a 9.4 T Bruker Avance III HD spectrometer under static conditions with the X channel tuned to ^{7}Li at $\omega_0/2\pi(^{7}\text{Li})$ = 156 MHz. All samples were flame sealed in Pyrex inserts under He atmosphere. All ^{7}Li NMR spectra were obtained with a hard 90^{o} pulse of 1.5 µs at rf amplitude of $\omega_1/2\pi(^{7}\text{Li})$ = 83 kHz. Spin-lattice relaxation rates in the laboratory frame (T_1^{-1}) were obtained using a saturation recovery pulse sequence and the data was fitted to a stretch exponential function of form $1 - \exp[-(\tau/T_1)^{\alpha}]$ where τ are the variable delays and α is the stretch exponential (values between 0.3 and 1) . Spin-lattice relaxation rates in the rotating frame ($T_{1\rho}^{-1}$) were recorded using a standard spin-lock pulse sequence at frequencies of $\omega_1/2\pi(^{7}\text{Li})$ = 20, 33 and 50 kHz and data were fitted to a stretch exponential function of form $\exp[-(\tau/T_{1\rho}^{-1})^{\beta}]$ where β values are between 0.5 and 1. Temperature calibrations were performed using the chemical shift thermometers $Pb(NO_3)_2$ using ^{207}Pb NMR and CuI and CuBr using ^{63}Cu NMR.[11-14] ^{7}Li NMR shifts were referenced to 10 M LiCl in D_2O at 0 ppm.

3.2 Results/discussion

3.2.1 Exploratory experiments studying compositional and temperature dependent phase formation

An initial catalogue of suitable binary metal sulphides was set up, including the following materials MgS, MnS, ZnS, CdS, CaS, SrS, PbS, BaS, Li_2S and Bi_2S_3. They were chosen as they have a d^0 electron configuration and are deemed to be electrochemical inactive. The binaries can be classified according to ionic radius, charge and structure type, as shown in Table 2.

Table 2: Binary metal sulphides used as reagents in the synthesis of high entropy rock salts (HERS). The ionic radius of the metal cations refers to an octahedral coordination.

Material	Ionic radius of cation[15] (CN= 6)/ Å	Cation charge	Structure type
MgS	0.72	+2	NaCl
MnS	0.67-0.83	+2	NaCl
ZnS	0.74	+2	Wurtzite
CdS	0.95	+2	Wurtzite, NaCl (high pressure)
CaS	1.00	+2	NaCl
SrS	1.18	+2	NaCl
PbS	1.19	+2	NaCl
BaS	1.35	+2	NaCl
Li_2S	0.76	+1	Antifluorite
Bi_2S_3	1.03	+3	Sb_2S_3
Y_2S_3	0.90	+3	Ho_2S_3

The aim of an initial set of reactions was to test and establish routes to sulphide based high entropy rock salts. The information given in Table 2 was used to select different reaction mixtures with different properties. Different combination of cations were chosen which would fulfil the following criteria: (a) use of reagents which are non-toxic; (b) use of materials with similar ionic radii, *i.e.*, a set of reactions with relatively small ionic radii and a set of reactions with relatively large cations; (c) investigation of the number of cations needed to form sulphide based HERS. The various reaction mixtures were quenched from different temperatures to investigate the dependency of phase formation on temperature.

Table 3: Overview of reactions undertaken: composition, quenching temperature T_{qu} and outcome (x indicates that no phase pure rock-salt was obtained, ✓indicates a single phase rock-salt structure with the corresponding unit cell parameter a of the cubic unit cell).

	Quenching temperature T_{qu}	Outcome	Selection criterion
$MgMnSrBaCaS_5$	1073 K	x	Five cations, non-toxic
	1223 K	x	Five cations, non-toxic
	1373 K	x	Five cations, non-toxic
$MgMnZnCdCaS_5$	1023 K	x	Five cations, small cations
	1173 K	x	Five cations, small cations
	1323 K	x	Five cations, small cations
	1473 K	✓ (a= 5.435(1) Å)	Five cations, small cations
$CdCaSrPbBaS5_5$	1023 K	x	Five cations, large cations
	1173 K	x	Five cations, large cations
	1323 K	x	Five cations, large cations
$MgMnCdCaS_4$	1023 K	x	Four cations
	1173 K	✓ (a= 5.4186(1) Å)	Four cations
	1323 K	✓ (a= 5.4176(1) Å	Four cations
$MgMnZnCaS_4$	1173 K	x	Four non-toxic cations
	1373 K	x	Four non-toxic cations

Table 3 gives an overview of the initial reactions attempted and the respective outcomes. The PXRD patterns of all reaction products are depicted in Figure 33 and Figure 34 in the appendix. Most reactions did not yield in a phase pure rock salt phase but resulted in mixtures of binaries or multiple rock salt related phases. The maximum quenching temperature T_{qu} is limited by the temperature at which strong reaction between the quartz tube and the reagents is observed. In accordance with expectations, quenching from higher temperatures increases the configurational entropy which is needed to stabilise a single rock salt phase, as can be seen in the example of $MgMnZnCdCaS_5$ (Figure 24).

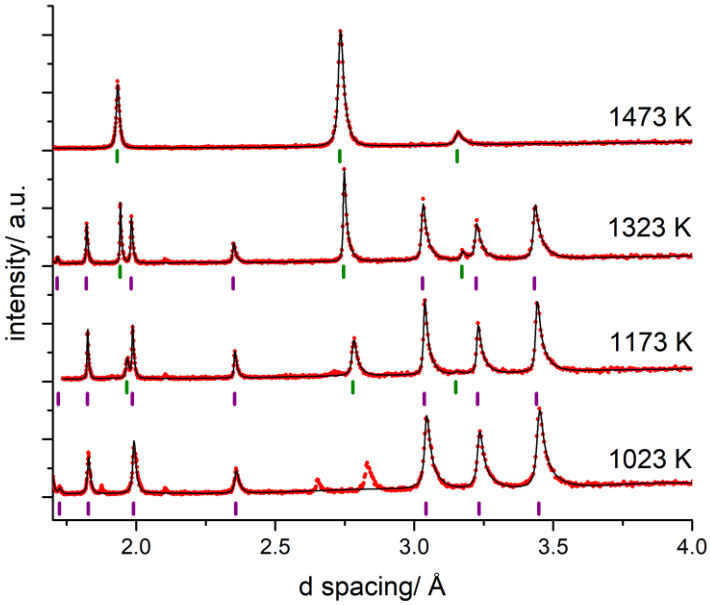

Figure 24: Pawley fits against PXRD patterns of $MgMnZnCdCaS_5$, which have been quenched from different temperatures T_{qu} (1023 K, 1173 K, 1323 K, 1473 K). The positions of calculated Bragg reflections are shown by tick marks (green: cubic unit cell, purple: hexagonal unit cell).

Quenching the reaction of $MgMnZnCdCaS_5$ from 1023 K results in at least two different phases; one which can be indexed to a hexagonal unit cell (space group: $P6_3mc$) (purple tick marks) and a second one which could not be identified. Based on lattice parameters of a= 3.981(5) Å and c= 6.466(1) Å the hexagonal phase can be related to the Wurtzite polymorph of ZnS (a= 3.8227(1) Å, c= 6.2607(1) Å).[16] Increasing the quenching temperature T_{qu} to 1173 K yields the formation of a second phase which can be clearly indexed to a cubic unit cell (space group: $Fm\bar{3}m$) relating it to the rock salt structure. With increasing T_{qu} the reflections of the cubic structure strengthen while the hexagonal phase diminishes and the lattice parameter of the cubic phase shifts to higher 2θ, indicating a decrease of the lattice parameter a in the unit cell. At a quenching temperature T_{qu} = 1473 K, a single cubic material is obtained with a lattice parameter a= 5.435(1) Å. This shows that the competing formation of Wurtzite (space group: $P6_3mc$) at lower temperatures and an entropically stabilised rock salt can be followed through this temperature range.

As the Wurtzite structure is formed by binary ZnS and CdS, it was assumed that it might be possible to reduce T_{qu} needed for the formation of the cubic phase, by removing ZnS or CdS from the reaction mixture. As CdS is also known to exhibit a high pressure cubic polymorph, ZnS was removed from the reaction mixture, giving the stoichiometry of $MgMnCdCaS_4$. Although this material incorporates fewer (four) cations, which reduces the configuration entropy, it is possible to obtain a cubic material by quenching from only 1173 K, as shown in

Figure 25 (an MgO impurity is detectable, due to MgO contamination of MgS). The lattice parameter of this material is a= 5.4186(1) Å.

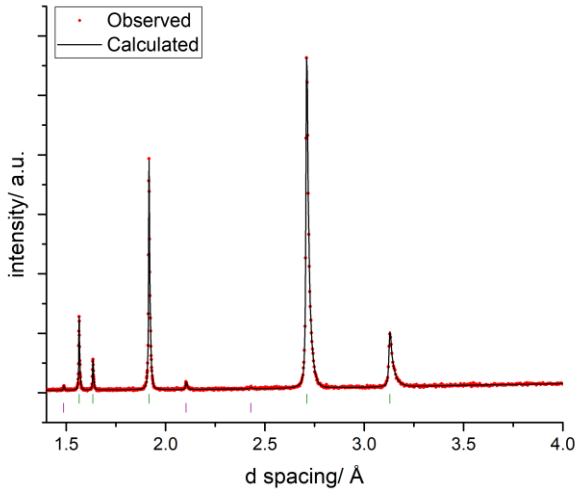

Figure 25: Pawley fit of the PXRD of $MgMnCdCaS_4$ quenched from 1173 K. The positions of calculated Bragg reflections are shown by tick marks (green: $MgMnCdCaS_4$, purple: MgO).

It is worth noting that quenching $MgMnCdCaS_4$ from 1023 K results in a mixture of a hexagonal phase and the cubic phase, which might be driven by the presence of CdS.

This first set of experiments established that the concept of entropically stabilised rock salts structures can be successfully transferred to sulphur based materials. Temperature and composition dependences of the formation of cubic phases were evaluated. The following preliminary conclusions were drawn:

a) higher T_{qu} increases the entropic contributions and thereby increases the likelihood of obtaining pure reactions products
b) the configurational entropy of four cations can be sufficient to stabilise cubic phases
c) the presence of materials which crystallise thermodynamically stable in the rock salt structure at ambient conditions increases enthalpic stabilisation and thereby favours formation of cubic phases

3.2.2 Lithium containing metal sulphide based high entropy rock salts

In order to yield materials which might have a practical application as solid state electrolytes, the incorporation of Li^+ into an HERS was attempted. As Li^+ is a monovalent cation different routes can be envisaged to maintain charge balance against the regular S^{2-} sublattice:

a) incorporation of two Li^+ ions in exchange of one M^{2+} cation (*i.e.* occupation of tetrahedral interstices of the S^{2-} sublattice)
b) incorporation of only one Li^+ cation – changing the formal S^- content to a non-integer number
c) co-doping with a trivalent cation – such as Al^{3+}, Ga^{3+}, Bi^{3+} or Y^{3+}.

In particular Bi^{3+} and Y^{3+} are promising co-dopants as both $LiBiS_2$ and $LiYS_2$ are known to crystallise in a rock salt structure. Table 4 gives an overview of reactions attempted for the incorporation of Li^+ and the respective outcomes. Routes a) and b) failed entirely as no phase pure cubic phases could be identified with PXRD. The PXRD patterns of the reaction products are shown in Figure 35 and Figure 36 in the appendix.

Table 4: Overview of attempted reactions which included Li: composition, quenching temperature T_{qu} and outcome (x indicates that no phase pure rock-salt was obtained, ✓indicates a single phase rock-salt structure with the corresponding unit cell parameter a of the cubic unit cell).

	Quenching temperature T_{qu}	Outcome (lattice parameter)	strategy
$Li_2MgMnCdCaS_5$	1173 K	x	a)
$LiMgMnCdCaS_{4.5}$	1173 K	x	b)
	1323 K	x	b)
$LiYMgMnCaS_5$	973 K	✓ (a= 5.4214(9) Å)	c)
	1173 K	x	c)
$LiBiMgMnCaS_5$	973 K	✓ (a= 5.5053(7) Å)	c)
	1173 K	✓	c)
$LiYMgCaS_4$	1073 K	x	c)
$LiYMgCaZnS_5$	1073 K	x	c)
$LiBiMgCaS_4$	1073 K	✓ (a= 5.54163(9) Å)	c)
$LiBiMgCaZnS_5$	1073 K	x	c)
$LiYMgCaS_4$	1173 K	x	c)
$LiYAl_{2/3}CaS_4$	1173 K	x	c)
$LiGaMgCaS_4$	1173 K	x	c)
$LiBiAl_{2/3}CaS_4$	1173 K	x	c)

More interestingly was the co-doping route. Both Bi^{3+} and Y^{3+} containing materials, such as $LiYMgMnCaS_5$ and $LiBiMgMnCaS_5$, could be stabilised in cubic phases. This can be related to the fact that both $LiBiS_2$ and $LiYS_2$ crystallise in the cubic rock salt structure, therefore favouring the formation of a rock salt phase enthalpically. Co-doping with Al^{3+} and Ga^{3+} however resulted in the formation of significant by-phases, which could not be identified by

PXRD analysis. But only in the case of $LiBiMgCaS_4$ it is possible to reduce the number of cations present to four and obtain a single cubic phase. As established in chapter 1, the conductivity is dependent on the charge carrier concentration (Li^+). Therefore, the focus of further work was set to the material with the highest nominal Li^+ content, $LiBiMgCaS_4$.

3.2.3 $LiBiMgCaS_4$

3.2.3.1 Structural investigations

$LiBiMgCaS_4$ was identified to be the most promising sulphide based HERS as lithium ion conductor. To probe the temperature dependent entropic contribution to the stabilisation, the influence of quenching versus slow cooling from 1073 K was investigated.

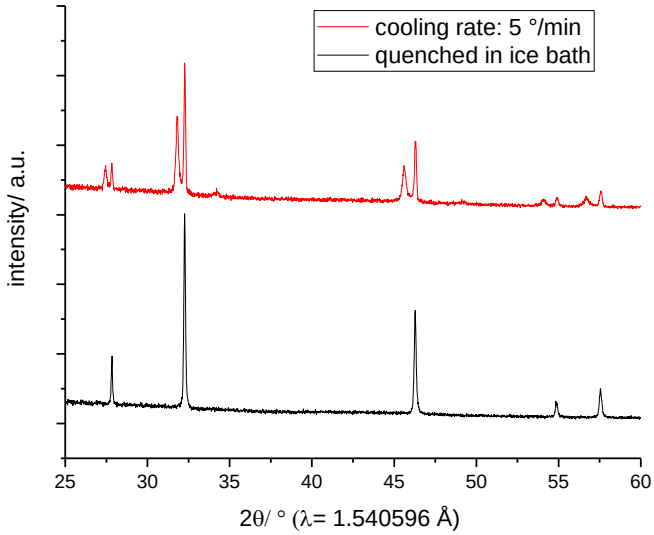

Figure 26: PXRD patterns of $LiBiMgCaS_4$ cooled down to RT in two different ways: slow cooling (cooling rate: 5 K/min) (red) versus quenching (black).

Figure 26 shows $LiBiMgCaS_4$ cooled to ambient temperature with a controlled cooling rate of 5 K min^{-1} (red) and a quenched sample (black). Slow cooling leads to the formation of two cubic phases, while fast cooling quenches only one cubic high temperature material. This experiment clearly demonstrates the crucial contribution of high temperatures to stabilise high entropy phases. The cation ratio was confirmed by ICP-OES to be $Li_{0.96(1)}Bi_{0.98(1)}Mg_{0.99(1)}Ca_{1.06(1)}S_x$. The sulphur content could not be determined due to the dissolution procedure using HCl. Hydrolysis and consequent H_2S formation were detected visually by the formation of yellow fumes. This indicates the loss of sulphur.

Even though many of the binary educts are very moisture sensitive, the obtained $LiBiMgCaS_4$ can be exposed to air, without perceptible degradation. The human olfactory sense is very susceptible towards the existence of H_2S and no such smell could be identified. Additionally

PXRD analysis on a sample heated to 423 K in air for two hours did not show significant change in the lattice parameter or formation of secondary impurity phases, as shown in Figure 27.

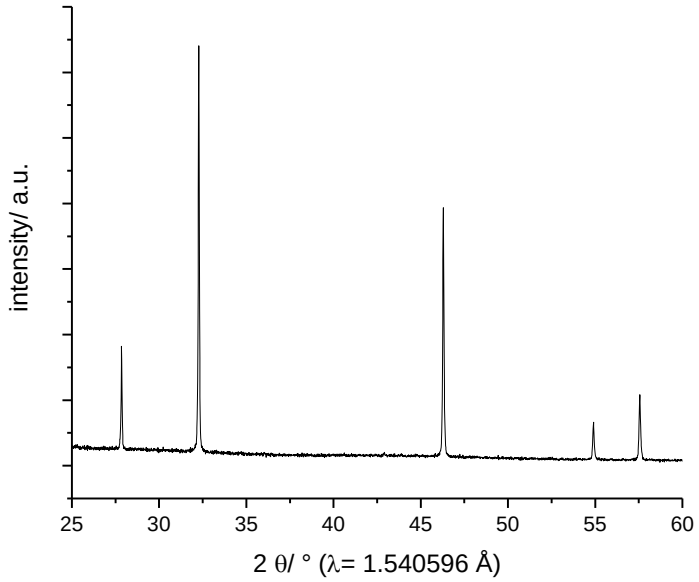

Figure 27: PXRD pattern of $LiBiMgCaS_4$ heated to 423 K in air for two hours. No formation of a secondary impurity phase is detectable.

Further structural analysis was performed on powder diffraction data obtained by synchrotron powder diffraction at I11 and NPD data obtained from on the GEM instrument at ISIS.

The SXRD pattern was indexed to a dominant cubic phase (a= 5.546(1) Å) while a small cubic impurity with a lattice parameter a_{imp}= 4.2115(3) Å can be detected. The impurity phase is more evident in the neutron data. This impurity was assigned to MgO based on the lattice parameter of MgO (a_{MgO}= 4.217(1)Å) and knowledge that the MgS precursor was contaminated with MgO (~2.5 wt % based on PXRD analysis). The lattice parameter a of $LiBiMgCaS_4$ is of similar magnitude as the lattice parameters of the two binary reagents, which crystallise in a rock salt structure (CaS, MgS). This implies that no long range ordering of the cations is present and that the metal cations are disordered.

The prototype structure of NaCl was used as a starting model for the structural refinement of $LiBiMgCaS_4$ in a combined Rietveld refinement. The structure of NaCl is based on a cubic close packed anion (Cl^-) array (crystallographic site: 4*b*) with full occupation of the octahedral interstices by the cation Na^+ (crystallographic site 4*a*). Both the 4*a* and 4*b* site are restricted by symmetry and have no positional degree of freedom. The structure of $LiBiMgCaS_4$ was

refined against this model with S^{2-} placed on the anion 4*b* site and the cations (here: Li^{+}, Bi^{3+}, Mg^{2+}, Ca^{2+}) placed on the cation 4*a* site. In order to develop a structural model for $LiBiMgCaS_4$ the following assumptions had to be made regarding the occupancies of the metal site: As there are four different cation species and only two sets of data (SXRD and NPD) are available, it is not possible to refine the fractional occupancy of the different cationic species on the 4*a* site. The individual occupancies of the mixed 4*a* site were therefore fixed to the result of the compositional analysis from ICP-OES, assuming a total occupation of 1. The only free parameters to refine were the atomic displacement parameters of the combined cationic site and of the anionic sulphur site. Subsequently Fourier difference maps were calculated and searched for tetrahedrally coordinated cations. But neither positive nor negative scattering intensity could be detected in tetrahedral 8*c* sites (or any other sites), confirming that $LiBiMgCaS_4$ was quenched in the rock salt structure with octahedral coordination of the cations. The combined refinement resulted in a total R_{wp} of 2.8 and a goodness of fit χ^2 of 5.9.

Figure 28 shows the resulting fit of the combined X-ray and neutron powder diffraction Rietveld refinement. The final structural model is given in Figure 29.

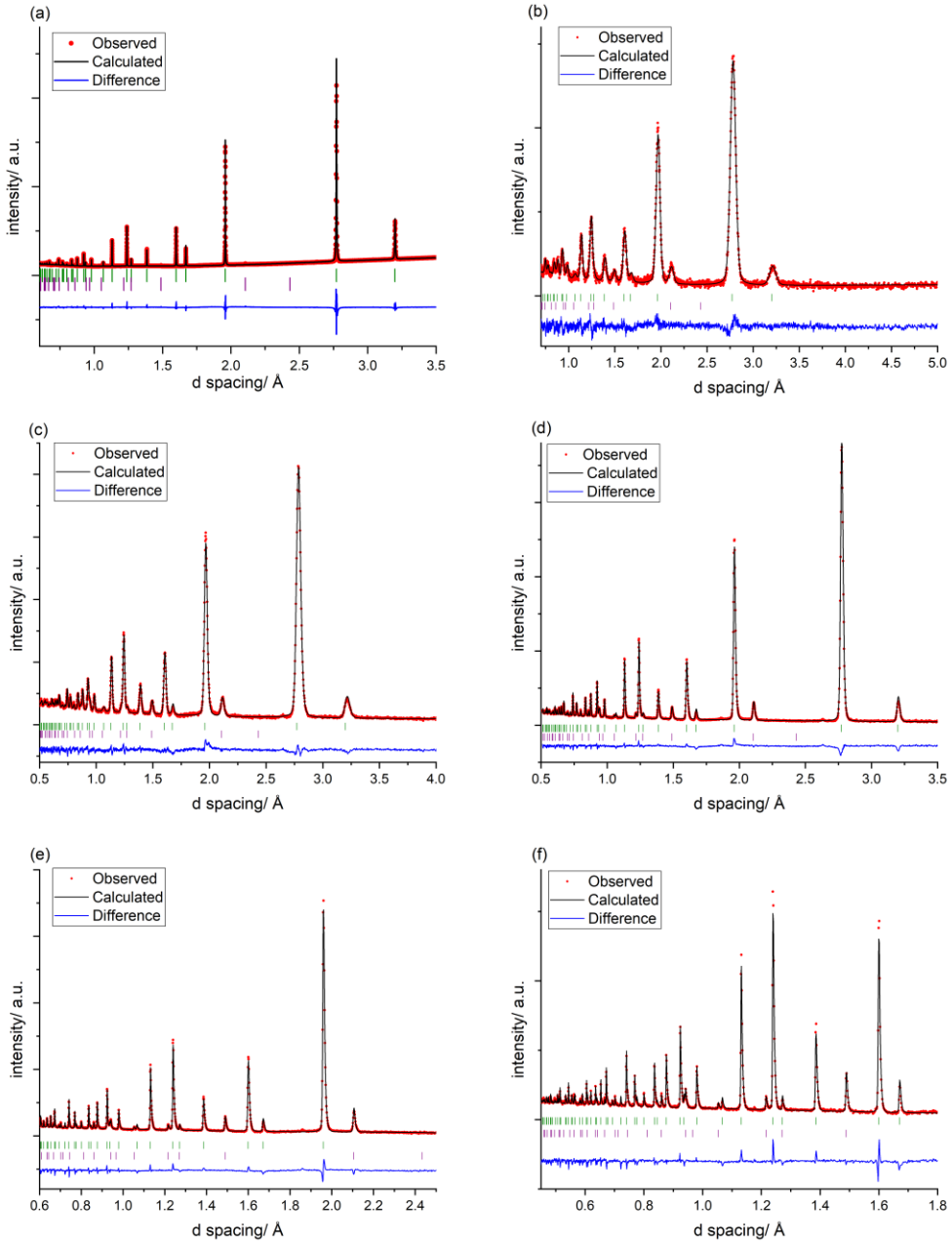

Figure 28: Combined Rietveld refinement of $LiBiMgCaS_4$ against (a) SXRD and (b) – (f) NPD data (ISIS neutron source, GEM, ambient temperature). The positions of calculated Bragg reflections are shown by tick marks (green: $LiBiMgCaS_4$ (98.9 wt %), purple: MgO (1.1 wt %)). (a) Diamond I11 beamline, λ= 0.825187 Å; (b) bank 2; (c) bank 3; (d) bank 4; (e) bank 5; (f) bank 6.

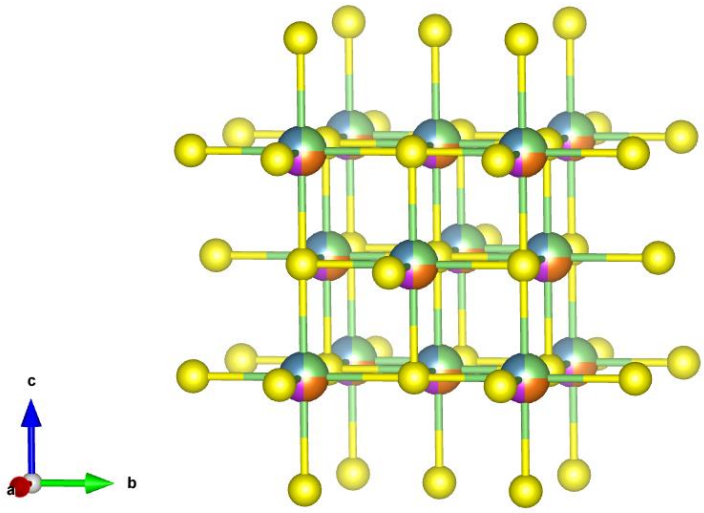

Figure 29: Crystal model of the HERS type $LiBiMgCaS_4$ (yellow: sulphur, green: lithium, orange: magnesium, purple: bismuth, blue: calcium).

Further crystallographic information is given in Table 5.

Table 5: Structural parameters of $LiBiMgCaS_4$ from a combined Rietveld refinement at ambient temperature using NPD and SXRD data measured on the GEM instrument at ISIS Neutron and Muon Source and the I11 beamline at Diamond Light Source respectively.

Atom	Wyckoff site	x	y	z	occupancy	U_{iso}/Å^2
Li1	4*a*	0.0	0.0	0.0	0.241	0.0085(1)
Mg1	4*a*	0.0	0.0	0.0	0.248	0.0085(1)
Bi1	4*a*	0.0	0.0	0.0	0.246	0.0085(1)
Ca1	4*a*	0.0	0.0	0.0	0.265	0.0085(1)
S1	4*b*	½	½	½	1.0	0.0179(5)

a= 5.5416(1) Å, Space group= $Fm\bar{3}m$, R_{wp}= 2.80, χ^2= 5.94, phases: $LiBiMgCaS_4$ (99.0 wt %), MgO (1.0 wt %).

3.2.3.2 Property measurements

Temperature dependent AC-impedance spectroscopy and temperature dependent solid state ^{7}Li-NMR were employed to investigate the Li^+ mobility in the new $LiBiMgCaS_4$ material. A typical AC-impedance spectrum is displayed in Figure 30(a).

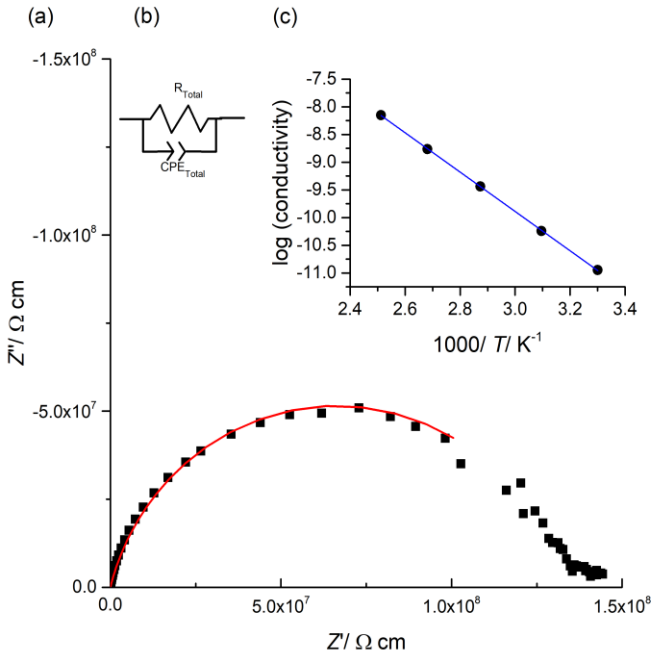

Figure 30: Typical AC-impedance spectrum of $LiBiMgCaS_4$ measured at 398 K. (a) The measured data points are indicated by black squares, while the equivalent model used for the calculated fit (red line) is shown in (b). Inset (c) shows the Arrhenius-like behaviour of the temperature dependent conductivity.

At 398 K a single semicircle can be detected at high frequencies, while at the low frequency side no further element (semicircle or spike) can be identified. The arc has a resistance of 1.3×10^{-8} Ω cm (corresponding to a conductivity $\sigma = 7.1 \times 10^{-9}$ Scm^{-1} at 398 K) and a capacitance of 6.25×10^{-12} Fcm^{-1}. The spectrum can therefore be interpreted as the bulk response of the material and modelled with a single RC element, as shown in Figure 30(b). As there is no indication of a low frequency electrode spike, it can be assumed that there is no build-up of charge at the pellet/electrode interface, meaning that the conducting species is probably not ionic but electronic.[17-18] The room temperature conductivity of $LiBiMgCaS_4$ is 1×10^{-11} Scm^{-1}, making it very hard to describe as a conductor, but it has rather to be referred to as an insulator. The temperature dependent Arrhenius plot is displayed in Figure 30(c). Evaluation of the slope of the regression gives a high activation energy of 0.70 eV, which is very high compared to good lithium ion conductors from literature. In summary, no Li^+/cation mobility can be deduced from the AC-impedance data.

As AC-impedance is a method to measure long-range bulk properties of materials, temperature dependent solid state ^{7}Li-NMR experiments were executed to explore the local mobility of Li^+ cations. All NMR experiments have been conducted by Kenneth K. Inglis in the research group of Dr. F. Blanc at the University of Liverpool. ^{7}Li spectra were obtained

between 242 K and 411 K (Figure 31(a)) and the full width at half maximum (*fwhm*) was extracted as a function of temperature (Figure 31(b)).

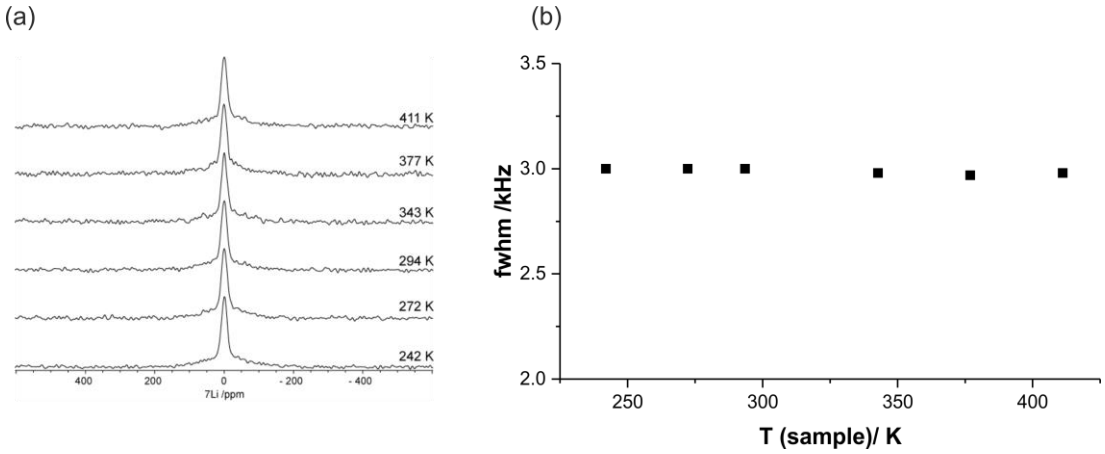

Figure 31: Solid state ^{7}Li-NMR experiments. (a) Temperature dependent ^{7}Li spectra of $LiBiMgCaS_4$ measured at temperatures between 242 K and 411 K; (b) plot of the full width at half maximum (fwhm) against temperature.

At 242 K one lithium signal at 0 ppm is detected with a full width at half maximum of the peak of ~3000 Hz, which is in the slow mobility regime. With increasing temperature neither a shift of the peak position nor a line-narrowing can be observed, which shows that no lithium mobility sets in.

$LiBiMgCaS_4$ is a black material, while all the reagents but Bi_2S_3 are colourless. Black Bi_2S_3 is reported to be a direct band gap semiconductor with a band gap E_g of 1.9 eV.[19-21] This suggests that $LiBiMgCaS_4$ might not be electronically insulating, but a semiconductor, which gives rise to a small electrical conductivity in the AC-impedance spectra.

Combining the results of AC-impedance spectroscopy and NMR spectroscopy leads to the conclusion that the lithium mobility in $LiBiMgCaS_4$ is negligible. The low lithium mobility can be explained by the findings of Ceder *et al.* in their investigations of lithium diffusion in disordered rock salts.[22-23] Using *ab initio* computation, they related lithium hopping through disordered transition metal oxide rock salt phases $Li_xTM_{2-x}O_2$ (TM: transition metal). In the rock salt structure lithium diffusion is enabled by a lithium atom hopping from one octahedral site to another octahedral site. In order to jump from one octahedral site to a neighbouring site, lithium atoms need to pass through a tetrahedral interstitial, as shown in Figure 32 (a). Three different cases were distinguished depending on the local environment of the tetrahedral interstitial site: no transition metal cation (0-TM) surrounding the interstitial (Figure 32(b)), one transition metal (1-TM) surrounding the interstitial (Figure 32(c)) and two transition metal cations (2-TM) surrounding the interstitial (Figure 32(d)).

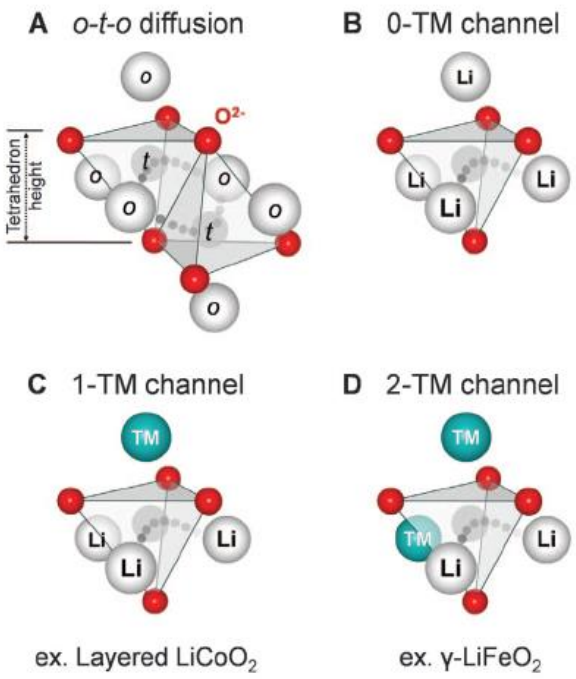

*Figure 32: (a) General octahedral-tetrahedral-octahedral (o-t-o) pathway: hopping of an octahedral atom (e.g. lithium) from an octahedral site to a neighbouring octahedral site via a tetrahedral interstitial; (b) 0-TM pathway: lithium passing through a tetrahedral interstitial which is coordinated by only lithium; (c) 1-TM pathway: lithium passing through a tetrahedral interstitial which coordinated by lithium and one transition metal cation; (d) 2-TM pathway: lithium passing through a tetrahedral interstitial which coordinated by lithium and two transition metal cation. From Science **343** (6170), 519-522. Reprinted with permission from AAAS.*

The Li^+ migration barriers were calculated for each pathway and it could be shown that diffusion *via* the 0-TM pathway is energetically the most favourable. For 0-TM pathways to dominate long-scale lithium diffusion in a material they must be connected throughout the entire material to form a penetrating diffusion network. The formation of this three dimensional network is dependent on the lithium concentration. A threshold value of x ≈1.1, as defined by the value of x in $Li_xTM_{2-x}O_2$, is needed to form penetrating 0-TM pathways through the material. In analogy to $LiBiMgCaS_4$, the divalent (Mg^{2+}, Ca^{2+}) and tetravalent cations (Bi^{3+}) correspond to the transition metal cations in the disordered rock salts. Following this argument, the cationic content of lithium needs to be 55 % in the HERS to form long-range percolating 0-TM pathways that lead to good mobility. Clearly the lithium content of 25 % in $LiBiMgCaS_4$ is too low, so any lithium mobility would have to be facilitated by energetically unfavoured 1-TM and 2-TM pathways. Consideration of the lithium transport pathways explains why there is no significant lithium diffusion in $LiBiMgCaS_4$ as shown experimentally by AC-impedance and NMR spectroscopy. No further synthetic efforts were made to increase the Li^+ content in similar materials. But this could prove a promising route towards new solid state lithium conductors.

These finding of low lithium mobility in sulphide based HERS are contrasting with the report of superionic lithium conductivity in $(MgCoNiCuZn)_{1-2x}Ga_xLi_xO$ (x= 0.33).[7] Bérardan *et al.* might have mistaken electronic conductivity for ionic conductivity or exchange of O^{2-} for S^{2-} might actually impede lithium mobility significantly. To our knowledge no working application of $(MgCoNiCuZn)_{1-2x}Ga_xLi_xO$ as a solid electrolyte in a battery has been reported.

3.3 Conclusion

The concept of entropy stabilisation was used to discover new sulphur-based rock salt materials. By changing the composition and quenching temperature T_{qu} the following high entropy stabilised rock salts (HERS) could be isolated: $MgMnZnCdCaS_5$, $MgMnCdCaS_4$, $LiBiMgMnCaS_5$ and $LiBiMgCaS_4$. Interestingly two materials were found ($MgMnCdCaS_4$, $LiBiMgCaS_4$) in which the presence of only four different cationic species increases the configurational entropy S_{conf} sufficiently to promote the formation of a single-phase rock salt. By studying the phase formation with temperature in the $MgMnZnCdCaS_5$ system, it is possible to follow the transition from a predominantly hexagonal phase into a single cubic rock salt type structure.

Eventually $LiBiMgCaS_4$ was identified to be the most promising material as a lithium conductor and was investigated further. Compositional analysis by ICP confirmed that the overall composition had been retained after the reaction. Rietveld refinement of SXRD and NPD data showed that the material crystallises in the rock salt structure type. The cations are fully disordered on the octahedral sites with no occupation of any tetrahedral sites. High lithium mobility can be ruled out by both AC-impedance and solid state ^{7}Li NMR. The charge-carrying species is most likely to be electronic in nature rather than ionic. These results were set in context to the investigations of disordered transition metal oxides, which suggest that a threshold value of the cationic lithium content of 0.55 % is needed, before low-energy percolation pathways can be expected. Increasing the lithium content in HERS to meet this threshold was not investigated in this project but could be an interesting target for future investigations. Overall the concept of high entropy stabilisation can be successfully applied in the synthesis of new sulphide based materials. Increase of the lithium content and concomitant discard of bismuth as a cation in HERS might lead to increased lithium mobility and decreased electrical conductivity. Then this class of materials might become suitable as electrolyte materials in battery application.

3.4 References

1. Yeh, J. W.; Chen, S. K.; Lin, S. J.; Gan, J. Y.; Chin, T. S.; Shun, T. T.; Tsau, C. H.; Chang, S. Y., Nanostructured High‐Entropy Alloys with Multiple Principal Elements: Novel Alloy Design Concepts and Outcomes. *Adv. Eng. Mater.* **2004,** *6* (5), 299-303.
2. Butler, K. T.; Walsh, A.; Cheetham, A. K.; Kieslich, G., Organised chaos: entropy in hybrid inorganic-organic systems and other materials. *Chem. Sci.* **2016,** *7* (10), 6316-6324.
3. Rost, C. M.; Sachet, E.; Borman, T.; Moballegh, A.; Dickey, E. C.; Hou, D.; Jones, J. L.; Curtarolo, S.; Maria, J. P., Entropy-stabilized oxides. *Nat. Commun.* **2015,** *6*.
4. Cantor, B.; Chang, I. T. H.; Knight, P.; Vincent, A. J. B., Microstructural development in equiatomic multicomponent alloys. *Mater. Sci. Eng. A* **2004,** *375-377*, 213-218.
5. Gludovatz, B.; Hohenwarter, A.; Catoor, D.; Chang, E. H.; George, E. P.; Ritchie, R. O., A fracture-resistant high-entropy alloy for cryogenic applications. *Science* **2014,** *345* (6201), 1153.
6. Gali, A.; George, E. P., Tensile properties of high- and medium-entropy alloys. *Intermetallics* **2013,** *39*, 74-78.
7. Berardan, D.; Franger, S.; Meena, A. K.; Dragoe, N., Room temperature lithium superionic conductivity in high entropy oxides. *J. Mater. Chem. A* **2016,** *4* (24), 9536-9541.
8. Wang, Y.; Richards, W. D.; Ong, S. P.; Miara, L. J.; Kim, J. C.; Mo, Y. F.; Ceder, G., Design principles for solid-state lithium superionic conductors. *Nat. Mater.* **2015,** *14* (10), 1026-1032.
9. Johnson, D. *ZView: A Software Program for IES Analysis* 3.5d; Scribner Associates In.: 2007.
10. Leube, B. T.; Inglis, K. K.; Carrington, E. J.; Sharp, P. M.; Shin, J. F.; Neale, A. R.; Manning, T. D.; Pitcher, M. J.; Hardwick, L. J.; Dyer, M. S.; Blanc, F.; Claridge, J. B.; Rosseinsky, M. J., Lithium Transport in $Li_{4.4}M_{0.4}M'_{0.6}S_4$ (M = Al^{3+}, Ga^{3+}, and M' = Ge^{4+}, Sn^{4+}): Combined Crystallographic, Conductivity, Solid State NMR, and Computational Studies. *Chem. Mater.* **2018,** *30* (20), 7183-7200.
11. Bielecki, A.; Burum, D. P., Temperature-Dependence of ^{207}Pb MAS Spectra of Solid Lead Nitrate - an Accurate, Sensitive Thermometer for Variable-Temperature MAS. *J. Magn. Reson., Ser. A* **1995,** *116* (2), 215-220.
12. Beckmann, P. A.; Dybowski, C., A thermometer for nonspinning solid-state NMR spectroscopy. *J. Magn. Reson.* **2000,** *146* (2), 379-380.
13. Becker, K. D., Temperature-Dependence of NMR Chemical-Shifts in Cuprous Halides. *J. Chem. Phys.* **1978,** *68* (8), 3785-3793.
14. Wu, J. S.; Kim, N.; Stebbins, J. F., Temperature calibration for high-temperature MAS NMR to 913 K: ^{63}Cu MAS NMR of CuBr and CuI, and ^{23}Na MAS NMR of $NaNbO_3$. *Solid State Nucl. Magn. Reson.* **2011,** *40* (2), 45-50.
15. Shannon, R., Revised effective ionic radii and systematic studies of interatomic distances in halides and chalcogenides. *Acta Cryst. A* **1976,** *32* (5), 751-767.
16. Kisi, E. H.; Elcombe, M. M., u parameters for the wurtzite structure of ZnS and ZnO using powder neutron diffraction. *Acta Cryst. C* **1989,** *45* (12), 1867-1870.
17. Irvine, J.; Sinclair, D.; West, A., Electroceramics: Characterization by Impedance Spectroscopy. *Adv. Mater.* **1990,** *2*, 132-138.
18. Quintana, P.; West, A. R., Conductivity of lithium gallium silicates. *Solid State Ion.* **1987,** *23* (3), 179-182.
19. Xiao, G.; Dong, Q.; Wang, Y.; Sui, Y.; Ning, J.; Liu, Z.; Tian, W.; Liu, B.; Zou, G.; Zou, B., One-step solution synthesis of bismuth sulfide (Bi_2S_3) with various hierarchical architectures and their photoresponse properties. *RSC Advances* **2012,** *2* (1), 234-240.
20. Bao, H.; Cui, X.; Li, C. M.; Gan, Y.; Zhang, J.; Guo, J., Photoswitchable Semiconductor Bismuth Sulfide (Bi_2S_3) Nanowires and Their Self-Supported Nanowire Arrays. *J. Phys. Chem. C* **2007,** *111* (33), 12279-12283.

21. Lukose, J.; Pradeep, B., Electrical and optical properties of bismuth sulphide [Bi_2S_3] thin films prepared by reactive evaporation. *Solid State Commun.* **1991,** *78* (6), 535-538.
22. Lee, J.; Urban, A.; Li, X.; Su, D.; Hautier, G.; Ceder, G., Unlocking the Potential of Cation-Disordered Oxides for Rechargeable Lithium Batteries. *Science* **2014,** *343* (6170), 519-522.
23. Urban, A.; Lee, J.; Ceder, G., The Configurational Space of Rocksalt-Type Oxides for High-Capacity Lithium Battery Electrodes. *Adv. Energy Mater.* **2014,** *4* (13).

3.5 Appendix

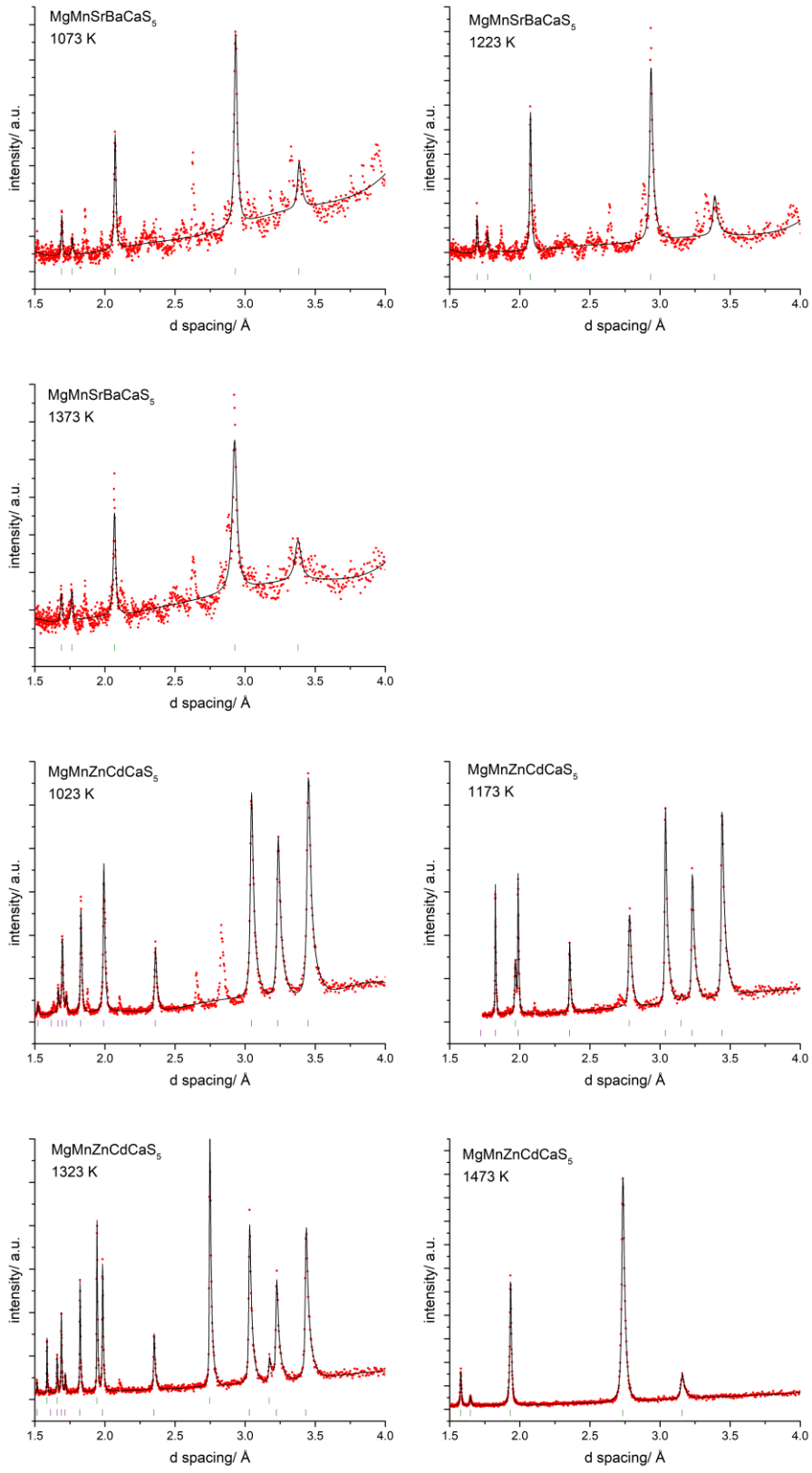

Figure 33: PXRD patterns of attempted high entropy rock salts corresponding to Table 3. The positions of calculated Bragg reflections are shown by tick marks (green: cubic phase, purple: hexagonal phase).

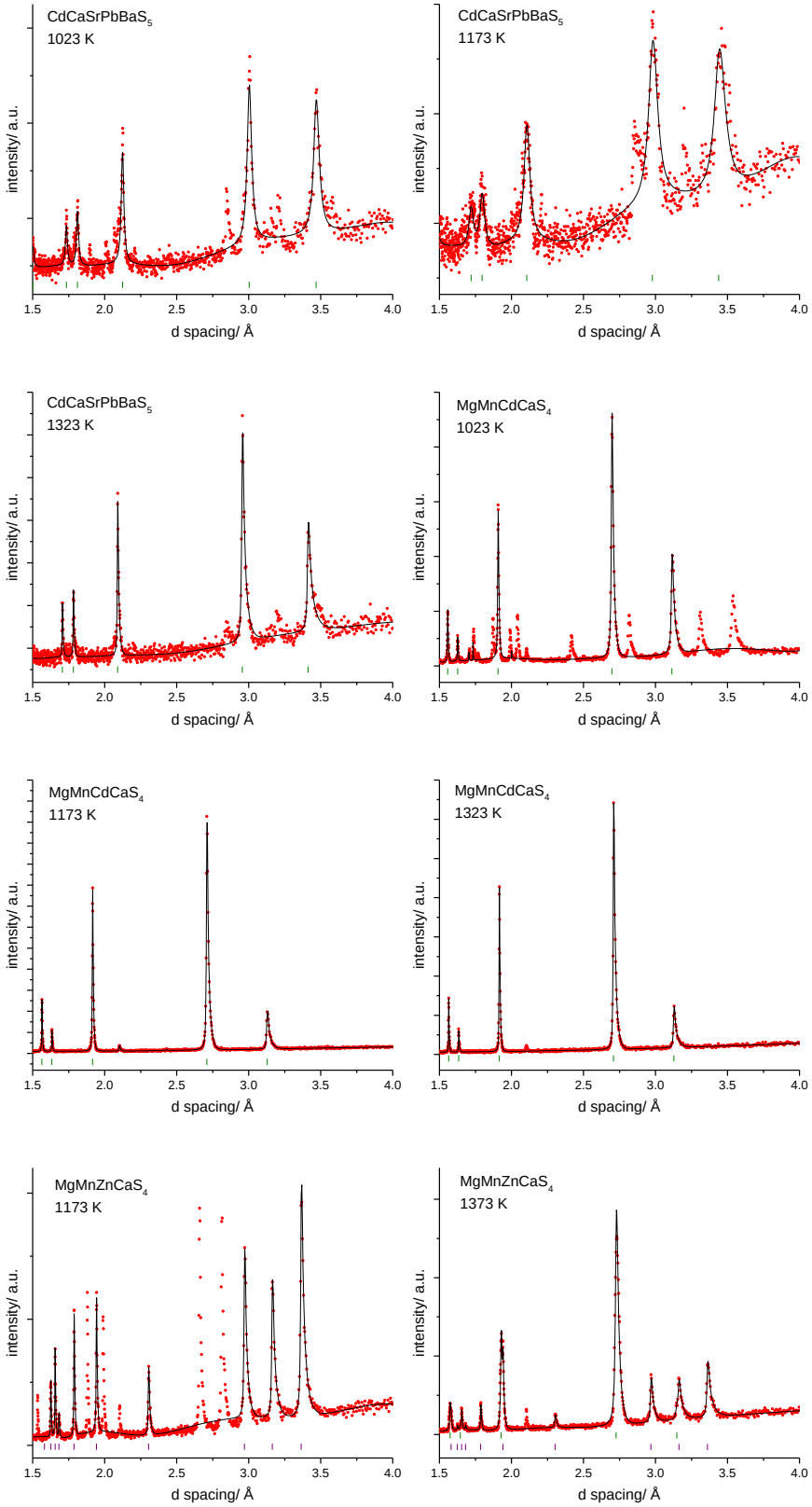

Figure 34: (continued) PXRD patterns of attempted high entropy rock salts corresponding to Table 3. The positions of calculated Bragg reflections are shown by tick marks (green: cubic phase, purple: hexagonal phase).

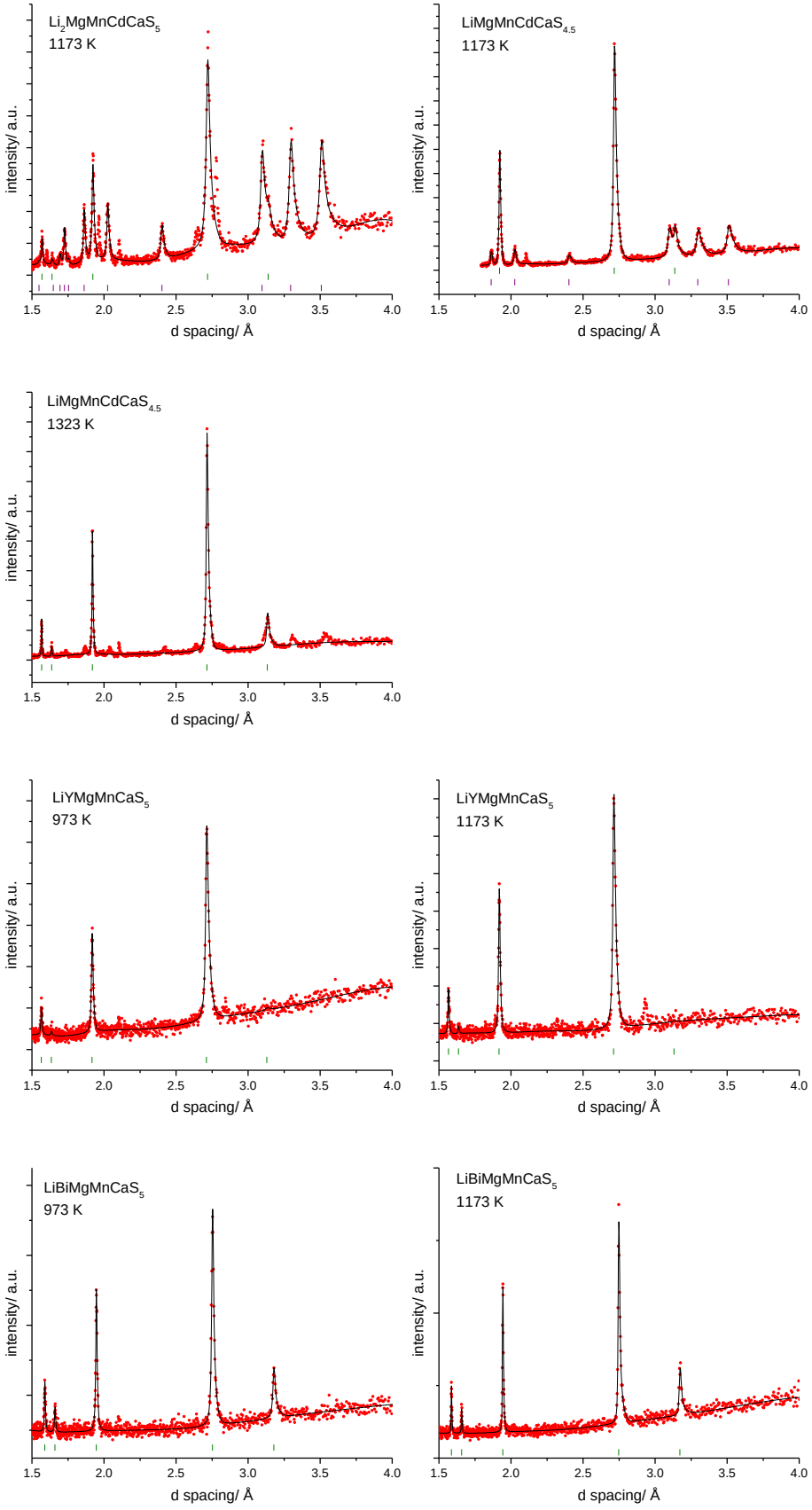

Figure 35: PXRD patterns of attempted lithium containing high entropy rock salts corresponding to Table 4. The positions of calculated Bragg reflections are shown by tick marks (green: cubic phase, purple: hexagonal phase).

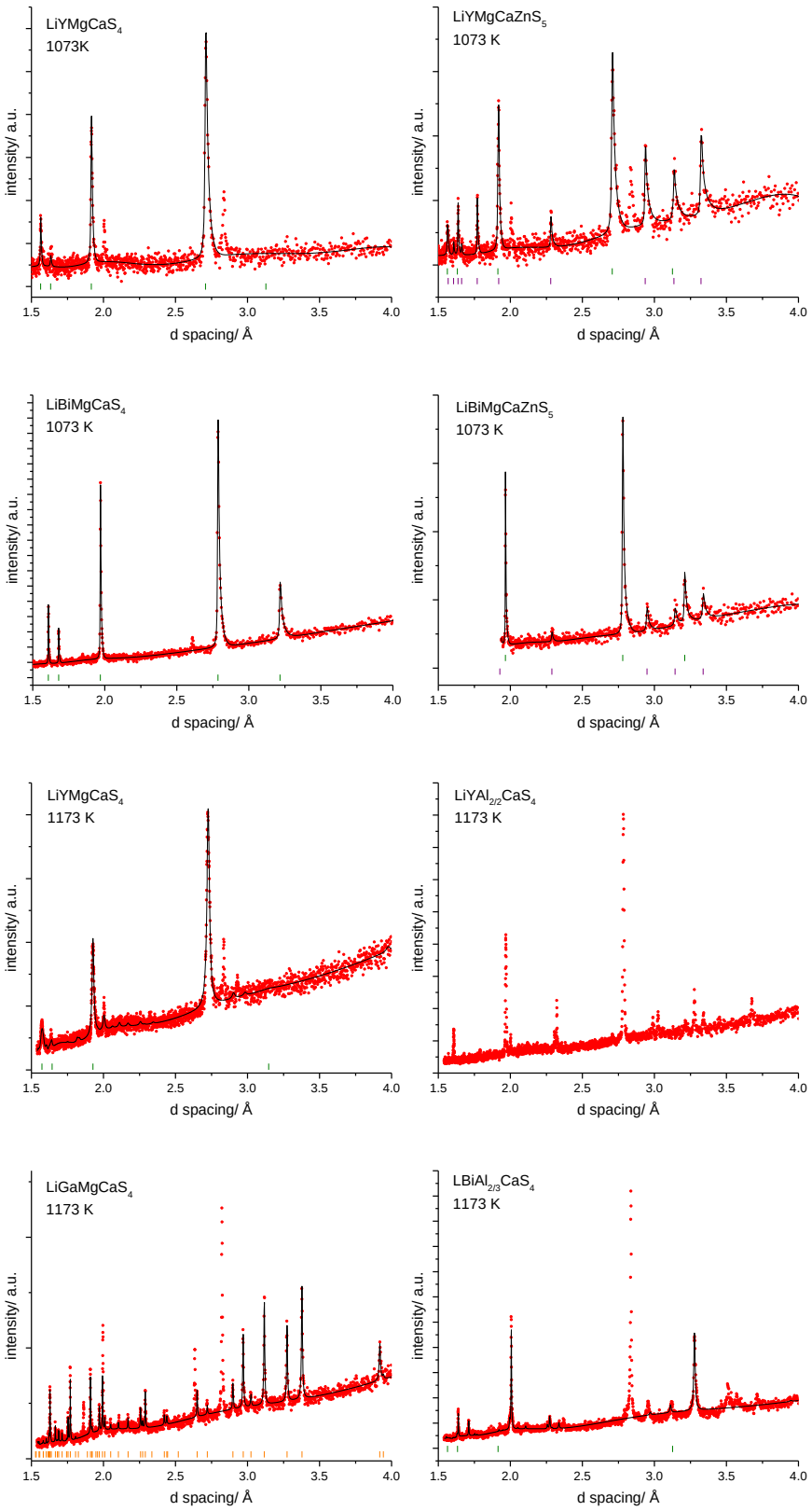

Figure 36: (continued) PXRD patterns of attempted high entropy rock salts corresponding to Table 4. The positions of calculated Bragg reflections are shown by tick marks (green: cubic phase, purple: hexagonal phase, orange: $LiGaS_2$).

4 Novel layered metal sulphide phases

4.1 Introduction

This chapter is going to present the exploratory synthesis and discovery of novel materials in the pseudo-ternary Li_5AlS_4-Li_4GeS_4-Li_3PS_4 phase field. Two interesting compositions were found. The first section of this chapter is dedicated to the novel $Li_{4.4}Al_{0.4}Ge_{0.6}S_4$ phase. Subsequent cation substitution in $Li_{4.4}M_{0.4}M'_{0.6}S_4$ (M= Al^{3+}, Ga^{3+}, In^{3+}; M'= Si^{4+}, Ge^{4+}, Sn^{4+}) led to the discovery of a big family of related materials which were studied crystallographically and electrochemically. In the second part of the chapter the second interesting phase found in the Li_5AlS_4-Li_4GeS_4-Li_3PS_4 phase field, $Li_{4.5}Al_{2/3}Ge_{1/6}P_{1/6}S_4$, will be discussed and related to $Li_{4.4}Al_{0.4}Ge_{0.6}S_4$.

4.1.1 The Li_5AlS_4-Li_4GeS_4-Li_3PS_4 phase field

The crystal structures of several lithium-containing metal sulphides can be derived from an hexagonal close packed (hcp) sulphur sublattice with metal cations occupying tetrahedral and octahedral sites, *e.g.* Li_5AlS_4,[1] Li_4GeS_4,[2-3] Li_3PS_4,[4] Li_4SnS_4,[5-6] Li_2FeS_2,[7] $LiGaS_2$[8]. Structures with 4:1 ratios of sulphur to non-lithium cations (from now on referred to as heavy cations, M) are predominant. These structures are based on isolated MS_4^{x-} tetrahedra and lithium atoms in tetrahedral or octahedral coordination. Synthesis along the tie-lines between two of those materials has repeatedly led to the formation of solid solutions and improvement of the ionic conductivity, *e.g.* Li_5AlS_4-Li_4SiS_4[9] or Li_5GaS_4-Li_4GeS_4.[10]

A very interesting case is that of $Li_{10}GeP_2S_{12}$ (LGPS), one of the leading solid ionic conductors with a reported conductivity σ of 1.2 x 10^{-2} S cm^{-1}.[11] This compound can formally be placed on the tie-line Li_4GeS_4-Li_3PS_4. Both parent phases, Li_4GeS_4 and Li_3PS_4, are based on a hexagonal close packed S^{2-} sublattice but exhibit different arrangements of the cations (Figure 37). Interestingly no solid solution between the endmembers is formed. Instead a new crystallographic phase was found, in which the sulphur sublattice can be related to a bcc (body-centred cubic) arrangement.[12] This transformation to a bcc sublattice is responsible for very low activation barriers E_a and concomitant very high lithium conductivities.

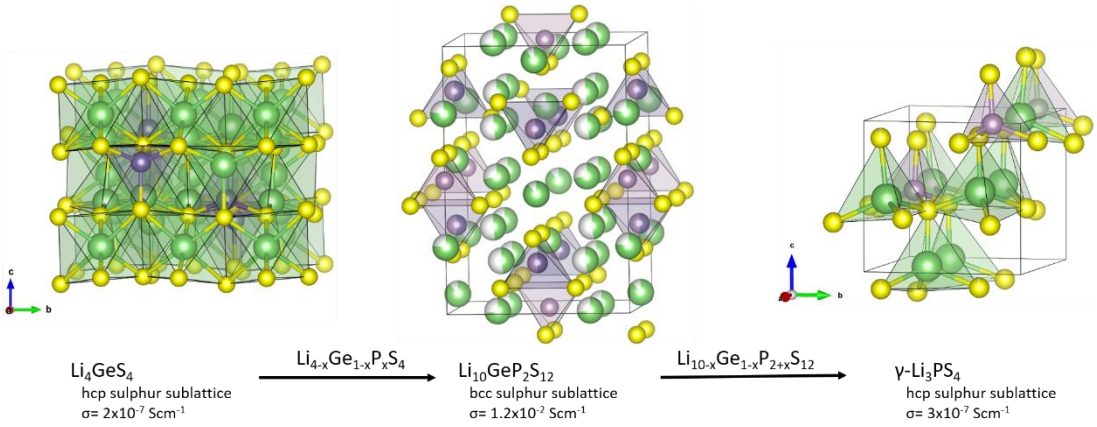

Figure 37: Compositional and structural relationship of $Li_{10}GeP_2S_{12}$ with endmembers Li_4GeS_4 and γ-Li_3PS_4.

The initial aim of this project was to target new materials in an underexplored phase field. Subsequent in-depth characterisation would enable to relate their structures to their transport and electrochemical properties. As a starting point, endmembers of a pseudo-ternary phase field were chosen, which are similar in respect to their sulphur sublattice, but different in their cationic arrangement. This could increase the chances of finding new materials with potentially new sulphur sublattices, as it had been shown in the case of LGPS. Therefore, the pseudo-ternary Li_5AlS_4-Li_4GeS_4-Li_3PS_4 was chosen. Figure 38 gives an overview of known phases and the previous literature reported work in the Li_5AlS_4-Li_4GeS_4-Li_3PS_4 phase field. Besides the endmembers, $Li_{3.45}Ge_{0.45}P_{0.55}S_4$ and $Li_{10}GeP_2S_{12}$ have been studied crystallographically and a $Li_{11}AlP_2S_{12}$[13] phase has been reported without conclusive structural analysis. Additionally, Kanno *et al.* studied the Li_4GeS_4-Li_3PS_4 edge.[14] In this particular study the LGPS compound was overlooked, as the reaction mixtures were heated to 973 K and the LGPS phase decomposed. A cohesive study of the Li_4GeS_4-Li_3PS_4 phase diagram later elucidated that LGPS has a melting temperature T_{melt} of 923 K, at which it decomposes incongruently into a melt and β-Li_3PS_4.[15] This is a good example how difficult it is to completely explore a phase field. A small change in synthetic conditions can result in the formation of new materials. Ooura *et al.* studied the formation amorphous materials by ball milling along the Li_5AlS_4-Li_3PS_4 edge[16] and found a maximum conductivity at ambient temperature of 6.0×10^{-4} S cm^{-1} for $Li_{3.26}Al_{0.13}P_{0.87}S_4$. Finally Amaresh *et al.* investigated crystalline compounds along $Li_{10+x}Al_xGe_{1-x}P_2S_{12}$, with highest conductivity of 1.7×10^{-3} S cm^{-1} for $Li_{10.3}Al_{0.3}Ge_{0.7}P_2S_{12}$.[17] Unfortunately no structural analysis was completed on this compound, so it remains unclear what mechanisms drive this decent lithium mobility.

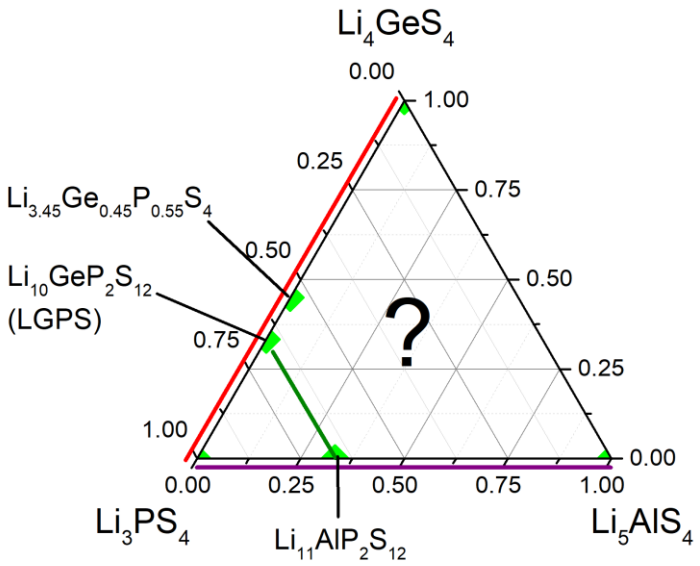

Figure 38: Known compositions and materials in the pseudo-ternary Li-Al-Ge-P-S phase field. green squares: crystalline phases, red line: Kanno et al. with the Li_4GeS_4-Li_3PS_4 tie line;[14] purple line: Ooura et al.: amorphous solid electrolytes in the Li_2S-Al_2S_3-P_2S_5 system;[16] green line: Amaresh et al. with the $Li_{10+x}Al_xGe_{1-x}P_2S_{12}$ solid solution.[17]

4.1.2 Crystal structures of hexagonal close packed lithium-containing metal sulphides

The crystal structures of three lithium containing materials with a hexagonal close packed (hcp) sublattice will be discussed in the following section. This discussion will help to guide the structural discussion of materials with hcp sublattices, which are described later in this chapter. Figure 39 shows the structures of Li_2FeS_2, Li_5AlS_4 and Li_4GeS_4, all based on hcp sublattices. In general, a hexagonal close packed sulphur sublattice has one octahedral and two tetrahedral interstitial sites per anion. The tetrahedral sites can further be distinguished according to their orientation along a stacking axis as T^+ and T^- sites, *i.e.* whether they point "up" or "down" (see Figure 39(a)). Li_2FeS_2 crystallises in the trigonal $P\bar{3}m1$ space group and is characterised by the alternating stacking of two layer types along the *c*-axis according to the coordination geometry of the metal cations: a tetrahedral layer and an octahedral layer. In the tetrahedral layer, Li2 and Fe occupy all tetrahedral interstitials (T^+ and T^-) in a disordered fashion, while the octahedral interstitials remain empty (Figure 39(b)). Stacked along the *c* axis is the octahedral layer, in which all octahedral sites are occupied by Li1, while tetrahedral sites remain empty (Figure 39(c)). In each layer all interstitials of the respective coordination type are occupied, while the other sites are empty; in total half the tetrahedral sites and half the octahedral sites are occupied in Li_2FeS_2.

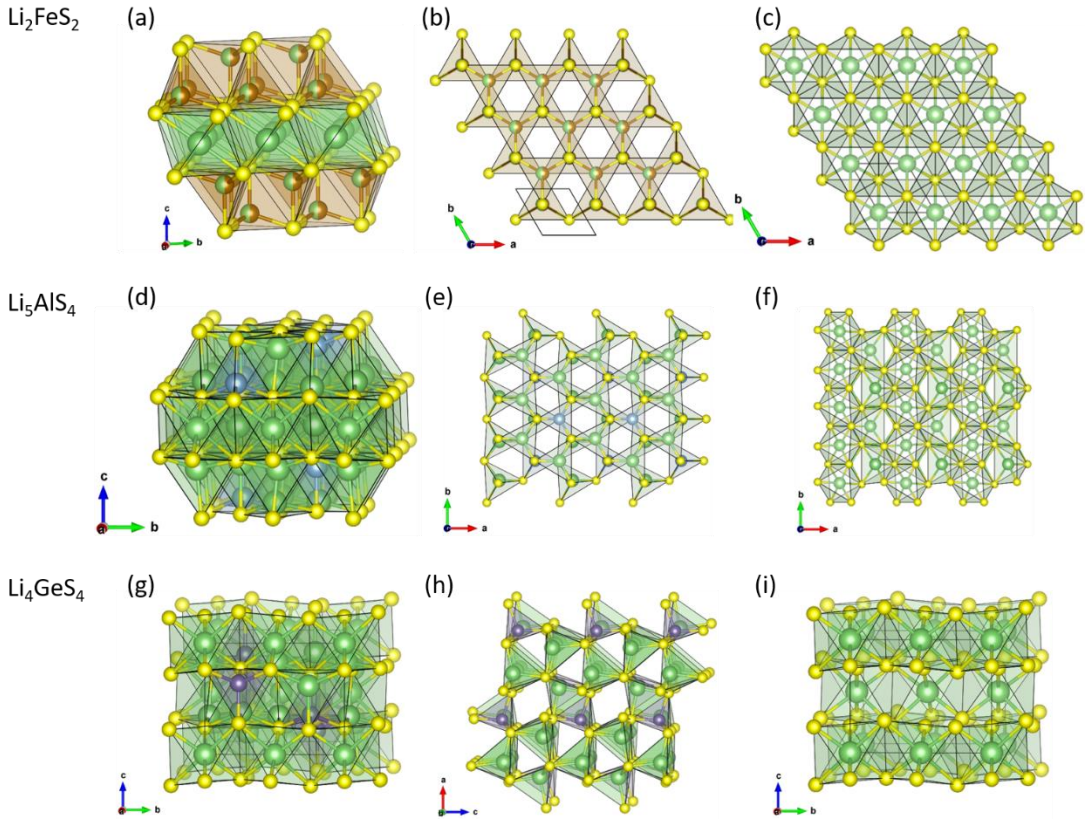

Figure 39: (a) Crystal structure of Li_2FeS_2 viewed along a. The tetrahedral layer consists of disordered mixed Li/Fe sites. (b) View of the tetrahedral layer of Li_2FeS_2 with a single tetrahedral site occupied in a disordered manner by Li^+ and Fe along c. Both the T^+ and T^- sites in the hexagonal close packed sulphide array are occupied in this layer. (c) View of the fully occupied octahedral layer of Li_2FeS_2 along c. (d) Layered crystal structure of Li_5AlS_4 viewed along a. (e) View of the tetrahedral layer of Li_5AlS_4 along c. (f) View of the octahedral layer of Li_5AlS_4 along c. (g) Crystal structure of Li_4GeS_4 viewed along a. (h) GeS_4 and LiS_4 tetrahedra in Li_4GeS_4 forming a γ-Li_3PO_4 type coordination network viewed along b. (i) Net formed by the octahedral Li^+ in Li_4GeS_4 viewed along a. Atoms and polyhedra are coloured as follows: brown, iron; yellow, sulphur; green, lithium; blue, aluminium; purple, germanium. Partially occupied atoms are coloured to represent fractional occupancies. From Chem. Mater. ***2018,*** *30, 7183-7200. Reprinted with permission from ACS Publications.*

The structure of Li_5AlS_4 is closely related to Li_2FeS_2, as a layered motif of cation coordination can be distinguished. It crystallises in the monoclinic space group $P2_1/m$. In the tetrahedral layer Li and Al are well ordered in a 3:1 arrangement (Figure 39(e)), expanding the unit cell from $P\bar{3}m1$ into the supercell $P2_1/m$ (**a**-**b**, 2**a**+2**b**, **c**). The difference in the formal oxidation state of Li^+ and Al^{3+}, which are similar in size, drives the ordering of the cations in the tetrahedral layer.[18] There are two distinct lithium sites in the fully occupied octahedral layer, with slightly different local environments. One Li is coordinated by six sulphur atoms in a near-regular octahedron, while the other (Li3) is coordinated to only five sulphur atoms, as it is displaced from the centre of the octahedral interstitial site as a result of electrostatic effects (Figure 40).

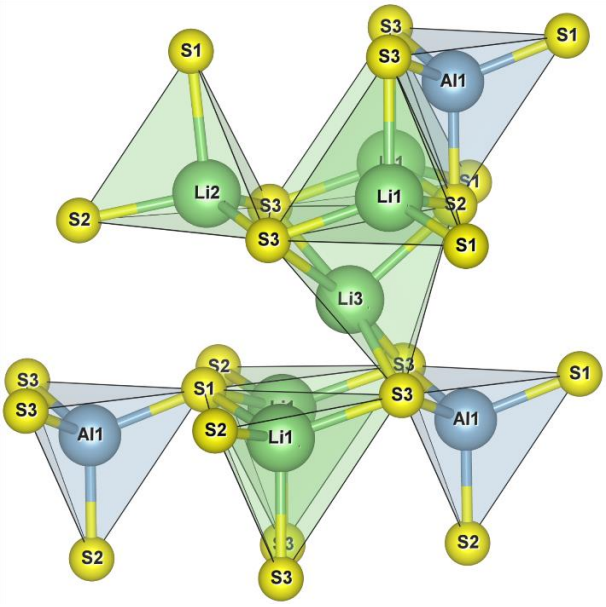

Figure 40: Fragment of the Li_5AlS_4 structure showing the displacement of Li3 towards S2, away from the triangular face shared by two Li1 tetrahedra and one Al1 tetrahedron towards a face containing two Li1 and a Li2 tetrahedra. From Chem. Mater. ***2018,*** *30, 7183-7200. Reprinted with permission from ACS Publications.*

In contrast Thio-LISICON Li_4GeS_4 does not adopt a layered structure but crystallises in a stuffed *γ*-Li_3PO_4 type structure. In each double sulphide slab, 25 % of the octahedral sites are occupied by Li, while 50 % of the tetrahedral T^- sites are occupied by Li and 50 % of the T^+ sites are occupied by Li and Ge (Figure 39(g-i)). The tetrahedral sites form a 3 dimensional network.

4.2 Experimental

4.2.1 Synthesis

The experimental section was taken and slightly adapted from the paper published by Leube *et al.* in 2018.[19]

General procedure. All sample handling was carried out in a dry box under a helium atmosphere (O_2 < 3 ppm). Compositions were mixed in appropriate stoichiometric ratios (typically in 500 mg batches), ground thoroughly and sealed as powders in evacuated carbon coated quartz tubes under a pressure of 1 x 10^{-4} mbar. Lithium sulphide (Li_2S, Sigma Aldrich, 99.98 %, containing 3 wt % of LiOH), aluminium sulphide (Al_2S_3, Alfa Aesar, 99+ %, containing Al_2S_3, with Al and S_8 as minority phases by PXRD), gallium sulphide (Ga_2S_3, Alfa Aesar, 99.99 %), indium sulphide (In_2S_3, Sigma Aldrich, 99.98 %), silicon powder (~325 mesh, 99.5 %, Alfa Aesar), germanium powder (Alfa Aesar, 99.999 %, containing 8.9 wt % GeO_2), tin sulphide, (SnS, Sigma Aldrich, ≥ 99.99 %), phosphorous pentasulphide (P_2S_5, Sigma Aldrich, 99 %) and elemental sulphur (Sigma Aldrich, 99.999 %) were used as provided, unless otherwise stated. Elemental sulphur develops a high vapour pressure at elevated temperatures, therefore for all first firings the reactions were heated to 673 K at a rate of 5 K min^{-1}, then slowly taken to the final temperature at a rate of 0.3 K min^{-1}, held at the temperature, and subsequently cooled to ambient temperature at a rate of 5 K min^{-1}. For further firings, the materials were reground, sealed in evacuated carbon coated quartz tubes as loose powders, and heated/cooled directly to the reaction temperature at a rate of 5 K min^{-1}.

Exploratory synthesis. For the initial exploration of phase formation in the Li_5AlS_4-Li_4GeS_4-Li_3PS_4 phase field, the reaction mixtures were subjected to a single firing to 973 K for 12 h, with reagents used as received.

$Li_{4.4}Al_{0.4}Ge_{0.6-x}Sn_xS_4$. To obtain high quality powder samples of $Li_{4.4}Al_{0.4}M_{0.6}S_4$ (M = Ge^{4+}, Sn^{4+}) it was necessary to reduce the Li_2S content in the initial reaction composition by 5 mol % in order to remove an Li_2S impurity phase, corresponding to a nominal stoichiometry $Li_{4.18}Al_{0.4}M_{0.6}S_{3.89}$ (M = Ge^{4+}, Sn^{4+}). This stoichiometry was used in all reactions described from here onwards, however the ICP- and Rietveld-validated "ideal" stoichiometry $Li_{4.4}Al_{0.4}M_{0.6}S_4$ (M= Ge^{4+}, Sn^{4+}) is used for consistency of discussion. $Li_{4.4}Al_{0.4}Ge_{0.6}S_4$ and materials in the $Li_{4.4}Al_{0.4}Ge_{0.6-x}Sn_xS_4$ (x= 0, 0.2, 0.4, 0.6) series were obtained, as described in the general procedure, by heating reaction mixtures twice to 973 K for 48 h with intermediate grinding. Samples of $Li_{4.4}Al_{0.4}Ge_{0.6}S_4$ prepared using this procedure with commercially sourced

reagents were analysed by ICP elemental analysis and used in the solid state NMR data collection.

Additional samples of $Li_{4.4}Al_{0.4}Ge_{0.6}S_4$ and $Li_{4.4}Al_{0.4}Sn_{0.6}S_4$ were synthesised using in-house prepared Li_2S and purified Ge and used for synchrotron powder diffraction (SXRD) and AC-impedance experiments. Li_2S was synthesised by heating lithium carbonate (Li_2CO_3, Sigma-Aldrich, $\geq$ 99 %) under a stream of CS_2 vapour to 923 K for 6 h and high purity elemental Ge was generated by heating germanium powder (Ge, Alfa Aesar, 99.999 %) in 10 % H_2 in argon to 873 K for 12 h to remove traces of GeO_2. To synthesise $Li_{4.4}Al_{0.4}Ge_{0.6}S_4$ and $Li_{4.4}Al_{0.4}Sn_{0.6}S_4$, reaction mixtures were fired twice to 973 K for 48 h with intermediate grinding. ICP compositional analysis and solid state NMR experiments were conducted on a sample of $Li_{4.4}Al_{0.4}Sn_{0.6}S_4$ prepared in this way.

Due to the large neutron absorption cross section of ^6Li, neutron powder diffraction (NPD) experiments were conducted on ^7Li-enriched samples of $^7Li_{4.4}Al_{0.4}Ge_{0.6}S_4$ and $^7Li_{4.4}Al_{0.4}Sn_{0.6}S_4$. Phase pure $^7Li_2S$ was synthesised by heating lithium carbonate ($^7Li_2CO_3$, Sigma-Aldrich, 99 % ^7Li) under a stream of CS_2 vapour to 923 K for 6 h. As a one-batch synthesis at 3.5 g led to impurity phases, neutron samples were prepared by mixing a single batch of reactants and subsequently dividing this into five carbon-coated quartz tubes which were fired twice at 973 K for 48 h with intermediate grinding. After completion of the reaction, the individual products were screened by PXRD yielding the same lattice parameters; the powders were combined to give ~ 2.5 g of ^7Li enriched samples in total.

$Li_{4.4}M_{0.4}M'_{0.6}S_4$. $Li_{4.4}M_{0.4}M'_{0.6}S_4$ (*M*= Ga^{3+}, In^{3+} and *M'*= Si^{4+}, Ge^{4+}, Sn^{4+}) phases were prepared using in-house prepared Li_2S and purified Ge. Reaction mixtures of the exact stoichiometry $Li_{4.4}M_{0.4}M'_{0.6}S_4$ were heated twice to 973 K for 24 h with intermediate grinding. A ^7Li enriched $^7Li_{4.4}In_{0.4}Sn_{0.6}S_4$ sample was synthesised in the same way using in-house prepared $^7Li_2S$ as a precursor material.

$Li_{10}GeP_2S_{12}$ (LGPS). $Li_{10}GeP_2S_{12}$ was synthesised following established routes from literature:[11] Li_2S, Ge, S and P_4S_{10} were mixed, ground and sealed in a carbon coated quartz tube. The reaction mixture was subjected to a single firing to 823 K for 8 h.

4.2.2 Characterisation

Compositional analysis. The composition of $Li_{4.4}Al_{0.4}Sn_{0.6}S_4$ was determined by measuring the lithium, aluminium and tin contents by ICP-OES (Agilent 5110 SVDV). A solution of $Li_{4.4}Al_{0.4}Sn_{0.6}S_4$ was prepared by dissolving 10.0 mg of sample in 4 ml aqua regia, and

subsequently making up to 100 mL with deionized H_2O. The sulphur content could not be determined due to hydrolysis and consequent H_2S evolution resulting in the loss of sulphur.

The composition of $Li_{4.4}In_{0.4}Sn_{0.6}S_4$ was determined by measuring the elemental contents by ICP-OES (Agilent 5110 SVDV). 11.8 mg of sample were readily dissolved in deionised water and the lithium, indium and tin content thereof could be measured. In order to obtain reasonable sulphur values, the solution had to be 10x diluted with NH_4OH solution (2 %). We speculate that a slightly basic milieu helps to prevent the formation of H_2S.

Elemental analysis of $Li_{4.4}Al_{0.4}Ge_{0.6}S_4$ was performed by Mikroanalytisches Labor Pascher at Remagen-Bandorf, Germany, after dissolution in a HF/HCl solution at elevated temperature and pressure.

X-ray powder diffraction. All powder X-ray diffraction (PXRD) experiments were carried out at ambient temperature on powders sealed in borosilicate glass capillaries under helium gas. Phase identification was carried out using Bruker D8 diffractometers with either a monochromated Mo source ($K\alpha_1$, λ= 0.7093 Å) or a monochromated Cu source ($K\alpha_1$, λ= 1.5406 Å) in Debye-Scherrer geometry. Structure determination and Rietveld refinements were carried out on synchrotron powder X-ray diffraction (SXRD) data collected from spinning capillaries (0.3mm diameter) at the I11 beamline (Diamond Light Source, UK) with an incident wavelength of 0.824878(10) Å, using the high resolution multi-analyser crystal (MAC) detectors. Variable-temperature SXRD from 100 – 500 K was carried out at I11 using an Oxford Cryostream Plus with the Mythen position sensitive detector (PSD).

Neutron powder diffraction. Time-of-flight neutron powder diffraction (NPD) data were collected on $Li_{4.4}Al_{0.4}Ge_{0.6}S_4$ and $Li_{4.4}Al_{0.4}Sn_{0.6}S_4$ using the High-Resolution Powder Diffractometer (HRPD) instrument (ISIS, UK) both at 10 K and at ambient temperature. Samples were contained in thin-walled vanadium cans of diameter 6 mm, sealed with an indium gasket under 1 atmosphere of helium gas. Low temperature data were collected using an in-situ closed-cycle refrigerator (CCR). Bragg features from the CCR were manually excluded from the Rietveld refinements. Ambient-temperature data were collected with no CCR, in order to minimise background scattering. For all samples, NPD data were collected on ^7Li enriched samples to minimise absorption effects.

Densification. For all compositions, pellets for AC-impedance spectroscopy and stability tests against lithium metal were prepared by uniaxial pressing of ~35 mg of the powdered material in a 5mm steel die at a pressure of 2.5 MPa, followed by sintering in evacuated carbon coated

quartz tubes at 923 K for 24 h. Densities in the range 75 % - 82 % were achieved by this method.

AC impedance spectroscopy. Temperature dependent AC-impedance spectroscopy was conducted to obtain the ionic conductivity and activation energy of each composition. Sintered pellets were painted with silver paste (RS silver conductive paint 186-3600) and dried under vacuum at ambient temperature. The measurements were performed from 303 to 398 K under argon (flow rate: 50 mL min^{-1}) using a custom-built sample holder and the Solartron 1296 dielectric interface coupled with the Solartron 1255B frequency response analyser. A sinusoidal amplitude of 50 mV was employed in the frequency range 1 MHz to 100 mHz. The obtained data was analysed with the ZView2 software package (ZView2 Version: 3.5d).[20]

Electrochemical cycling. The stabilities of $Li_{4.4}Al_{0.4}Ge_{0.6}S_4$, $Li_{4.4}Al_{0.4}Sn_{0.6}S_4$, $Li_{10}GeP_2S_{12}$ and $Li_{4.4}In_{0.4}Sn_{0.6}S_4$ were tested against lithium metal electrodes. Symmetric Li|SE|Li cells were assembled in Swagelok-type cells using pellets of the respective solid electrolytes. Cells were prepared and sealed inside an Ar-filled glovebox (O_2; H_2O < 0.1 ppm). Two lithium metal disk electrodes (12 mm diameter) were punched from Li ribbon (0.38 mm thickness, Sigma Aldrich) and then mechanically pressed onto a sintered SE pellet. The sealed cells were allowed to equilibrate to 323 K for 30 minutes in order to increase lithium mobility. The symmetrical cells were then cycled galvanostatically, using a VSP potentiostat/galvanostat (Biologic Science Instruments) for 100 plating and stripping cycles (J= ± 0.01 mA cm^{-2} for 1 h per half-cycle).

Plating experiment. Li|SE|Cu asymmetrical Swagelok-type cells were likewise prepared wherein one Li disk is replaced with a 12 mm diameter Cu foil (Advent RM) disk working electrode acting as the Li deposition substrate. Prior to use, the Cu disks were soaked in 1 mol dm^{-3} HCl solution for 15 minutes, subsequently rinsed with ethanol and ultra-pure water and then dried at 373 K under vacuum. Li|SE|Cu cells were prepared and sealed inside the glovebox and then Li was deposited onto the Cu substrate under galvanostatic control for 20 h at 0.01 mA cm^{-2} (T= 323 K). The resulting cells were dismantled inside an Ar-filled glovebox and the Cu working electrode was photographed.

DC polarization experiment. DC polarization experiments were conducted on pellets of $Li_{4.4}In_{0.4}Sn_{0.6}S_4$ which were covered with a silver electrode. Voltages of 0.01 V, 0.05 V and 0.1 V were applied and the currents were recorded for 12 min each using an Autolab 84515 instrument.

NMR. All solid state NMR analysis of $Li_{4.4}Al_{0.4}Ge_{0.6}S_4$ and $Li_{4.4}Al_{0.4}Sn_{0.6}S_4$ was carried out by Kenneth K. Inglis in the Dr F. Blanc research group at the University of Liverpool. Detailed experimental procedures and parameters are given in Leube *et al*:[19]

Variable temperature ^{7}Li NMR experiments were recorded on a 4 mm HXY MAS probe in double resonance mode (between 110 K – 400 K) and a 4 mm HX High Temperature MAS Probe (above room temperature), both on a 9.4 T Bruker Avance III HD spectrometer under static conditions with the X channel tuned to ^{7}Li at $\omega_0/2\pi(^7Li)$ = 156 MHz. All samples were flame sealed in Pyrex inserts under He atmosphere. All ^{7}Li NMR spectra were obtained with a hard 90^o pulse of 1.5 µs at rf amplitude of $\omega_1/2\pi(^7Li)$ = 83 kHz. Spin-lattice relaxation rates in the laboratory frame (T_1^{-1}) were obtained using a saturation recovery pulse sequence and the data was fitted to a stretch exponential function of form $1 - \exp[-(\tau/T_1)^{\alpha}]$ where τ are the variable delays and α is the stretch exponential (values between 0.3 and 1) . Spin-lattice relaxation rates in the rotating frame ($T_{1\rho}^{-1}$) were recorded using a standard spin-lock pulse sequence at frequencies of $\omega_1/2\pi(^7Li)$ = 20, 33 and 50 kHz and data were fitted to a stretch exponential function of form $\exp[-(\tau/T_{1\rho}^{-1})^{\beta}]$ where β values are between 0.5 and 1. Temperature calibrations were performed using the chemical shift thermometers $Pb(NO_3)_2$ using ^{207}Pb NMR and CuI and CuBr using ^{63}Cu NMR.[21-24] ^{7}Li NMR shifts were referenced to 10 M LiCl in D_2O at 0 ppm.

Ab-initio molecular dynamics simulations. All *ab initio* molecular dynamics simulations on $Li_{4.4}Al_{0.4}Ge_{0.6}S_4$ were carried out by Dr Paul M. Sharp in the Prof M. Rosseinsky research group at the University of Liverpool. Detailed experimental procedures and parameters are given in Leube *et al*. [19]

Periodic, plane-wave based, density functional theory (DFT) calculations were performed using VASP[25], the PBE functional[26] and the projector augmented wave approach.[27] Calculations were performed in (**a**−**b**, 2**a**+3**b**, 2**c**) supercells of $Li_{4.4}Al_{0.4}Ge_{0.6}S_4$, where the supercells have a total composition of $Li_{88}Al_8Ge_{12}S_{80}$. Crystallographic disorder was taken into account by ranking one hundred different ordered atomic configurations within this supercell by energy. These configurations were generated by randomly distributing atoms in the structure under the following constraints: i) each of the four tetrahedral layers within a supercell contained 2 Al and 3 Ge atoms, ii) one of the two square-pyramidal Li3 sites close to the centre of each octahedron was randomly chosen to be occupied, iii) one octahedral interstice containing Li3 sites in each of the two octahedral layers in a supercell was randomly chosen to be vacant, leading to one vacant Li3 octahedron within each half of a supercell,

and iv) one quarter of the face sharing pairs of Li1 and Li2 tetrahedral sites were randomly chosen to be Li2 sites, and three quarters Li1 sites. This generates supercells where neighbouring Li1 and Li2 sites are never simultaneously occupied, and the two nearest Li3 sites are never simultaneously occupied.

The unit cell and atomic positions of the one hundred generated configurations were optimised using "fast" parameters. Reciprocal space was only sampled at the Γ point, an energy cutoff of 600 eV was used, and optimisation was completed once forces fell below 0.02 eV/Å. The configurations were ranked according to the resulting energies, and the lowest five labelled with A-E, starting with the lowest in energy (Table S1). Supercells A and B were chosen to take forward as good representative models for further study. More accurate "slow" parameters were used to reoptimise the structures of the lowest five configurations. Reciprocal space was sampled with a 3×2×3 k-point grid, and forces optimised to a tighter convergence of 0.01 eV/Å. The relative energies of supercells A–C agree well with those calculated with the "fast" parameters (Table S1). Supercell D becomes significantly more stable using the "slow" parameters, and becomes the most stable configuration. This is due to optimisation into a new configuration of cations. Subsequent optimisation using the "fast" parameters and starting from the new configuration, results in a very similar computed stability. Supercell E remains the least stable configuration. These results give us confidence that the "fast" parameters are sufficiently accurate to use for subsequent *ab initio* molecular dynamics (AIMD) calculations.

AIMD calculations were performed on supercells A and B using the "fast" parameters. A 0.5 fs time step was used throughout using the NVT ensemble. Both AIMD trajectories were initialised by performing a temperature ramp from 0 to 400 K over ~10 ps, and then an equilibration run at 400 K for ~8 ps using velocity rescaling to set the temperature. Production runs of 120 ps were performed at a set temperature of 400 K, using a Nosé thermostat, and resetting the electron density after every 8 ps.

Variations of supercell A were optimised using the "slow" parameters where one of the two Li3 vacancies was occupied by one of the surrounding Li2 atoms, in order to investigate potential Li^+ transport pathways. This was done for each of the four Li2 atoms neighbouring one vacant Li3 site, and the two Li2 atoms neighbouring a second vacant Li3 site. For the first Li3 site, we found that all four of the Li^+ ions relaxed back from the Li3 site onto their original Li2 sites. It was, however, possible to stabilise Li^+ on the second previously vacant Li3 site, defining one end of a transport pathway, with Li^+ in the Li2 site at the other end. The barrier

for the Li3 to Li2 transport along this pathway was determined by performing nudged elastic band (NEB) calculations. We used nine images constructed by placing the Li atom at equal intervals between the Li3 and Li2 positions, with the default VASP settings for the spring constant, and the “slow” parameters for optimisation.

The free energies of Li^+ ions along the c axes of supercells A and B were determined by placing a series of Gaussians, each centred on a Li^+ ion, in the supercell. All of the Gaussians had a standard deviation of 0.05 Å. For a given point along the c axis, the sum of all of the Gaussians at that point gives the density of Li^+ ions. The free energy is then given by $F = k_B T \, ln \, W$, where *W* is the density of Li^+ ions and the value of T is 400K, from the AIMD calculations

4.3 Results/discussion

4.3.1 Overview of explorative synthesis in the Li_5AlS_4-Li_4GeS_4-Li_3PS_4 phase field

The five-dimensional Li-Al-Ge-P-S phase field was restricted to the pseudo-ternary Li_5AlS_4-Li_4GeS_4-Li_3PS_4 phase field. While ensuring the nominal oxidation states of Li^+, Al^{3+}, Ge^{4+}, P^{5+} and S^{2-}, this reduces the chemical space drastically.

An initial set of eight compositions was synthesised, aiming to cover the phase field evenly. The task was to minimise the total number of reactions required but explore sufficient chemical space so as to efficiently identify any new compound. Synthetic conditions were chosen to resemble those used in the literature for known compounds such as $Li_{4+x}Si_{1-x}Al_xS_4$ or $Li_{4-x}Si_{1-x}P_xS_4$ (*i.e.* T= 973 K, t= 12 h).[10]

Figure 41(a) gives an overview of the explored Li_5AlS_4-Li_4GeS_4-Li_3PS_4 pseudo-ternary phase field including known phases and synthesised compositions.

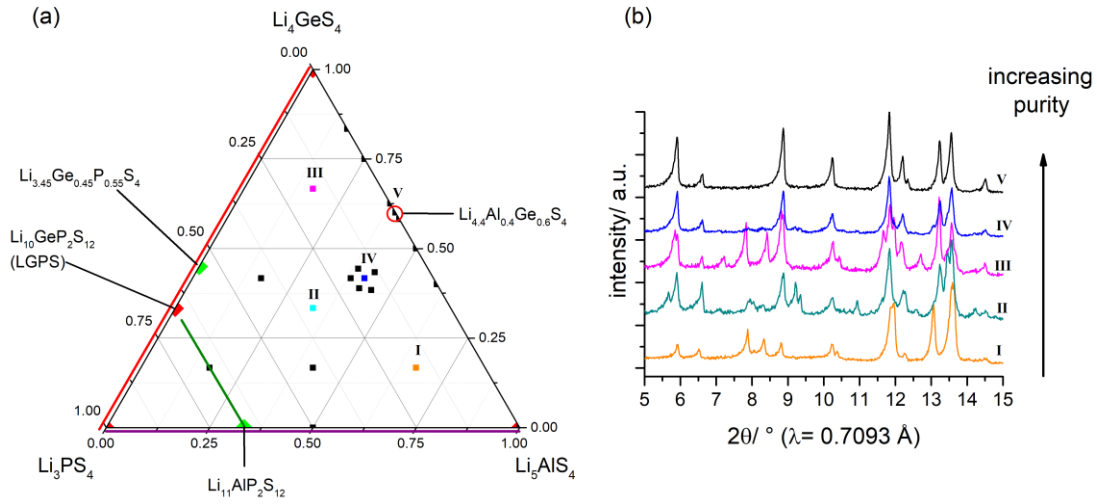

Figure 41: Identification of $Li_{4.5}Al_{2/3}Ge_{1/6}P_{1/6}S_4$ and $Li_{4.4}Al_{0.4}Ge_{0.6}S_4$ as stable phases in the pseudo-ternary Li_5AlS_4-Li_4GeS_4-Li_3PS_4 phase field. (a) overview of all known compounds and synthesised compositions including the location of $Li_{4.5}Al_{2/3}Ge_{1/6}P_{1/6}S_4$ (I), which can be fully indexed to the space group of Li_5AlS_4, and a new phase $Li_{4.4}Al_{0.4}Ge_{0.6}S_4$ (V). All other compositions result in the formation of multiple-phase mixtures; (b) PXRD patterns of selected compositions showing how the newly discovered phase $Li_{4.4}Al_{0.4}Ge_{0.6}S_4$ (V) was compositionally refined.

The PXRD pattern of each synthesised composition was carefully analysed and matched against known phases to identify un-indexed reflections which can indicate the presence of a new phase. Remarkably the pattern of I ($Li_{4.5}Al_{2/3}Ge_{1/6}P_{1/6}S_4$) could be fully indexed to the same space group of Li_5AlS_4 despite one third of the Al^{3+} cations having been exchanged for Ge^{4+} and P^{5+}. Further structural analysis and AC-impedance spectroscopy on this material will be presented in the second part of the chapter. The PXRD patterns of composition III and in

particular IV showed new features (*i.e.* the absence of reflections, in particular between 2θ= 7 °- 9 ° and changing relative intensities) while those features were less pronounced for compositions II and not detectable in I (compare to Figure 41(b)). This information guided the synthesis towards point V; eventually a single-phase material V was isolated corresponding to the composition $Li_{4.4}Al_{0.4}Ge_{0.6}P_0S_4$, focussing the attention on the phosphorous free part of the phase field. Investigation on the new compound V and related materials will be presented in detail in the following sections. The PXRD patterns of all other synthesised compositions in the Li_5AlS_4-Li_4GeS_4-Li_3PS_4 phase field were fully indexed to known phases.

4.3.2 $Li_{4.4}Al_{0.4}M_{0.6}S_4$ (*M*= Ge^{4+}, Sn^{4+})

4.3.2.1 Synthetic optimisation and compositional analysis

The exploratory synthesis in the Li_5AlS_4-Li_4GeS_4-Li_3PS_4 phase field led to the discovery of the new phase with nominal composition of $Li_{4.4}Al_{0.4}Ge_{0.6}S_4$. Extensive work was undertaken to optimise the synthetic conditions: optimisation of synthesis temperature and duration, refiring, the value of *x* in $Li_{4+x}Al_xGe_{1-x}S_4$ and use of carbon coated quartz tubes were necessary to obtain powders of satisfactory purity. A Li_2S impurity was removed by reducing the initial Li_2S content in the reaction mixture by 5 mol %, giving a formal stoichiometry of $Li_{4.18}Al_{0.4}Ge_{0.6}S_{3.89}$ (compared to $Li_{4.4}Al_{0.4}Ge_{0.6}S_4$). ICP-OES analysis of this reaction product gave an overall composition of $Li_{4.40(9)}Al_{0.44(1)}Ge_{0.64(1)}S_{3.99(8)}$. After optimising the synthetic conditions, SXRD analysis still revealed the presence of a small Li_2S impurity (< 1 wt %) in addition to Li_4GeS_4 and α-Al_2O_3 (Figure 42). It is very challenging to derive a precise composition for the new phase from the compositional bulk measurement. As such, the material will be referred to as $Li_{4.4}Al_{0.4}Ge_{0.6}S_4$.

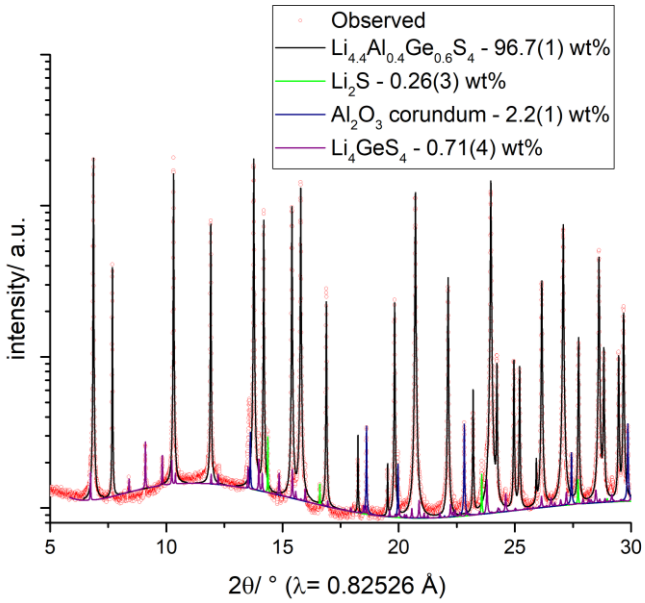

Figure 42: Multi-phase Rietveld fit to the SXRD pattern of $Li_{4.4}Al_{0.4}Ge_{0.6}S_4$ sample used for elemental analysis and NMR experiments (synthesised using commercial Li_2S and Ge without further purification). Intensities are plotted in a logarithmic scale. Colours of individual components are: black: $Li_{4.4}Al_{0.4}Ge_{0.6}S_4$, green: Li_2S, blue: Al_2O_3, purple: Li_4GeS_4. From Chem. Mater. ***2018,*** *30, 7183-7200. Reprinted with permission from ACS Publications.*

The presence of these impurities, particularly α-Al_2O_3, indicated that the starting materials were contaminated with oxides and hydroxides. The reagent Li_2S was contaminated with LiOH (3 wt %), and the Ge source contained 8.9 wt % GeO_2. Experimental procedures were therefore developed for the synthesis of Li_2S from Li_2CO_3 under a stream of CS_2 and the reduction of Ge/GeO_2 under a flow of 10 % H_2/Argon. Despite being able to remove the α-Al_2O_3 impurity from the reaction product by using high purity reagents, small amounts of $LiAlS_2$ and elemental Ge were still detectable by SXRD analysis in the final product.

4.3.2.2 Solving the crystal structure of $Li_{4.4}Al_{0.4}Ge_{0.6}S_4$

The structure of $Li_{4.4}Al_{0.4}Ge_{0.6}S_4$ was solved in collaboration with Dr Elliot J. Carrington and Dr Michael J. Pitcher of the Rosseinsky group, Liverpool.

Initially the SXRD pattern of $Li_{4.4}Al_{0.4}Ge_{0.6}S_4$ was indexed to an orthorhombic unit cell (space group: *Pmmm*) of the following dimensions: *a*= 6.8847(7) Å, *b*= 6.1566(5) Å, *c*= 7.9494(7) Å, which is closely related to the unit cell parameters of monoclinic Li_4SiS_4: *a*= 6.893 Å, *b*= 7.768 Å, *c*= 6.124 Å, β= 91.23 ° (space group: $P2_1/m$). A Pawley fit using this unit cell is shown in Figure 43(a). But attempts to refine the structure using Li_4SiS_4 as a starting model in Rietveld refinements failed repeatedly, as severe intensity mismatches were observed.

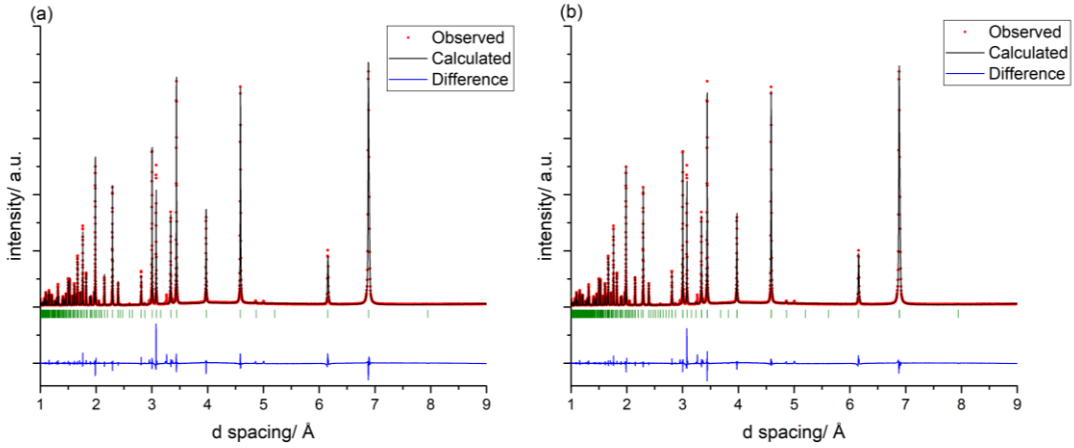

Figure 43: Pawley fits of $Li_{4.4}Al_{0.4}Ge_{0.6}S_4$ against two unit cells of orthorhombic symmetry with different lattice parameters. (a) space group: Pnma, a= *6.8847(7) Å,* b= *6.1566(5) Å,* c= *7.9494(7) Å; (b)* space group: Pmmm, a= *13.776(5) Å,* b= *7.946(1) Å,* c= *6.157(1) Å. The positions of calculated Bragg reflections are shown by green tick marks.*

An alternative route to solve the crystal structure was successfully undertaken, based on the assumption that the new material is based on an hcp S^{2-} sublattice and the non-lithium metal site is a disordered Al/Ge site. The SXRD pattern could be indexed to a unit cell of the dimension of the unit cell of Li_4GeS_4 (space group type: *Pnma*), but in a different space group type: *Pmmm* (*a*= 13.776(5) Å, *b*= 7.946(1) Å, *c*= 6.157(1) Å), as shown in Figure 43(b). As a starting model the positions of the sulphur atoms in Li_4GeS_4 were used to construct an hcp S^{2-} sublattice. Then simulated annealing was applied to find the positions of the non-lithium metal sites in *P*1 symmetry. The program FindSymm[28] was then used to find the symmetry of the structure, which transformed the unit cell into a hexagonal setting in the trigonal space group $P\bar{3}m1$ (*a*= 7.91914(6) Å, *c*= 6.13319(7) Å), the same space group as Li_2FeS_2. Further relationship to Li_2FeS_2 is given by doubling of the **a** vector and **b** vector, resulting in a (2**a**, 2**b**, **c**) expanded cell. This model was subsequently refined by the Rietveld method to obtain accurate fractional coordinates of the sulphur and the metal sites, as shown by the good fit to the observed data to the model in Figure 44.

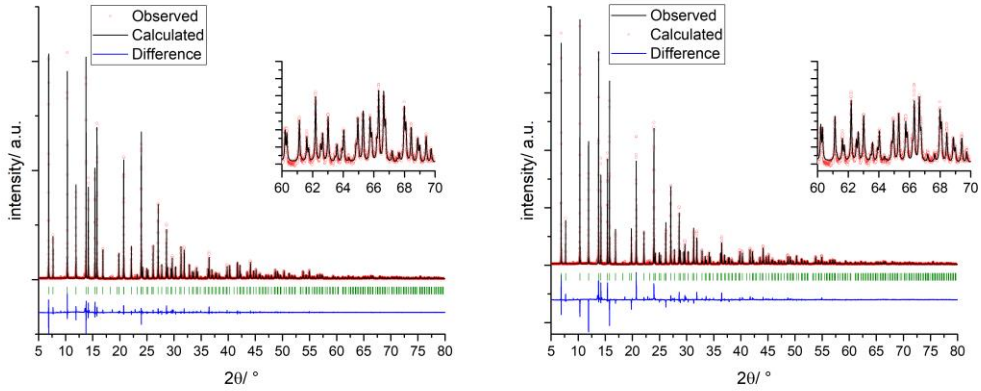

Figure 44: Pawley and Rietveld fits of the preliminary lithium-free model of $Li_{4.4}Al_{0.4}Ge_{0.6}S_4$ in the trigonal space group P$\bar{3}$m1 (a= 7.91914(6) Å, c= 6.13319(7) Å), taking into account only the sulphur-heavy metal framework without any lithium sites, against SXRD data (I11 beamline, MAC detector, λ= 0.82526 Å, room temperature). The positions of calculated Bragg reflections are shown by tick marks, the insets show the good fit to high angle data. (a) Pawley fit, R_{wp}= 11.72, χ^2= 40.424 (b) Rietveld fit, R_{wp}= 13.54, χ^2= 51.471. From Chem. Mater. ***2018,*** *30, 7183-7200. Reprinted with permission from ACS Publications.*

This preliminary lithium-free model described $Li_{4.4}Al_{0.4}Ge_{0.6}S_4$ as a layered hcp structure with a mixed Al^{3+}/Ge^{4+} site ordered into a quarter of the tetrahedral interstices of the tetrahedral layer. Even though Li^+ has a very low diffraction scattering factor, due to the low number of electrons, the excellent quality of the data allowed for the construction of Fourier difference maps, which were used to find provisional Li^+ positions. Residual diffraction intensity, relating to the Li^+ ions, could be found in the remaining tetrahedral interstices of the tetrahedral layer (6*i*) and in three-quarters of the octahedral interstices of the octahedral layer (3*f*). One-quarter of the octahedral interstices in the octahedral layer remained vacant (1*b*). The resultant SXRD model is given in Figure 45.

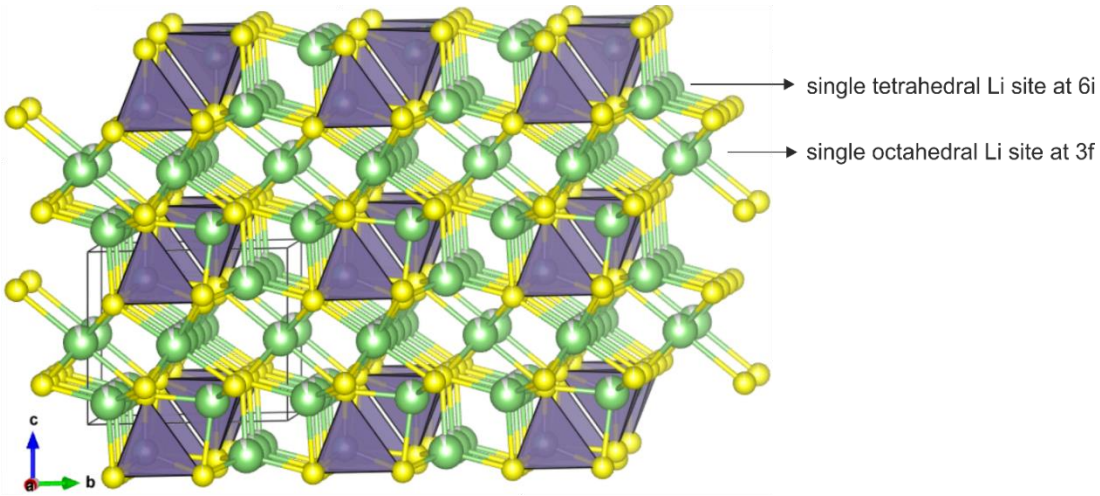

Figure 45: Structural model of $Li_{4.4}Al_{0.4}Ge_{0.6}S_4$ from SXRD with preliminary/approximate lithium sites (corresponding to the Rietveld fit in Figure 44(b)). Atoms and polyhedra are coloured as follows: yellow: sulphur, green: lithium, purple: mixed Al^{3+}/Ge^{4+} site. Partially occupied atoms are coloured to represent fractional occupancies. From Chem. Mater. ***2018,*** *30, 7183-7200. Reprinted with permission from ACS Publications.*

Eventually this preliminary SXRD model was further refined using neutron powder diffraction (NPD) data collected at the ISIS neutron source, UK, on a ^{7}Li enriched sample. The thermally dependent displacement/movement of Li^{+} can be quite significant in materials with high lithium mobility, making it difficult to accurately determine the positions and occupancies of the lithium sites. Thus, initial refinements were conducted on NPD data recorded at low temperature (10 K). Fitting the neutron data against the model derived from SXRD data and refining atomic coordinates, occupancy parameters and atomic displacement parameters, resulted in a reasonable fit, but left several mismatches between the observed and measured intensities (χ^2= 2.76). A Fourier difference map, calculated from NPD data, revealed the presence of two points of negative scattering intensity about the octahedral lithium site, indicating a displacement of 0.2 Å along the $\bar{1}11$ direction. Another negative peak was identified in a tetrahedral site, located within the octahedral layer, displaced by 1 Å from the tetrahedral 6*i* site along the 001 direction. The structural model was adjusted by moving the octahedral Li^{+} off the centre of the octahedron along $\bar{1}11$, creating a split 6*i* site, with the occupancy halved. A third crystallographically-independent lithium site was created by populating the tetrahedral Li site (6*i*) in the octahedral layer. The occupancies of lithium in this model were refined, which eliminated the distinct mismatches and resulted in a fit yielding χ^2= 1.69. The resulting fits of the final model are shown in Figure 46. Freely refined occupancies and isotropic displacement correspond well to the nominal composition.

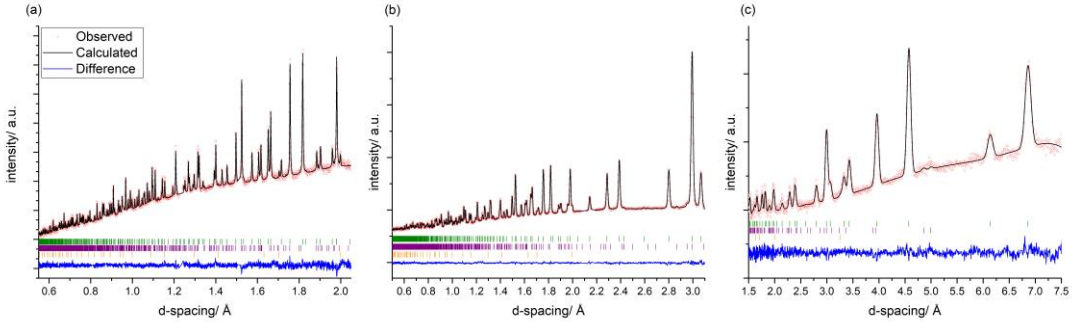

Figure 46: Rietveld refinements of $^{7}Li_{4.4}Al_{0.4}Ge_{0.6}S_4$ (synthesised using purified reactants) against NPD data (ISIS neutron source, HRPD, 10 K). The positions of calculated Bragg reflections are shown by tick marks (green: $Li_{4.4}Al_{0.4}Ge_{0.6}S_4$, purple: $LiAlS_2$, orange: Ge). (a) bank 1, 2θ= 168.3 °, (b) bank 2, 2θ= 89.6 ° and (c) bank 3, 2θ= 30.0 °. Note that all data banks contain a significant background contribution from the closed-cycle refrigerator sample environment. From Chem. Mater. ***2018,*** *30, 7183-7200. Reprinted with permission from ACS Publications.*

This NPD model was then tested by Rietveld refinement against ambient NPD and SXRD data. This produced similarly satisfying fits (χ^2= 2.04), using Li occupancies and displacement parameters, which did not diverge significantly compared to the values refined at 10 K. Ambient temperature fits of the final model are shown in Figure 47.

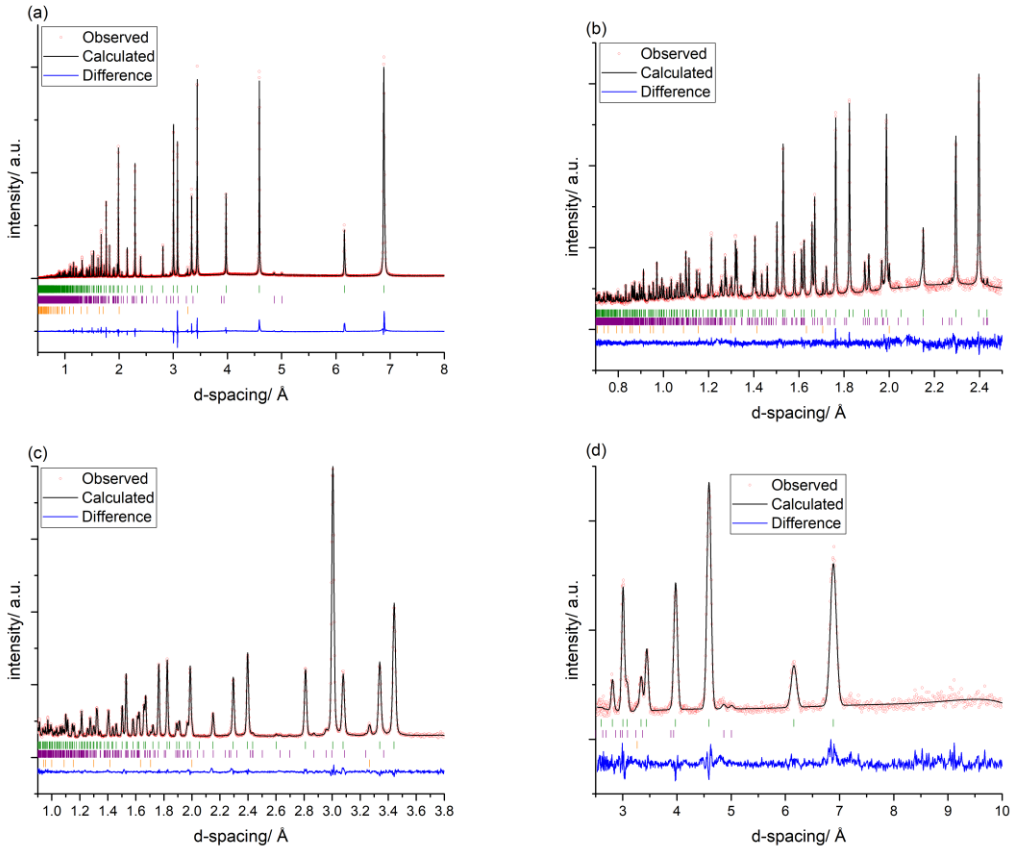

Figure 47: Ambient temperature Rietveld refinements of $^{7}Li_{4.4}Al_{0.4}Ge_{0.6}S_4$ (synthesised using purified reactants) against SXRD data (I11 beamline, MAC-detector, λ= 0.824878 Å) and NPD data (ISIS neutron source, HRPD beam line). The positions of calculated Bragg reflections are shown by tick marks (green: $^{7}Li_{4.4}Al_{0.4}Ge_{0.6}S_4$, purple: $LiAlS_2$, orange: Ge). (a) SXRD pattern, (b) NPD pattern, bank 1, 2θ = 168.3 °, (c) NPD pattern, bank2, 2θ = 89.6 ° (d) NPD pattern, bank 3, 2θ = 30.0 °. From Chem. Mater. ***2018,*** *30, 7183-7200. Reprinted with permission from ACS Publications.*

Full crystallographic information for the Rietveld fits at 10 K and at ambient temperature is given in Table 13 and Table 14 respectively.

4.3.2.3 Crystal structure description of $Li_{4.4}Al_{0.4}Ge_{0.6}S_4$

Figure 48 visualises the finalised model for the crystal structure of $Li_{4.4}Al_{0.4}Ge_{0.6}S_4$. The material crystallises in the trigonal $P\bar{3}m1$ space group with two formula units per unit cell. Sulphur atoms form a hcp sublattice, while the distinct occupation of tetrahedral ((Al^{3+}/Ge^{4+}) and Li1) interstices and octahedral (Li2 and Li3) interstices create a layered motif (Figure 48(a)) similar to Li_2FeS_4.

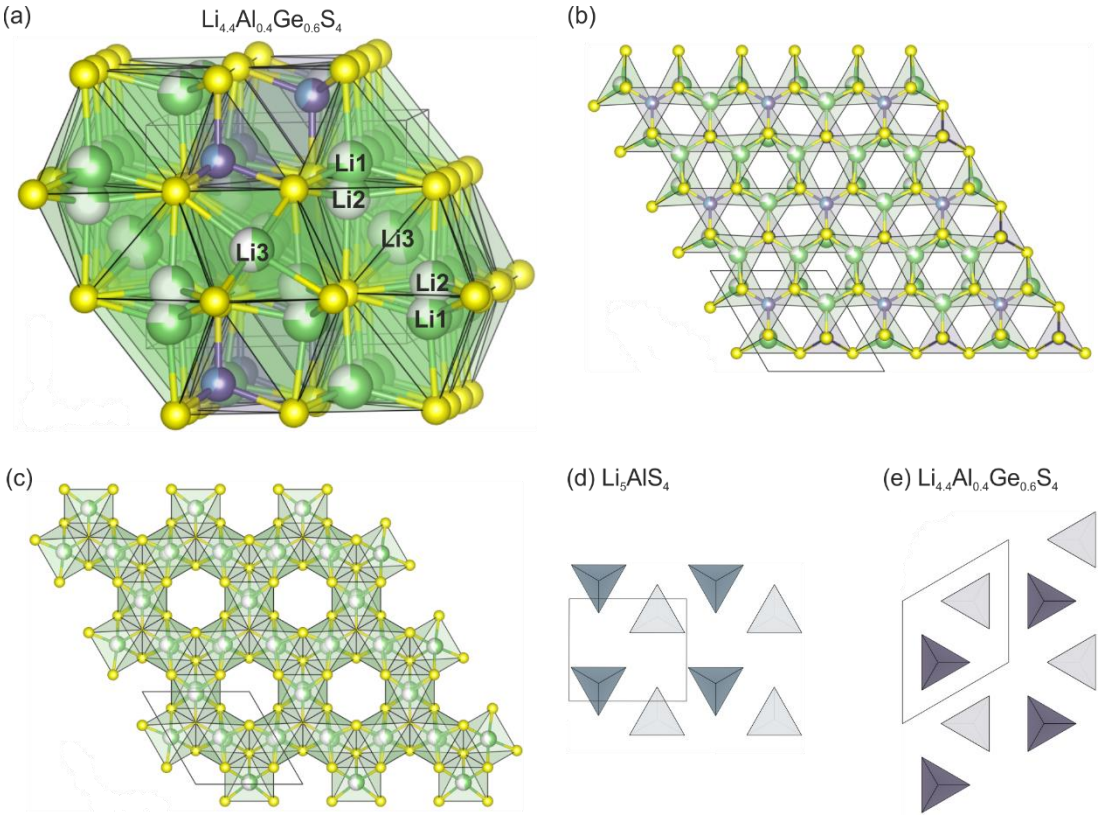

Figure 48: (a) Refined crystal structure of $Li_{4.4}Al_{0.4}Ge_{0.6}S_4$ at 10 K viewed perpendicular to the stacking direction. (b) View of the tetrahedral layer of $Li_{4.4}Al_{0.4}Ge_{0.6}S_4$ along the c axis illustrating the ordering of the fully occupied mixed (Al^{3+}/Ge^{4+}) site and the partially occupied Li1 site. (c) View of octahedral layer of $Li_{4.4}Al_{0.4}Ge_{0.6}S_4$ along the c axis, illustrating the 3:1 ordering of the lithium-occupied sites with vacant sites. Yellow: sulphur, green: lithium, blue-purple: mixed Al^{3+}/Ge^{4+} site. (d) Arrangement of AlS_4 tetrahedra in Li_5AlS_4, viewed along the stacking axis. (e) Arrangement of MS_4 tetrahedra in the tetrahedral layer of $Li_{4.4}Al_{0.4}Ge_{0.6}S_4$ for comparison. From Chem. Mater. ***2018,*** *30, 7183-7200. Reprinted with permission from ACS Publications.*

The fully occupied tetrahedral heavy-metal sites order against the partially occupied Li sites (Li1) in a 1:3 fashion, expanding the unit cell (2**a**, 2**b**, c) compared to the disordered Li_2FeS_2 parent phase. Each Al^{3+}/Ge^{4+} site shares edges only with three adjacent Li tetrahedra, maximising the distance between each Al^{3+}/Ge^{4+} site and thus minimising electrostatic repulsion (Figure 48(b)). The tetrahedral lithium sites Li1 and Li2 refine to occupancies of 0.738(5) and 0.254(4) respectively. These values are consistent with the idea of having a single lithium atom disordered over two face sharing sites in two neighbouring layers, as the combined occupancy is 0.992(6) (Figure 49(a)). The proximity of the two sites precludes simultaneous occupancy. The octahedral layer is characterised by the ordered vacancy in every fourth octahedral site (Figure 48(c)). This contrasts the fully occupied octahedral layers in Li_2FeS_2 or Li_5AlS_4. The ordering of the vacancy can be related to the ordering of the tetrahedral sites: the highly charged (Al^{3+}/Ge^{4+}) are linked to the ordered vacancy by corner sharing, thus lying furthest away (Figure 49(b)). The low charged Li1 share faces and edges with the vacant octahedra in adjacent layers.

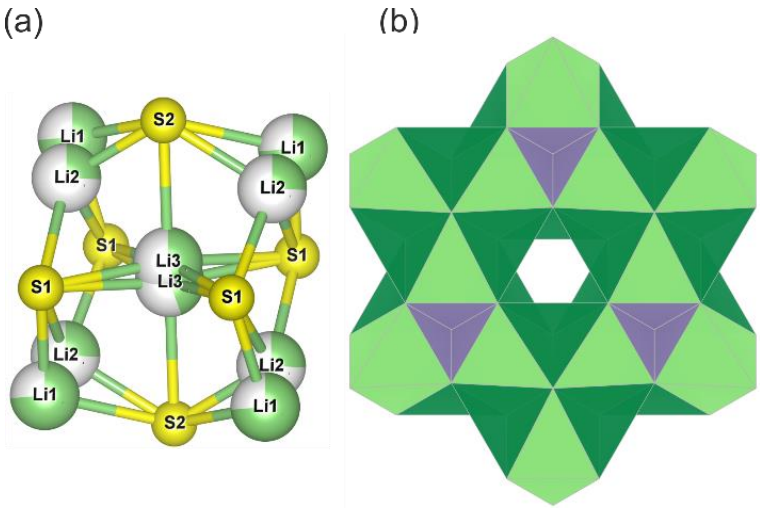

*Figure 49: (a) Average arrangement of partially-occupied nearest-neighbour tetrahedral lithium ions surrounding the octahedral Li3 sites, showing Li2 sites coordinated to four octahedral faces and Li1 coordinated to four octahedral edges, with the Li3 site split by displacement from the octahedral centroid due to the dominance of non-centrosymmetric local configurations. (b) View of the octahedral layer in $Li_4Al_{0.4}Ge_{0.6}S_4$ along **c** showing the ordering of mixed Al^{3+}/Ge^{4+} tetrahedra (purple) which are corner-linked to the empty octahedral sites (centre). Note that the partially occupied Li2 (dark green) tetrahedra in the octahedral layer share faces with both empty and occupied (light green) octahedral sites. From Chem. Mater. **2018,** 30, 7183-7200. Reprinted with permission from ACS Publications.*

The split Li3 site refines to an occupancy of 0.441(7), introducing a disordered vacancy of 0.067 per occupied octahedron in the octahedral layer. The displacement of Li3 towards the S2 vertices results in a pseudo-square-pyramidal coordination environment with four equatorial Li3-S1 bonds in the range of 2.614(6)-2.672(5) Å, a short axial Li3-S2 bond of 2.634(6) Å and a long axial Li3-S2 bond of 3.305(6) Å. The idealised Li3-S2 distance from the middle of the centroid would be 2.835 Å, which is longer than the typical Li-S bond. But this displacement is not simply due to size effects and therefore related to the bond valence requirements. The bond valence sums (BVS) for Li3 in the middle of the centroid is 0.91, increasing only marginally by 0.01 by moving towards S2. These values compare well to the BVS values for the octahedral lithium sites in Li_5AlS_4 (0.85) and Li_4GeS_4 (0.94) and thus cannot justify the displacement. It is the disorder of the neighbouring Li2 sites, which are found in the same layer only 2.53 Å away, which creates an electrostatic driving force for the displacement of Li3. Statistically every fourth Li2 site is occupied (occupancy 0.254(4)), thus the most common local arrangement is that Li3 is repelled electrostatically from one shared Li2-Li3 face off the centre off the octahedral interstice (compare to Figure 49(a)). Li_5AlS_4 and Li_4GeS_4 do not exhibit the disordering of the tetrahedral Li. Thus, there is no local electrostatic repulsion and the lithium atoms can be found in a fully centric octahedral coordination (Figure 50). More information on bond length for the lithium cations in $Li_{4.4}Al_{0.4}Ge_{0.6}S_4$, Li_5AlS_4 and Li_4GeS_4 is tabulated in the appendix Table 15 - Table 17.

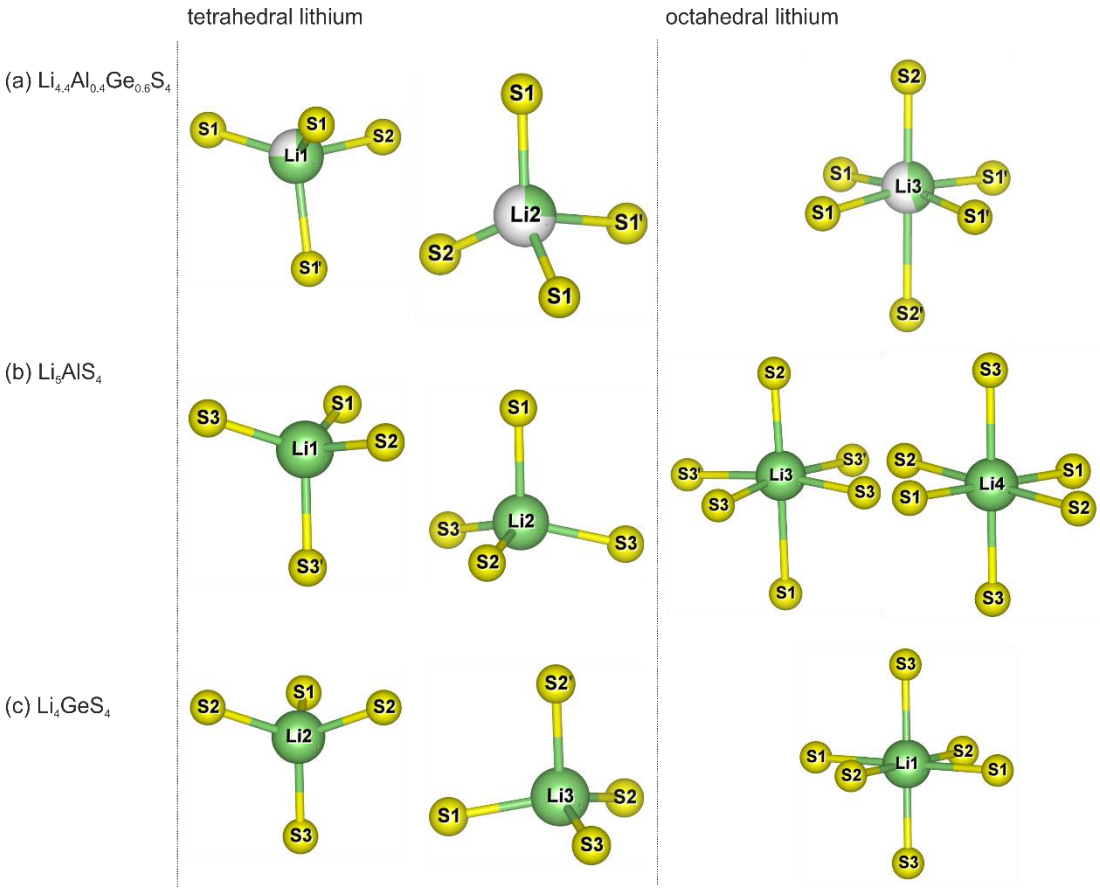

Figure 50: (a) Local lithium coordination geometries for $Li_4Al_{0.4}Ge_{0.6}S_4$ (determined at 10 K) with two tetrahedral sites (Li1 and Li2) and Li3 in octahedral/pseudo-square-pyramidal coordination geometry. (b) Local lithium coordination geometries in Li_5AlS_4 with two tetrahedral lithium sites (Li1 and Li2) two lithium sites in the octahedral layer (Li3 and Li4). (c) Local lithium coordination geometries in Li_4GeS_4 with an undistorted octahedral site (Li1) and two tetrahedral lithium sites (Li2 and Li3). From Chem. Mater. ***2018,*** *30, 7183-7200. Reprinted with permission from ACS Publications.*

$Li_{4.4}Al_{0.4}Ge_{0.6}S_4$ has a reduced metal: sulphur ratio of 5.4:4 compared to Li_2FeS_2 ($Li_4Fe_2S_4$) or Li_5AlS_4 (6:4). The reduced metal content of 0.6 cations per formula unit is accommodated by the vacancies in the octahedral layer: the ordered octahedral vacancy (0.5 vacancy per formula unit) and the disordered vacancy in the occupied octahedra (in total 0.1 vacancy per formula unit) needed to preserve charge neutrality. The refined Li occupancies are stated in Table 6.

Table 6: Refined occupancies of the three different lithium sites in $Li_{4.4}Al_{0.4}Ge_{0.6}S_4$ at 10 K and ambient temperature. From Chem. Mater. ***2018,*** *30, 7183-7200. Reprinted with permission from ACS Publications.*

	T/ K	occ. Li1	occ. Li2	occ. Li3
$Li_{4.4}Al_{0.4}Ge_{0.6}S_4$	10	0.738(5)	0.254(4)	0.441(7)
$Li_{4.4}Al_{0.4}Ge_{0.6}S_4$	298	0.767(6)	0.221(5)	0.461(5)

It was noted that the PXRD pattern of $Li_{4.4}Al_{0.4}Ge_{0.6}S_4$ resembles strikingly the PXRD patterns given for $Li_{4.25}Ga_{0.25}Ge_{0.75}S_4$ in the report by Kanno *et al.* in 2000,[10] however, no crystallographic structure solution was given in this report. This indicated that $Li_{4.4}Al_{0.4}Ge_{0.6}S_4$ might not be an isolated stable phase but could be part of a larger structural family. Thus, systematic synthesis along $Li_{4.4}Al_{0.4}Ge_{0.6-x}Sn_xS_4$ was undertaken to find new materials crystallising with the same structure type. According to CAS Registry, ICSD and Pearson structural databases, no materials in the Li-Al-Sn-S phase field have been so far reported.

4.3.2.4 Solid solution $Li_{4.4}Al_{0.4}Ge_{0.6-x}Sn_xS_4$

A full solid solution exists between $Li_{4.4}Al_{0.4}Ge_{0.6}S_4$ and $Li_{4.4}Al_{0.4}Sn_{0.6}S_4$. Figure 51(a) shows the PXRD patterns along $Li_{4.4}Al_{0.4}Ge_{0.6-x}Sn_xS_4$ with x= 0.0, 0.2, 0.4 and 0.6. The lattice parameters were extracted using Pawley fits and are plotted in Figure 51(b). The lattice parameters increase linearly, following Vegard's law, as Ge^{4+} is exchanged for the larger Sn^{4+} ion (0.39 Å *vs* 0.55 Å). The SXRD patterns do not indicate the formation of major impurity phases or any structural transitions. The optimised synthetic conditions explored for the synthesis of $Li_{4.4}Al_{0.4}Ge_{0.6}S_4$ were used to obtain relatively pure $Li_{4.4}Al_{0.4}Sn_{0.6}S_4$ from the nominal starting mixture of $Li_{4.18}Al_{0.4}Sn_{0.6}S_{3.89}$. ICP-OES analysis of the endmember gave a metal composition of $Li_{4.40(4)}Al_{0.43(1)}Sn_{0.60(2)}S_x$ and will be referred to as $Li_{4.4}Al_{0.4}Sn_{0.6}S_4$. The sulphur content could not be reliably determined, as the compound had to be dissolved in aqua regia, leading to the formation of H_2S and consequent loss of sulphur.

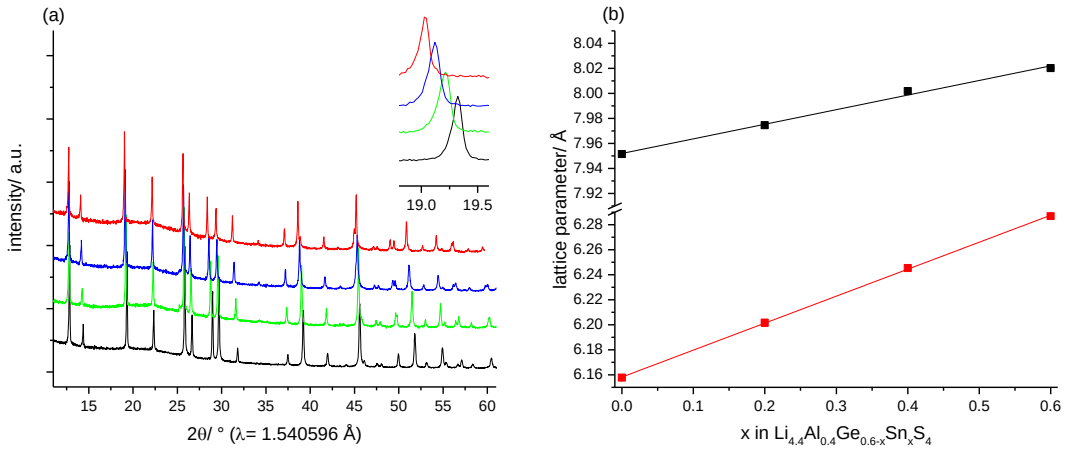

Figure 51: (a) PXRD patterns of the solid solution $Li_{4.4}Al_{0.4}Ge_{0.6-x}Sn_xS_4$ (black: x= 0, green: x= 0.2, blue: x= 0.4, red: x= 0.6); inset: Close up view of the 110 reflection which continually shifts towards larger d-spacing with increasing x. (b) Lattice parameters a (black) and c (red) in the solid solution $Li_{4.4}Al_{0.4}Ge_{0.6-x}Sn_xS_4$. From Chem. Mater. ***2018,*** *30, 7183-7200. Reprinted with permission from ACS Publications.*

In $Li_{4.4}Al_{0.4}Sn_{0.6}S_4$ small impurity phases could only be picked up on by SXRD ($LiAlS_2$) and additional impurity reflections could be detected in the NPD data. This impurity phase indexed to a face centred cubic cell (*a*= 3.95 Å) and could not be assigned to any known phases.

4.3.2.5 Crystal structure description of $Li_{4.4}Al_{0.4}Sn_{0.6}S_4$

Structural Rietveld refinement against low temperature NPD data of $^7Li_{4.4}Al_{0.4}Sn_{0.6}S_4$ showed that the material crystallises isostructural to $Li_{4.4}Al_{0.4}Ge_{0.6}S_4$ in the trigonal $P\bar{3}m1$ space group (*a*= 8.01711(6) Å, *c*= 6.26461(8) Å). The expansion of the S^{2-} sublattice, driven by the larger Sn^{4+} radius compared to Ge^{4+}, results in increased S1-S1 (3.767(1) Å) and S1-S2 ((3.808(3) Å) distances, compared to 3.6016(9) Å and 3.768(3) Å respectively. A significant change could be seen in the occupation of the Li1 and Li2 sites. A higher proportion of tetrahedral Li1 ions are displaced into the face sharing Li2 site in the tetrahedral layer, resulting in occupancies of 0.575(4) and 0.422(4) respectively (compared to 0.7385(5) and 0.254(4) in $Li_{4.4}Al_{0.4}Ge_{0.6}S_4$) (Table 7).

*Table 7: Refined occupancies of the three different lithium sites in $Li_{4.4}Al_{0.4}Sn_{0.6}S_4$ at 10 K and ambient temperature respectively. From Chem. Mater. **2018,** 30, 7183-7200. Reprinted with permission from ACS Publications.*

	T/ K	occ. Li1	occ. Li2	occ. Li3
$Li_{4.4}Al_{0.4}Sn_{0.6}S_4$	10	0.575(4)	0.422(4)	0.435(7)
$Li_{4.4}Al_{0.4}Sn_{0.6}S_4$	298	0.584(4)	0.427(3)	0.460(5)

But still a combined Li1+Li2 occupancy of one lithium atom is found. This couples with an increased displacement of Li3 off the centroid of octahedral interstice, as discussed previously. This increase in displacement is as follows: from 0.202(3) Å to 0.259(6) Å off the octahedral centre. The finalised low temperature crystallographic model is shown in Figure 52.

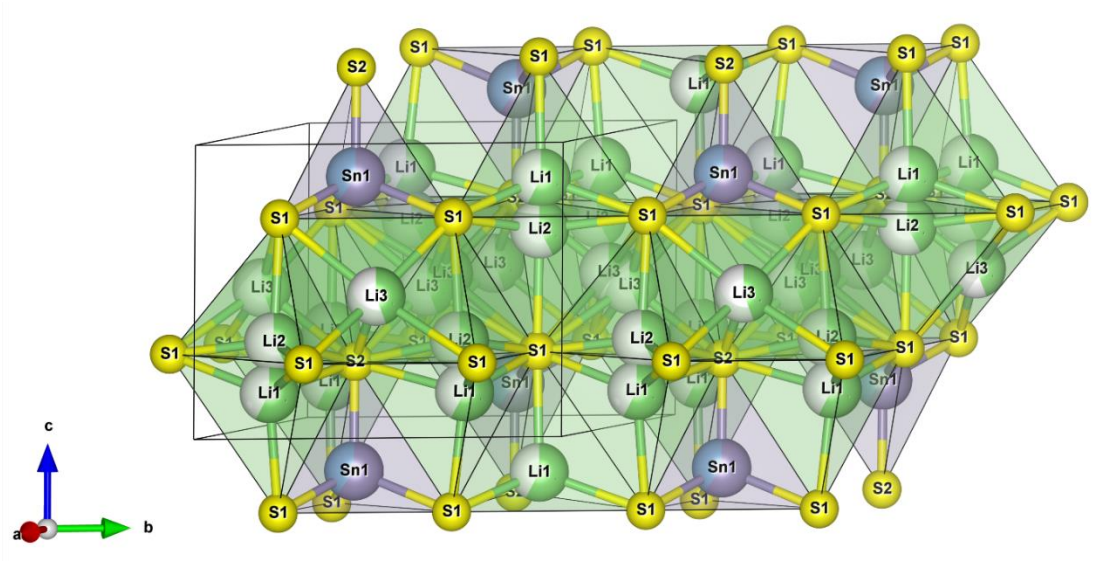

Figure 52: Crystal structure of $^{7}Li_{4.4}Al_{0.4}Sn_{0.6}S_4$ at 10 K. There are two sites in the tetrahedral layer, one occupied by Li1/vacancies and the other by Al/Sn. In the octahedral layer Li2 and Li3 can be found in tetrahedral and octahedral interstices respectively. Atoms and polyhedra are coloured as follows: yellow: sulphur, green: lithium, blue: aluminium and purple: tin. Partially occupied atoms are coloured to represent fractional occupancies. From Chem. Mater. ***2018,*** *30, 7183-7200. Reprinted with permission from ACS Publications.*

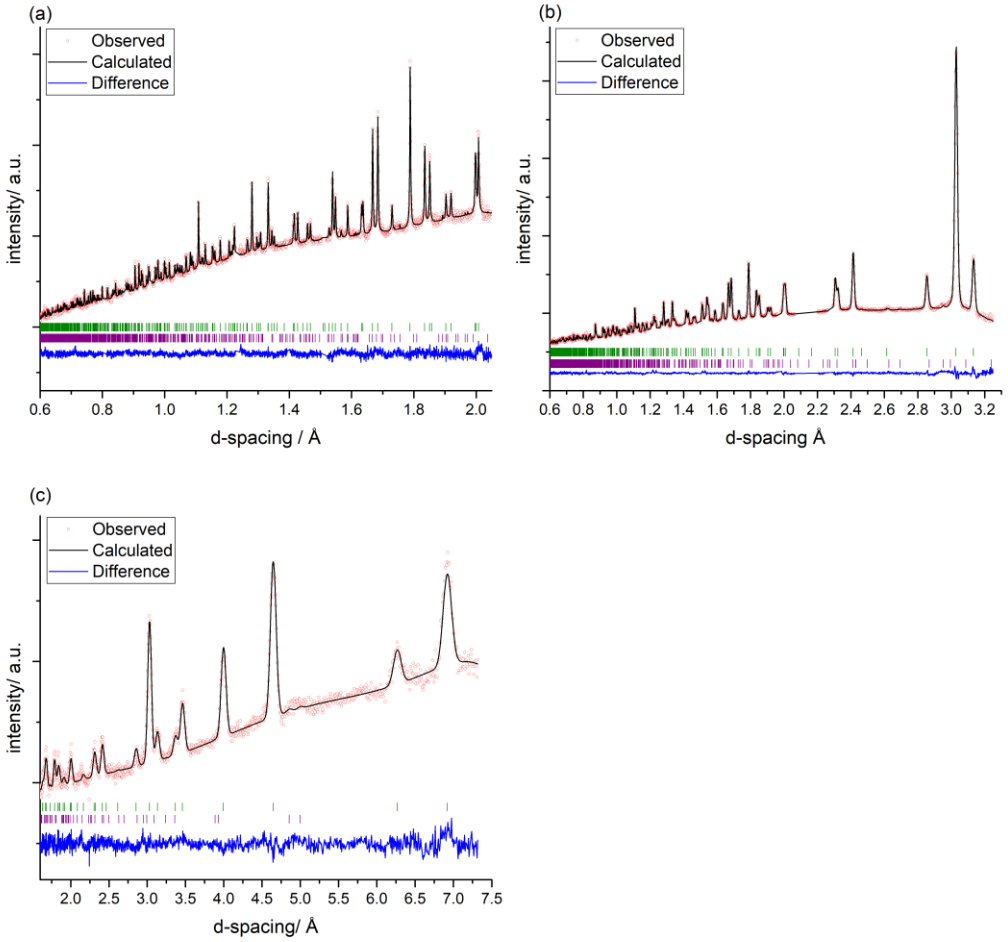

Figure 53: Low temperature Rietveld refinements of $^{7}Li_{4.4}Al_{0.4}Sn_{0.6}S_4$ (synthesised using purified reactants) against NPD data (ISIS neutron source, HRPD line, T= 10 K). The positions of calculated Bragg reflections are shown by tick marks (green: $^{7}Li_{4.4}Al_{0.4}Sn_{0.6}S_4$, purple: $LiAlS_2$). (a) bank 1, 2θ = 169 ° (b) bank 2, 2θ = 90 ° (c) bank3, 2θ = 30 °. From Chem. Mater. ***2018,*** *30, 7183-7200. Reprinted with permission from ACS Publications.*

The corresponding fits of the $^{7}Li_{4.4}Al_{0.4}Sn_{0.6}S_4$ model against low temperature NPD data are shown in Figure 53. As in the case of $^{7}Li_{4.4}Al_{0.4}Ge_{0.6}S_4$ no major changes or rearrangement occur after increasing the temperature to ambient conditions. Figure 54 depicts the finalised Rietveld refinement of SXRD and NPD data at ambient temperature. The refined parameters for low temperature and ambient temperature refinements can be found in Table 19 and Table 20 of the appendix respectively.

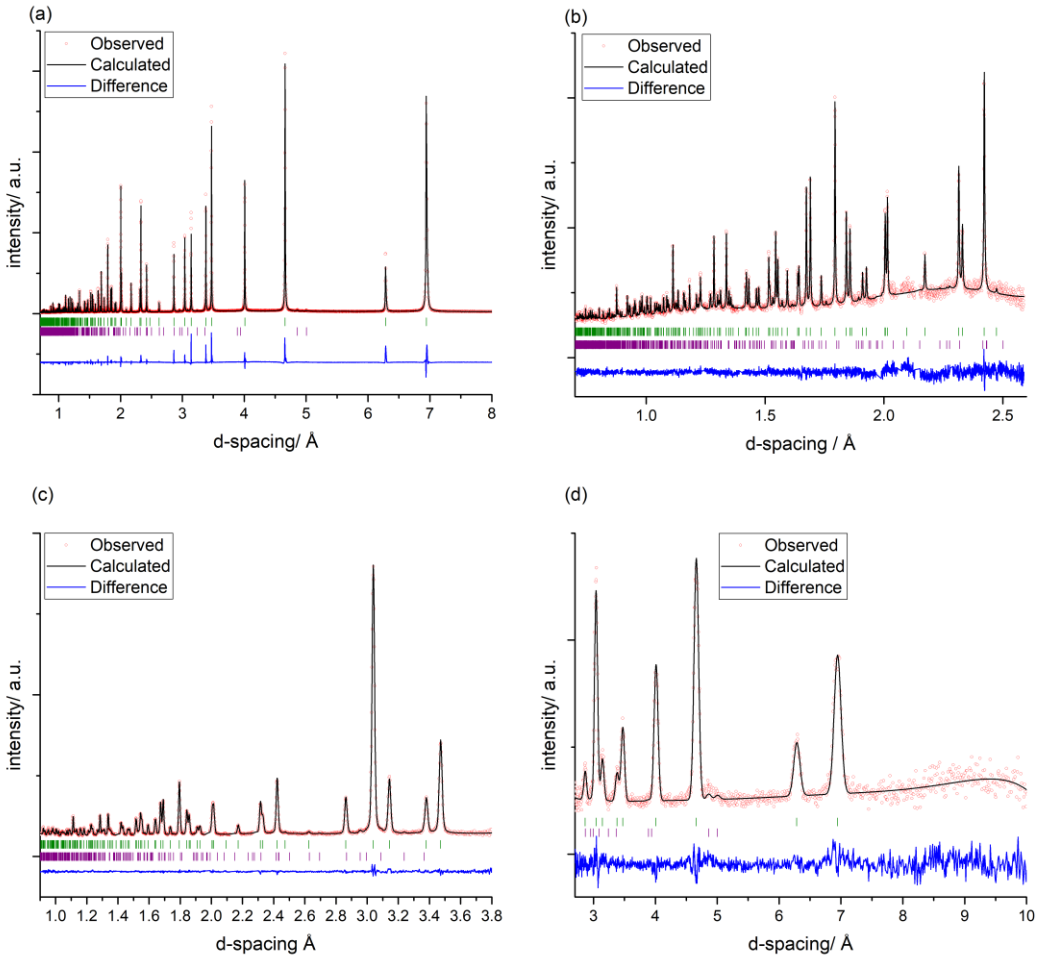

Figure 54: Ambient temperature Rietveld refinements of $^{7}Li_{4.4}Al_{0.4}Sn_{0.6}S_4$ (synthesised using purified reactants) against SXRD data (I11 beamline, MAC-detector, λ= 0.824878 Å) and NPD data (ISIS neutron source, HRPD beam line). The positions of calculated Bragg reflections are shown by tick marks (green: $^{7}Li_{4.4}Al_{0.4}Sn_{0.6}S_4$, purple: $LiAlS_2$). (a) SXRD pattern, (b) NPD pattern, bank 1, 2θ= 169 °, (c) NPD pattern, bank 2, 2θ= 90 ° (d) NPD pattern, bank 3, 2θ= 30 °. From Chem. Mater. ***2018,*** *30, 7183-7200. Reprinted with permission from ACS Publications.*

4.3.2.6 Li^+ mobility in $Li_{4.4}Al_{0.4}Ge_{0.6}S_4$ and $Li_{4.4}Al_{0.4}Sn_{0.6}S_4$

Long range lithium conductivity in solid electrolytes can be assessed by AC-impedance spectroscopy. The resistance can be measured in a single measurement, while temperature dependent experiments can give insight to the activation energy E_a of the diffusion process. Experiments were run on sintered pellets with crystallographic densities ρ of 75 % < ρ < 85 %. Typical Nyquist plots (complex plane plots) for $Li_{4.4}Al_{0.4}Ge_{0.6}S_4$ and $Li_{4.4}Al_{0.4}Sn_{0.6}S_4$ at ambient temperature are shown in Figure 55. They comprise a single semicircle at high frequencies and a spike at lower frequencies.

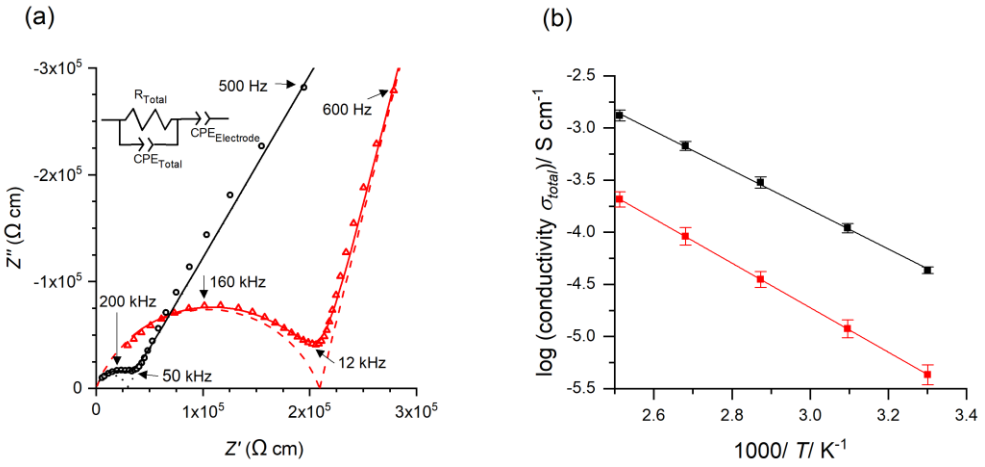

Figure 55: (a) Complex plane impedance plots for $Li_{4.4}Al_{0.4}Ge_{0.6}S_4$ (black circles) and $Li_{4.4}Al_{0.4}Sn_{0.6}S_4$ (red triangles) at 303 K along with equivalent circuit model (inset); the dashed lines give the contribution of the individual components of the equivalent circuit while the solid line depicts the calculated values for the complete equivalent circuit (b) Arrhenius plots of $Li_{4.4}Al_{0.4}Ge_{0.6}S_4$ (black) and $Li_{4.4}Al_{0.4}Sn_{0.6}S_4$ (red). From Chem. Mater. ***2018,*** *30, 7183-7200. Reprinted with permission from ACS Publications.*

The spike was associated with the Li^+ blocking SE|electrode interface, which can be modelled by a constant phase element ($CPE_{Electrode}$) in the equivalent circuit. Constant phase elements are commonly used to describe nonidealities of samples compared to the ideal equivalent element.[29] The capacitance of the semicircle in $Li_{4.4}Al_{0.4}Ge_{0.6}S_4$ was calculated by fitting the data with the equivalent circuit model shown in Figure 55, consisting of a resistor (R_{total}) in parallel with a CPE (CPE_{total}). A capacitance of 8.68×10^{-10} F cm^{-1} was obtained, which corresponds to a relative permittivity ε_R= 9803. This value is too large to be associated with bulk response alone. Therefore, the modulus plots, depicted for $Li_{4.4}Al_{0.4}Ge_{0.6}S_4$ in Figure 56, were consulted.

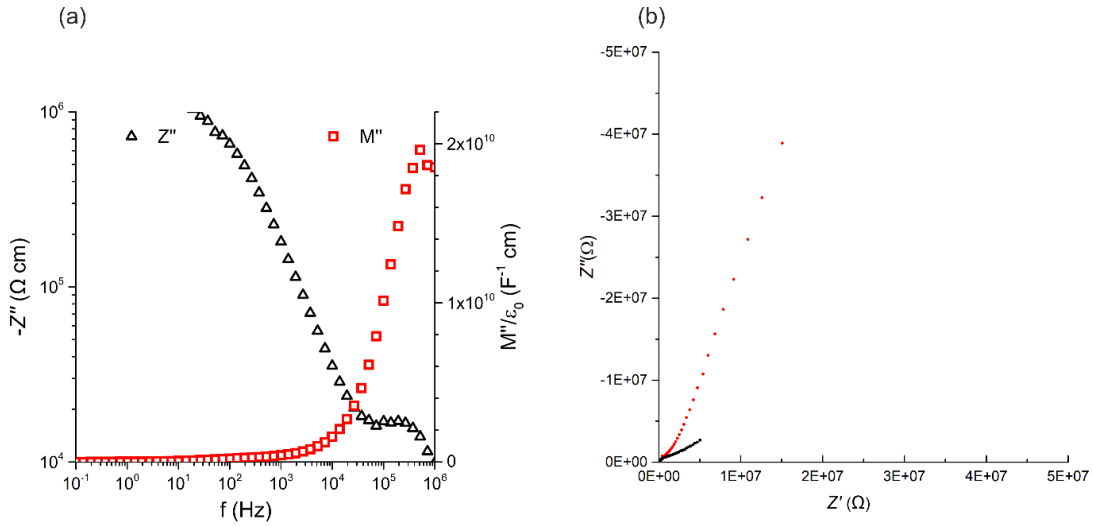

Figure 56: (a) Modulus plot of AC-impedance experiment on $Li_{4.4}Al_{0.4}Ge_{0.6}S_4$. (b) Full AC-impedance plot of $Li_{4.4}Al_{0.4}Ge_{0.6}S_4$ (black) and $Li_{4.4}Al_{0.4}Sn_{0.6}S_4$ (red) measured from 1MHz to 100 mHz at 303 K. From Chem. Mater. ***2018,*** *30, 7183-7200. Reprinted with permission from ACS Publications.*

Modulus plots can be used to distinguish between electrochemical contributions, which might not be resolved in the complex plane plot. Complex plane plots are dominated by the most resistive element and thus can be hiding processes with small resistances. In contrast, the imaginary component of the electric modulus *M''* plot is dominated by the element with the smallest capacitance value. The capacitance of a common bulk process is in the order of 10^{-12} F cm^{-1} while grain boundary processes are in the order of 10^{-11}-10^{-8} F cm^{-1}.[30] Therefore bulk processes can be identified more easily in Modulus plots, compared to complex plane plots. In the Modulus plot of Figure 56(a) no further peak that might correspond to bulk processes can be detected. Therefore the semicircle in the complex plane plot is interpreted as a combined bulk and grain boundary response and total conductivities σ_{tot} will be reported, as is common for this type of material.[9, 14]

Figure 55(b) confirms that the diffusion process follows the Arrhenius law over the measured temperature range. By plotting log(conductivity) against 1000/*T* a linear regression can be fitted, which was used to calculated activation energies of the diffusion processes. Conductivities σ_{tot} and activation energy E_a values for $Li_{4.4}Al_{0.4}Ge_{0.6}S_4$ and $Li_{4.4}Al_{0.4}Sn_{0.6}S_4$ are: σ_{tot}= 4.3(3) x 10^{-5} S cm^{-1}, E_a= 0.38(1) eV and σ_{tot}= 4.3(9) x 10^{-6} S cm^{-1}, E_a= 0.42(1) eV respectively.

4.3.2.7 Electrochemical stability of $Li_{4.4}Al_{0.4}Ge_{0.6}S_4$ and $Li_{4.4}Al_{0.4}Sn_{0.6}S_4$ against Li metal

One of the crucial disadvantages of current sulphide based solid electrolytes are their instable behaviour against Li metal electrodes. A symmetric Li|SE|Li can be used to assess the stability of a solid electrolyte by galvanostatically plating and stripping lithium. The change of overpotential required to achieve a current density, can be interpreted as a proxy for reaction and degradation of the Li|SE interface. An increasing overpotential indicates instability at the interfaces, while stable materials do not show a change of the overpotential. The stabilities of $Li_{4.4}Al_{0.4}Ge_{0.6}S_4$, $Li_{4.4}Al_{0.4}Sn_{0.6}S_4$ and LGPS (for comparison) were studied in such galvanostatic plating and stripping experiments. Due to the relatively low conductivities of the new materials, low current densities of ±0.01mA cm^{-2} were applied, while the temperature was increased to 323 K to increase lithium mobility. Figure 57 (a) shows an overview of all three materials.

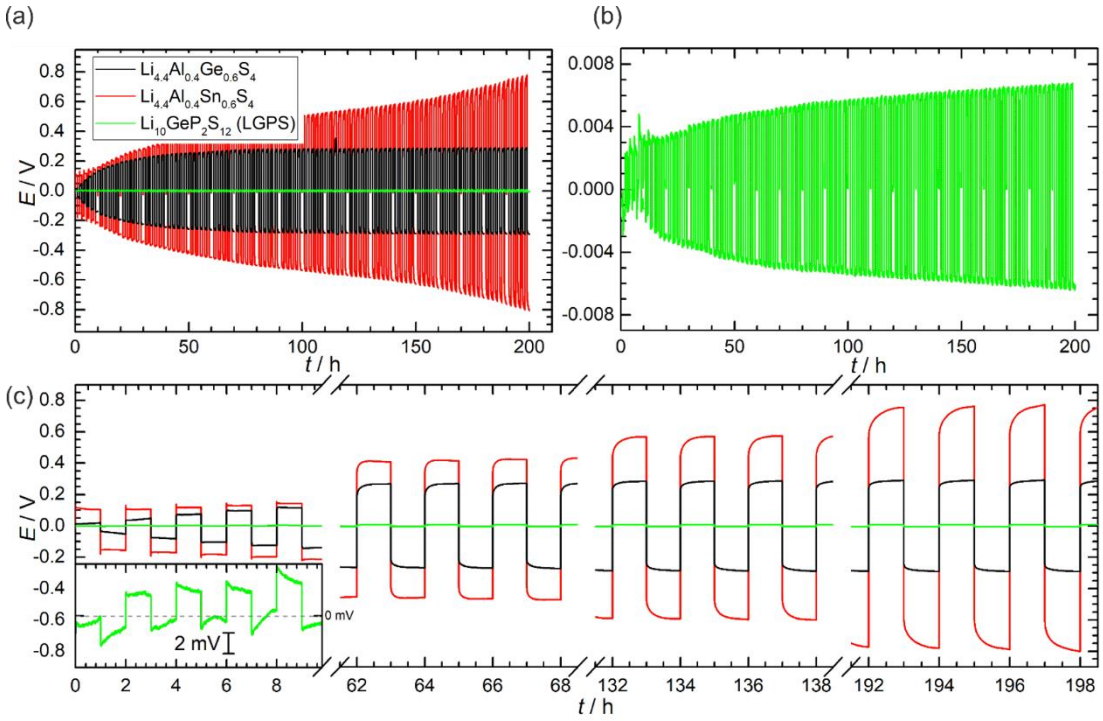

Figure 57: Galvanostatic plating and stripping experiments in symmetric Li|SE|Li cells obtained at 323 K at ±0.01 mA cm^{-2} for 1 h (0.01 mAh cm^{-2}) per half-cycle. (a) overview for $Li_{4.4}Al_{0.4}Ge_{0.6}S_4$ (black), $Li_{4.4}Al_{0.4}Sn_{0.6}S_4$ (red) and LGPS (green), (b) detailed view of the voltage profile of LGPS (c) enlarged voltage profiles for selected time intervals. From Chem. Mater. ***2018,*** *30, 7183-7200. Reprinted with permission from ACS Publications.*

$Li_{4.4}Al_{0.4}Ge_{0.6}S_4$ and $Li_{4.4}Al_{0.4}Sn_{0.6}S_4$ show large plating/stripping plateaus (0.1 - 0.8 V) compared to LGPS (0.003 – 0.008 V), which can be linked to their low intrinsic Li^+ conductivity. However, the profile shapes and therefore the change in overpotential differ from one SE to the other. The cell polarization of $Li_{4.4}Al_{0.4}Sn_{0.6}S_4$ increases continuously during the experiment, while the cell polarization of $Li_{4.4}Al_{0.4}Ge_{0.6}S_4$ stabilises after ~100 h. LGPS degrades continuously (Figure 57(b). The relative change in overpotential during the last 50 h summarises this behaviour: $Li_{4.4}Al_{0.4}Sn_{0.6}S_4$: increase of 22 %; LGPS: increase of 10 %; $Li_{4.4}Al_{0.4}Ge_{0.6}S_4$: increase of 1 %.

SXRD patterns of the ground pellets were measured following the plating and stripping experiment (Figure 58). The bulk materials remained intact as shown by their diffraction patterns, indicating that degradation of the materials was restricted to the interfaces only. Although the ionic conductivity of both materials is too low for practical applications, they could in principle function as lithium solid state electrolytes in all-solid state devices due to the enhanced long-term stability of $Li_{4.4}Al_{0.4}Ge_{0.6}S_4$.The rate of degradation can be controlled through selection of metal cations. Conductors in the Li-Al-Ge-S phase field could exhibit improved stability over LGPS or further materials in the Li-Al-Sn-S phase field.

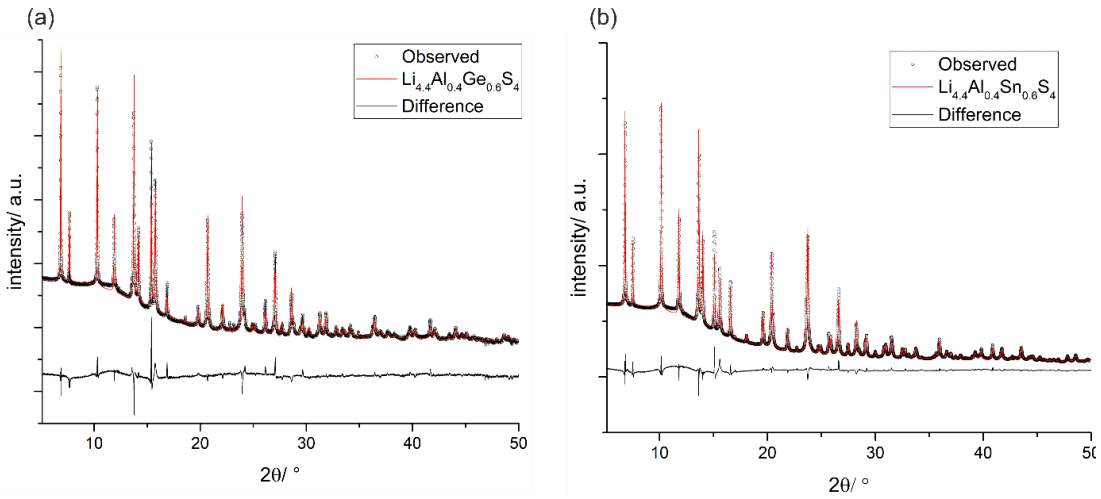

Figure 58: Rietveld refinements of solid electrolytes against SXRD data after cycling against lithium metal showing that the bulk structure of each compound has been retained after cycling. (a) $Li_{4.4}Al_{0.4}Ge_{0.6}S_4$ (a= 7.9494(4) Å, c= 6.1559(2) Å; (b) $Li_{4.4}Al_{0.4}Sn_{0.6}S_4$ (a= 8.0233(4) Å, c= 6.281(2) Å. (I11 beamline, PSD-detector, λ= 0.825015 Å, room temperature). From Chem. Mater. ***2018,*** *30, 7183-7200. Reprinted with permission from ACS Publications.*

Electrochemical experiments, such as the above-described plating and stripping experiment, rely on the use of proxy parameters (currents, voltages) to follow processes. As such, this data requires careful interpretation, as no direct method of characterization is applied (*e.g.* PXRD, NMR) and can therefore be prone to misinterpretation of processes.

To confirm that the charge carrying species in the plating and stripping experiment was metallic Li^0, non-symmetrical Li|SE|Cu cells were assembled for both $Li_{4.4}Al_{0.4}Ge_{0.6}S_4$ and $Li_{4.4}Al_{0.4}Sn_{0.6}S_4$. A single plating cycle was run to deposit Li^0 on the Cu substrate. This led to rapid polarization and cell failure in the case of the less conducting $Li_{4.4}Al_{0.4}Sn_{0.6}S_4$ material, while $Li_{4.4}Al_{0.4}Ge_{0.6}S_4$ showed a consistent polarization of -0.4 to -0.6 V vs Li^+/Li. After the experiment the cell containing $Li_{4.4}Al_{0.4}Ge_{0.6}S_4$ was dissembled and visual inspection confirmed that Li metal had been plated onto the Cu surface, see Figure 59.

Figure 59: Cu-electrode of Li|SE|Cu cell after plating experiment, showing evidence for lithium metal plating. From Chem. Mater. ***2018,*** *30, 7183-7200. Reprinted with permission from ACS Publications.*

4.3.2.8 NMR

All NMR experiments and figure preparation have been conducted by Kenneth K. Inglis in the Dr F. Blanc research group at the University of Liverpool. Experimental details and data analysis are published in *Leube* et al.[19] Variable temperature ^{7}Li NMR spectra (Figure 60) are used to confirm the results of the AC-impedance experiments, showing that $Li_{4.4}Al_{0.4}Ge_{0.6}S_4$ exhibits higher lithium mobility than $Li_{4.4}Al_{0.4}Sn_{0.6}S_4$. The ^{7}Li NMR spectra were measured as a function of temperature (Figure 60(a) and (b) for $Li_{4.4}Al_{0.4}Ge_{0.6}S_4$ and $Li_{4.4}Al_{0.4}Sn_{0.6}S_4$ respectively). At low temperature broad ^{7}Li spectra are measured. In the absence of lithium mobility the 1/2 <-> 1/2 transition is broadened by ^{7}Li-^{7}Li homonuclear dipolar interactions.

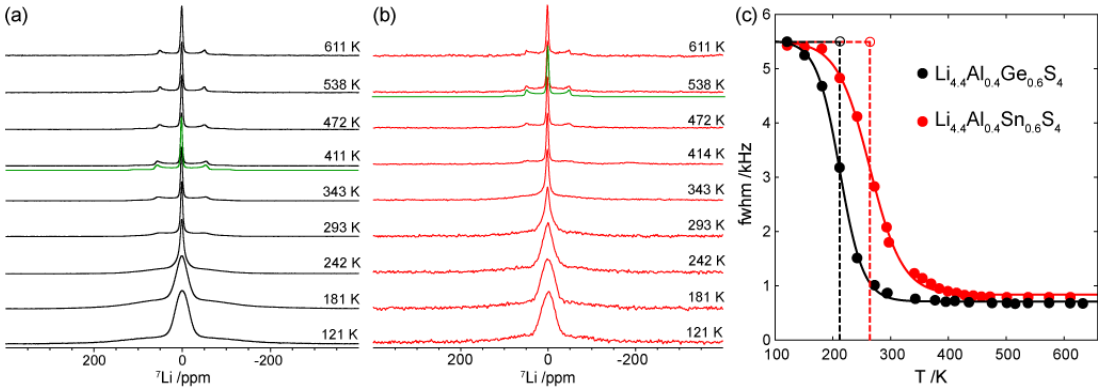

Figure 60: ^{7}Li NMR spectra as a function of temperature for (a) $Li_{4.4}Al_{0.4}Ge_{0.6}S_4$ and (b) $Li_{4.4}Al_{0.4}Sn_{0.6}S_4$. (c) Temperature dependence of ^{7}NMR line width of $Li_{4.4}Al_{0.4}Ge_{0.6}S_4$ (black) and $Li_{4.4}Al_{0.4}Sn_{0.6}S_4$ (red) fitted with sigmoidal regression curve (solid lines). The vertical and horizontal dashed lines give the temperatures corresponding to the inflection point of the regression curve and the NMR line width used to determine the Li^+ jump rates τ^{-1}, respectively. All NMR experiments and figure preparation have been conducted by Kenneth K. Inglis in the Dr F. Blanc research group at the University of Liverpool. From Chem. Mater. ***2018,*** *30, 7183-7200. Reprinted with permission from ACS Publications.*

Line narrowing is observed upon heating, as dipolar interactions average to zero due to increasing Li^+ mobility. At high temperatures a narrow peak and two broad shoulders are observed arising from the 3/2 <-> 3/2 satellite transitions. This line narrowing can be quantified by plotting the full width at half maximum of the central peak against the temperature *T* (Figure 60(c)). The point of inflection indicates the onset of lithium mobility in the material. As such, ^{7}Li NMR can be used to probe the local kinetics associated with Li^+ ion mobility. Line narrowing, due to the onset of lithium mobility, occurs at lower temperatures in $Li_{4.4}Al_{0.4}Ge_{0.6}S_4$ compared to $Li_{4.4}Al_{0.4}Sn_{0.6}S_4$ indicating slower Li^+ dynamics in the latter material. These results correlate well with the relative lithium mobility obtained by AC-impedance spectroscopy.

4.3.2.9 Ab initio molecular dynamic simulations

Ab initio molecular dynamic simulations and figure preparation were performed on a supercell of $Li_{4.4}Al_{0.4}Ge_{0.6}S_4$ by Dr Paul Sharp. Experimental details and data analysis are published in *Leube* et al.[19] The Li^+ trajectories were calculated for 88 ps and the information was used to elucidate the long range diffusion mechanism as shown in Figure 61. Lithium transport is based on the interplay of disordered Li vacancies on the Li3 site with the displaced tetrahedral lithium ions in the Li2 site: A Li2 ion can hop into a disordered Li3 vacancy, moving the vacancy into the tetrahedral layer. This vacancy is then occupied by a Li ion from an occupied Li3 site moving the vacancy back into the tetrahedral layer. Crucially this confines the lithium diffusion to the a-b plane rendering two-dimensional conduction in the octahedral layer. No hopping events involving the ordered vacancy in the octahedral layer or across the tetrahedral layer were observed.

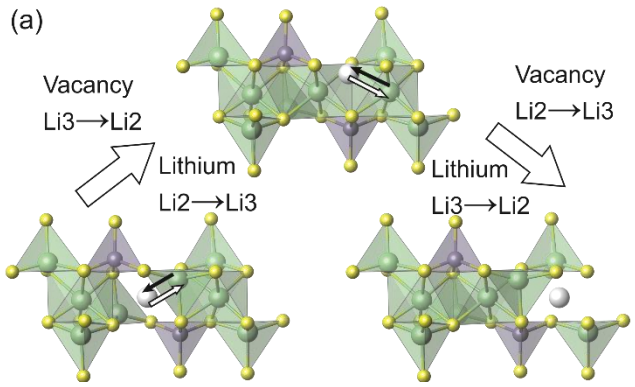

Figure 61: Schematic representation of long-range Li^+ ion transport between Li2 sites via the disordered vacancy in a Li3 site. The Li^+ ion in a Li2 site hops into the Li3 vacancy, and the now vacant Li2 site is filled by a Li^+ ion from a Li3 site. Ab initio *molecular dynamic simulations were performed on a supercell of $Li_{4.4}Al_{0.4}Ge_{0.6}S_4$ by Dr Paul Sharp. From Chem. Mater.* ***2018,*** *30, 7183-7200. Reprinted with permission from ACS Publications.*

4.3.3 $Li_{4.4}Ga_{0.4}M_{0.6}S_4$ (*M*= Ge, Sn)

Kanno's *et al.* paper on $Li_{4.25}Ga_{0.25}Ge_{0.75}S_4$ highlighted the potential of exchanging Al^{3+} for Ga^{3+} in $Li_{4.4}Al_{0.4}M'_{0.6}S_4$ (*M'*= Ge^{4+}, Sn^{4+}) and was attempted in this work.[10] This cation substitution yielded two new materials: $Li_{4.4}Ga_{0.4}Ge_{0.6}S_4$ and $Li_{4.4}Ga_{0.4}Sn_{0.6}S_4$. Pawley fits of the SXRD patterns showed that both materials could be indexed to the trigonal $P\bar{3}m1$ space group (Figure 62(a), Figure 63(a)) with $LiGaS_2$ as a minor impurity phase in $Li_{4.4}Ga_{0.4}Sn_{0.6}S_4$.

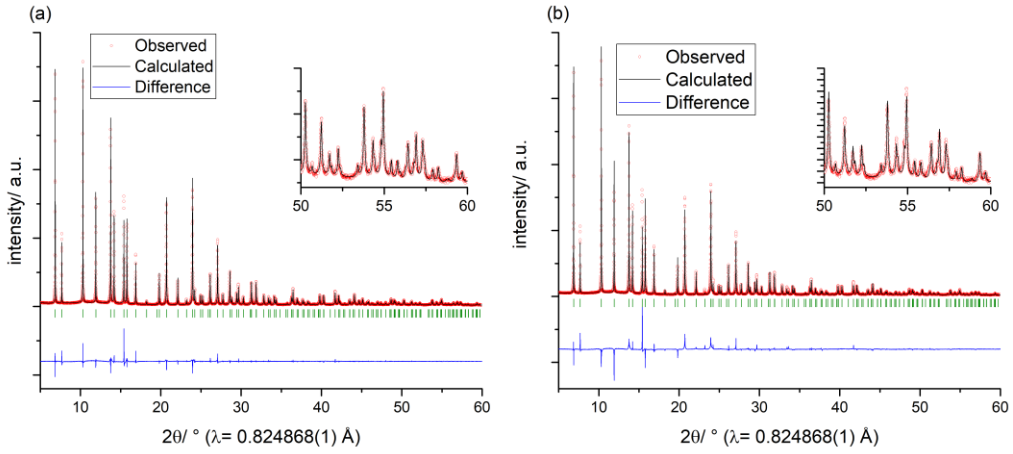

Figure 62: Refinement of $Li_{4.4}Ga_{0.4}Ge_{0.6}S_4$ (synthesised using purified reactants) against SXRD data (I11 beamline, MAC-detector, λ= 0.824868(1) Å, room temperature). The positions of calculated Bragg reflections are shown by green tick marks. (a) Pawley fit: R_{wp}=6.37, χ^2= 20.62. (b) Rietveld fit: R_{wp}= 9.62, χ^2= 45.75.

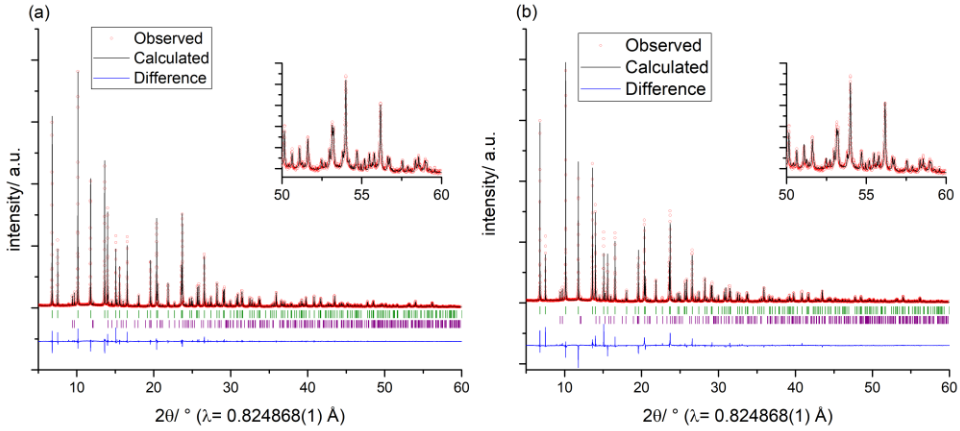

Figure 63: Refinement of $Li_{4.4}Ga_{0.4}Sn_{0.6}S_4$ (synthesised using purified reactants) against SXRD data (I11 beamline, MAC-detector, λ= 0.824868(1) Å, room temperature). The positions of calculated Bragg reflections are shown by tick marks (green: $Li_{4.4}Ga_{0.4}Sn_{0.6}S_4$, purple: $LiGaS_2$). (a) Pawley fit: R_{wp}: 6.29, χ^2= 16.56 (b): Rietveld fit: R_{wp}= 8.55, χ^2= 28.59.

Synthesis of the Si^{4+} analogue did not result in the formation of the desired phase. The diffraction pattern of $Li_{4.4}Ga_{0.4}Si_{0.6}S_4$ could be indexed to $P2_1/m$, which corresponds to the unit cell of Li_4SiS_4 and was therefore not investigated any further.

Structural Rietveld refinements were carried out on $Li_{4.4}Ga_{0.4}Ge_{0.6}S_4$ and $Li_{4.4}Ga_{0.4}Sn_{0.6}S_4$ based on SXRD data only. Li was excluded from the refinement with the model including the framework sulphur and non-lithium cations. The lattice parameters of the unit cell, zero error shift, the positions of the heavy atoms and their isotropic displacement parameters were refined. The resultant structural parameters for $Li_{4.4}Ga_{0.4}Ge_{0.6}S_4$ and $Li_{4.4}Ga_{0.4}Sn_{0.6}S_4$ are stated in Table 21 and Table 22 and the fits are visualised in Figure 62(b) and Figure 63(b) respectively. χ^2 values for the Rietveld refinements of 45.75 and 28.59 respectively (compared to Pawley χ^2 values of 20.62 and 16.56) are satisfactory considering the exclusion of Li from the model. No significant distortion or rearrangement of the framework structures compared against $Li_{4.4}Al_{0.4}M_{0.6}S_4$ could be identified via SXRD Rietveld refinement.

The lithium conductivities in the two Ga^{3+} analogues were measured by temperature dependent AC-impedance spectroscopy. As with the Al^{3+} analogues, the impedance spectra consist of a semicircle associated with the total conductivity σ_{tot} and a spike at low frequencies corresponding to the lithium blocking electrode response. Total conductivities of σ_{tot} of 1.6(3) x 10^{-5} S cm^{-1} and 3(2) x 10^{-6} S cm^{-1} and activation energies E_a of 0.40(1) eV and 0.43(1) eV were found for $Li_{4.4}Ga_{0.4}Ge_{0.6}S_4$ and $Li_{4.4}Ga_{0.4}Sn_{0.6}S_4$ respectively.

4.3.4 $Li_{4.4}In_{0.4}M_{0.6}S_4$ (*M*= Si, Ge, Sn)

4.3.4.1 Synthesis

The logical next step was to synthesise the In^{3+} analogues of the $Li_{4.4}M_{0.4}M'_{0.6}S_4$ phase. It is known that conductivities are reliant on the fine-tuned interplay of structural features, such as unit cell volume, atomic polarizabilities, ratio of cationic radii or the extent of disorder.[29] [31] The aim of this section was to study the effect of chemical substitution on structure and electrochemical properties by changing the ionic radius of the trivalent *M* metal from 0.39 Å and 0.47 Å (Al^{3+}, Ga^{3+} respectively) to 0.62 Å (In^{3+}). Although indium is too scarce to be a commercial candidate, the substitution would reveal new aspects of the structure-property-composition relationships in these systems.

All compositions in the $Li_{4.4}In_{0.4}M'_{0.6}S_4$ (*M'*= Si^{4+}, Ge^{4+}, Sn^{4+}) series crystallise in the trigonal $P\bar{3}m1$ space group. Pawley fits against SXRD data are depicted in Figure 64 and Table 8 shows the corresponding lattice parameters. The unit cell expands significantly with incorporation of larger tetravalent cations, as expected. Only small impurity phases are detected in individual phases, *i.e.* Li_2S, $LiInS_2$ and Li_4SnS_4.

Table 8: Lattice parameters of $Li_{4.4}In_{0.4}M_{0.6}S_4$ (M= Si^{4+}, Ge^{4+}, Sn^{4+}), space group: $P\bar{3}m1$

	a/ Å	c/ Å	V/ Å^3	Impurity phases
$Li_{4.4}In_{0.4}Si_{0.6}S_4$	7.98361(4)	6.17331(4)	340.54(2)	Li_2S, $LiInS_2$
$Li_{4.4}In_{0.4}Ge_{0.6}S_4$	8.0198(7)	6.2159(3)	346.237(5)	Li_2S
$Li_{4.4}In_{0.4}Sn_{0.6}S_4$	8.09349(3)	6.34401(3)	359.827(2)	Li_2S, Li_4SnS_4

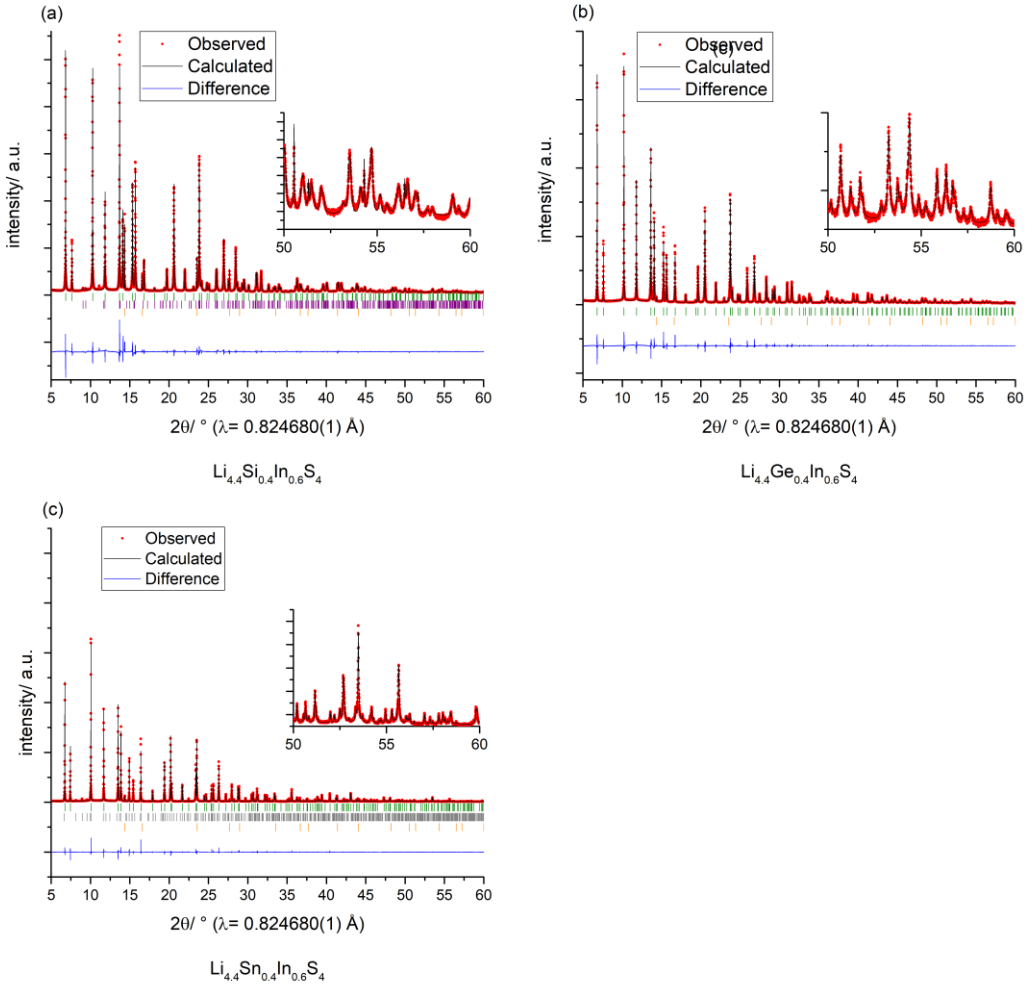

Figure 64: Pawley fits of $Li_{4.4}In_{0.4}M_{0.6}S_4$ (M= Si^{4+}, Ge^{4+}, Sn^{4+}) against SXRD data. The positions of calculated Bragg reflections are shown by tick marks (green: $Li_{4.4}In_{0.4}M_{0.6}S_4$; purple: $LiInS_2$; orange: Li_2S; grey: Li_4SnS_4). (a) $Li_{4.4}In_{0.4}Si_{0.6}S_4$; (b) $Li_{4.4}In_{0.4}Ge_{0.6}S_4$; (c) $Li_{4.4}In_{0.4}Sn_{0.6}S_4$.

The Si^{4+} analogues of the $Li_{4.4}M_{0.4}M'_{0.6}S_4$ phase are not accessible in $Li_{4.4}M_{0.4}Si_{0.6}S_4$ (M= Al^{3+}, Ga^{3+}), as instead materials along the solid solutions Li_4SiS_4-Li_5MS_4 are formed. Interestingly $Li_{4.4}In_{0.4}Si_{0.6}S_4$ does crystallise in a trigonal structure which is related to the new $Li_{4.4}M_{0.4}M'_{0.6}S_4$ phase. The introduction of In^{3+} as the trivalent metal changes structural chemistry considerably. The formation of the new trigonal phase might be driven by two parameters:

- variance of the ionic radius on the shared metal site ($\sigma^2 = \langle r^2 \rangle - \langle r \rangle^2$, with r as the ionic radius and the angular brackets as the average), as the phase formation might be driven by the difference in the cationic radii.
- average ionic radius on the shared heavy metal site ($r_{av} = 0.4 \times r(M) + 0.6 \times r(M')$)

Table 9 gives an overview of the phases formation of materials with the $Li_{4.4}M_{0.4}M'_{0.6}S_4$ composition and compares it to the variance σ^2 and the average ionic radius r_{av} on the shared heavy metal site.

Table 9: Overview of phases formation in the $Li_{4.4}M_{0.4}M'_{0.6}S_4$ phase field compared to variance in ionic radii σ^2 ($\sigma^2 = \langle r^2 \rangle - \langle r \rangle^2$) and the average ionic radius r_{av} ($r_{av} = 0.4 \times r(M) + 0.6 \times r(M')$) and on the shared heavy metal site.

Material	Phase formed	σ^2/ Å^2	r_{av}/ Å
Li-Al-Si-S	Li_4SiS_4 related	0.0054	1.16
Li-Al-Ge-S	New trigonal phase	0	1.25
Li-Al-Sn-S	New trigonal phase	0.0096	1.37
Li-Ga-Si-S	Li_4SiS_4 related	0.0096	1.18
Li-Ga-Ge-S	New trigonal phase	0.0006	1.27
Li-Ga-Sn-S	New trigonal phase	0.0054	1.39
Li-In-Si-S	New trigonal phase	0.0486	1.28
Li-In-Ge-S	New trigonal phase	0.0216	1.37
Li-In-Sn-S	New trigonal phase	0.0024	1.49

No clear correlation between the variance σ^2 and the phase formation can be identified. The cation size variance in the trigonal $Li_{4.4}Al_{0.4}Ge_{0.6}S_4$ phase is 0 while it reaches 0.0486 in the $Li_{4.4}In_{0.4}Si_{0.6}S_4$ phase. Compositions which crystallise in the monoclinic Li_4SiS_4 structure have variances of 0.0054 Å and 0.0096 Å. It is interesting to note that despite increasing differences between the metal radii, no ordering of those can be detected.

Contrary the average ionic radius on the metal site has a crucial impact on which phase forms: the two materials with the lowest average ionic radius $r_{av} < 1.18$ Å on the shared heavy metal site crystallise in phases related to monoclinic Li_4SiS_4 (Li-Al-Si-S, Li-Ga-Si-S). But all materials with an average ionic radius of $r_{av} > 1.25$ Å crystallise in the new trigonal phase. An increase on the shared metal site drives therefore the formation of the trigonal phase.

Temperature dependent AC-impedance data were collected for all three indium-based phases to probe the lithium conductivities of the materials. The main characteristics of the spectra are a semicircle at high frequencies and a spike at lower frequencies. As discussed

previously, the semicircle is associated with the total Li^+ conductivity while the spike can be related to the lithium blocking electrode (a detailed and fully fitted spectrum can be found in Figure 68(b)). The Arrhenius plots for the impedance data are shown in Figure 65 and allow for determination of the activation energies, which are in the range from 0.46(2) eV to 0.31(5) eV. The Arrhenius plots for $Li_{4.4}M_{0.4}M_{0.6}S_4$ (M= Al^{3+}, Ga^{3+} and M'= Ge^{4+}, Sn^{4+}) are included for comparison. Total conductivities at ambient temperature σ_{tot} of 1.6(2) x 10^{-5} S cm^{-1} and 2.6 x 10^{-6} S cm^{-1} were determined for $Li_{4.4}In_{0.4}Ge_{0.6}S_4$ and $Li_{4.4}In_{0.4}Si_{0.6}S_4$ respectively. These values compare well to $Li_{4.4}M_{0.4}M'_{0.6}S_4$ (M= Al^{3+}, Ga^{3+} and M'= Ge^{4+}, Sn^{4+}) which are be in the range 10^{-6}-10^{-5} S cm^{-1}. Surprisingly, the conductivity of $Li_{4.4}In_{0.4}Sn_{0.6}S_4$ is an order of magnitude higher (1.5(3) x 10^{-4} S cm^{-1}). In the indium-series the total conductivities σ_{total} rise with increasing ionic radius $r_{M'}$: $\sigma_{Si} < \sigma_{Ge} < \sigma_{Sn}$, but this trend does not hold considering the results from previously reported $Li_{4.4}M_{0.4}M'_{0.6}S_4$ (M= Al^{3+}, Ga^{3+} and M'= Ge^{4+}, Sn^{4+}) structures.

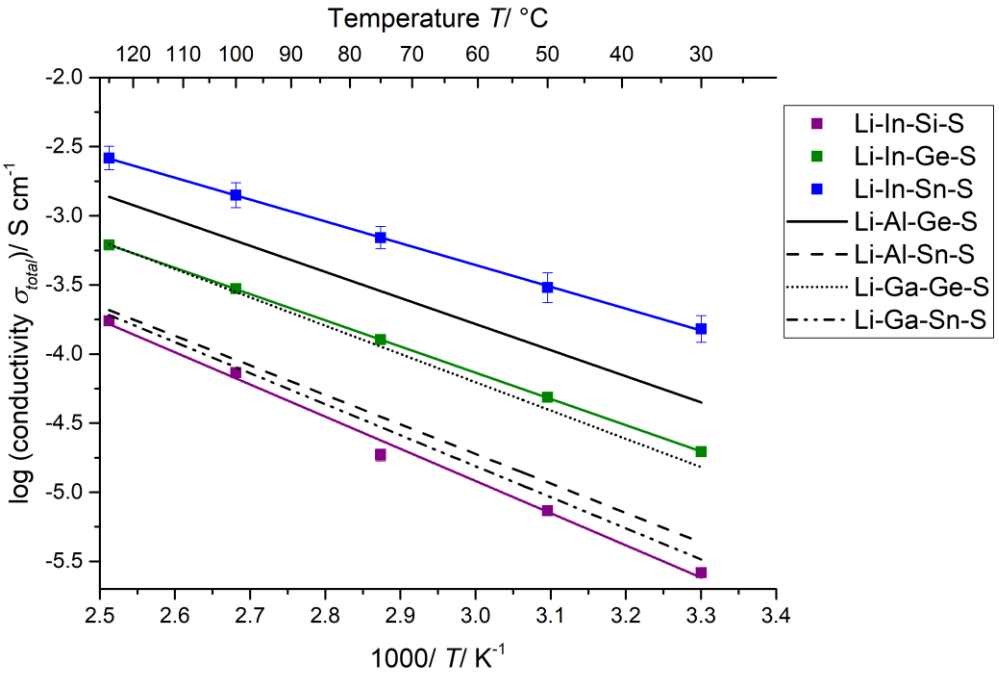

Figure 65: Arrhenius plots of temperature dependent AC-impedance experiments on the indium-series. (blue: $Li_{4.4}In_{0.4}Sn_{0.6}S_4$, green: $Li_{4.4}In_{0.4}Ge_{0.6}S_4$, purple: $Li_{4.4}In_{0.4}Si_{0.6}S_4$). $Li_{4.4}In_{0.4}Sn_{0.6}S_4$ shows the highest ionic conductivity of 1.5(3) x 10^{-4} S cm^{-1} at ambient temperature. Results for the $Li_{4.4}M_{0.4}M'_{0.6}S_4$ (M= Al^{3+}, Ga^{3+} and M'= Ge^{4+}, Sn^{4+}) are included for comparison.

The increased conductivity in $Li_{4.4}In_{0.4}Sn_{0.6}S_4$ cannot be attributed to electronic conductivity as a negligible electronic contribution could be confirmed in a DC polarization experiment, shown in Figure 66(a).

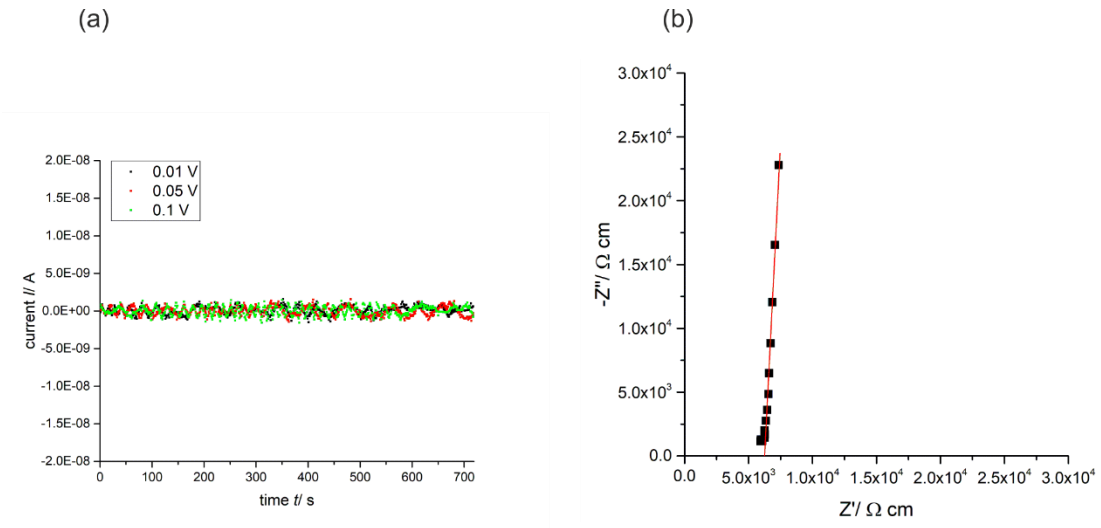

Figure 66: (a) DC polarization experiment on a silver painted pellet of $Li_{4.4}In_{0.4}Sn_{0.6}S_4$. No electronic contribution is detectable. (b) AC impedance spectrum measured to test the instrumental set-up. Red line: extrapolation of the intercept of the electrode spike with the x-axis.

A current *I* of 0 A is established almost instantly after application of the external voltage. This shows that the material is an electrical insulator. To confirm that a good contact between potentiostat and pellet had been established for the measurement an initial AC impedance measurement was conducted. Figure 66 (b) shows the AC impedance spectrum comprising only an electrode spike while the conductivity contributions cannot be resolved. This motif is commonly encountered for materials with relatively high ionic conductivity such as $Li_7Ge_3PS_{12}$.[32] Extrapolating the intercept of the electrode spike with the x-axis gives an ionic conductivity of 1.5 x 10^{-4} S cm^{-1} for $Li_{4.4}In_{0.4}Sn_{0.6}S_4$ (a more detailed and fully fitted spectrum can be found in Figure 68(b)).

4.3.4.2 Synthesis along $Li_{4+x}In_xSn_{1-x}S_4$

As $Li_{4.4}In_{0.4}Sn_{0.6}S_4$ has the highest Li^+ conductivity in $Li_{4.4}M_{0.4}M'_{0.6}S_4$ (*M*= Al^{3+}, Ga^{3+}, In^{3+} and *M'*= Si^{4+}, Ge^{4+}, Sn^{4+}), synthetic efforts were undertaken to further improve the conductivity. Previous reports of the $Li_{4+x}Ga_xGe_{1-x}S_4$ system ($0.25 < x < 0.5$) showed a strong correlation between x and the conductivity. The conductivity changes by almost two orders of magnitude from 4.5 x 10^{-7} S cm^{-1} (x= 0.5) to 6.2 x 10^{-5} S cm^{-1} (x= 0.25) as plotted in Figure 67.[10]

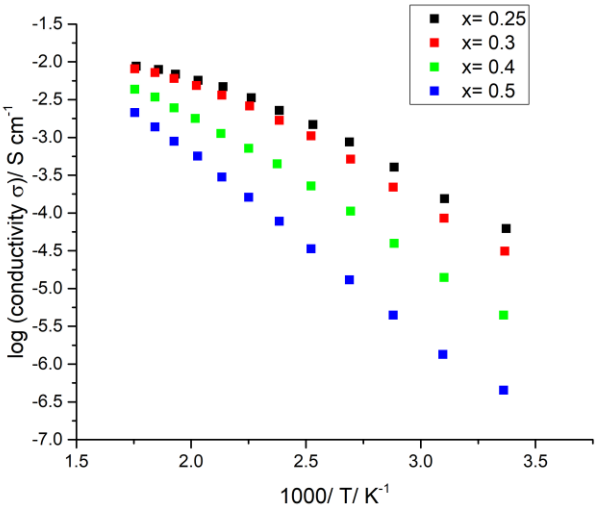

Figure 67: Arrhenius plots of the materials $Li_{4+x}Ga_xGe_{1-x}S_4$, showing the increase of the conductivity with decrease of x. The data was extracted from a graph in Solid State Ionics 2000, 130, 97-104.[10]

These findings can be explained by considering the previously discussed *ab initio* molecular dynamic simulations performed for $Li_{4.4}Al_{0.4}Ge_{0.6}S_4$. These found that a vacancy-controlled diffusion pathway is responsible for long range Li^+ diffusion the trigonal $Li_{4.4}M_{0.4}M'_{0.6}S_4$ phase. With decreasing x the vacancy concentration on the Li3 site is increased and correspondingly the Li^+ mobility is enhanced. Consequently, synthesis along $Li_{4+x}In_xSn_{1-x}S_4$ was carried out to determine the boundaries of phase formation in dependence of x.

Figure 68(a) shows the SXRD patterns along $Li_{4+x}In_xSn_{1-x}S_4$ ($0.3 < x < 0.6$). For $x= 0.3$ and $x= 0.35$ significant contributions of Li_4SnS_4 can be detected in the patterns. For $0.4 < x < 0.55$ formation of only the target phase is observed, while further increase of x entails the formation of $LiInS_2$ and increased formation of Li_2S.

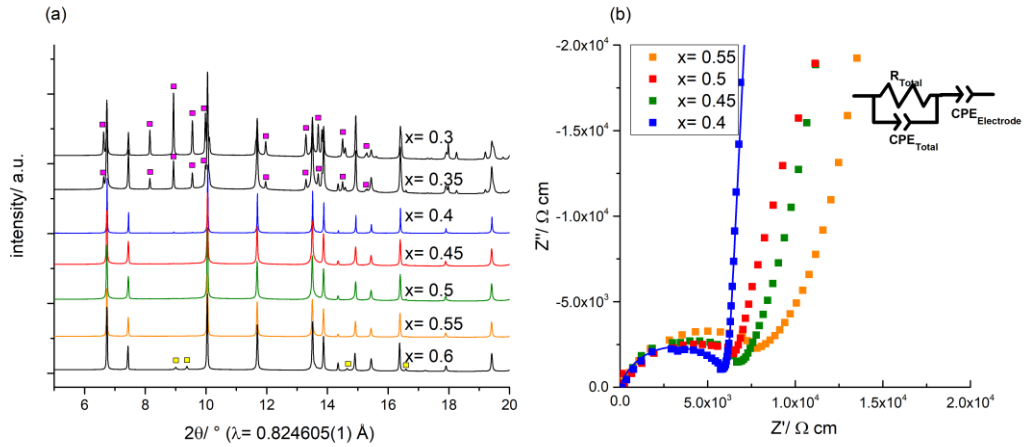

Figure 68: (a) SXRD patterns along $Li_{4+x}In_xSn_{1-x}S_4$ (0.3 < x < 0.6); the violet and yellow marks denote reflections indexed to Li_4SnS_4 and $LiInS_2$ respectively. (b) AC-impedance spectra of crystallographically pure compounds in $Li_{4+x}In_xSn_{1-x}S$; with decreasing values of x, a slight increase of conductivity is observed; insert: equivalent circuit used to model the total conductivity and the electrode response.

Figure 68(b) displays the room temperature AC-impedance spectra of the four pure $Li_{4+x}In_xSn_{1-x}S_x$ ($0.4 \leq x \leq 0.55$) phases. As common for this class of materials AC impedance does not allow for the distinction of the bulk and grain boundary contribution to the resistance. A single RC element was used to model the total resistivity of $Li_{4.4}In_{0.4}Sn_{0.6}S_4$ (x= 0.4). In analogy to $Li_{4+x}Ga_xGe_{1-x}S_4$ increasing Li^+ conductivity is observed with decreasing x, but the change is small compared to that reported for the $Li_{4+x}Ga_xGe_{1-x}S_4$ series. In $Li_{4+x}Ga_xGe_{1-x}S_4$ the conductivity changed by two orders of magnitude. In contrast the $Li_{4+x}In_xSn_{1-x}S_4$ system shows only slight increase of conductivity from 1.0×10^{-4} S cm^{-1} to $1.5(3) \times 10^{-4}$ S cm^{-1} with decreasing x.

To test for chemical stability of $Li_{4.4}In_{0.4}Sn_{0.6}S_4$ against lithium metal, a galvanostatic plating and stripping experiment of the material in a symmetric Li|SE|Li cell was performed (Figure 69). The overpotential *E* continues to rise until cell failure after 70 h.

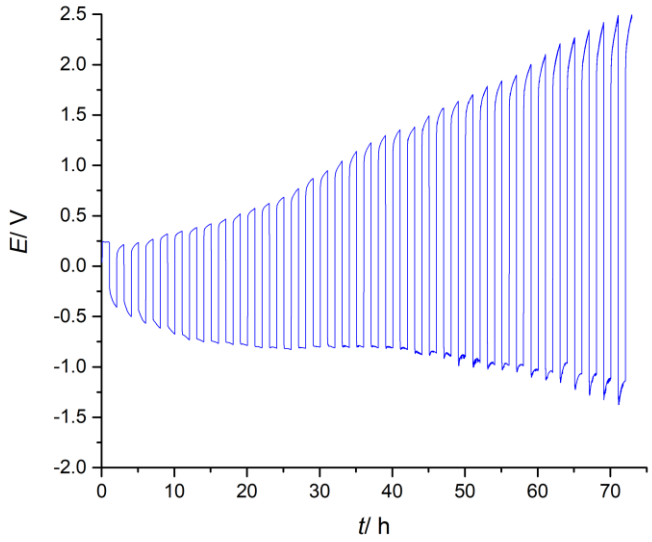

Figure 69: Galvanostatic plating and stripping experiment of $Li_{4.4}In_{0.4}Sn_{0.6}S_4$ in symmetric Li|Se|Li cell obtained at 323 K at ±0.01 mA cm^{-2} for 1 h (0.01 mAh cm^{-2}) per half-cycle. After 70 h an overpotential of 2.5 V was reached and the experiment aborted.

This rapid and continuous degradation can be attributed to the intrinsically lower electrochemical stability and easier reduction of In^{3+} and Sn^{4+} compared to its lighter homologues in $Li_{4.4}Al_{0.4}Ge_{0.6}S_4$. The standard electrode potentials can be used as a proxy to follow this trend, as tabulated in Table 10.[33]

Table 10: Standard electrode potentials E° for selected red-ox couples.[33]

	Al	Ga	In	Ge	Sn
Reaction	$Al^{3+} + 3e^- \rightleftharpoons Al$	$Ga^{3+} + 3e^- \rightleftharpoons Ga$	$In^{3+} + 3e^- \rightleftharpoons In$	$Ge^{4+} + 4e^- \rightleftharpoons Ge$	$Sn^{4+} + 2e^- \rightleftharpoons Sn^{2+}$
E°/V	-1.67	-0.55	-0.34	0.12	0.15

The red-ox couple $Al^{3+} + 3e^- \rightleftharpoons Al$ has a significantly lower standard electrode potential compared to the $In^{3+} + 3e^- \rightleftharpoons In$, indicating that it is harder to fully reduce (-1.67 V vs. -0.34 V respectively). Similarly, Ge^{4+} is assumed to be slightly more stable than Sn^{4+} (0.12 V vs. 0.15 V).

4.3.4.3 Structure refinement of $Li_{4.4}In_{0.4}Sn_{0.6}S_4$

Elemental analysis of the $Li_{4.4}In_{0.4}Sn_{0.6}S_4$ material was carried out by ICP-OES and gave a composition $Li_{4.40(1)}In_{0.37(1)}Sn_{0.61(1)}S_{3.94(4)}$ which is in excellent agreement with the formal stoichiometry $Li_{4.4}In_{0.4}Sn_{0.6}S_4$. Ambient temperature neutron and synchrotron radiation powder data were collected on the highest conducting $^7Li_{4.4}In_{0.4}Sn_{0.6}S_4$ to carry out a full structural solution. This could enable us to relate any differences in structure to changes in Li^+ mobility. The structure of $Li_{4.4}Al_{0.4}Sn_{0.6}S_4$ was used as a starting model for a combined NPD and SXRD Rietveld refinement. A satisfactory refinement could be achieved by refining the

unit cell parameters, fractional coordinates, occupancies and displacement parameters, giving an overall χ^2 of 9.52 and yielding the model shown in Figure 70(a). Figure 70(b) shows the fit of the final model against neutron diffraction data (ISIS neutron source, Polaris, bank 5), while Figure 71 shows the fit to banks 1 - 4 and Table 23 in the appendix states the refined structural parameters of $Li_{4.4}In_{0.4}Sn_{0.6}S_4$. As expected, sulphur atoms (crystallographic sites S1 and S2) form a hexagonal close packed sublattice. A layered structure is formed by the alternated occupation of tetrahedral and octahedral interstices by Li along the *c*-axis analogous to $Li_{4.4}Al_{0.4}Sn_{0.6}S_4$, while In^{3+} and Sn^{4+} cations mix on the same tetrahedral site. The ratio of In^{3+} to Sn^{4+} refines to 0.45(1): 0.55(1) which is slightly off the initial reagent stoichiometry of 0.4: 0.6. This subtle difference is corroborated by the finding of a small Li_4SnS_4 (1.00(1) % wt) impurity phase in the SXRD pattern. There are two tetrahedral Li sites (Li1 and Li2) in the tetrahedral layer which are occupied by 0.58(1) and 0.39(1) Li respectively. This in agreement with the idea of one disordered tetrahedral lithium cation which can move between both sites. The octahedral layer is constituted by octahedral coordination of the split Li3 site, which refines to 0.44(1) lithium. This is close to the value of 0.46 needed to charge the formal composition of $Li_{4.4}In_{0.4}Sn_{0.6}S_4$. In comparison to the $Li_{4.4}Al_{0.4}Sn_{0.6}S_4$ phase,

an increased isotropic displacement parameter of the Li3 site (0.057(2) vs. 0.077(3)) indicates faster mobility of the species.

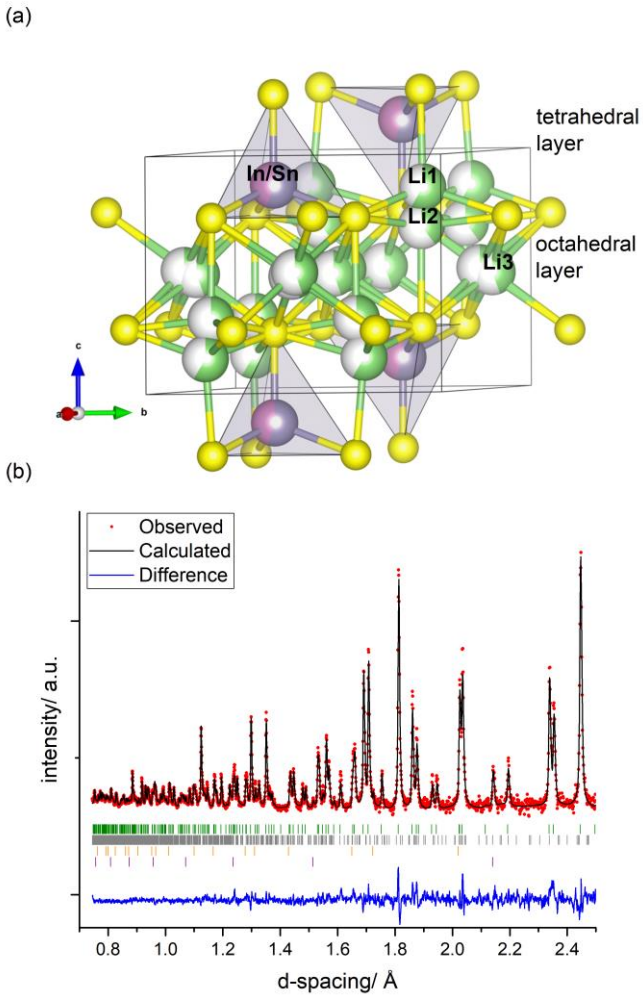

Figure 70: (a) Refined crystal structure of $Li_{4.4}In_{0.4}Sn_{0.6}S_4$; Atoms and polyhedra are coloured as follows: yellow: sulphur, green: lithium, violet-pink: mixed In^{3+}/Sn^{4+} sites. (b) Rietveld refinement of $^7Li_{4.4}In_{0.4}Sn_{0.6}S_4$ against NPD data (ISIS neutron source, Polaris, bank 5 (2θ= 146.72 °), room temperature). The positions of calculated Bragg reflections are indicated by tick marks (green: $^7Li_{4.4}In_{0.4}Sn_{0.6}S_4$, grey: Li_4SnS_4, orange: Li_2S, purple: vanadium (sample can)).

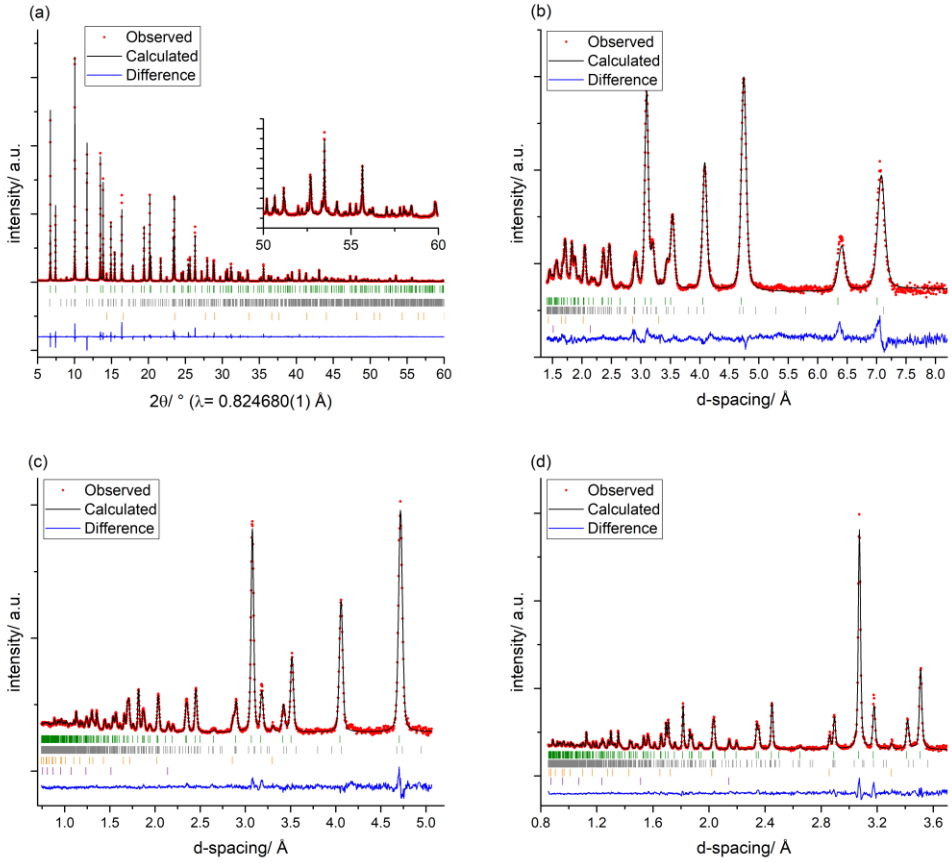

Figure 71: Ambient temperature Rietveld refinements of $^{7}Li_{4.4}In_{0.4}Sn_{0.6}S_4$ against SXRD (I11 beamline, MAC detector) and NPD (ISIS neutron source, Polaris beam line) data. The positions of calculated Bragg reflections are shown by tick marks (green: $^{7}Li_{4.4}In_{0.4}Sn_{0.6}S_4$, grey: Li_4SnS_4, orange: Li_2S, purple: vanadium (sample canister)). (a) SXRD pattern (b) NPD pattern, bank 2 (2θ= 25.99 °) (c) NPD pattern, bank 3 (2θ= 52.21 °) (d) NPD pattern, bank 4 (2θ= 92.59 °).

To check for unaccounted scattering density, which can indicate the presence of further lithium sites, Fourier-difference maps were constructed from neutron diffraction data. But no further Li sites were identified. The refined structure does not allow to deduct an obvious reason for the improved conductivity compared to the fully solved structures of $Li_{4.4}Al_{0.4}Ge_{0.6}S_4$ and $Li_{4.4}Al_{0.4}Sn_{0.6}S_4$.

4.3.5 Structure-property relationship in $Li_{4.4}M_{0.4}M'_{0.6}S_4$ (M= Al^{3+}, Ga^{3+}, In^{3+} and M'= Si^{4+}, Ge^{4+}, Sn^{4+})?

The new lithium containing metal sulphide phases $Li_{4.4}M_{0.4}M'_{0.6}S_4$ (M= Al^{3+}, Ga^{3+}, In^{3+} and M'= Si^{4+}, Ge^{4+}, Sn^{4+}) exhibit conductivities in a range of three orders of magnitude: 10^{-6} – 10^{-4} S cm^{-1}. This section is an attempt to find correlations between experimental or compositional factors to the conductivities. This would improve our understanding of the materials and the resulting properties. Table 11 gives an overview of experimental parameters X of the materials obtained by AC-impedance measurements, solid state NMR

experiments and diffraction experiments (Pawley and Rietveld refinements). Unfortunately, full structure solution, including refinement of lithium positions and occupancies, could only be conducted on three materials ($Li_{4.4}Al_{0.4}Ge_{0.6}S_4$, $Li_{4.4}Al_{0.4}Sn_{0.6}S_4$ and $Li_{4.4}In_{0.4}Sn_{0.6}S_4$).

Table 11: Comparison of experimental parameters X of the different $Li_{4.4}M_{0.4}M'_{0.6}S_4$ (M= Al^{3+}, Ga^{3+}, In^{3+} and M'= Si^{4+}, Ge^{4+}, Sn^{4+}) materials obtained from, AC-impedance measurements, solid state NMR experiments and fitting diffraction data (Pawley or Rietveld fits)

	Al-Ge	Al-Sn	Ga-Ge	Ga-Sn	In-Si	In-Ge	In-Sn
σ_{tot} / S cm^{-1}	4.3(3)x10^{-5}	4.3(9)x10^{-6}	1.6(3)x10^{-5}	3(2)x10^{-6}	2.6x10^{-6}	1.6(2)x10^{-5}	1.5(3)x10^{-4}
E_a/ eV	0.38(1)	0.42(1)	0.40(1)	0.43(1)	0.46	0.38(1)	0.31(5)
fwhm/ Hz	860	2000	1200	1850	950	950	850
a/ Å	7.9496(3)	8.0184(2)	7.94866(6)	8.0296(8)	7.9817(2)	8.01986(5)	8.09271(2)
c/ Å	6.1566(3)	6.2856(2)	6.1521(2)	6.2851(7)	6.1722(2)	6.21596(4)	6.34417(1)
V/ Å^3	336.959(3)	349.992(2)	336.626(3)	350.949(3)	340.54(2)	346.237(5)	359.827(2)
c/*a*	0.7745	0.7839	0.7740	0.7827	0.7733	0.7751	0.7839
occ(Li1)/ occ(Li2)	2.9	1.36	x	x	x	x	1.47

The conductivities σ_{tot} of the individual phases were plotted against the experimental parameters *X* to check for clear correlations. There is a negative correlation between the conductivity σ_{tot} and the activation energy E_a (Figure 72(a)), which agrees with the idea that lower activation barriers for diffusion result in higher conductivities. The plot of the full width half maximum, obtained from ambient temperature NMR measurements, is more ambiguous (Figure 72(b)). But the concept of relating *fwhm* values to conductivities can be confirmed. No correlations can be found to link the conductivity σ_{tot} to any experimental parameter measurable by SXRD, *i.e.* lattice parameters, unit cell volume and the ratio of lattice parameter *c* over *a* (Figure 72(c)-(e)). The Li-In-Sn-S compound is out of scale for most plotted parameters, indicating that it is unique in its properties.

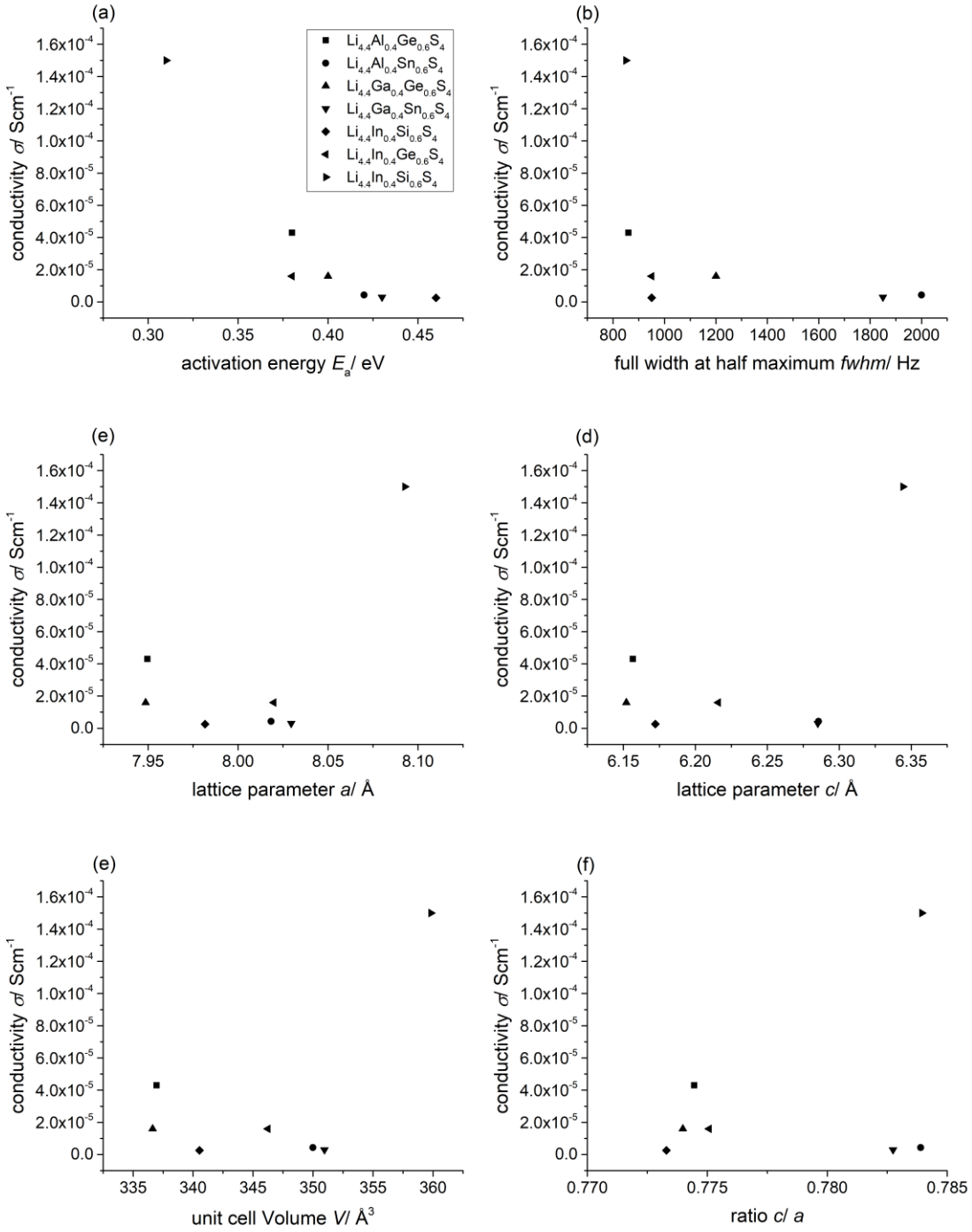

Figure 72: Plots of ambient temperature conductivity σ_{tot} of $Li_{4.4}M_{0.4}M'_{0.6}S_4$ vs experimental parameters X; (a) σ_{tot} vs activation energy E_a; (b) σ_{tot} vs the full width at half maximum fwhm from ambient temperature NMR measurements; (c) σ_{tot} vs lattice parameter a; (d) σ_{tot} vs lattice parameter c; (d) σ_{tot} vs unit cell volume V; (f) σ_{tot} vs the ratio of the unit cell parameters c/a.

As no relationship between Li^+ mobility and an experimental parameter *X* was found, physical descriptors *Y* of the non-lithium cations were investigated (Table 12). The descriptors were chosen to reflect parameters used in literature to argue low/high ionic conductivity, *i.e.* atomic radii, ionic radii, electronegativity differences and polarizability of the cations.

Table 12: Physical descriptors Y for Al^{3+}, Ga^{3+}, In^{3+}, Si^{4+}, Ge^{4+}, Sn^{4+}.

	Al^{3+}	Ga^{3+}	In^{3+}	Si^{4+}	Ge^{4+}	Sn^{4+}
Atomic radius/ Å	1.18	1.36	1.56	1.11	1.25	1.45
Ionic radius/ Å	1.25	1.3	1.55	1.10	1.25	1.45
Pauling electronegativity	1.61	1.81	1.78	1.90	2.01	1.96
Polarizability/ $Å^3$	8.3	8.1	9.7	5.4	6.1	7.7

For each material the variance in the descriptors *Y*, $\sigma^2 = \langle Y_{atom}^2 \rangle - \langle Y_{atom} \rangle^2$, and the weighted average $\bar{Y}$= 0.4*Y*(*M*) – 0.6*Y*(*M'*) were calculated and plotted in Figure 73.

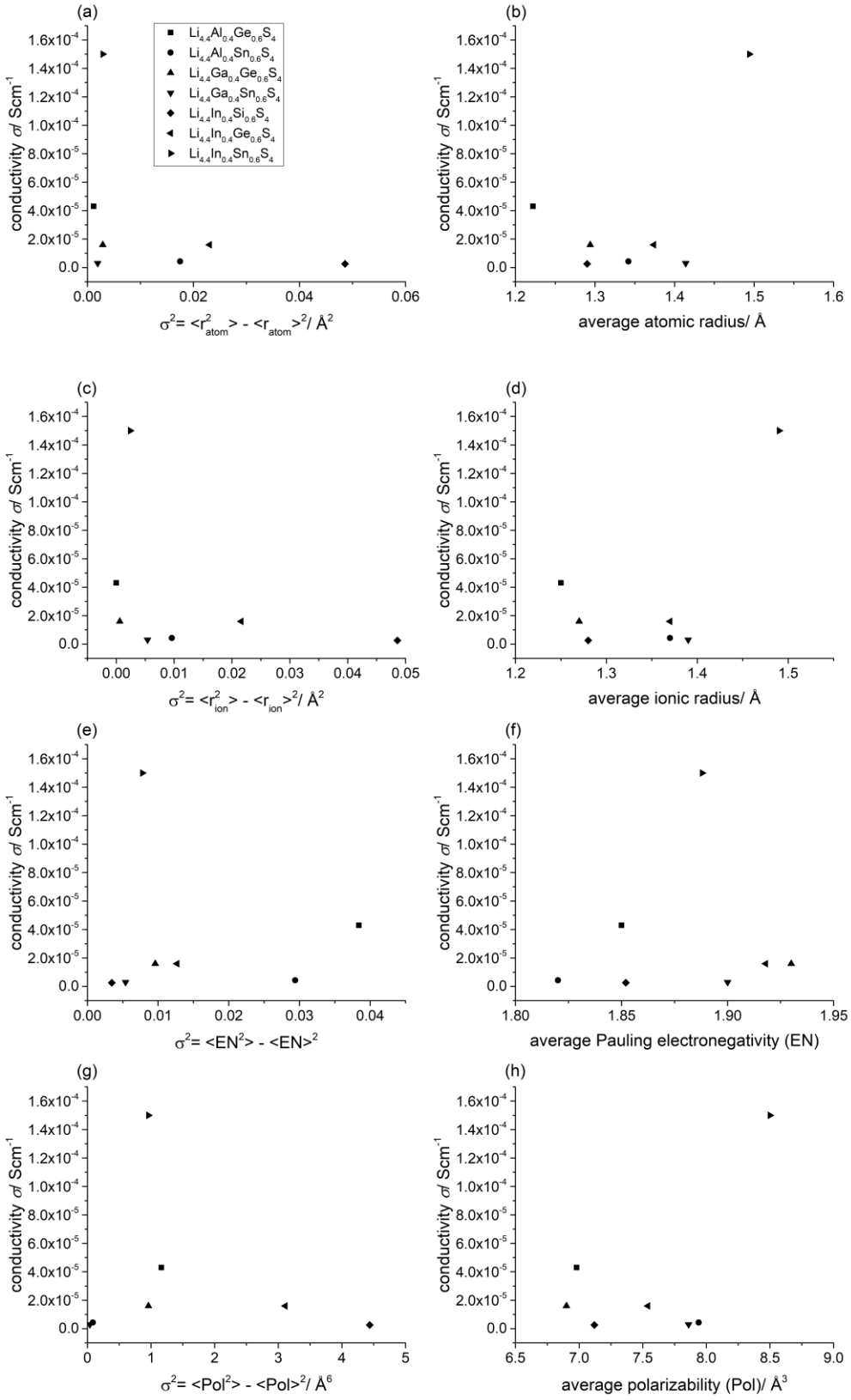

Figure 73: Plots of ambient temperature conductivity σ_{tot} of $Li_{4.4}M_{0.4}M'_{0.6}S_4$ vs physical parameters Y; (a) σ_{tot} vs σ^2(atomic radius); (b) σ_{tot} vs average atomic radius; (c) σ_{tot} vs σ^2(ionic radius); (d) σ_{tot} vs average ionic radius; (e) σ_{tot} vs σ^2(Pauling electronegativity); (f) σ_{tot} vs average Pauling electronegativity; (g) σ_{tot} vs σ^2(polarizability); (h) σ_{tot} vs average polarizability.

No clear correlation between the ionic conductivity σ_{tot} and a physical parameter *Y* can be inferred from Figure 73(a)-(h). Considering that no changes in the crystal structure, no correlations between structural parameters *X* or physical parameters *Y* can be identified, the reason for improved can be a multifactorial correlation which cannot be easily understood (or a parameter which has not been accounted for).

Although a completely different approach renders the attempt to link structure to AC-impedance conductivity invalid: The total conductivities σ_{tot} were extracted from AC-impedance spectroscopy only. The spectra do not allow for the distinction between bulk and grain boundary resistance. On a local scale the local Li^+ mobility (*i.e.* bulk conductivity) could be very similar. But the total conductivity could σ_{tot} be dominated by the grain boundary contribution, which is based differences in processing instead of structural differences. Looking for explanations based on structural models would thus be futile. Additionally, new diffusion pathways might be formed in Li-In-Sn-S which might be responsible for the drastic increase in conductivity. But this could not be probed by AC-impedance spectroscopy, instead further solid state NMR experiments and computational methods (*e.g. ab initio* molecular simulation or bond valence sum calculations) would be needed.

4.3.6 $Li_{4.5}Al_{2/3}Ge_{1/6}P_{1/6}S_4$

4.3.6.1 Structure of $Li_{4.5}Al_{2/3}Ge_{1/6}P_{1/6}S_4$

The SXRD pattern of $Li_{4.5}Al_{2/3}Ge_{1/6}P_{1/6}S_4$ resembles strongly the PXRD pattern of Li_5AlS_4 by visual inspection. The crystal structure of Li_5AlS_4 was recently fully solved by SXRD and NPD data and reported to have an ionic conductivity σ of 9.7×10^{-9} S cm^{-1}.[1] The unit cell parameters of *a*= 6.8583(4) Å, *b*= 7.8369(4) Å, *c*= 6.2488(4) Å, β= 90.333(4)° were taken as a starting point for a Pawley fit in space group $P2_1/m$, to refine the unit cell parameters of the new phase. The following unit cell parameters were obtained: *a*= 6.8656(3) Å, *b*= 7.8471(3) Å, *c*= 6.2386(2) Å, β= 90.104(3)°. The *a* and *b* parameters increase slightly, while the *c* axis shrinks and the β angle closer to 90° is found. The resultant fit is depicted in Figure 74(a). All reflections can be indexed fully, except for one broad feature at d-spacing ~5 Å. The existence of further impurity phases cannot be ruled out, as thiophosphate containing materials are known to form amorphous by-phases, which could not be detected by PXRD analysis.[34-36]

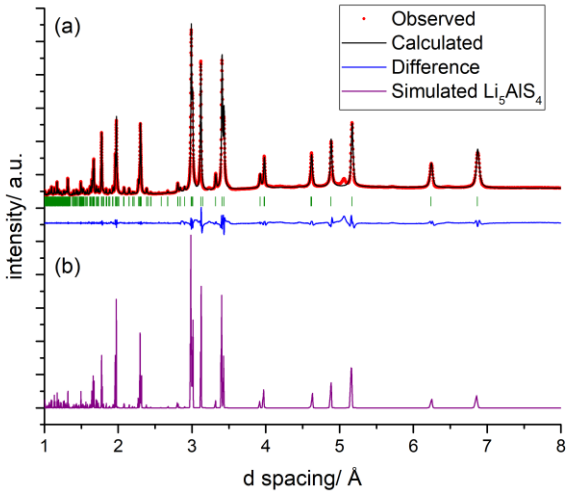

Figure 74: Comparison of the SXRD pattern of $Li_{4.5}Al_{2/3}Ge_{1/6}P_{1/6}S_4$ and simulated pattern of Li_5AlS_4; (a) Pawley fit of the SXRD pattern of $Li_{4.5}Al_{2/3}Ge_{1/6}P_{1/6}S_4$ measured at the I11 beamline (space group: $P2_1/m$). The positions of calculated Bragg reflections are shown by green tick marks*; (b) simulated PXRD pattern of Li_5AlS_4*

Figure 74(b) shows a simulate pattern of Li_5AlS_4 (ICSD entry # 433369). The two patterns strongly resemble each other, and it can be assumed that the structure of the S^{2-} sublattice and the positions of the heavy cations are retained – assuming that Al^{5+}, Ge^{4+} and P^{3+} share one crystallographic site. Thus, $Li_{4.5}Al_{2/3}Ge_{1/6}P_{1/6}S_4$ is a Ge^{4+} and P^{5+} doped Li_5AlS_4 analogue. Further structural Rietveld refinement is prevented by the assumed mixing of three different cations (Al^{3+}, Ge^{4+}, P^{5+}) on one crystallographic site, which cannot be deconvoluted by SXRD data only. Additional NPD data would be needed to accurately refine the occupancy of this site and check whether indeed the ideal ratio of 4:1:1 is maintained. This data could also be used to investigate the rearrangement of the Li atoms. As $Li_{4.5}Al_{2/3}Ge_{1/6}P_{1/6}S_4$ can be classed a Li-deficient Li_5AlS_4 analogue, it would be interesting to see whether there is a preference for vacancy formation; either in the octahedral or the tetrahedral layer of the structure.

4.3.6.2 Lithium mobility in $Li_{4.5}Al_{2/3}Ge_{1/6}P_{1/6}S_4$

Temperature dependent AC-impedance spectra were recorded on $Li_{4.5}Al_{2/3}Ge_{1/6}P_{1/6}S_4$ in the temperature range 303 K to 398 K. A typical spectrum obtained at 303 K is shown in Figure 75(a).

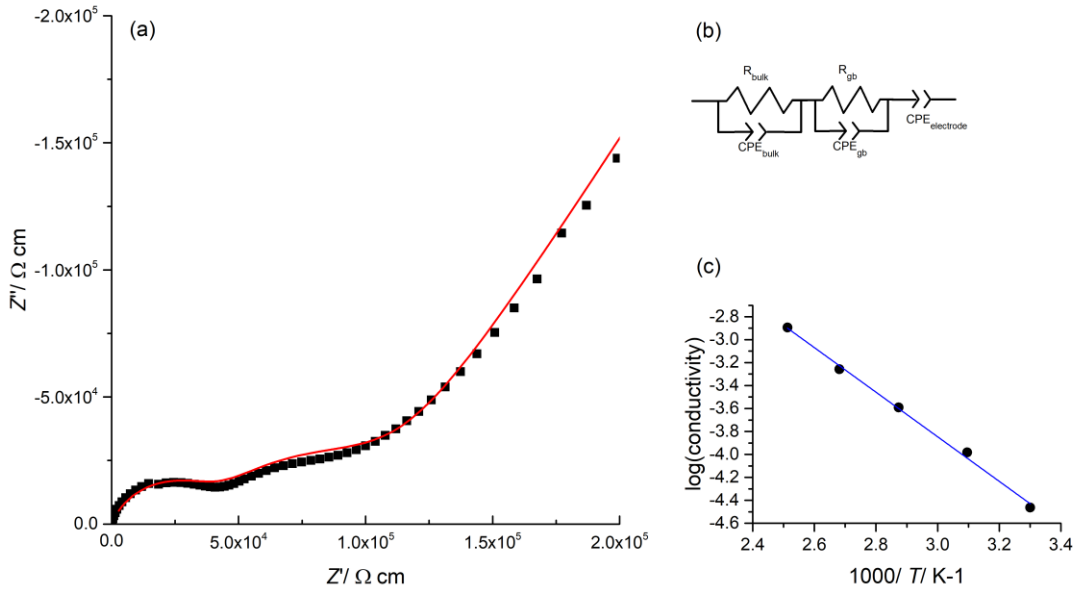

Figure 75: (a) AC-impedance spectrum of $Li_{4.5}Al_{2/3}Ge_{1/6}P_{1/6}S_4$ at 303 K (black square: measured data points, red line: fit to the equivalent circuit); (b) equivalent circuit used to fit the data, including two RCPE elements to fit the bulk and grain boundary response and a CPE element to simulate the electrode response; (c) Arrhenius plot

The ambient temperature spectrum is distinctly different to the spectra measured on the $Li_{4.4}M_{0.4}M'_{0.6}S_4$ materials. At high frequencies an arch is present, while at intermediate frequencies an additional depressed arch is detectable. The low frequency response consists of a spike. The observed data was fitted with an equivalent circuit shown in Figure 75(b). The capacitance values for the bulk and the grain boundary contributions are 7.2 x 10^{-12} F cm^{-1} and 7.2 x 10^{-10} F cm^{-1} respectively. These results can be interpreted as a bulk response coupled to a grain boundary response and eventually a lithium blocking electrode. The bulk ionic conductivity σ_b is 3.4 x 10^{-5} S cm^{-1}. The conductivity value is not exceptionally high, but if compared to the conductivity of 9.7 x 10^{-9} S cm^{-1} of the parent Li_5AlS_4 compound, this is a remarkable increase of four orders of magnitude. The activation barrier E_a of 0.39 eV was calculated from the Arrhenius plot, which is significantly lower than the activation barrier E_a of 0.61 eV reported for Li_5AlS_4.

Based on SXRD analysis $Li_{4.5}Al_{2/3}Ge_{1/6}P_{1/6}S_4$ crystallises in the Li_5AlS_4 structure, described in the introduction. In layered Li_5AlS_4 all tetrahedral interstices in the tetrahedral layer and all octahedral interstices in the octahedral layer are occupied by Al^{3+}/Li^+ and Li^+ respectively. Therefore, no vacant interstitial sites are present, which could facilitate lithium diffusion, and the material shows insulating behaviour despite being stuffed with lithium cations. The significant increase of conductivity in $Li_{4.5}Al_{2/3}Ge_{1/6}P_{1/6}S_4$ can be related to the results of the

ab initio molecular dynamic simulations performed on $Li_{4.4}Al_{0.4}Ge_{0.6}S_4$. By substitution of Al^{3+} for higher charged Ge^{4+} and P^{5+} in Li_5AlS_4 the lithium content is reduced. If the resulting lithium vacancies are accommodated in the octahedral layer, then vacancy-controlled lithium diffusion pathways can be formed in the octahedral layer. This would enable two-dimensional lithium transport in the a-b plane. It would be interesting to investigate, the scope of possible cation doping in Li_5AlS_4, as increased lithium vacancies might improve the conductivity further.

4.4 Summary and conclusion

Exploratory synthesis in the pseudo ternary Li_5AlS_4-Li_4GeS_4-Li_3PS_4 phase field resulted in the discovery of two new materials: trigonal $Li_{4.4}Al_{0.4}Ge_{0.6}S_4$ which forms a new structure, closely related to other layered hcp sulphides and $Li_{4.5}Al_{2/3}Ge_{1/6}P_{1/6}S_4$ which crystallises in the Li_5AlS_4 structure type.

Cation substitution in trigonal $Li_{4.4}Al_{0.4}Ge_{0.6}S_4$ showed that this material is not a singular compound but part of an expanded structural family $Li_{4.4}M_{0.4}M'_{0.6}S_4$ (M= Al^{3+}, Ga^{3+}, In^{3+} and M'= (Si^{4+}), Ge^{4+}, Sn^{4+}). It was possible to relate the formation of the new trigonal phase to a threshold value of the average ionic radius on the shared metal site r_{av}. Below an average radius r_{av} of 1.18 Å the formation of a monoclinic structure related to Li_4SiS_4 is preferred (*i.e.* $Li_{4.4}Al_{0.4}Si_{0.6}S_4$, $Li_{4.4}Ga_{0.4}Si_{0.6}S_4$). AC-impedance spectroscopy was applied on all trigonal materials to establish the ionic conductivities. These range from $10^{-6} – 10^{-4}$ S cm^{-1}, with $Li_{4.4}In_{0.4}Sn_{0.6}S_4$ exhibiting the highest conductivity by an order of magnitude. The stability against lithium metal was assessed for $Li_{4.4}Al_{0.4}Ge_{0.6}S_4$, $Li_{4.4}Al_{0.4}Sn_{0.6}S_4$ and $Li_{4.4}In_{0.4}Sn_{0.6}S_4$ by assembling symmetric Li|SE|Li cells and conducting galvanostatic plating and stripping experiments. $Li_{4.4}Al_{0.4}Ge_{0.6}S_4$ showed promising electrochemical stability, as the overpotential plateaued after ~100 h indicating a stabilised SE|Li interface. The latter two did not feature any stabilisation, which is due to the relatively high reducibility of In^{3+} and Sn^{4+} compared to Al^{3+} and Ge^{4+}. Full structural characterisation was carried out using SXRD and NPD data on $Li_{4.4}Al_{0.4}Ge_{0.6}S_4$, $Li_{4.4}Al_{0.4}Sn_{0.6}S_4$ and $Li_{4.4}In_{0.4}Sn_{0.6}S_4$. The materials crystallise isostructural and are based on hexagonal close packed sulphur sublattice. Distinct occupation of octahedral and tetrahedral interstices by the cations results in layered structure type and two-dimensional lithium transport. Besides a significant increase of the cell volume in $Li_{4.4}In_{0.4}Sn_{0.6}S_4$ compared to the Al-homologues no structural differences could be detected, which could help explain the widely different Li^+ conductivities.

The discovery and investigation of $Li_{4.5}Al_{2/3}Ge_{1/6}P_{1/6}S_4$ is a good example how cation substitution can result in improving lithium mobility in crystalline phases. The phase was structurally related to Li_5AlS_4 although full structural refinement could not be carried out. The well-studied material Li_5AlS_4 shows negligible lithium conductivity as no vacant sites are available for lithium migration. Doping with high valent Ge^{4+} and P^{5+} leads to a decreasing lithium content and consequent formation of vacancies. The lithium conductivity could be increased from 9.7×10^{-9} S cm^{-1} in Li_5AlS_4 to 3.4×10^{-5} S cm^{-1} in isostructural $Li_{4.5}Al_{2/3}Ge_{1/6}P_{1/6}S_4$.

The approach of exploring under-investigated phase fields is a promising strategy towards the discovery of new materials. By using reasonable starting assumptions, the synthesis of only eight compositions led to the detection of two new materials ($Li_{4.4}Al_{0.4}Ge_{0.6}S_4$ and $Li_{4.5}Al_{2/3}Ge_{1/6}P_{1/6}S_4$), even though considerable synthetic effort had to be made to refine the optimal synthetic conditions. Still, it is unreasonable to assume that all crystalline phases in this phase field have been identified. The compositional restraint of keeping the metal: sulphur ratio to 1:4 makes it hard to find materials with a different stoichiometry, *e.g.* argyrodite related compounds with a metal: sulphur ratio of 1:6 and changes in the synthetic conditions (firing temperatures/times) can lead to the formation of additional phases, as seen in the case of $Li_{10}GeP_2S_{12}$.

4.5 References

1. Lim, H.; Kim, S. C.; Kim, J.; Kim, Y. I.; Kim, S. J., Structure of Li_5AlS_4 and comparison with other lithium-containing metal sulfides. *J. Solid State Chem.* **2018,** *257*, 19-25.
2. Murayama, M.; Kanno, R.; Kawamoto, Y.; Kamiyama, T., Structure of the thio-LISICON, Li_4GeS_4. *Solid State Ion.* **2002,** *154-155*, 789-794.
3. Matsushita, Y.; Kanatzidis, M. G., Synthesis and structure of Li_4GeS_4. *Z Naturforsch B* **1998,** *53* (1), 23-30.
4. Homma, K.; Yonemura, M.; Kobayashi, T.; Nagao, M.; Hirayama, M.; Kanno, R., Crystal structure and phase transitions of the lithium ionic conductor Li_3PS_4. *Solid State Ion.* **2011,** *182* (1), 53-58.
5. MacNeil, J. H.; Massi, D. M.; Zhang, J. H.; Rosmus, K. A.; Brunetta, C. D.; Gentile, T. A.; Aitken, J. A., Synthesis, structure, physicochemical characterization and electronic structure of thio-lithium super ionic conductors, Li_4GeS_4 and Li_4SnS_4. *J. Alloys Compd.* **2014,** *586*, 736-744.
6. Kaib, T.; Haddadpour, S.; Kapitein, M.; Bron, P.; Schroder, C.; Eckert, H.; Roling, B.; Dehnen, S., New Lithium Chalcogenidotetrelates, LiChT: Synthesis and Characterization of the Li^+ Conducting Tetralithium ortho-Sulfidostannate Li_4SnS_4. *Chem. Mater.* **2012,** *24* (11), 2211-2219.
7. Batchelor, R. J.; Einstein, F. W. B.; Jones, C. H. W.; Fong, R.; Dahn, J. R., Crystal-Structure of Li_2FeS_2. *Phys. Rev. B* **1988,** *37* (7), 3699-3702.
8. Isaenko, L.; Yelisseyev, A.; Lobanov, S.; Titov, A.; Petrov, V.; Zondy, J. J.; Krinitsin, P.; Merkulov, A.; Vedenyapin, V.; Smirnova, J., Growth and properties of $LiGaX_2$ (X = S, Se, Te) single crystals for nonlinear optical applications in the mid-IR. *Cryst. Res. Technol.* **2003,** *38* (3-5), 379-387.
9. Murayama, M.; Kanno, R.; Irie, M.; Ito, S.; Hata, T.; Sonoyama, N.; Kawamoto, Y., Synthesis of New Lithium Ionic Conductor Thio-LISICON—Lithium Silicon Sulfides System. *J. Solid State Chem.* **2002,** *168* (1), 140-148.
10. Kanno, R.; Hata, T.; Kawamoto, Y.; Irie, M., Synthesis of a new lithium ionic conductor, thio-LISICON-lithium germanium sulfide system. *Solid State Ion.* **2000,** *130* (1-2), 97-104.
11. Kamaya, N.; Homma, K.; Yamakawa, Y.; Hirayama, M.; Kanno, R.; Yonemura, M.; Kamiyama, T.; Kato, Y.; Hama, S.; Kawamoto, K.; Mitsui, A., A lithium superionic conductor. *Nat. Mater.* **2011,** *10* (9), 682-686.
12. Wang, Y.; Richards, W. D.; Ong, S. P.; Miara, L. J.; Kim, J. C.; Mo, Y. F.; Ceder, G., Design principles for solid-state lithium superionic conductors. *Nat. Mater.* **2015,** *14* (10), 1026-1032.
13. Zhou, P. F.; Wang, J. B.; Cheng, F. Y.; Li, F. J.; Chen, J., A solid lithium superionic conductor $Li_{11}AlP_2S_{12}$ with a thio-LISICON analogous structure. *Chem. Commun.* **2016,** *52* (36), 6091-6094.
14. Kanno, R.; Maruyama, M., Lithium ionic conductor thio-LISICON - The Li_2S-GeS_2-P_2S_5 system. *J. Electrochem. Soc.* **2001,** *148* (7), A742-A746.
15. Hori, S.; Kato, M.; Suzuki, K.; Hirayama, M.; Kato, Y.; Kanno, R., Phase Diagramof the Li_4GeS_4-Li_3PS_4 Quasi-Binary System Containing the Superionic Conductor $Li_{10}GeP_2S_{12}$. *J. Am. Ceram. Soc.* **2015,** *98* (10), 3352-3360.
16. Ooura, Y.; Machida, N.; Naito, M.; Shigematsu, T., Electrochemical properties of the amorphous solid electrolytes in the system Li_2S-Al_2S_3-P_2S_5. *Solid State Ion.* **2012,** *225*, 350-353.
17. Amaresh, S.; Karthikeyan, K.; Kim, K. J.; Lee, Y. G.; Lee, Y. S., Aluminum based sulfide solid lithium ionic conductors for all solid state batteries. *Nanoscale* **2014,** *6* (12), 6661-6667.

18. Davies, P. K.; Wu, H.; Borisevich, A. Y.; Molodetsky, I. E.; Farber, L., Crystal chemistry of complex perovskites: New cation-ordered dielectric oxides. *Annu. Rev. Mater. Res.* **2008,** *38*, 369-401.
19. Leube, B. T.; Inglis, K. K.; Carrington, E. J.; Sharp, P. M.; Shin, J. F.; Neale, A. R.; Manning, T. D.; Pitcher, M. J.; Hardwick, L. J.; Dyer, M. S.; Blanc, F.; Claridge, J. B.; Rosseinsky, M. J., Lithium Transport in $Li_{4.4}M_{0.4}M'_{0.6}S_4$ (M = Al^{3+}, Ga^{3+}, and M' = Ge^{4+}, Sn^{4+}): Combined Crystallographic, Conductivity, Solid State NMR, and Computational Studies. *Chem. Mater.* **2018,** *30* (20), 7183-7200.
20. Johnson, D. *ZView: A Software Program for IES Analysis* 3.5d; Scribner Associates In.: 2007.
21. Bielecki, A.; Burum, D. P., Temperature-Dependence of ^{207}Pb MAS Spectra of Solid Lead Nitrate - an Accurate, Sensitive Thermometer for Variable-Temperature MAS. *J. Magn. Reson., Ser. A* **1995,** *116* (2), 215-220.
22. Beckmann, P. A.; Dybowski, C., A thermometer for nonspinning solid-state NMR spectroscopy. *J. Magn. Reson.* **2000,** *146* (2), 379-380.
23. Becker, K. D., Temperature-Dependence of NMR Chemical-Shifts in Cuprous Halides. *J. Chem. Phys.* **1978,** *68* (8), 3785-3793.
24. Wu, J. S.; Kim, N.; Stebbins, J. F., Temperature calibration for high-temperature MAS NMR to 913 K: ^{63}Cu MAS NMR of CuBr and CuI, and ^{23}Na MAS NMR of $NaNbO_3$. *Solid State Nucl. Magn. Reson.* **2011,** *40* (2), 45-50.
25. Kresse, G.; Furthmuller, J., Efficient iterative schemes for ab initio total-energy calculations using a plane-wave basis set. *Phys. Rev. B* **1996,** *54* (16), 11169-11186.
26. Perdew, J. P.; Burke, K.; Ernzerhof, M., Generalized gradient approximation made simple. *Phys. Rev. Lett.* **1996,** *77* (18), 3865-3868.
27. Kresse, G.; Joubert, D., From ultrasoft pseudopotentials to the projector augmented-wave method. *Phys. Rev. B* **1999,** *59* (3), 1758-1775.
28. Stokes, H. T.; Hatch, D. M., FINDSYM: program for identifying the space-group symmetry of a crystal. *J. Appl. Crystallogr.* **2005,** *38* (1), 237-238.
29. Kraft, M. A.; Culver, S. P.; Calderon, M.; Böcher, F.; Krauskopf, T.; Senyshyn, A.; Dietrich, C.; Zevalkink, A.; Janek, J.; Zeier, W. G., Influence of Lattice Polarizability on the Ionic Conductivity in the Lithium Superionic Argyrodites Li_6PS_5X (X = Cl, Br, I). *J. Am. Chem. Soc.* **2017,** *139* (31), 10909-10918.
30. Irvine, J.; Sinclair, D.; West, A., Electroceramics: Characterization by Impedance Spectroscopy. *Adv. Mater.* **1990,** *2*, 132-138.
31. Kraft, M. A.; Ohno, S.; Zinkevich, T.; Koerver, R.; Culver, S. P.; Fuchs, T.; Senyshyn, A.; Indris, S.; Morgan, B. J.; Zeier, W. G., Inducing High Ionic Conductivity in the Lithium Superionic Argyrodites $Li_{6+x}P_{1-x}Ge_xS_5I$ for All-Solid-State Batteries. *J. Am. Chem. Soc.* **2018,** *140* (47), 16330-16339.
32. Inoue, Y.; Suzuki, K.; Matsui, N.; Hirayama, M.; Kanno, R., Synthesis and structure of novel lithium-ion conductor Li7Ge3PS12. *J. Solid State Chem.* **2017,** *246*, 334-340.
33. Vanysek, P., *CRC Handbook of Chemistry and Physiks*. Boca Raton, 2005; Vol. 5.
34. Dietrich, C.; Koerver, R.; Gaultois, M. W.; Kieslich, G.; Cibin, G.; Janek, J.; Zeier, W. G., Spectroscopic characterization of lithium thiophosphates by XPS and XAS – a model to help monitor interfacial reactions in all-solid-state batteries. *Phys. Chem. Chem. Phys.* **2018,** *20* (30), 20088-20095.
35. Berbano, S. S.; Mirsaneh, M.; Lanagan, M. T.; Randall, C. A., Lithium Thiophosphate Glasses and Glass–Ceramics as Solid Electrolytes: Processing, Microstructure, and Properties. *Int. J. Appl. Glass Sci.* **2013,** *4* (4), 414-425.
36. Lotsch, B. V.; Maier, J., Relevance of solid electrolytes for lithium-based batteries: A realistic view. *J. Electroceram.* **2017,** *38* (2), 128-141.

4.6 Appendix

Table 13: Structural parameters of $Li_{4.4}Al_{0.4}Ge_{0.6}S_4$ from a Rietveld refinement at 10 K using NPD data.

Atom	Wyckoff site	x	y	z	occupancy	U_{iso}/Å^2
S1	6*i*	0.18174(7)	0.36347(13)	0.26092(30)	1	0.00791(25)
S2	2*d*	1/3	2/3	-0.22674(30)	1	0.0034(4)
Ge1	2*d*	1/3	2/3	0.13408(18)	0.6	0.00532(18)
Al1	2*d*	1/3	2/3	0.13408(18)	0.4	0.00532(18)
Li1	6*i*	0.31591(35)	0.15794(18)	0.1557(5)	0.738(5)	0.0156(6)
Li3	6*i*	0.4871(4)	0.5129(4)	0.5159(13)	0.441(7)	0.0256(16)
Li2	6*i*	0.3394(10)	0.1697	0.3175(11)	0.254(4)	0.0156(6)

a= 7.91914(6) Å, *c*= 6.13319(7) Å, Space group= $P\bar{3}m1$, R_{wp}= 0.0122, χ^2= 1.687, impurity phases: $LiAlS_2$ (2.0 wt %), Ge (0.4 wt %).

Table 14: Structural parameters of $Li_{4.4}Al_{0.4}Ge_{0.6}S_4$ from a Rietveld refinement at ambient temperature using NPD data.

Atom	Wyckoff site	x	y	z	occupancy	U_{iso}/Å^2
S1	6*i*	0.18173(7)	0.36346(13)	0.26202(27)	1	0.01863(35)
S2	2*d*	1/3	2/3	-0.22694(29)	1	0.0135(5)
Ge1	2*d*	1/3	2/3	0.13364(17)	0.595(4)	0.01443(25)
Al1	2*d*	1/3	2/3	0.13364(17)	0.405(4)	0.01443(25)
Li1	6*i*	0.3191(4)	0.15954(20)	0.1611(7)	0.767(6)	0.0330(7)
Li3	6*i*	0.48487(35)	0.51513(35)	0.5185(14)	0.461(5)	0.0420(15)
Li2	6*i*	0.3344(12)	0.1671(6)	0.3156(18)	0.221(5)	0.0330(7)

a= 7.94785(5) Å, *c*= 6.15520(7) Å, Space group= $P\bar{3}m1$, R_{wp}= 0.0275, χ^2= 2.044, impurity phases: $LiAlS_2$ (2.0 wt %), Ge (0.4 wt %).

Table 15: Bond distances of MS_4 tetrahedra and octahedra in $Li_{4.4}Al_{0.4}Ge_{0.6}S_4$ at 10 K. Atoms marked with primes (') relate to Figure 50.

$Li_{4.4}Al_{0.4}Ge_{0.6}S_4$	Bond length/ Å			
	Al/Ge	Li1	Li2	Li3
S1	2.2201(9)	2.4338(17)	2.439(5)	2.614(6)
S1'	x	2.576(4)	2.591(7)	2.673(5)
S2	2.213(3)	2.4447(18)	2.312(6)	2.634(6)
S2'	x	x	x	3.035(6)

Table 16: Bond distances of MS_4 tetrahedra and MS_6 octahedra in Li_5AlS_4 at ambient temperature.[1] Atoms marked with primes (') relate to Figure 50.

Li_5AlS_4	Bond length/ Å				
	Al	Li1	Li2	Li3	Li4
S1	2.2425(10)	2.3944(9)	2.638(13)	3.1389(12)	2.6562(5)
S2	2.2786(8)	2.4385(8)	2.382(14)	2.5934(11)	2.8508(5)
S3	2.2901(6)	2.3465(10)	2.433(7)	2.5541(7)	2.7284(6)
S3'	x	2.5657(11)	x	2.9100(8)	x

Table 17: Bond distances of MS_4 tetrahedra and MS_6 octahedra in Li_4GeS_4 at ambient temperature.[2] Atoms marked with primes (') relate to Figure 50.

Li_4GeS_4	Bond length/ Å			
	Ge	Li1	Li2	Li3
S1	2.2168(12)	2.9094(9)	2.493(4)	2.406(3)
S2	2.2096(12)	2.5894(14)	2.4503(19)	2.383(4)
S2'	x	x	x	2.576(3)
S3	2.228(4)	2.5572(11)	2.498(4)	2.550(4)

Table 18: Bond distances of MS_4 tetrahedra and MS_6 octahedra in $Li_{4.4}Al_{0.4}Sn_{0.6}S_4$ at 10 K.

$Li_{4.4}Al_{0.4}Sn_{0.6}S_4$	Bond length/ Å			
	Al/Sn	Li1	Li2	Li3
S1	2.3251(11)	2.435(4)	2.386(4)	2.662(6)
S1	x	2.572(5)	2.613(5)	2.730(6)
S2	2.321(4)	2.519(3)	2.386(4)	2.673(6)
S2	x	x	x	3.105(6)

Table 19: Structural parameters of $Li_{4.4}Al_{0.4}Sn_{0.6}S_4$ from a Rietveld refinement at 10 K using NPD data.

Atom	Wyckoff site	x	y	z	occupancy	U_{iso}/Å^2
S1	6*i*	0.17617(9)	0.35233(17)	0.26535(30)	1	0.01007(31)
S2	2*d*	1/3	2/3	-0.23562(33)	1	0.0102(4)
Sn1	2*d*	1/3	2/3	0.13475(24)	0.6	0.00687(24)
Al1	2*d*	1/3	2/3	0.13475(24)	0.4	0.00687(24)
Li1	6*i*	0.3118(4)	0.15589(22)	0.1431(6)	0.575(4)	0.0149(6)
Li3	6*i*	0.4835(4)	0.5165(4)	0.5202(13)	0.435(7)	0.0331(19)
Li2	6*i*	0.3302(6)	0.16504(32)	0.3189(6)	0.422(4)	0.0149(6)

a= 7.98832(6) Å, *c*= 6.2646(7) Å, Space group= $P\bar{3}m1$, R_{wp}= 0.0114, χ^2= 1.56, impurity phase: $LiAlS_2$ (1.5 wt %)

Table 20: Structural parameters of $Li_{4.4}Al_{0.4}Sn_{0.6}S_4$ from a Rietveld refinement at ambient temperature using NPD data.

Atom	Wyckoff site	x	y	z	occupancy	U_{iso}/Å^2
S1	6*i*	0.17658(8)	0.35315(16)	0.26304(27)	1	0.02224(35)
S2	2*d*	1/3	2/3	-0.23539(29)	1	0.0177(4)
Sn1	2*d*	1/3	2/3	0.13622(21)	0.6	0.01733(27)
Al1	2*d*	1/3	2/3	0.13622(21)	0.4	0.01733(27)
Li1	6*i*	0.3130(5)	0.15649(23)	0.1428(6)	0.584(4)	0.0293(6)
Li3	6*i*	0.4820(4)	0.5181(4)	0.5249(12)	0.460(5)	0.0573(18)
Li2	6*i*	0.3288(6)	0.16434(30)	0.3092(6)	0.4271(31)	0.0293(6)

a= 8.01711(6) Å, *c*= 6.26461(8) Å, Space group= $P\bar{3}m1$, R_{wp}= 0.0245, χ^2= 1.39, impurity phase: $LiAlS_2$ (1.5 wt %).

Table 21: Structural parameters of $Li_{4.4}Ga_{0.4}Ge_{0.6}S_4$ from a Rietveld refinement against room temperature SXRD data only, modelled without any lithium sites (I11 beamline, MAC-detector, λ= 0.824868(1) Å). Only the lattice parameters of the unit cell, the positions of the heavy atoms and displacement parameters were refined. The occupancy of sulphur and the combined Ga/Ge site were fixed to one respectively

Atom	Wyckoff site	x	y	z	Occupancy	U_{iso}/Å^2
S1	6*i*	0.17907(8)	0.3581(2)	0.2629(2)	1	0.0138(5)
S2	2*d*	1/3	2/3	0.7638(3)	1	0.0105(6)
Ga	2*d*	1/3	2/3	0.1317(2)	0.4	0.0102(4)
Ge	2*d*	1/3	2/3	0.1317(2)	0.6	0.0102(4)

a= 7.94866(6) Å, *c*= 6.1521(2) Å, Space group= $P\bar{3}m1$, R_{wp}= 9.62, χ^2= 45.75.

Table 22: Structural parameters of $Li_{4.4}Ga_{0.4}Sn_{0.6}S_4$ from a Rietveld refinement against room temperature SXRD data only, modelled without any lithium sites (I11 beamline, MAC-detector, λ= 0.824868(1) Å). Only the lattice parameters of the unit cell, the positions of the heavy atoms and displacement parameters were refined. The occupancy of sulphur and the combined Ga/Sn site were fixed to one respectively.

Atom	Wyckoff site	x	y	z	Occupancy	U_{iso}/Å^2
S1	6*i*	0.17499(8)	0.3499(2)	0.2665(2)	1	0.0163(4)
S2	2*d*	1/3	2/3	0.7564(3)	1	0.0129(5)
Ga	2*d*	1/3	2/3	0.1319(1)	0.4	0.0159(4)
Sn	2*d*	1/3	2/3	0.1319(1)	0.6	0.0159(4)

a= 8.0296(8) Å, *c*= 6.2851(7) Å, Space group= $P\bar{3}m1$, R_{wp}= 8.55, χ^2= 28.59, impurity phase: $LiGaS_2$ (3.5 wt %).

Table 23: Structural parameters of $Li_{4.4}In_{0.4}Sn_{0.6}S_4$ from a combined Rietveld refinement against room temperature SXRD (I11 beamline, MAC-detector, λ= 0.824868(1) Å) and NPD (ISIS neutron source, Polaris, bank 2 (2θ= 25.99 °), bank 3 (2θ= 52.21 °), bank 4 (2θ= 92.59 °), bank 5 (2θ= 146.72 °) data.

Atom	Wyckoff site	x	y	z	Occupancy	U_{iso}/Å^2
S1	6*i*	0.17174(5)	0.3435(1)	0.2651(1)	1	0.0182(2)
S2	2*d*	1/3	2/3	-0.2490(2)	1	0.0156(3)
In	2*d*	1/3	2/3	0.13155(7)	0.548(3)	0.0195(1)
Sn	2*d*	1/3	2/3	0.13155(7)	0.452(3)	0.0195(1)
Li1	6*i*	0.3088(6)	0.1544(4)	0.1443(8)	0.581(7)	0.0277(9)
Li2	6*i*	0.339(1)	0.1694(6)	0.3095(8)	0.394(6)	0.0277(9)
Li3	6*i*	0.488(1)	0.512(1)	0.509(3)	0.44(1)	0.077(3)

a= 8.09277(1) Å, *c*= 6.343931(8) Å, Space group= $P\bar{3}m1$, R_{wp}= 5.17, χ^2= 9.52, impurity phases: Li_4SnS_4 (1.0 wt %), Li_2S (1.6 wt %).

5 Novel Li-M(II)-Si-S Argyrodites

5.1 Introduction

5.1.1 Laves phase

The Laves phases (named after Fritz Laves) are a large group of intermetallic compounds (containing > 1400 members) of the stoichiometry AB_2. These materials are characterised by a tetrahedral close packing (topological close packing) of the metal atoms, which crystallise either in a cubic (*e.g.* Cu_2Mg, space group: $Fd\bar{3}m$) or a hexagonal unit cell (*e.g.* $MgZn_2$, space group: $P6_3/mmc$). The Laves phases can be classified according to the ratio of the ionic radii (r_A/r_B) and are known to be stable within the range of 1.05 to 1.67. The ideal ratio is ~1.225; which results in the highest packing density with an average coordination number of 13.3.[3] Figure 76(a) and (b) show the arrangement of Cu and Mg in Cu_2Mg, the connecting lines are not to indicate bonds but to represent connectivity. The name tetrahedrally close packing refers to the fact, that there are only (distorted) tetrahedral interstices in-between the metal atoms and therefore the structure can be thought of as being constructed solely of tetrahedra. This packing contrasts the hexagonal or cubic close packing motifs (hcp and ccp respectively), in which both tetrahedral and octahedral interstices are formed. The tetrahedral interstices remain empty in the Laves phase.

5.1.2 Argyrodites

Structurally related to the Laves phase are the argyrodites *e.g.* Ag_8GeS_6.[4] The structures of the argyrodites can be linked to the Laves phase by group-subgroup relations. In the cubic high temperature (HT) argyrodites, anions form a tetrahedral close packing equivalent to the Laves phase. The occupation of some of the resulting tetrahedral interstices with cations leads to a translationsgleiche reduction in symmetry from $Fd\bar{3}m$ to $F\bar{4}3m$ as depicted in Figure 76(c). A wide variety of compositions has been reported for argyrodites of the type $L^{m+}_{(12-n-x)/m}M^{n+}Y^{2-}_{6-x}X_x$ with the mobile cations *L*= Li^+, Ag^+, Cu^+, Cd^{2+}, Hg^{2+}; the higher valent cations *M*= Si^{4+}, Ge^{4+}, Sn^{4+}, P^{5+}, As^{5+}; and a range of anions *Y*= S^{2-}, Se^{2-}, Te^{2-} and *X*= Cl^-, Br^-, I^-.[5] Additionally there exist argyrodites with two aliovalent cation species on the *L* site ($Cu_{1.5}In_{1.5}PS_5I$) or on the *M* site ($Li_{6+x}P_{1-x}Ge_xS_5I$)[6].

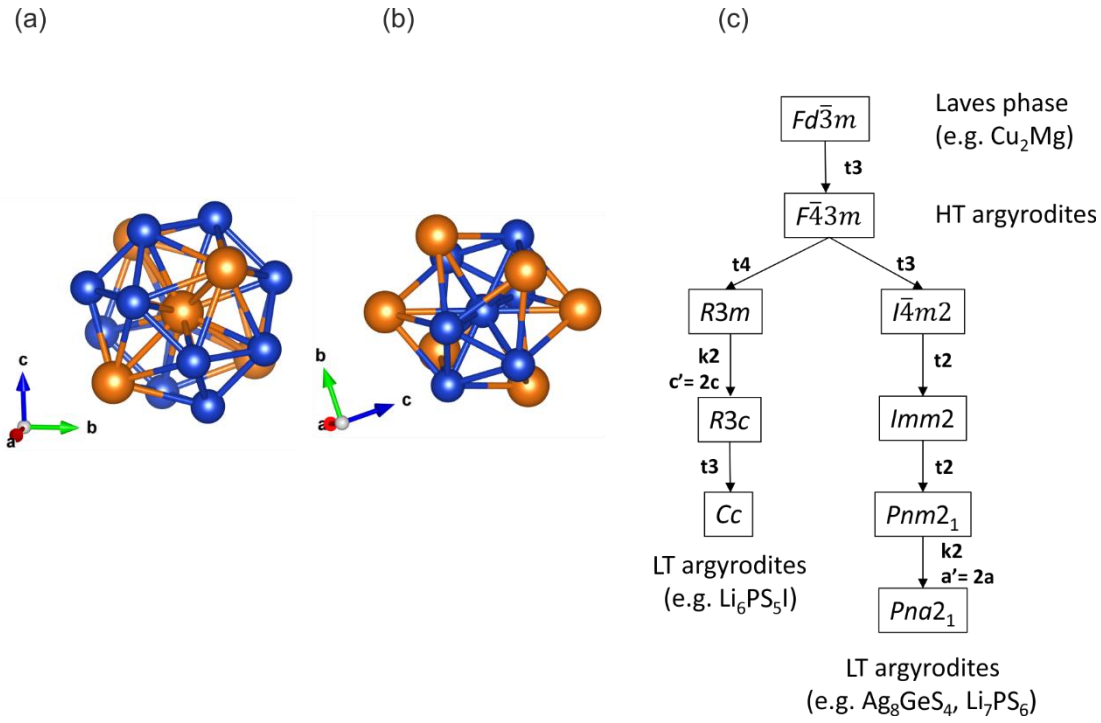

Figure 76 (a) Local coordination of Cu in Cu_2Mg. (b) local coordination of Mg in Cu_2Mg. (c) group-subgroup relation between the cubic high temperature and the orthorhombic low temperature polymorph of Ag_8GeS_6. (orange: Cu, blue: Mg)

At low temperatures many argyrodites crystallise in lower symmetry space groups. Low temperature (LT) polymorphs of Ag_8GeS_6[7] and Li_7PS_6[8] crystallise in the orthorhombic space group $Pna2_1$, while Li_6PS_5I crystallises in the monoclinic *Cc* space group at 170 K. The space groups $Pna2_1$ and *Cc* are general subgroups of $F\bar{4}3m$ related by the more complicated group-subgroup relationships shown in Figure 76(c).[9]

Isotypic Ag_8GeS_6 and Li_7PS_6 are typical examples of cubic HT argyrodites, crystallising in the $F\bar{4}3m$ space group with 4 formula units per unit cell giving the following unit cell content: 24 sulphur anions, 4 $M^{4+/5+}$ cations and 32/28 monovalent *L* cations (Ag/Li). The sulphur atoms form the tetrahedral close packing (Wyckoff positions: 16*e*, 4*c*, 4*a*) (Figure 77(a)), which creates 136 distorted tetrahedra that are connected through shared corners, edges and faces. The four high valent cations (Ge^{4+} and P^{5+} respectively) occupy the 4*b* tetrahedral interstitials without direct connection to each other, as shown in Figure 77(b). This arrangement minimises electrostatic repulsion.

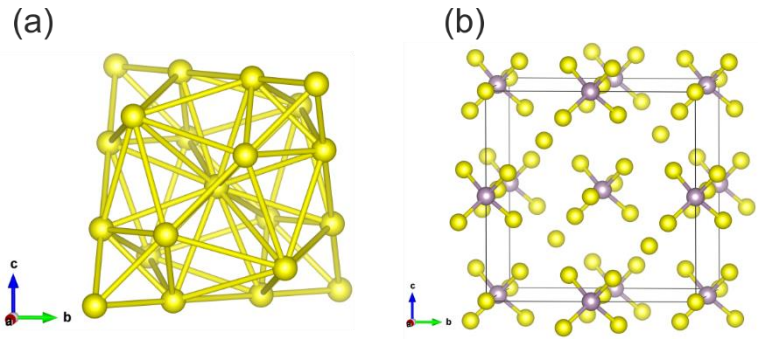

Figure 77: (a) S^{2-} sublattice of cubic Li_7PS_6 forming a tetragonal close packing analogous to the Laves phase. (b) P^{5+} occupation of the tetrahedral 4b site in Li_7PS_6 (shown without Li atoms for clarity). (yellow: sulphur, purple: phosphorous)

Each of the remaining 132 empty tetrahedral sites can be occupied by the mobile cation *L*, but the sites differ in respect to their position and connectivity to the PS_4^{3-} site. Deiseroth *et al.* distinguished between 5 symmetrically distinct tetrahedral sites and one trigonal planar site (type 5a) as shown in Figure 78.

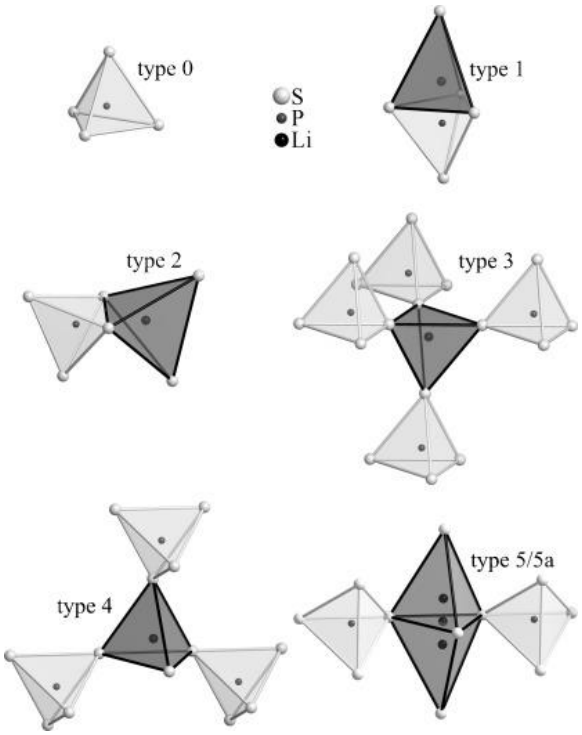

*Figure 78: Simplified representation of the tetrahedron types with respect to their orientation relative to the PS_4 groups. The trigonal planar position 5a is located in the common face of two type 5 tetrahedra. From Chem. Eur. J. **2010,** 16, 2198-2206. Reprinted with permission from John Wiley and Sons.*[8]

Based on how many edges, corners or faces the void tetrahedral sites share with PS_4 units Deiseroth *et al.* ranked the sites according to their suitability to accommodate mobile cations *L*. The more faces/edges/corners a tetrahedron shares with PS_4 units the more electrostatic repulsion is expected and the less likely is the occupation of the site (compare to Table 24).[8]

The site of type 5 is most suitable for Li atoms, as it shares only two corners with neighbouring PS_4 tetrahedra and the electrostatic repulsion is minimised. Type 5 sites are on the 48*h* Wyckoff positions and represent locally face sharing double tetrahedra as shown in Figure 78. These two tetrahedra are connected by the trigonal planar site of type 5a (Wyckoff position: 24*g*). The distances between the centres of the face sharing tetrahedra and the intermediate trigonal planar position are very short and only one of them can be occupied at a time. Thus, the combination of a double tetrahedron of type 5 and the trigonal planar site of type 5a represents in total only one mobile cation *L*. The distribution of Li atoms in the different tetrahedral types is given for Li_6PS_5I[10] and $Li_{6.15}Al_{0.15}Si_{1.35}S_6$[11] in Table 24.

*Table 24: Crystal chemical analysis of the 136 tetrahedral interstices formed by the S atoms in the unit cell of HT-Li_7PS_6, according to Chem. Eur. J. **2010,** 16, 2198-2206.[8] The occupation of the different sites is exemplarily compared to HT-Li_6PS_5I and $Li_{6.15}Al_{0.15}Si_{1.35}S_6$.*

Type	Wyckoff position in the cubic polymorph	Connectivity with PS_4 unit	Suitability for occupation by monovalent cations	Occupation in HT-Li_6PS_5I[10]	Occupation in $Li_{6.15}Al_{0.15}Si_{1.35}S_6$[11]
0	4*b*	occupied by P	unfavourable	x	x
1	16*e*	Common faces	unfavourable	x	x
2	48*h*	Common edges	less unfavourable	x	x
3	4*d*	Four corners	favourable	x	x
4	16*e*	Three corners	favourable	x	0.38
5	48*h*	Two corners	most favourable	0.391	0.43
5a	24*g*	x	x	0.219	x

In Li_6PS_5I all mobile lithium atoms are found on the 48*h* and the intermediate 24*g* site. In materials in which the mobile *L* cation to anion ratio exceeds 1:1 the *L* cations must occupy less favourable tetrahedral sites. Exemplarily in $Li_{6.15}Al_{0.15}Si_{1.35}S_6$ the additional 16*e* site of type 4 is partially occupied.

Typically, the cubic HT and the low symmetry LT argyrodites are similar in respect to their S^{2-} sublattice and the occupation of the high valent cation site. The HT polymorphs are characterised by large degrees of disorder of the monovalent cation site; usually the 48*h* site is fractionally occupied by a mobile *L* cation and sometimes there is evidence of occupancy of the intermediate 24*g* site (compare to Table 24). Reducing the temperature results in phase transition to lower symmetry space groups through the group-subgroup relationships depicted in Figure 76(c), as monovalent cations become frozen out/ordered from their disordered sites. Additional sites with linear coordination or trigonal planar coordination geometry are occasionally occupied. Figure 79 shows the comparison between the cubic HT

polymorph (space group: $F\bar{4}3m$) of Li_7PS_6 and the orthorhombic LT polymorph (space group: *Pna*2_1). While every 48*h* site is partially occupied by 0.53 Li in the HT cubic polymorph of Li_7PS_6 (a), the Li atoms are fully ordered in the LT phase (b).

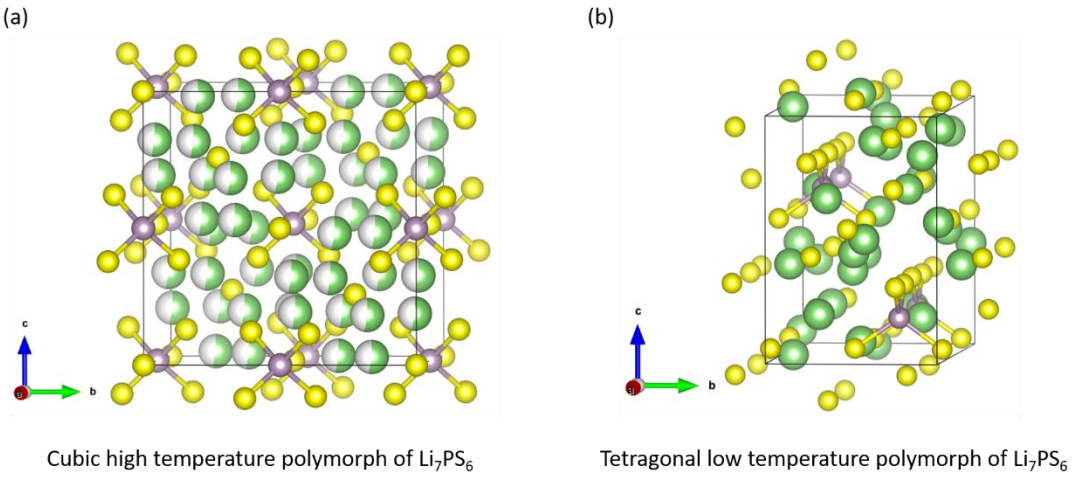

Cubic high temperature polymorph of Li_7PS_6 Tetragonal low temperature polymorph of Li_7PS_6

Figure 79: Comparison of (a) the HT cubic Li_7PS_6 argyrodite with (b) the LT orthorhombic Li_7PS_6 argyrodite. The transition temperature is 483 K.[12] The arrangement of the PS_4 tetrahedra remains unchanged while lithium ordering is responsible for the phase transition. (yellow: sulphur, green: lithium, purple: phosphorous).

5.1.3 Lithium containing argyrodites as solid electrolytes

Argyrodites can be excellent solid state conductors and enable the movement of the mobile cation *L* through the bulk material. Silver based argyrodites are known to exhibit high silver conductivities of up to 2.15 x 10^{-2} S cm^{-1} for Ag_7SiS_5Br and 5.97 x 10^{-2} S cm^{-1} in Ag_7SnS_5I.[13] Recently lithium containing argyrodites have raised the interest of the scientific community as potential solid state electrolytes in all solid state batteries. The fully ordered LT argyrodite polymorph of Li_7PS_6 has a reported lithium conductivity of 1.6 x 10^{-6} S cm^{-1} at room temperature.[14] Halogen doping according to Li_6PS_5X (*X*= Cl, Br, I) stabilises the cubic argyrodite structure and introduces disorder on the lithium sites. Consequently the materials show significantly improved conductivities of 1.9 x 10^{-3} S cm^{-1}, 0.7 x 10^{-4} S cm^{-1} and 1.3 x 10^{-6} S cm^{-1} respectively.[15] [16] Figure 80 shows exemplarily the crystal structure of the cubic argyrodite Li_6PS_5I. Contrary to the previous discussion of argyrodites, the structure of Li_6PS_5I can most conveniently be described by recognising the face-centred cubic sublattice formed by I^- anions. Half of the occurring tetrahedral interstices are occupied by non-phosphorous bound ("free") sulphide anions (compare Figure 80(a)). All octahedral interstices all are subsequently occupied by PS_4 building blocks (see Figure 80(b)). The full structure with all lithium atoms is given in panel (c).

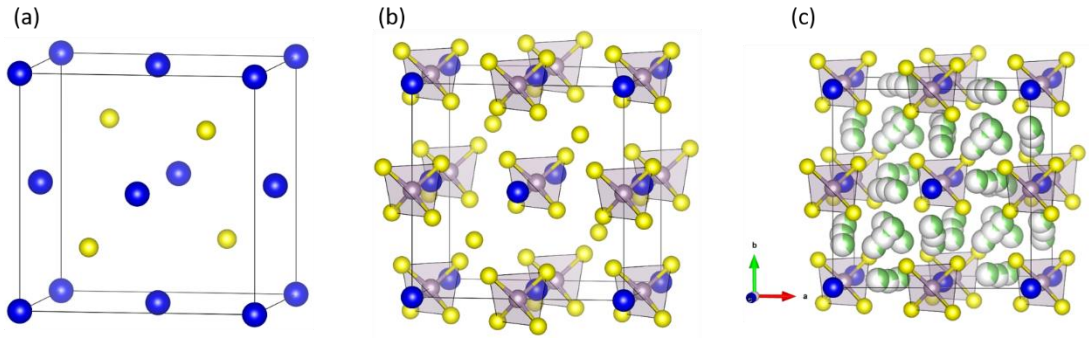

Figure 80: Structure of Li_6PS_5I (a): fcc sublattice formed by I and occupation of four tetrahedral interstices by sulphur ("free" sulphur). (b) Occupation of all octahedral interstices by PS_4 building blocks. (c) Full structure of Li_6PS_5I. (yellow: sulphur, blue: iodine, purple: phosphorous, green: lithium)

The "free" sulphur anions are pseudo-octahedrally coordinated in a cage-like fashion by disordered lithium atoms on the 24*g* and 48*h* sites. The local lithium arrangement around those cages is shown in Figure 81. The lithium diffusion in cubic argyrodites can most easily be discussed by considering how lithium moves from one cage to the other. Three lithium jump processes have been identified by molecular simulation calculations:[6, 17] the doublet jump (48*h*-24*g*-48*h*), intra-cage jump (48*h*-48*h*) and the inter-cage jump (48*h*-48*h*). The latter is responsible for long range lithium migration and considered to limit the macroscopic diffusion.

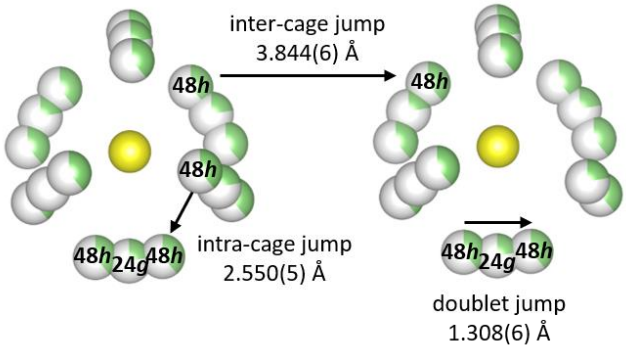

Figure 81: Local lithium arrangement around the "free" sulphur anion. Different lithium jumps are indicated: inter-cage jump between two cages (48h-48h), intra-cage jump (48h-48h) and doublet jump (48h-24h-48h). (yellow: sulphur, green: lithium, purple: phosphorous, blue: iodine).

Numerous reports have been published on aliovalent doping of sulphide-halogen based lithium argyrodites: $Li_{7+x}M_xP_{1-x}S_6$ (M= Si, Ge),[18] $Li_{6+x}Si_xP_{1-x}S_5Br$, [19] $Li_{6+x}Ge_xP_{1-x}S_5I$, [6] $Li_{6+x}M_xP_{1-x}S_5I$ (M= Si, Ge, Sn)[20] leading to conductivities up to 1.8×10^{-2} S cm^{-1} in a sintered sample of $Li_{6.6}P_{0.4}Ge_{0.6}S_5I$.[6] Furthermore, changing the anion framework according to $Li_6PS_5Cl_{0.5}Br_{0.5}$ [21] or $Li_{6-x}PS_{5-x}Cl_{1+x}$[22] resulted in excellent lithium mobility of 9×10^{-3} S cm^{-1} in $Li_{5.5}PS_{4.5}Cl_{1.5}$. Shao *et al.* co-doped Li_6PS_5Cl with Cl^- and Te^{2-} and reported the new material $Li_{6.25}PTe_{0.125}S_{5.125}Cl_{0.75}$ with a conductivity of 4.5×10^{-3} S cm^{-1}.[23]

An ambiguity exists regarding the stability of phosphorous based materials against lithium metal. Numerous studies indicate that phosphorous containing argyrodites are inherently instable against lithium anodes shown by *in situ* XPS, molecular dynamic simulations and AC-impedance studies.[24-26] It could be shown that Li_6PS_5X brought in contact with lithium metal decomposes forming an interface of Li_3P, Li_2S and Li*X*. However, both $Li_{6.25}PTe_{0.125}S_{5.125}Cl_{0.75}$ and $Li_{7.25}Si_{0.25}P_{0.75}S_6$ have been cycled in symmetric Li|SE|Li cells without any sign of degradations, as would be indicated by increased overpotentials.[18, 23]

5.1.4 $LiS_{0.5}$-ZnS-SiS_2 phase field

Materials which are investigated in relation to solid electrolytes are judged by two main criteria: conductivity and stability against lithium anodes. Additional parameters are toxicity, costs and processability. The stability of solid electrolytes against lithium anodes is one of the key limitations of the best materials $Li_{10}GeP_2S_{12}$ or Li_6PS_5X (*X*= Cl, Br, I). It is challenging to find new materials in multi-dimensional phase fields and almost impossible to predict the conductivity of undiscovered materials. But the red-ox stability of materials can be assessed by chemical knowledge and experience (*e.g.* $Li_{4.4}Al_{0.4}Ge_{0.6}S_4$ is more stable against lithium metal than $Li_{4.4}In_{0.4}Sn_{0.6}S_4$, as the larger homologues are more easily reduced, Chapter 5). Therefore, this project aimed to discover new lithium conducting materials in phase fields which could to result in materials with enhanced red-ox stability. The $LiS_{0.5}$-ZnS-SiS_2 phase field was chosen as a starting point due to the electrochemical stability of ZnS and SiS_2. The only reported compound in the $LiS_{0.5}$-ZnS-SiS_2 phase field is Li_2ZnSiS_4, which was crystallographically characterised and studied in respect to its optical properties.[27]

5.2 Experimental

General procedure. All sample handling was carried out in a He filled dry (O_2 < 3 ppm). Compositions were mixed in the appropriate stoichiometric ratio (typically in 300 mg batches), ground thoroughly and sealed as powders in evacuated carbon-coated quartz tubes under a pressure of 1 x 10^{-4} mbar. All first firing of the reactions were heated to 673 K at a rate of 5 K min^{-1}, then slowly taken to the final temperature at a rate of 0.5 K min^{-1}, held at the temperature and subsequently cooled to ambient temperature at a rate of 5 k min^{-1}. Lithium sulphide (Li_2S, Sigma Aldrich, 99.98 %), zinc sulfide (ZnS, Sigma Aldrich, 99.99 %), magnesium powder (Mg, Alfa Aesar, ~325 mesh, 99.8 %), silicon powder (Si, Alfa Aesar, ~325 mesh, 99.5 %), aluminium sulphide (Al_2S_3, Sigma Aldrich, 98 %), phosphorous pentasulphide (P_4S_{10}, Sigma Aldrich, 99 %), elemental sulphur (S, Sigma Aldrich, 99.999 %), lithium chloride (LiCl, Sigma Aldrich, 99.99 %) and lithium bromide (LiBr, Alfa Aesar, ultra-dry, 99.998 %) were used as provided. The commercially available lithium iodide (LiI, Sigma Aldrich, 99.9 %) was contaminated with hydrated LiI ·nH_2O. It was dried under reduced pressure at 573 K for 12h.

Exploratory synthesises in $LiS_{0.5}$-ZnS-SiS_2 phase field. For the initial exploration of phase formation in the $LiS_{0.5}$-ZnS-SiS_2 phase field, the reaction mixtures were subjected to a single firing to 973 K for 24 h.

Synthesis of $Li_{14}ZnSi_2S_{12}$. Stoichiometric reaction mixtures were fired to 973 K for 24 h, ground thoroughly and subjected to the same sealing-heating routine again.

$Li_{14}MgSi_2S_{12}$. It was necessary to add 5 mol % additional MgS to the initial composition ($Li_{14}Mg_{1.05}Si_2S_{12.05}$) to improve the purity of the product. The sample was subjected to two firings to 973 K for 24 h each.

Li_{12}*M*Si_2S_{12}*X*$_2$ (*M*= Zn, Mg; *X*= Cl, Br, I). Reaction mixtures were fired to 973 K for 10 h, ground thoroughly and subjected to the same sealing-heating routine again.

$^7Li_2S$. The synthesis of $^7Li_2S$ is described in Chapter 5.

$^7Li_{14}ZnSi_2S_{12}$. A sample of ^{7}Li enriched $^7Li_{14}ZnSi_2S_{12}$ was prepared for neutron powder diffraction experiments using $^7Li_2S$ as a reagent (batch size: 3 g). The sample was subjected to two firings to 973 K for 48 h each.

$^7Li_{14}MgSi_2S_{12}$. It was necessary to add 5 mol % additional MgS to the initial composition ($^7Li_{14}Mg_{1.05}Si_2S_{12.05}$) to improve the purity of the product. A sample of ^{7}Li enriched $^7Li_{14}MgSi_2S_{12}$ (batch size: 3 g) was prepared for neutron powder diffraction experiments using $^7Li_2S$ as a reagent. The sample was subjected to two firings to 973 K for 24 h each.

X-ray powder experiments. PXRD and SXRD experiments were carried out on samples which were sealed in borosilicate glass capillaries. Phase identification was carried out using a Bruker D8 diffractometer with a monochromated Cu source ($K\alpha_1$, λ= 1.5406 Å) or Mo source ($K\alpha_1$, λ= 0.9073 Å) in Debye-Scherrer geometry. Structure determination and Rietveld refinements were carried out on SXRD data collected from spinning capillaries (0.3 mm diameter) at the I11 beamline (Diamond Light Source, UK) with an incident wavelength of λ= 0.824878(10) Å. Variable-temperature SXRD experiments from ambient temperature to 448 K in 25 K intervals were carried out at I11 using an Oxford Cryostream Plus with the Mythen position sensitive detector (PSD).

Neutron powder diffraction experiments. Time-of flight neutron powder diffraction (NPD) data were collected on $^{7}Li_{14}ZnSi_2S_{12}$ and $^{7}Li_{14}MgSi_2S_{12}$ using the POLARIS instrument (ISIS, UK) both at ambient temperature and 448 K. Samples were contained in thin-walled vanadium cans (diameter: 6 mm) and sealed with a cupper gasket under 1 atmosphere of helium gas.

AC-impedance. Temperature dependent AC-impedance measurements were carried out on cold pressed pellets, which were sputtered with gold. The samples were heated and cooled in a glove box with argon atmosphere at rate of 3 K min^{-1} from 303 K to 503 K. Measurements were taken every 20 K with 10 min to equilibrate at each target temperature. Impedance data was recorded using the Keysight Impedance Analyzer E4990A setup. A sinusoidal amplitude of 50 mV was employed in the frequency range 100 MHz to 100 mHz.

Electrochemical cycling. The stabilities of $Li_{14}MSi_2S_{12}$ (*M*= Zn^{2+}, Mg^{2+}) were tested against lithium metal electrodes. Symmetric Li|SE|Li cells were assembled in Swagelok-type cells using pellets of the respective solid electrolytes. Cells were prepared and sealed inside an Ar-filled glovebox (O_2; H_2O < 0.1 ppm). Two lithium metal disk electrodes (12 mm diameter) were punched from Li ribbon (0.38 mm thickness, Sigma Aldrich) and then mechanically pressed onto a sintered SE pellet. The sealed cells were allowed to equilibrate at 323 K for 30 minutes in order to increase lithium mobility. The symmetrical cells were then cycled galvanostatically, using a VSP potentiostat/galvanostat (Biologic Science Instruments) for plating and stripping cycles (*J*= ± 0.01 mA cm^{-2} for 1 h per half-cycle).

DC polarization experiment. DC polarization experiments were conducted on pellets of $Li_{14}MSi_2S_{12}$ (*M*= Zn^{2+}, Mg^{2+}), which were sputtered with a gold electrode. Voltages of 0.05 V, 0.1 V, 0.5 V and 1.0 V were applied and the currents were recorded for 120 min each using an Autolab 84515 instrument.

DSC. DSC measurements were performed using on samples (~ 20 mg) sealed air-tight in a Ni/Cr crucible using a Netzsch DSC 404 F1 instrument according to the following temperature profile:

$$303\ K \rightarrow 773\ K\ (\text{heating rate: } 1\ \text{K min}^{-1}) \quad (1)$$

$$773\ K \rightarrow 773\ K\ (20\ \text{min}) \quad (2)$$

$$773\ K \rightarrow 303\ K\ (\text{cooling rate: } 1\ \text{K min}^{-1}) \quad (3)$$

The measurement was carried out twice on each sample.

Raman spectroscopy. Raman spectra were measured on samples sealed under helium in boron silicate capillaries (r= 0.5 mm) using an inVia™ Qontor® confocal Raman microscope with a laser wavelength λ= 523/785 nm.

5.3 Results/discussion

5.3.1 Exploration of the pseudo ternary $LiS_{0.5}$-ZnS-SiS_2 phase field

The $LiS_{0.5}$-ZnS-SiS_2 phase field was investigated systematically, as shown in Figure 82. Li_4SiS_4, Li_2ZnSiS_4 and an imaginary "Li_6ZnS_4" composition were chosen as endmembers of potential solid solutions. Compositions along $Li_{4+2x}Zn_xSi_{1-x}S_4$, $Li_{4-2x}Zn_xSi_{1-x}S_4$, $Li_{2+4x}ZnSi_{1-x}S_4$ solid solutions and additional compositions to evenly cover the phase field were synthesised. PXRD patterns were recorded and matched carefully against known phases.

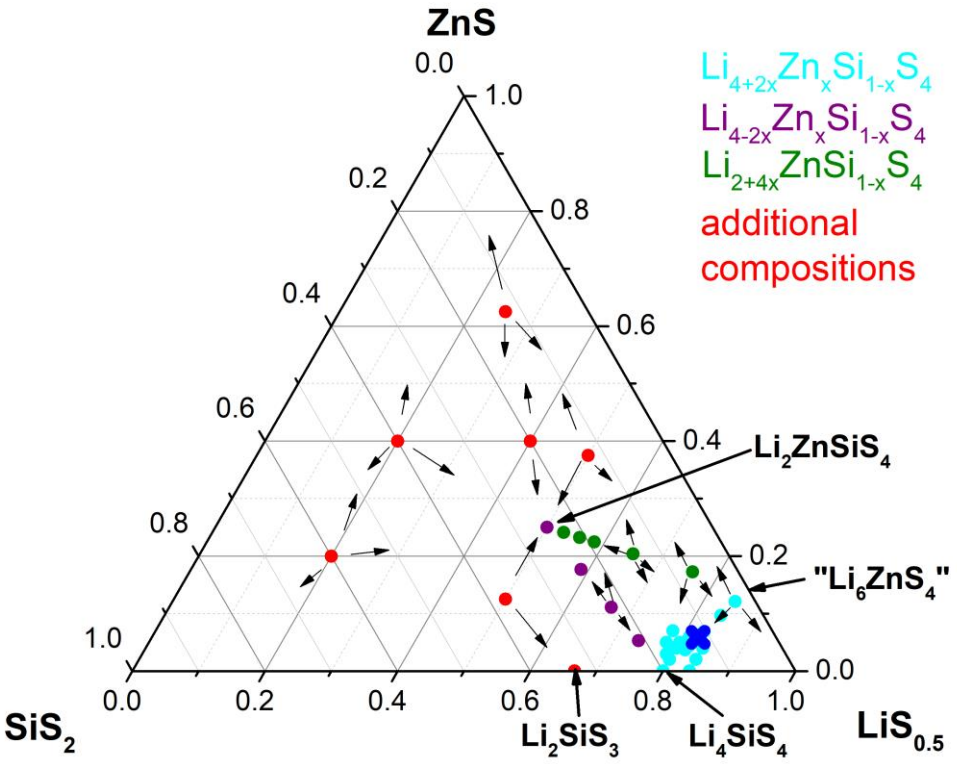

Figure 82: Explored pseudo ternary $LiS_{0.5}$-ZnS-SiS_2 phase field. Different colours of the compositions indicate along which imaginary tie-line compositions were synthesised (cyan: $Li_{4+2x}Zn_xSi_{1-x}S_4$, pink: $Li_{4-2x}Zn_xSi_{1-x}S_4$, green: $Li_{2+4x}ZnSi_{1-x}S_4$, red: additional compositions to cover the phase field); the small arrows indicate which sulphide phases could be detected in the respective PXRD pattern. The dark blue cross gives the position of the new $Li_{14}ZnSi_2S_{12}$ phase.

The arrows in Figure 82 point towards the known phases which the obtained PXRD patterns could be indexed to. Most reaction mixtures formed binary sulphides and Li_2ZnSiS_4 while the compositions along the tie line $Li_{4-2x}Zn_xSi_{1-x}S_4$ formed the endmembers Li_4SiS_4 and Li_2ZnSiS_4 with no evidence of a solid solution between those. All compositions close to the imaginary "Li_6ZnS_4" compound yielded Li_2S, Li_4SiS_4 and ZnS. The composition $Li_{4.4}Zn_{0.2}Si_{0.8}S_4$ (close to the blue cross) along the tie-line $Li_{4+2x}Zn_xSi_{1-x}S_4$ (cyan) showed a significant set of new reflection. This set of reflections could also be detected in $Li_{4.8}Zn_{0.4}Si_{0.6}S_4$, but with significantly lower

intensity. The composition was varied to optimise the composition by synthesising targets around the two initial hits in a circular way (Figure 83(a)). But changes in the PXRD patterns could not be understood according to changes in the reaction compositions. Key to understanding the PXRD patterns of the products and to identify the stoichiometry of the new phase was to refire all materials. Mixtures, which had not shown the new set of reflections after the first firing, exhibited them strongly after the second firing (*e.g.* $Li_{4.267}Zn_{0.267}Si_{0.733}S_4$). A close up of surrounding compositions and exemplary PXRD patterns after the 2nd firing is shown in Figure 83(b). PXRD patterns of the compositions I, II and III show the presence of the new phase but significant by-products (Li_2S and Li_4SiS_4) are detected in the respective PXRD patterns. Only the reaction of stoichiometric $Li_{14}ZnSi_2S_{12}$ resulted in a reaction product in which neither Li_2S nor Li_4SiS_4 could be detected by lab PXRD analysis.

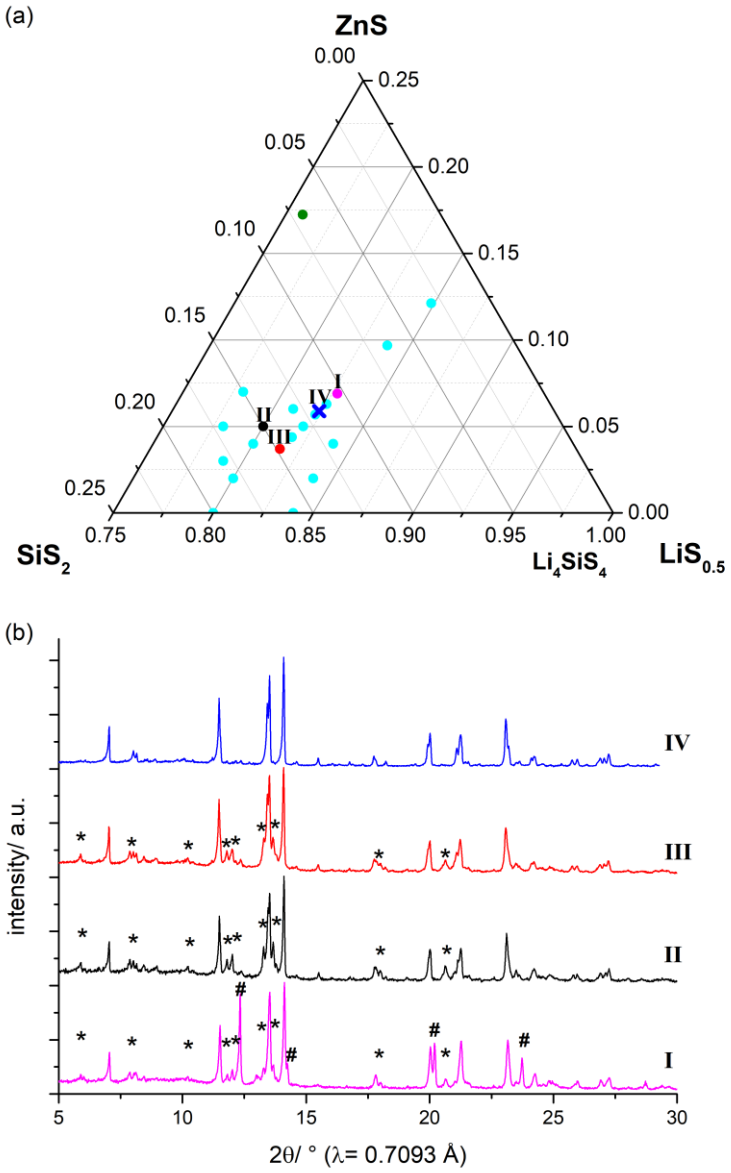

*Figure 83: (a) Close up of explored $LiS_{0.5}$-SiS_2-ZnS phase field with $Li_{12}ZnSi_2S_{12}$ shown as dark blue cross. PXRD patterns of selected compositions after the 2nd firing are shown in panel (b). Li_2S and Li_4SiS_4 are marked by # and * respectively.*

Temperature-dependent experiments showed that the new phase does not form at 873 K and 923 K even after repeated refiring, but only at a temperature of at least 973 K. The PXRD patterns of the corresponding reactions are shown in Figure 84.

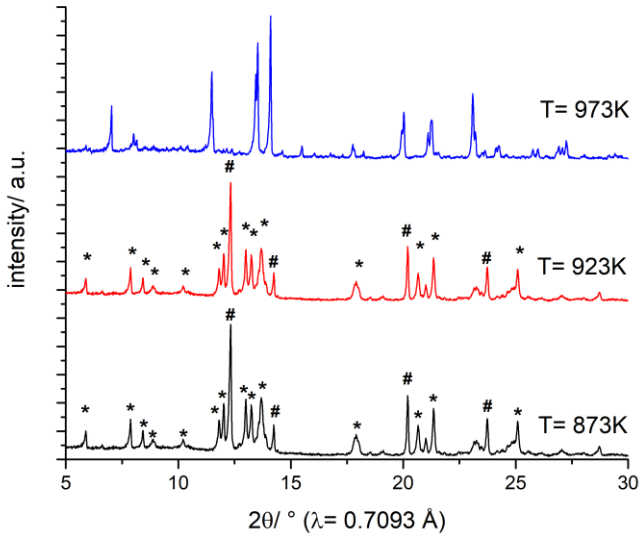

*Figure 84: PXRD patterns of temperature dependent experiments. The reactions fired to 873 K (black) and 923 K (red) resulted in a mixture of Li_2S (marked by #) and Li_4SiS_4 (marked by *). Increasing the temperature to 973 K (blue) resulted in the formation of the new phase.*

5.3.1.1 Indexing of $Li_{14}ZnSi_2S_{12}$

Indexing of unit cell of the new $Li_{14}ZnSi_2S_{12}$ phase was carried out on SXRD data. Minor reflections stemming from Li_2S and Li_4SiS_4 were identified in the SXRD pattern and excluded from the reflection list. Using the Dicvol06 program[28] as implemented in FullProf suite,[29] the remaining reflections could be indexed to the tetragonal $I\bar{4}m2$ space group with the lattice parameters *a*= 21.1506(2) Å and *c*= 10.0564(2) Å. A Pawley fit of $Li_{14}ZnSi_2S_{12}$ to the tetragonal $I\bar{4}m2$ space group is depicted in Figure 85. No reflections remain unindexed and only a few reflections have zero or very low intensity.

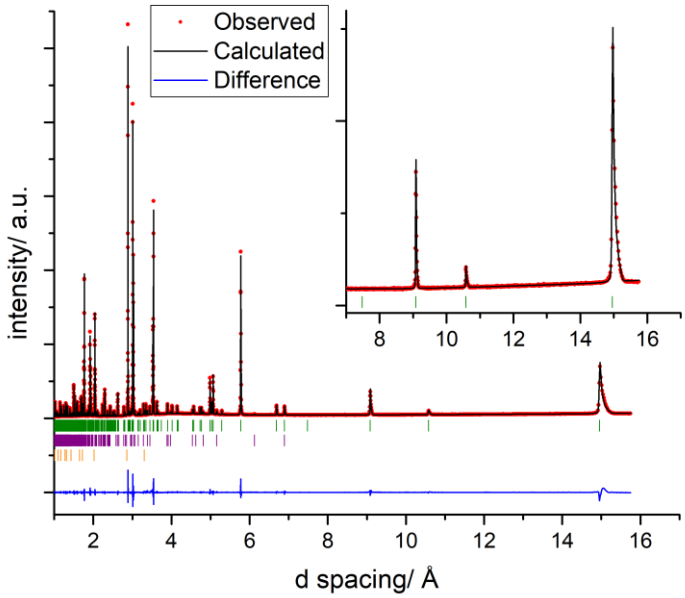

Figure 85: Pawley fit of $Li_{14}ZnSi_2S_{12}$ in the tetragonal $I\bar{4}m2$ space group (a= 21.1506(2) Å and c= 10.0564(2) Å) against SXRD data (I11 beamline, MAC detector, λ= 0.82526 Å, ambient temperature). The positions of calculated Bragg reflections are shown by tick marks (green: $Li_{14}ZnSi_2S_{12}$, purple: Li_4SiS_4, orange: Li_2S).

5.3.1.2 Partial crystal structure solution of the S^{2-} sublattice

The structure of $Li_{14}ZnSi_2S_{14}$ was partially solved using charge flipping as implemented in Jana2006[30]. The sulphur sublattice could be established, as shown in Figure 86(b). 108 S atoms on 12 different crystallographic sites were identified. Each unit cell contains 9 formula units of $Li_{14}ZnSi_2S_{12}$, giving an overall atom count of $Li_{126}Zn_9Si_{18}S_{108}$ per unit cell. Dr John B. Claridge related the S^{2-} sublattice to packing of the metal atoms in the Laves phase Cu_2Mg by group-supergroup relationships using the PSEUDO[31] program as implemented on the Bilbao Crystallographic server.[32] The resulting group-supergroup relationships are shown in Figure 86(b). Interestingly the cubic argyrodites are a subgroup of the Laves phase and a supergroup of $Li_{14}ZnSi_2S_{12}$.

For comparison, the anion sublattice of a cubic HT argyrodite was subjected to the symmetry transformations given in Figure 86(b). The resultant anion sublattice is shown in Figure 86(c). Visual inspection of the model obtained form charge flipping and the model of the symmetry reduced argyrodite framework indicates close structural relationship.

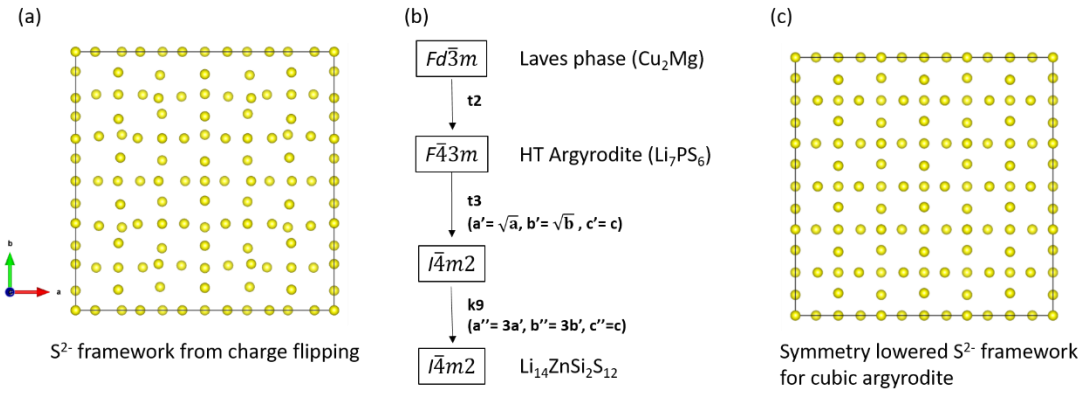

Figure 86: (a) S^{2-} framework of $Li_{14}ZnSi_2S_{12}$ as established by charge flipping (b) group-subgroup graph connecting the Laves phase ($Fd\bar{3}m$) with $Li_{14}ZnSi_2S_{12}$ ($I\bar{4}m2$) via the argyrodite structure ($F\bar{4}3m$). (c) S^{2-} framework resulting from symmetry lowering via group-subgroup relationships starting from cubic argyrodite.

The group-supergroup relation of the S^{2-} framework to the HT argyrodites phase shows that $Li_{14}ZnSi_2S_{12}$ might be a low temperature (LT) argyrodite. This would render it a unique argyrodite polymorph, as no LT argyrodites crystallising in $I\bar{4}m2$ are reported. The unusually large lattice parameter of a_{tet}= 21.1506(2) Å can be related to the lattice parameter of cubic Li_7PS_6 (a_c= 9.9926(12) Å)[12] argyrodite *via* the following unit cell transformation:

$$a_c = \frac{a_{tet}}{3} \cdot \sqrt{2} \qquad (4)$$

The unit cell transformation from the cubic face centred cell into the body centred cell involves division of *a* and *b* by $\sqrt{2}$ and results in halving the unit cell volume. The second step is expanding the *a* and *b* axis by a factor of 3 according to the above described relationship. The resultant unit cell has a 4.5-fold increased unit cell volume, compared to the cubic argyrodite aristotype.

The metal positions could not be unequivocally determined by refinement of SXRD and NPD data, as the refinement of the occupancies did not converge to a stable model.

5.3.1.3 ICP – compositional analysis

As the crystal structure solution did not progress, the overall composition of the new phase had to be confirmed. Chemical reactions between the reaction mixture and the quartz glass could not be ruled out at 973 K, which might result in loss of reagents. Thiosilicates are notoriously difficult to digest and therefore a single sample was sent away to Mikroanalytisches Labor Pascher for compositional analysis. The result is summarised in Table 25. The normalised composition of $Li_{14.00}Zn_{0.93}Si_{2.11}S_{11.89}$ is in reasonable agreement with the nominal composition.

Table 25: Result of the compositional analysis of $Li_{14}ZnSi_2S_{12}$.

element	Calculated ($Li_{14}ZnSi_2S_{12}$)/ wt %	Measured/ wt %	Normalised composition
Li	16.1	15.9	14.00
Zn	10.83	10.0	0.93
Si	9.31	9.7	2.11
S	63.76	62.4	11.89

5.3.1.4 Raman spectrum of $Li_{14}ZnSi_2S_{12}$

The Raman spectrum of $Li_{14}ZnSi_2S_{12}$ was recorded by Dr Troy D. Manning and is shown in Figure 87 in comparison to the Raman spectrum of the argyrodite Cu_8SiS_6.[33]

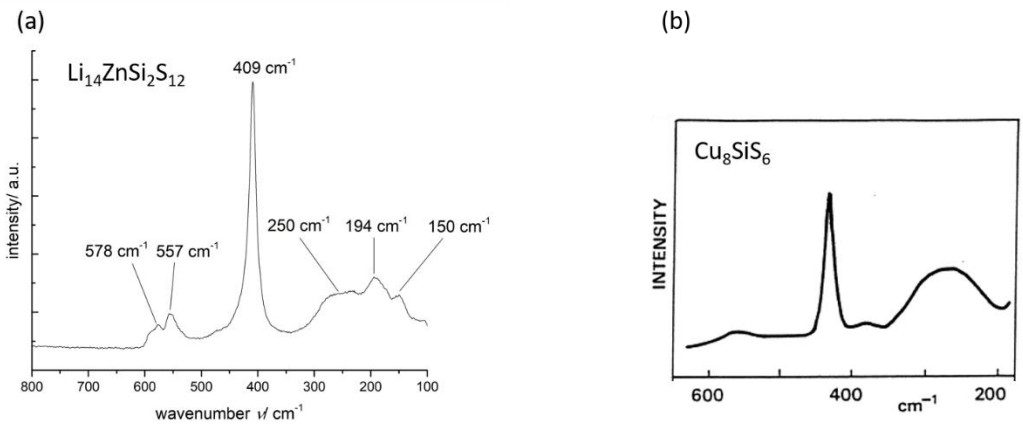

*Figure 87: (a) Raman spectrum of $Li_{14}ZnSi_2S_{12}$ (recorded by Dr Troy D. Manning). Raman spectrum of Cu_8SiS_8. From Solid State Ion. **1999,** 1, 11-18. Reprinted with permission from ScienceDirect.[33]*

Raman spectra of sulphide based argyrodites show characteristic resonance frequencies at ~600 cm^{-1}, a sharp peak at ~420 cm^{-1} and broad features at ~280 cm^{-1}, which are associated with the SiS_4^{4-} or PS_4^{3-} clusters.[33-35] Visual comparison to Cu_8SiS_6 and qualitative analysis of the $Li_{14}ZnSi_2S_{12}$ Raman spectrum reveals similar features. Broad features are found at 578 cm^{-1}, 557 cm^{-1} and 250 cm^{-1}, 194 cm^{-1}, 150 cm^{-1}, while a sharp peak is found at 409 cm^{-1}. As Raman spectroscopy is governed by symmetry considerations, it is likely that PS_4^{3-} units have been substituted for SiS_4^{4-} units which are symmetrically equivalent. This corroborates the idea that a lithium containing argyrodite analogue without phosphorous has formed.

5.3.1.5 DSC

DSC experiments were carried out to check for potential reversible phase transitions of the $Li_{14}ZnSi_2S_{12}$. If the material was an argyrodite related phase of low symmetry, one expects a transition into a high-symmetry cubic phase at elevated temperatures. The material was heated to 800 K and cooled to ambient temperature twice. During heating a clear

endothermic peak can be detected at 411 K in Figure 88, and during cooling an exothermic process is happening at 405 K. The reversibility of those two processes is proven by the well matching second heating-cooling cycle which does not display major peak shift or flattening.

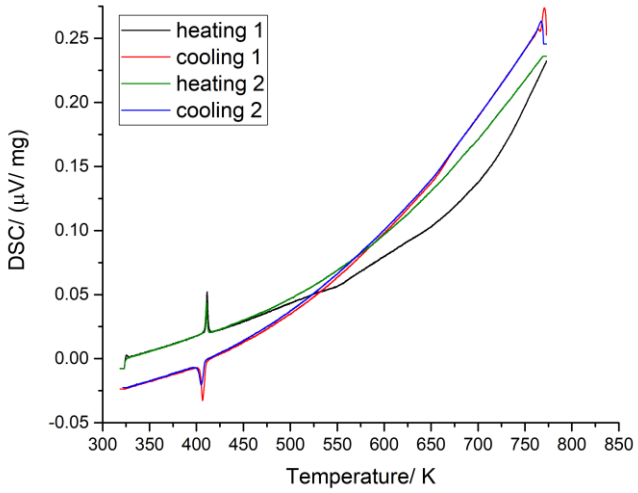

Figure 88: Differential scanning calorimetry curve of $Li_{14}ZnSi_2S_{12}$ from ambient temperature to 773 K. The two processes at ~ 370 K correspond to a reversible phase transition.

5.3.1.6 Variable temperature SXRD experiment

Variable temperature X-ray diffraction experiments were carried out to investigate the nature of the reversible phase transition observed at 410 K in DSC measurements. SXRD patterns were recorded at the Diamond Light Source facility, UK, from ambient temperature to 448 K in 25 K intervals. Figure 89(a) shows an overview of all patterns, while part (b) highlights 2θ ranges which are indicative for the changes happening. At 323 K the (011) reflection is clearly visible at 2θ= 3.2°, gradually diminishes as the sample is heated and fully vanishes at 423 K. Upon cooling the (011) reflection starts to emerge again at a temperature of 398 K. A similar temperature dependent behaviour can be detected for the reflections 2θ= 15.2 °, as two reflections converge upon heating and split during the cooling process. The transitions observed on heating and cooling correlate well with the transition temperatures determined through DSC experiments.

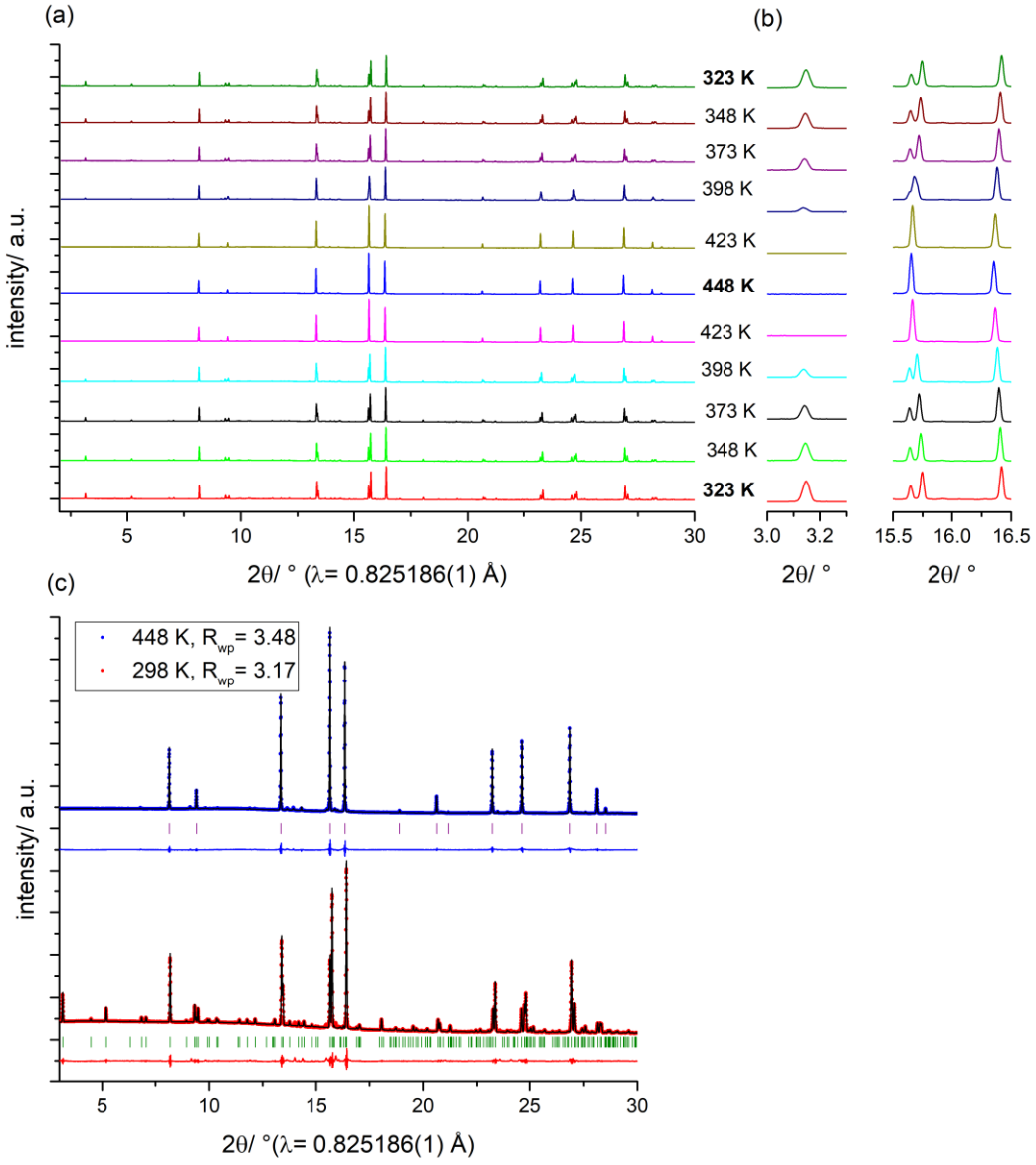

Figure 89: (a) Temperature dependent SXRD experiment measured on $Li_{14}ZnSi_2S_{12}$ in the range of 323 K and 448 K in 25 K intervals. A reversible phase transition from tetragonal to cubic is detectable at T~ 423 K during heating and cooling. (b) Zoom into region around 2θ= 3 ° and 2θ= 16.0 °. (c) Pawley plot of $Li_{14}ZnSi_2S_{12}$ at 298 K (red) and 448 K (blue). The low temperature phase is fitted to a tetragonal unit cell (green tick marks, space group: $I\bar{4}m2$, a= 21.149(1) Å, c= 10.059(1) Å). The high temperature phase is fitted to a cubic unit cell (purple tick marks, space group: $F\bar{4}3m$, a= 10.0440(1) Å). The tick marks for the impurity phases (Li_4SiS_4 and Li_2S) are omitted for reasons of clarity.

The high temperature phase could be indexed to the cubic space group $F\bar{4}3m$, which matches the high temperature symmetry of many known argyrodites. Figure 89(c) shows Pawley fits of $Li_{14}ZnSi_2S_{12}$ at 298 K and 448 K respectively. The room temperature data is fitted to the tetragonal $I\bar{4}m2$ space group with *a*= 21.149(1) Å and *c*= 10.059(1) Å; the high temperature phase is fitted to the cubic space group $F\bar{4}3m$, *a*= 10.0440(1) Å. These findings show that $Li_{14}ZnSi_2S_{12}$ crystallises in a lower symmetry argyrodite related crystal structure at room temperature and transitions into the cubic argyrodite phase at high temperatures.

Further quantitative analysis was performed by fitting the refining unit cells by Pawley fits. For comparability all lattice parameters of low temperature tetragonal cells are adapted according to the unit cell transformation necessary to convert from a *F*-centred cubic cell into the enlarged *I*-centred tetragonal cell as stated in Figure 86: $a = a'/3*1.414$, $c = c'$. The results are plotted in Figure 90 (a)-(d).

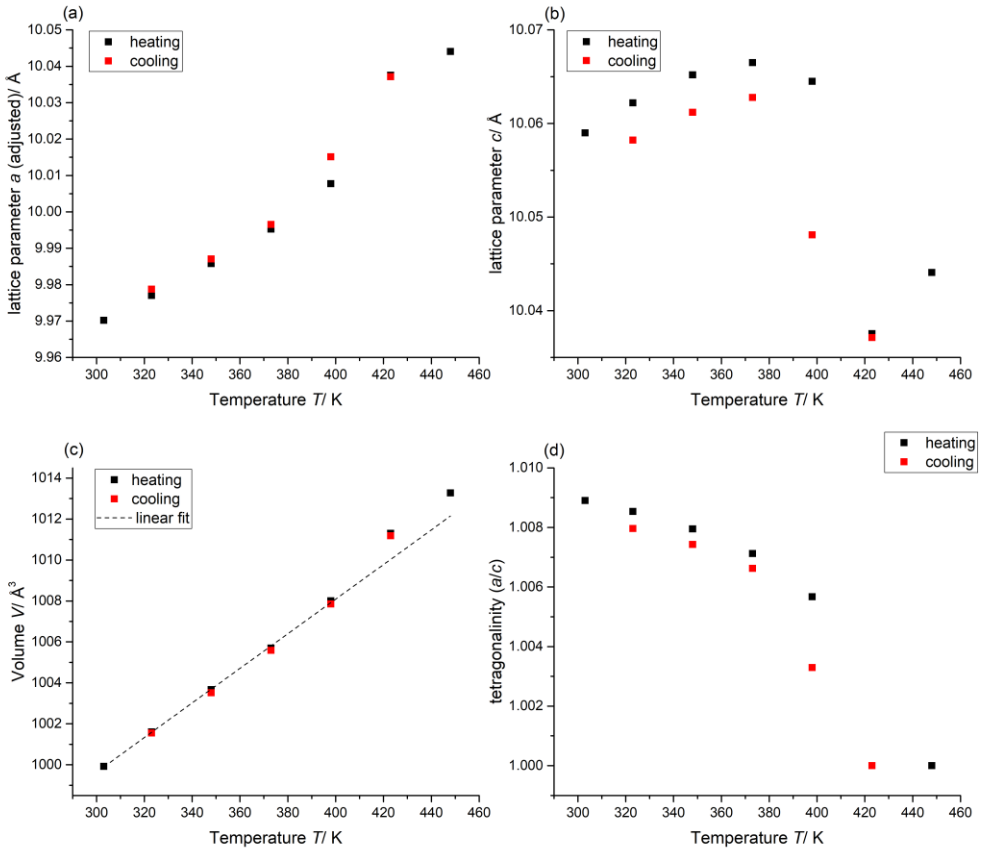

Figure 90: Graphical analysis of parameters extracted from Pawley fits of the T-dependent SXRD experiment for $Li_{14}ZnSi_2S_{12}$: (a) change of lattice parameter a (b) change of lattice parameter c (c) change of the unit cell Volume V (d) change of tetragonalinity a/c.

At low temperatures the lattice parameters *a* and *c* increase linearly with increasing temperature. Close to the temperature of phase transition T_{trans} a non-linear behaviour is detected for both *a* and *c*. In particular *c* shows abnormal behaviour as it decreases with increasing *T* between 380 K and 440 K. During cooling small hysteresis is visible in the lattice parameter *c*. Further high temperature data points would be needed to investigate the continued expansion of *a* and *c* with temperature. Figure 90(c) shows the change of the adapted unit cell volume *V* with temperature. Initially the unit cell expands linearly as indicated by the linear fit. The phase transition leads to a discontinuity which can be related to the increased expansion along *a*. The tetragonalinity *c*/*a* is plotted in panel (d). With

increasing temperature, the tetragonal distortion of the cell decreases until a fully unit cell is obtained at the transition temperature T_{trans}.

5.3.1.7 High temperature crystal structure of $Li_{14}ZnSi_2S_{12}$

$Li_{14}ZnSi_2S_{12}$ crystallises at elevated temperature in higher symmetry and in a smaller unit cell compared to the low temperature polymorph. Structural refinement of the HT phase is simplified as the number of free parameters is reduced. An initial structural model could be developed using SXRD data only. The sulphur sublattice was established by the charge flipping method. Three crystallographically independent S atoms form an arrangement equivalent to the anion sublattice in cubic Li_7PS_6. Fourier difference maps were then calculated to determine the positions of the metal sites. Strong scattering intensity, which was related to the silicon positions, was found in the both 4*b* and 4*c* site. The occupation of both sites deviates from the canonical argyrodite structure but is physically feasible. In cubic argyrodites only the 4*b* are occupied with the heavy cations *M* while the 4*c* site remains vacant. Additional scattering density was found on the 48*h* and 24*g* sites, which were associated with the mobile cations lithium and zinc. Eventually two different models were refined as far as possible, which are different in respect to the silicon ordering:

(a) Silicon atoms fully occupy the 4*b* site (equivalent to P^{5+} in Li_7PS_6), while lithium and zinc are disordered on the same 48*h* site. The 24*g* refined to a small occupation of 0.069(6) lithium. This refinement resulted in a R_{wp} of 3.57. Analysis of Fourier difference maps did not indicate the presence of further occupied crystallographic positions.

(b) Silicon atoms occupy the 4*b* site with an occupancy of 0.5 and half the tetrahedral sites (4*c*) connecting the 4*b* sites, forming a three dimensional network. Two different sites (48*h* and 24*g*) are occupied by disordered Li and zinc. This refinement resulted in a R_{wp} of 4.79.

The S^{2-} and Si^{4+} arrangements for the two different models are shown in Figure 91(a)-(d) together with the corresponding Rietveld models (for clarity Lithium atoms are not included).

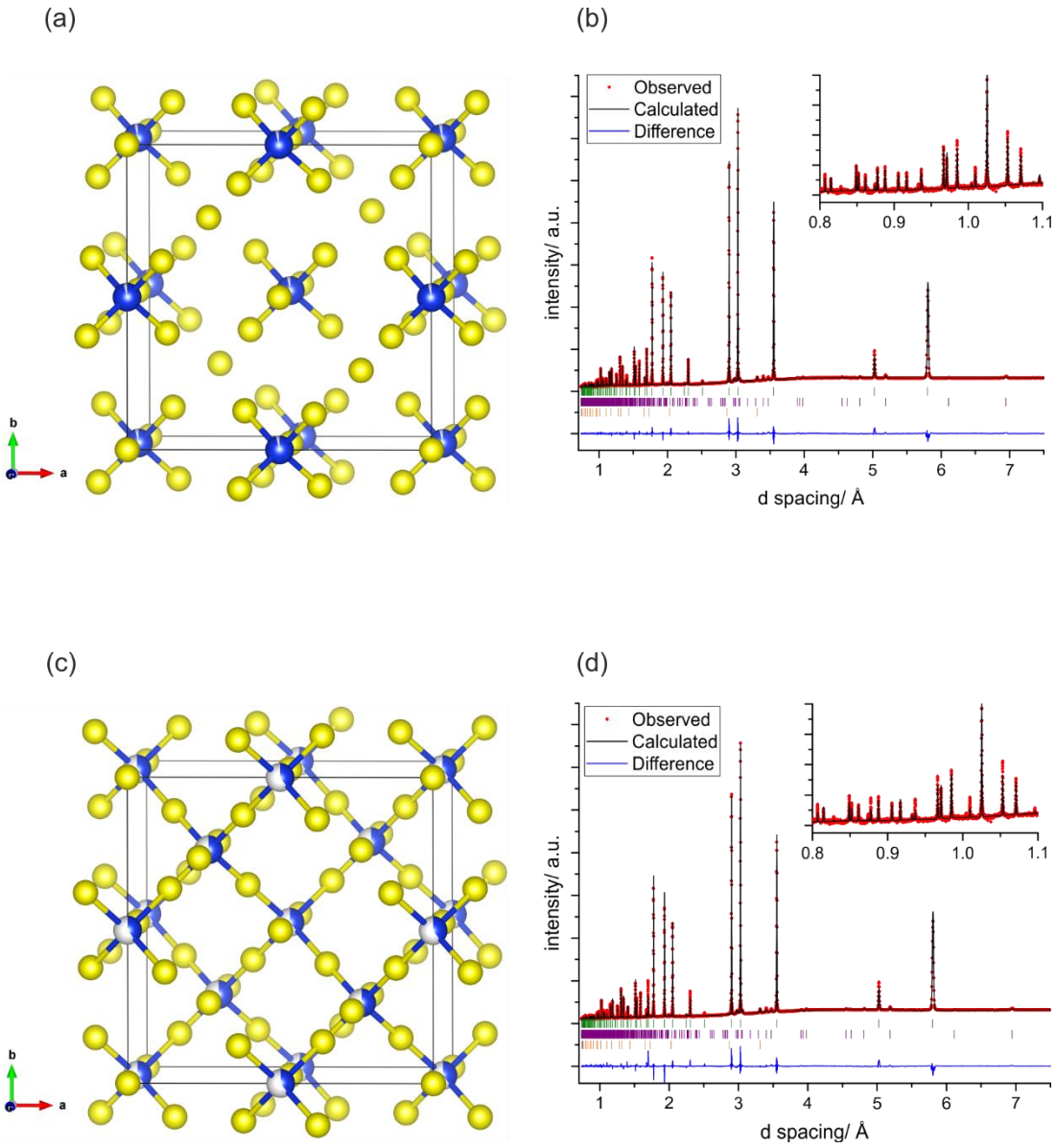

Figure 91: Two different structural models and Rietveld fits of $Li_{14}ZnSi_2S_{12}$ against SXRD data at 448 K (for clarity lithium atoms are not depicted). The positions of calculated Bragg reflections are shown by tick marks (green: $Li_{14}ZnSi_2S_{12}$; purple: Li_4SiS_4; orange: Li_2S). (a) model a: full silicon occupation on the 4b site. (b) Rietveld fit corresponding to model a. (c) model b: occupation of the 4b and 4c with 0.5 silicon. (d) Rietveld fit corresponding to model b.

Refinement (a) resulted in a significantly lower R_{wp} of 3.57 compared to model (b) (R_{wp}= 4.79). The analogy of model (a) to the Li_7PS_6 argyrodite is apparent, corroborating that this is the correct structure. In refinement (b) the silicon occupancies of both sites never refined to or close to zero. This demonstrates that the choice of starting conditions is crucial for Rietveld refinement. If they are not close enough to the real structure, Rietveld refinements can converge into local minima.

To eliminate any biased decisions made by the crystallographer, a second *ab initio* algorithm was employed to solve the HT crystal structure. The direct method algorithm as

implemented in EXPO2014[36] was used to solve the structure from SXRD data. This resulted in the structure given in Figure 92 which is equivalent to solution (a).

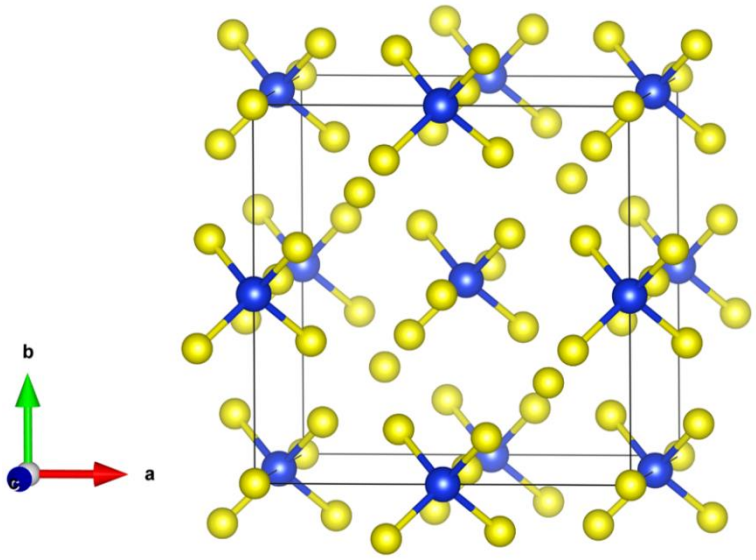

Figure 92: Si/S framework as calculated from SXRD data only using EXPO2014.

Based on the analysis of SXRD data the structure of the HT polymorph $Li_{14}ZnSi_2S_{12}$ is a canonical argyrodite: S^{2-} anions form a tetragonal packing, Si^{4+} cations fully occupy the 4*b* site and the lithium cations are on the split 48*h* site and 24*g* site. The role of the zinc atoms remained unclear and could not be unequivocally be solved by SXRD analysis alone. It was assumed that zinc is disordered on the 48*h* site together with lithium, which was corroborated by finding higher electron density than expected for 28 lithium atoms alone. The ionic radii of Li^+ and Zn^{2+} are almost identical in tetrahedral coordination: 0.59 Å vs 0.60 Å respectively.[37] The mixing of different mobile cations on the *L*-site had been reported before in the argyrodites $(Cu_{1.5}In_{1.5})PS_5Br$ and $(Cu_{1.5}In_{1.5})PS_5I$.[5] But occupation of only the 48*h* and the face-sharing 24*g* sites by Li^+ and Zn^{2+} would result in total occupation of > 1 for each combined double tetrahedron. This is unphysical due to the short interatomic distances between the cations (1.936 Å) (compare to Figure 93(a)). In total 30 atoms (28 lithium + 2 zinc) must be accommodated on 28 double tetrahedra per unit cell. In Li_7PS_6 an occupation of 0.53 on the 48*h* site has been reported, showing the difficulty in modelling "smeared" crystallographic positions and the difficulty of finding all Li atoms based on SXRD data only.[12]

The full preliminary crystallographic model is shown in Figure 93(b), further crystallographic data is given in the appendix Table 36.

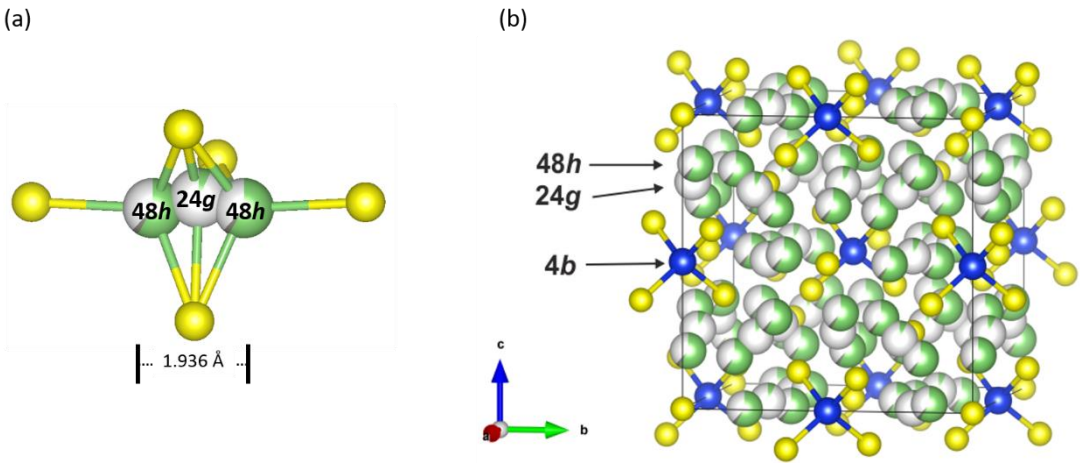

Figure 93: (a) Occupation of a double tetrahedron by more than one cation: this results in unphysical short cation-cation distances. (b)Preliminary model of high temperature cubic $Li_{14}ZnSi_2S_{12}$, based on the analysis of SXRD data only (T= 448 K) (yellow: sulphur, blue: silicon, grey: zinc, green: lithium).

To unequivocally establish the crystallographic structure of HT-$Li_{14}ZnSi_2S_{12}$ NPD data was collected at 448 K. Pawley fits of the cubic unit cell (space group $F\bar{4}3m$, *a*= 10.0440(1) Å) against individual NPD banks are shown in Figure 94. Small reflections were indexed to the vanadium canister and the two impurity phases Li_2S and Li_4SiS_4. Two reflections at *d*= 4.1 Å and 4.6 Å could not be assigned to any known phases.

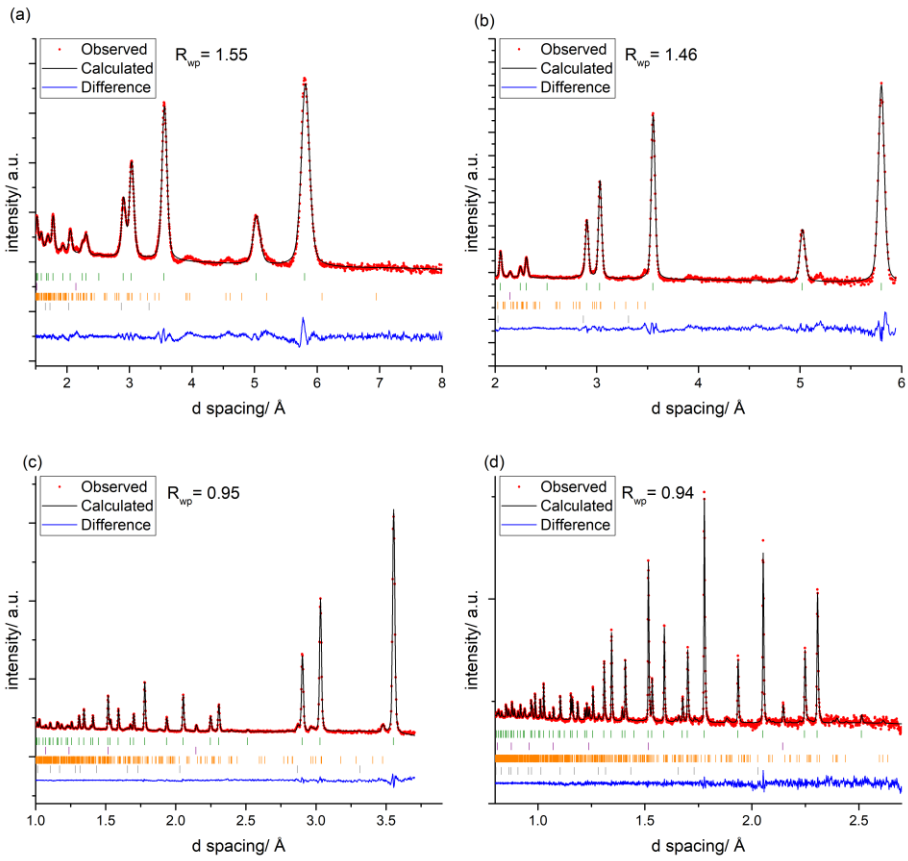

Figure 94: Pawley fits of the $Li_{14}ZnSi_2S_{12}$ in the cubic $F\bar{4}3m$ space group (a= 10.0440(1) Å) against NPD data: (a) bank 2, (b) bank 3, (c) bank 4, (d) bank5. The positions of calculated Bragg reflections are shown by tick marks (green: HT $Li_{14}ZnSi_2S_{12}$, purple: V, orange: Li_4SiS_4, grey: Li_2S).

The preliminary SXRD model was used as a starting point for Rietveld refinements. Major discrepancies between the model and the observed NPD data indicated that the SXRD model had severe shortcomings. The Fourier difference map (FDM) of the preliminary SXRD model against NPD data (bank 5) was calculated and is shown in Figure 95. Analysis of the FDM identified an additional site of negative scattering density on the crystallographic 16*e* site. ^{7}Li has a negative coherent scattering length of -2.22 while all the other elements in the material have positive scattering lengths.[38] Therefore this initially vacant site was associated with an additional Li site.

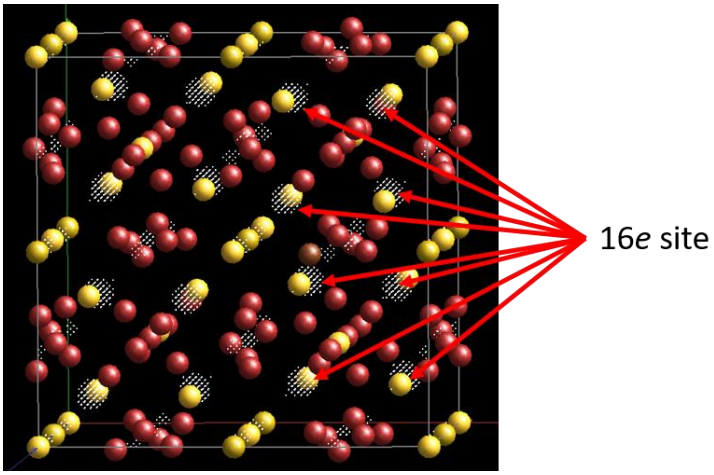

Figure 95: Fourier difference map of the preliminary SXRD model against NPD data (bank 5). Negative scattering density is indicated by white clouds. Due to the negative coherent scattering length of Li these can be associated with Li positions (yellow: sulphur and silicon, red: lithium, white: negative scattering density).

The occupation of an additional tetrahedral site on the 16*e* site has previously been reported only in the cation rich $Li_{6.15}Al_{0.15}Si_{1.35}S_6$ argyrodite.[11] This site corresponds to a tetrahedron of type 4 according to the classification of Zahn *et al.* (compare to Table 24). It shares three corners with PS_4 units and is energetically most favourable after full occupation of the 48*h* site of type 5.[8] The coordination environment of the identified 16*e* site and connectivity to the PS_4 units are shown in Figure 96.

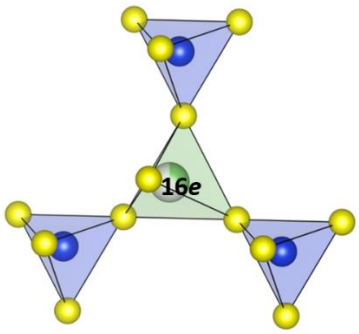

Figure 96: Coordination environment of new 16e site.

Combined analysis of SXRD and NPD data showed that the zinc atom is only found in the 48*h* site, as the zinc occupation refined to 0 on the 24*g* and the 16*e* site.

The final crystallographic model was developed by refinement of the NPD data only. The overall composition was constrained to $Li_{14}ZnSi_2S_{12}$. The sulphur and silicon occupancies were set to 1. All zinc (2 atoms per unit cell) was fixed to the 48*h* site. Finally, the total lithium content was constrained to 28 lithium ions per unit cell and refined on the 48*h*, 24*g* and 16*e* sites. Fractional coordinates were refined for all crystallographic sites. The good quality of the high temperature NPD data enabled the refinement of anisotropic displacement

parameters for all crystallographic positions. Most crystallographic sites show well behaved anisotropic displacement parameters. Only the lithium on the 24*g* site had to be refined isotropically, as anisotropic refinement resulted in unphysical parameters. This might be due to the low occupancy of this site. The occupational refinement of the 48*h*, 24*g* and 16*e* sites showed that in combination the 48*h* and 24*g* sites are fully occupied by Li and Zn. All additional lithium is found on the 16*e* site. The distribution of the mobile cations *L* in HT $Li_{14}ZnSi_2S_{12}$ is summarised in Table 26.

Table 26: Distribution of the mobile cations L in HT $Li_{14}ZnSi_2S_{12}$.

	Li	Zn
48*h*	0.438(2)	1/24
24*g*	0.076(3)	0
16*e*	0.321(3)	0

The final model and corresponding NPD fits are shown in Figure 97. An overall R_{wp} value of 1.62 was achieved, further crystallographic information is given in the appendix in Table 37**.**

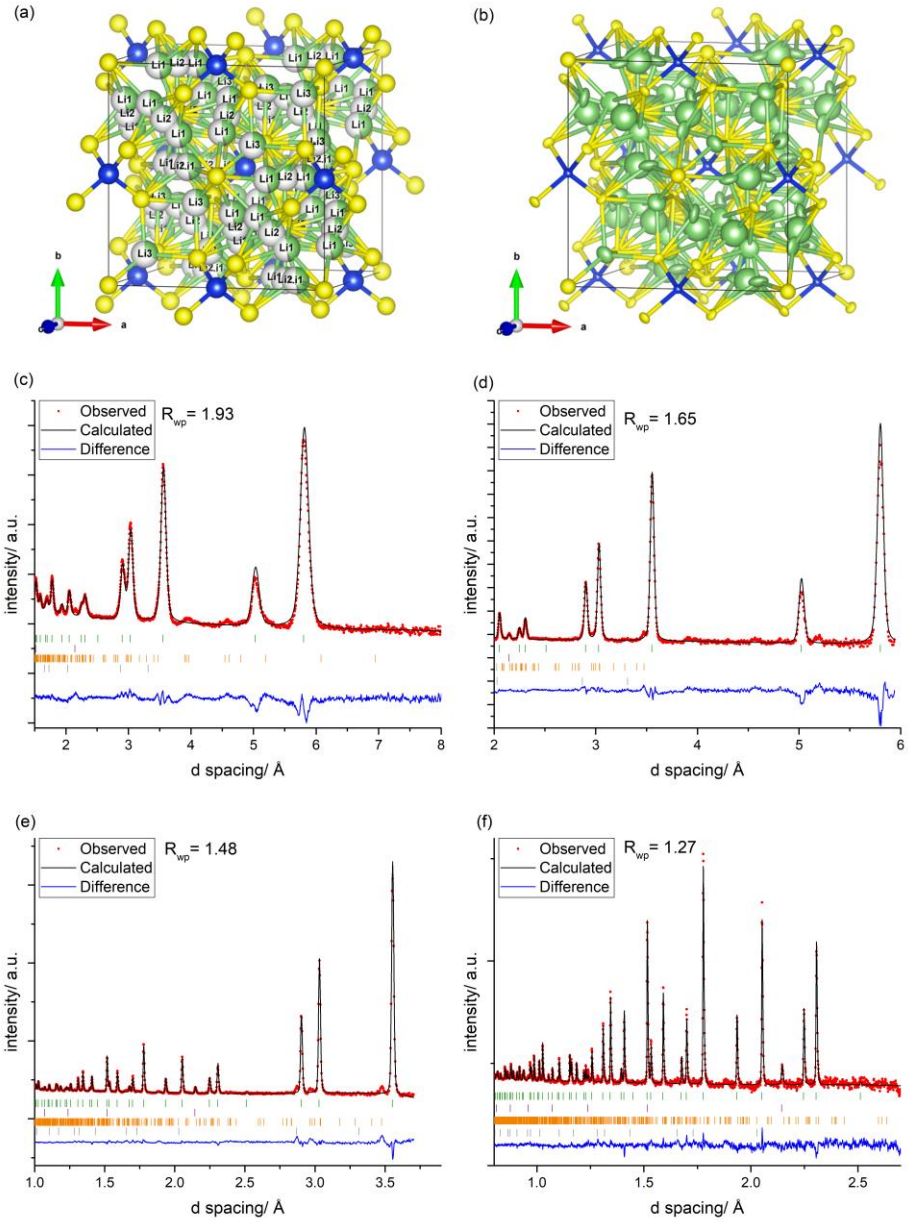

Figure 97: (a) Fully refined crystallographic model for HT $Li_{14}ZnSi_2S_{12}$.(b) Visualisation of the anisotropic displacement of the atoms in HT $Li_{14}ZnSi_2S_{12}$. (c) NPD fit bank 2, (b) NPD fit bank 3, (c) NPD fit bank 4, (d) NPD fit bank 5. The positions of calculated Bragg reflections are shown by tick marks (green: HT $Li_{14}ZnSi_2S_{12}$, purple: V, orange: Li_4SiS_4, grey: Li_2S) (yellow: sulphur, green: lithium, blue: silicon, grey: zinc).

Coordination environments for the individual cations in the final model are shown in Figure 98.

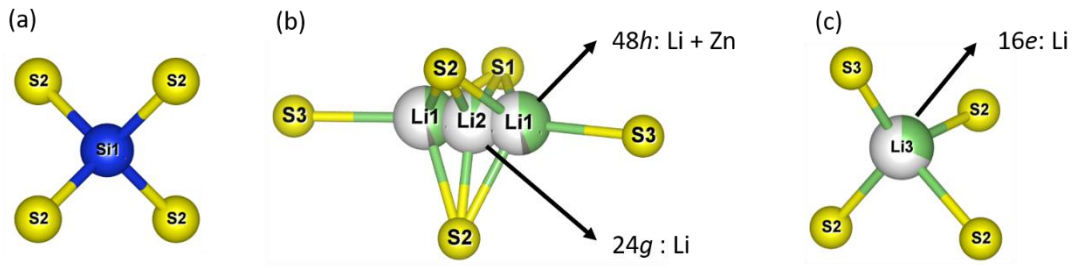

Figure 98: Coordination environments of the individual cations in HT-$Li_{14}ZnSi_2S_{12}$ (a): SiS_4 tetrahedron (4b site) (b): Li1 tetrahedron (48h site) and trigonal planar Li2 (24g site) (c): tetrahedral Li3 (16e site) (yellow: sulphur, green: lithium, blue: silicon, grey: zinc).

Individual bond distances of the cations are listed in Table 27 and compared to the crystal structure of Li_6PS_5I. All bond distances in $Li_{14}ZnSi_2S_{12}$ deviate by maximal 10 % from the equivalent distances in Li_6PS_5I.

Table 27: Bond distances of MS_x coordination environments of the cations in $Li_{14}ZnSi_2S_{12}$ at 448 K compared to bond distances in Li_6PS_5I.

	$Li_{14}ZnSi_2S_{12}$				**Li_6PS_5I**		
	Si	Li1/Zn1	Li2	Li3	P	Li1	Li2
S1	x	2.4566(5) Å	2.320(3) Å	x	x	2.358(4) Å	2.353(3) Å
S2	2.0934(5) Å	2.5345(5) Å	2.313(4) Å	2.4925(3) Å	2.0428(11) Å	2.491(4) Å	2.352(12) Å
S3/I	x	2.6083(5) Å	3.556(4) Å	2.2976(3) Å	x	2.944(4) Å	3.590(15) Å

5.3.1.8 Transport property measurements

Temperature dependent AC-impedance measurements were conducted to investigate the lithium conductivity of the new $Li_{14}ZnSi_2S_{12}$ phase. Measurements were taken every 20 K from 303 K to 503 K during heating and cooling. Two full temperature cycles were completed, so that in total 4 data points per temperature were recorded. The Nyquist plots of ambient temperature spectra comprise two elements: an arch at higher frequencies and a spike at low frequencies, which can be associated with the total conductivity σ and the solid electrolyte-electrode response respectively (compare Figure 99(a)). At ambient temperature a total conductivity of 2(1) x 10^{-7} S cm^{-1} is obtained for $Li_{14}ZnSi_2S_{12}$.

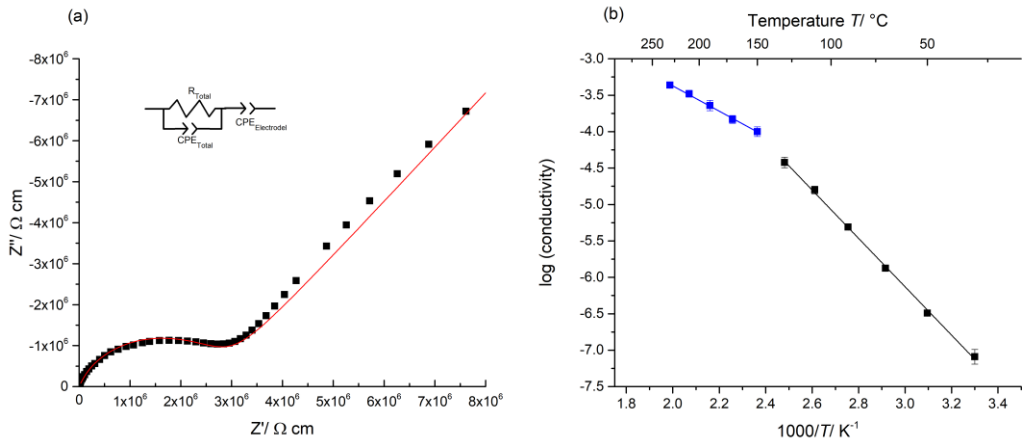

Figure 99: (a) AC-impedance spectrum of $Li_{14}ZnSi_2S_{12}$ (black) fitted to the model in the inset. (b) Arrhenius plot of the conductivity of $Li_{14}ZnSi_2S_{12}$. A low temperature region (black) can be distinguished from a high temperature region (blue).

Figure 99(b) displays the temperature dependent conductivities of $Li_{14}ZnSi_2S_{12}$ in an Arrhenius type plot. The data exhibits two different regions which can be fitted separately with a linear regression. At temperatures (black) between 303 K and 383 K an activation barrier of 0.66(1) eV is obtained, while at higher temperature (blue) the activation energy is reduced to 0.34(1) eV. This change in activation energy can be related to the tetragonal-to-cubic phase transition occurring between 398 K and 423 K. Typical activation barriers for cubic argyrodites are 0.30 eV – 0.45 eV for Li_6PS_5Cl and Li_6PS_5Br respectively.[10] The phase transition is fully reversible as the conductivity did not change significantly during two complete heating-cooling cycles.

DC-polarization experiments can be used to determine the electronic contribution of the overall conductivity. A range of different DC voltages (0.01 V, 0.05 V, 0.1 V, 0.5 V, 1.0 V) was applied to a gold sputtered pellet and the resulting current was recorded as a function of time. The data for 0.01 V had to be removed, as only noise was measured. The results are plotted in Figure 100.

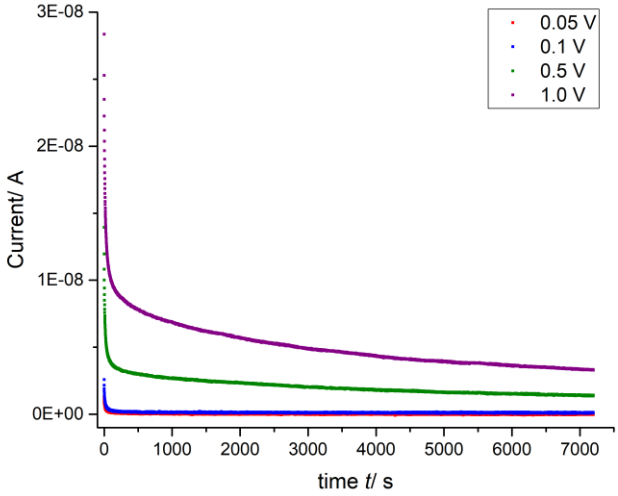

Figure 100: DC polarization experiment on $Li_{14}ZnSi_2S_{12}$ with applied voltages of 0.05 V, 0.1 V, 0.5V and 1.0 V respectively.

The measurements with 1.0 V (purple) and 0.5 V (green) are not fully relaxed and cannot be used in the evaluation. By comparing the starting current with the final relaxed current, one can estimate the electronic contribution for each voltage individually. For the measurements with an applied voltage of 0.05 V and 0.1 V one obtains electronic contributions of 2 % and 4 % respectively, which is not significant.

5.3.1.9 Electrochemical stability

The cyclability and stability of $Li_{14}ZnSi_2S_{12}$ was investigated against lithium metal electrodes at 323 K in a galvanostatic plating and stripping experiment. The results are plotted in Figure 101(a). The signal of the overpotential *E* fluctuates strongly and no smooth plating and stripping plateaus are observed. The overpotential decreases over time, which is different to the findings of the plating and stripping experiments on materials in the $Li_{4.4}M_{0.4}M'_{0.6}S_4$ phase field (Chapter 4). After 8 h the cell is short-circuited, which indicates fast degradation at the Li|SE interface. Contrary to $Li_{4.4}Al_{0.4}Ge_{0.6}S_4$ the interface is not a passivation layer, protecting the SE, but must be electrically and ionically conducting in order to allow for continued break down. After cycling the cell was dissembled to visually inspect the SE. A colour change from initially white/grey to black bulk material was observed.

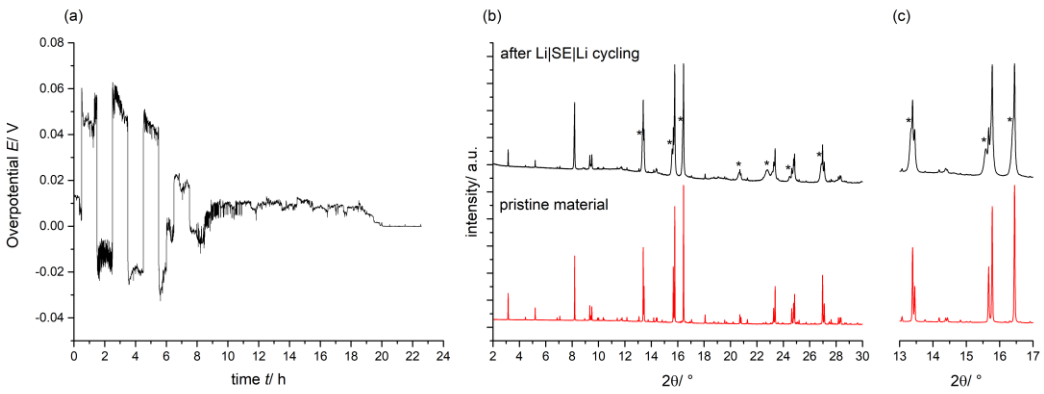

*Figure 101: (a) Galvanostatic plating and stripping experiment in symmetric Li|$Li_{14}ZnSi_2S_{12}$|Li cell obtained at 323 K at ± 0.01 $mAcm^{-2}$ for 1 h per half-cycle. A strong fluctuating signal is observed, eventually after 8 h the cell is short circuited. (b) and (c) SXRD patterns of pristine $Li_{14}ZnSi_2S_{12}$ (red) and the material after cycling (black), newly formed impurity phases are indicated by *.*

SXRD patterns of the pristine material and the material after cycling are compared in Figure 101(b) and (c). At least one new impurity phase has formed during the experiment marked by *. The new phase has very broad peaks and couldn't be indexed to any known phases. It is speculated that this newly formed phase is electrically conducting and short circuited the cell. This finding is different to stability experiments conducted on $Li_{4.4}M_{0.4}M'_{0.6}S_4$ (Chapter 4) in which no change of the bulk material was observed in PXRD analysis.

The bulk decomposition of $Li_{14}ZnSi_2S_{12}$ is an unreported behaviour for lithium containing sulphide based argyrodites. It is known that argyrodites can degrade in contact with lithium metal, but this does not result in full decomposition of the solid electrolyte. Interestingly both $Li_{6.25}PTe_{0.125}S_{5.125}Cl_{0.75}$ and $Li_{7.25}Si_{0.25}P_{0.75}S_6$ have been cycled in symmetric Li|SE|Li cells without any sign of degradations.[18, 23] The origin of this rapid decomposition of $Li_{14}ZnSi_2S_{12}$ against lithium metal could be an interesting objective in future works.

5.3.2 Attempted synthesis of Li_8SiS_6

All structural characterisation of $Li_{14}ZnSi_2S_{12}$ indicated that silicon and sulphur form the canonical argyrodite framework, while lithium and zinc occupy the same disordered crystallographic sites. Hypothetically, $Li_{14}ZnSi_2S_{12}$ can be placed on the $Li_8Zn_0SiS_6$-$Li_0Zn_4SiS_6$ tie line. The endmember, $Li_{16}Si_2S_{12}$ (= Li_8SiS_6), would be a very interesting material, if it existed. The ideal argyrodite stoichiometry Li_8SiS_6 was targeted synthetically using the established experimental procedure. Analysis of the PXRD pattern showed that Li_8SiS_6 does not form, but the binary Li_2S and ternary Li_4SiS_4 are synthesised, as shown in Figure 102.

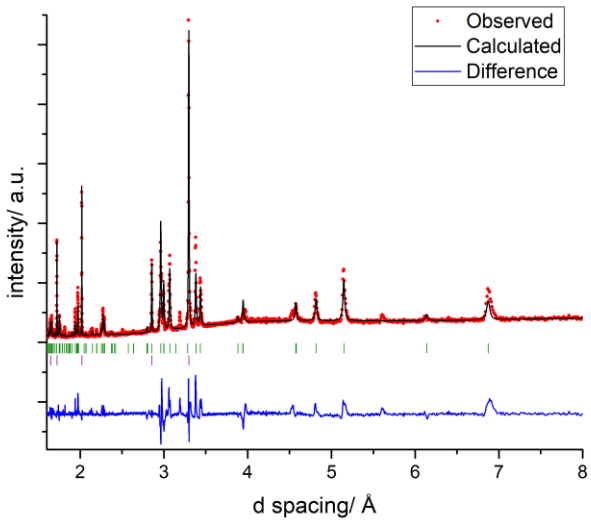

Figure 102: Rietveld fit of "Li_8SiS_6". The mixture does not crystallise in a single argyrodite related material but forms a mixture Li_4SiS_4 (green tick marks) and Li_2S (purple tick marks).

The presence of divalent Zn^{2+} is needed to stabilise the formation of a single phase material. As described previously, there is only a limited number of energetically favourable tetrahedral lithium sites in tetrahedral close packed sublattices and there are not enough stable sites to accommodate 8 lithium atoms per formula unit. Substitution of monovalent Li^+ for divalent Zn^{2+} reduces the number of cations which must be accommodated. This may stabilize $Li_{14}ZnSi_2S_{12}$ compared to $Li_{16}Si_2S_{12}$. No lithium-based argyrodites are known in which the Li:S ratio exceeds 7/6 (*i.e.* Li_7PS_6). In contrast, silver-based argyrodites are known with a Ag:S ratio as high as 9/6 (*i.e.* Ag_9GaS_6).[39]

5.3.3 Mg analogue $Li_{14}MgSi_2S_{12}$

5.3.3.1 Synthesis

The work on the $Li_{4.4}M_{0.4}M'_{0.6}S_4$ phase (Chapter 4) has shown that isovalent cation substitution is a good strategy to find further materials and tune properties. The divalent Zn^{2+} cation was therefore fully substituted for Mg^{2+}, using the synthetic conditions established for $Li_{14}ZnSi_2S_{12}$. PXRD analysis of the reaction product revealed the formation of an argyrodite related phase, together with significant Li_4SiS_4 and Li_2S impurities. Experiments targeted at the elimination of the by-products were undertaken. It was found that the best results could be achieved by using a 5 mol % excess of MgS (resulting in a starting stoichiometry of $Li_{14}Mg_{1.05}Si_2S_{12.05}$) to synthesise $Li_{14}MgSi_2S_{12}$. Small impurity phases of Li_2S and Li_4SiS_4 remain present in SXRD patterns.

Preliminary indexing attempts fitted the phase to a small tetragonal unit cell (space group: $I\bar{4}m2$, *a*= 7.0648(1) Å *c*= 10.0665(1) Å), without tripling of the *a* and *b* axis. But close inspection of SXRD data revealed the presence of weak reflections which relate to the enlarged cell (*a*= 21.1919(2) Å, *c*= 10.0651(1) Å) in $I\bar{4}m2$ symmetry. The cell parameters of $Li_{14}MgSi_2S_{12}$ are very similar to the cell parameters of $Li_{14}ZnSi_2S_{12}$ (*a*= 21.1506(2) Å, *c*= 10.0564(2) Å). The corresponding Pawley fit of $Li_{14}MgSi_2S_{12}$ is plotted in Figure 103.

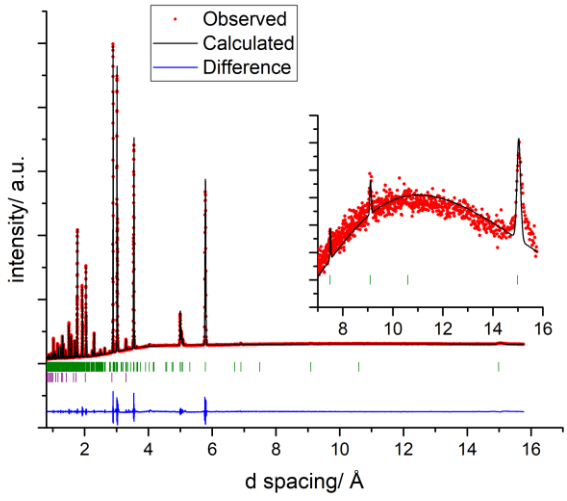

Figure 103: Pawley fit of $Li_{14}MgSi_2S_{12}$ in the tetragonal $I\bar{4}m2$ space group against SXRD data (I11 beamline, MAC detector, λ= 0.82526 Å, ambient temperature, a= 21.1919(2) Å, c= 10.0651(1) Å). The positions of calculated Bragg reflections are shown by tick marks (green: $Li_{14}MgSi_2S_{12}$, purple: Li_2S).

5.3.3.2 ICP

$Li_{14}MgSi_2S_{12}$ could not be dissolved in concentrated acids or *aqua regia*, therefore a single sample was sent to Mikroanalytisches Labor Pascher for compositional analysis. The result is

given in Table 28. The normalised composition of $Li_{14.00}Mg_{1.04}Si_{2.21}S_{11.83}$ is in reasonable agreement with the nominal composition.

Table 28: Result of the compositional analysis of $Li_{14}MgSi_2S_{12}$.

	Calculated wt % ($Li_{14}Mg_{1.00}Si_2S_{12.00}$)	Calculated wt % ($Li_{14}Mg_{1.05}Si_2S_{12.05}$)	Measured/ wt %	Normalised composition
Li	17.28	17.19	16.6	14.00
Mg	4.32	4.51	4.31	1.04
Si	9.99	9.94	10.6	2.21
S	68.41	68.36	64.8	11.83

5.3.3.3 Raman spectrum of $Li_{14}MgSi_2S_{12}$

A Raman spectrum of $Li_{14}MgSi_2S_{12}$ was recorded by Dr Troy D. Manning. It shows very similar features compared to $Li_{14}ZnSi_2S_{12}$: broad features around ~ 550-600 cm^{-1} and 100-250 cm^{-1} and the sharp peak at 409 cm^{-1}. The maxima of the broad features shifted ± 2 cm^{-1} compared to $Li_{14}ZnSi_2S_{12}$, as shown in comparison in Figure 104. The S/Si framework structures of $Li_{14}MgSi_2S_{12}$ and $Li_{14}ZnSi_2S_{12}$ are assumed to be very similar, as the differences in the spectra are very small.

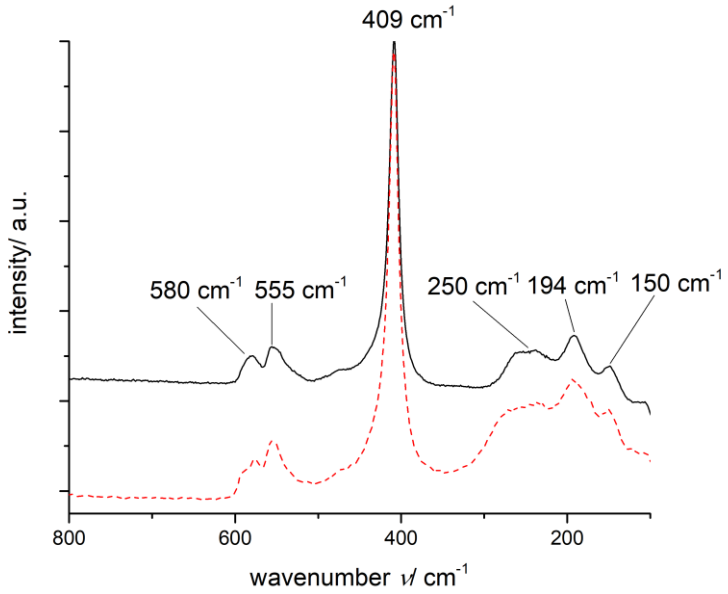

Figure 104: Raman spectrum of $Li_{14}MgSi_2S_{12}$ (black line); the Raman spectrum of $Li_{14}ZnSi_2S_{12}$ is included for comparison (red dashes) (measured by Dr Troy D. Manning).

5.3.3.4 DSC

A DSC (Differential scanning calorimetry) scan of $Li_{14}MgSi_2S_{12}$ is shown in Figure 105. An endothermic event can be detected during the first heating scan at ~ 350 K, but it does not reappear during consecutive cooling and heating cycles and was therefore discarded as an initial side reaction/change in heat flux. At 380.5 K a reversible endothermic event takes place, while the reversible exothermic process occurs at 374 K. Compared to $Li_{14}ZnSi_2S_{12}$

(heating: 411 K, cooling: 405 K) both transition events are shifted towards lower temperatures.

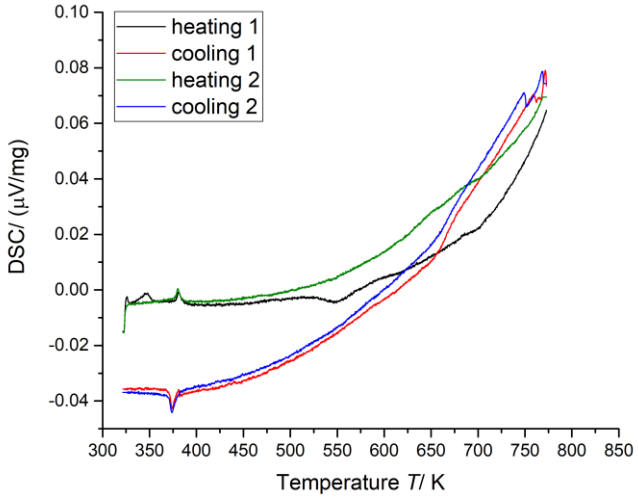

Figure 105: Differential scanning calorimetry curve of $Li_{14}MgSi_2S_{12}$ from ambient temperature to 773 K. The two reversible processes at ~ 370 K correspond to a reversible phase transition.

5.3.3.5 Variable temperature SXRD experiment

Variable temperature SXRD patterns of $Li_{14}MgSi_2S_{12}$ are plotted in Figure 106(a). SXRD patterns were recorded every 25 K from 323 to 448 K and vice versa.

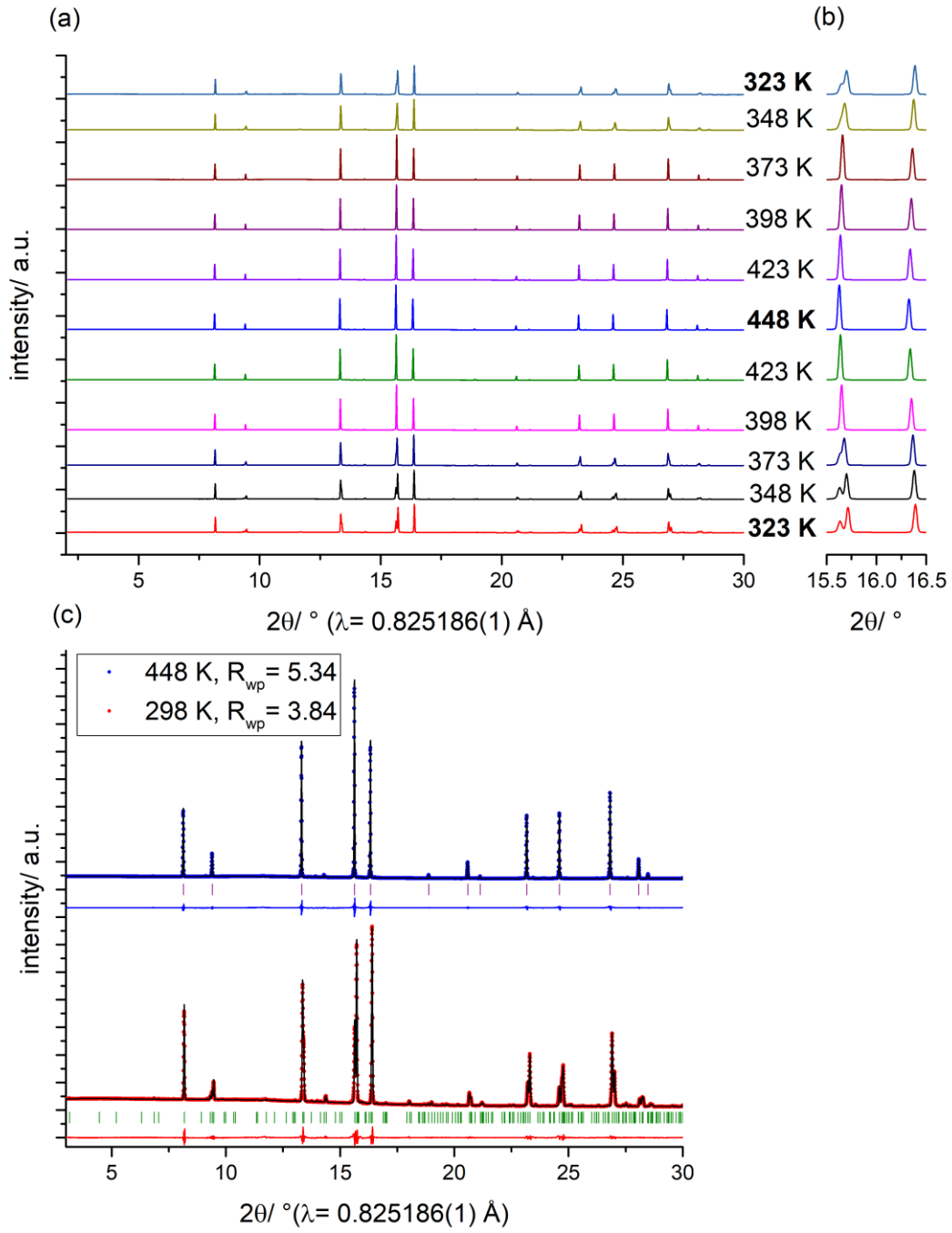

Figure 106: (a) Temperature dependent SXRD experiment measured on $Li_{14}MgSi_2S_{12}$ in the range of 323 K and 448 K in 25 K intervals. A partially reversible phase transition from tetragonal to cubic is detectable at T~ 398 K during heating and cooling. (b) Zoom into region around 2θ= 16.0 °. (c) Pawley plot of $Li_{14}MgSi_2S_{12}$ at 298 K (red) and 448 K (blue). The low temperature phase is fitted to a tetragonal unit cell (green tick marks, space group: $I\bar{4}m2$, a= 21.1925(2)Å, c= 10.0654(1) Å), the high temperature phase is fitted to a cubic unit cell (purple tick marks, space group: $F\bar{4}3m$, a= 10.0608(3) Å). The tick marks for the impurity phase (Li_2S) were omitted for reasons of clarity.

Similarly, to $Li_{14}ZnSi_2S_{12}$ a tetragonal-to-cubic phase transition takes place during heating and the reverse cubic-to-tetragonal transition occurs upon cooling. The transition temperature is slightly lower (398 K vs 423 K), as already indicated by the DSC scans. The changes are best followed by considering the reflections at 2θ~16 °, plotted in Figure 106(b). Interestingly the

phase transition is not fully reversible. Comparing the pattern at 323 K before heating and the pattern at 323 K after cooling shows that peak splitting at 2θ~16 ° is less pronounced after the heating-cooling cycle. This is due to hysteresis in the phase transition. The high temperature phase can be indexed to the cubic $F\bar{4}3m$ space group, as shown in the Pawley fit in Figure 106(c).

A more detailed analysis of the parameters extracted from Pawley fits on the temperature dependent SXRD experiment is presented in Figure 107. Compared to $Li_{14}ZnSi_2S_2$ the changes in *a*, *c*, *V* and the tetragonalinity show more pronounced hysteresis. This corroborates the slightly irreversible nature of the temperature induced phase transition in $Li_{14}MgSi_2S_{12}$ as found by visual inspection in Figure 106(b).

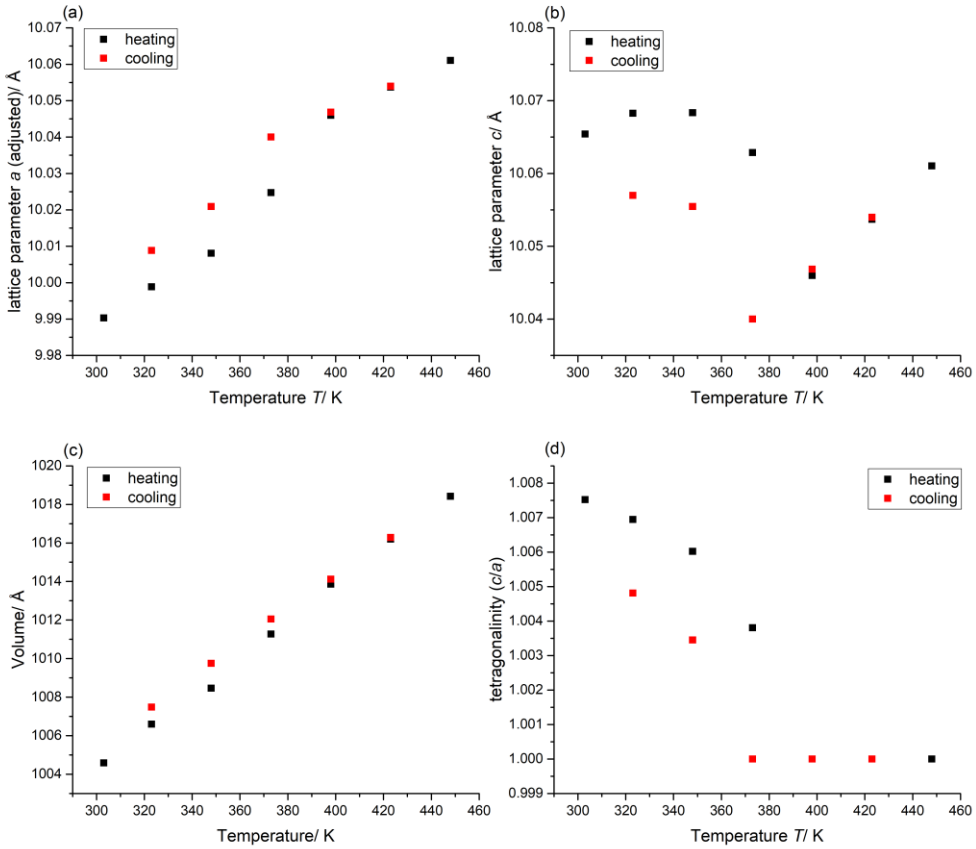

Figure 107: Analysis of parameters extracted from Pawley fits of the T-dependent SXRD experiment for $Li_{14}MgSi_2S_{12}$: (a) change of lattice parameter a (b) change of lattice parameter c (c) change of the unit cell Volume V (d) change of tetragonalinity c/a.

5.3.3.6 High temperature crystal structure of $Li_{14}MgSi_2S_{12}$

NPD and SXRD experiments were carried out on the $Li_{14}MgSi_2S_{12}$ phase at 448 K. Figure 108 shows the Pawley fits for banks 2–5. The patterns were fitted to the cubic space group $F\bar{4}3m$ (*a*= 10.0608(3) Å). Small reflections could be indexed to the sample container (vanadium),

and the impurity phases Li_2S and Li_4SiS_4. Two reflections at d= 4.1 Å and 2.9 Å (shoulder in panel (b)) could not be identified.

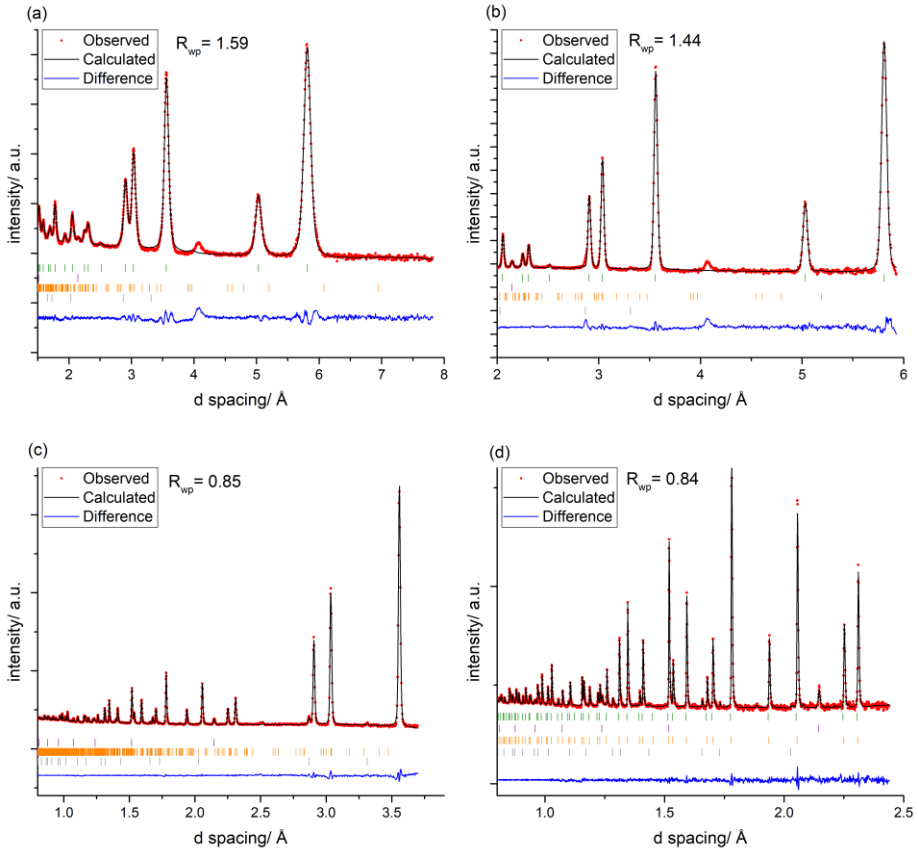

Figure 108: Pawley fits of the $Li_{14}MgSi_2S_{12}$ in the cubic $F\bar{4}3m$ space group (a= 10.0608(3) Å) against NPD data: (a) bank 2, (b) bank 3, (c) bank 4, (d) bank 5. The positions of calculated Bragg reflections are shown by tick marks (green: HT $Li_{14}MgSi_2S_{12}$, purple: V, orange: Li_4SiS_4, grey: Li_2S).

The crystal structure of the high temperature cubic polymorph of $Li_{14}MgSi_2S_{12}$ was refined against NPD data using the HT-structure of $Li_{14}ZnSi_2S_{12}$ as a starting model. It was assumed that Mg^{2+} substitutes Zn^{2+} on the disordered 48*h* site. The same constraints were used in the Rietveld refinement of $Li_{14}MgSi_2S_{12}$:

(a) full occupation of the sulphur and silicon sites

(b) anisotropic displacement parameters for all positions but Li2

(c) compositional constraint to $Li_{14}MgSi_2S_{12}$ (*i.e.* $Li_{28}Mg_2Si_4S_{24}$ per unit cell)

It was found that HT $Li_{14}MgSi_2S_{12}$ crystallises isostructural to HT $Li_{14}ZnSi_2S_{12}$ with a similar distribution of the mobile cations on the 48*h*, 24*g* and 16*e* site. The magnesium is only found on the tetrahedral 48*h* site, while lithium can be found on the 48*h* site, the trigonal planar 24*g* site and the tetrahedral 16*e* site. The distribution of the mobile cations *L* is given in Table 29:

Table 29: Distribution of the mobile cations L in HT $Li_{14}MgSi_2S_{12}$.

	Li	Mg
48*h*	0.446(2)	1/24
24*g*	0.047(5)	0
16*e*	0.340(3)	0

The fully refined model is depicted in Figure 109 with corresponding fits of the NPD data. Full crystallographic information is given in the appendix in Table 39.

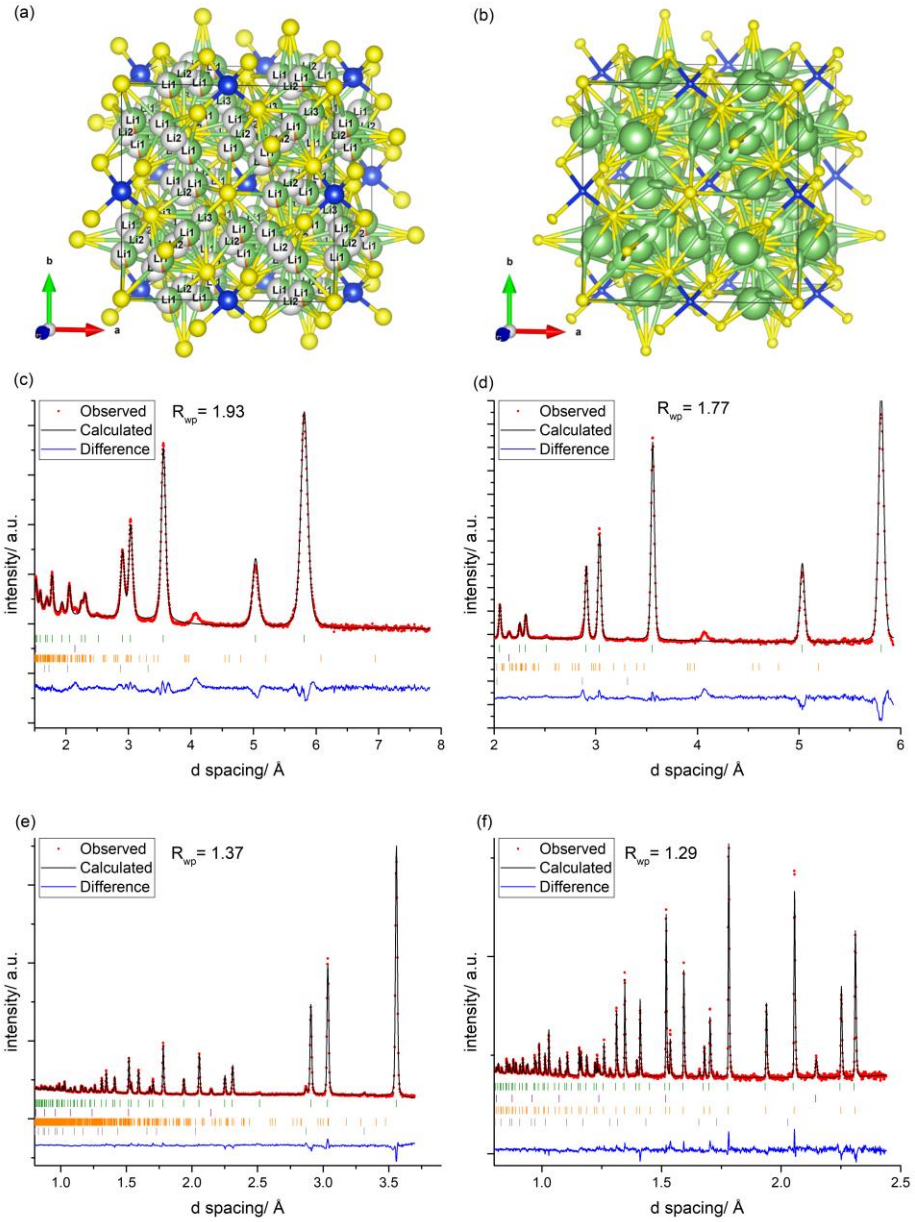

Figure 109: (a) Fully refined crystallographic model for HT $Li_{14}MgSi_2S_{12}$. (b) Visualisation of the anisotropic displacement of the atoms in HT $Li_{14}MgSi_2S_{12}$. (c) NPD fit bank 2, (b) NPD fit bank 3, (c) NPD fit bank 4, (d) NPD fit bank 5. The positions of calculated Bragg reflections are shown by tick marks (green: HT $Li_{14}MgSi_2S_{12}$, purple: V, orange: Li_4SiS_4, grey: Li_2S) (yellow: sulphur, green: lithium, blue: silicon, orange: magnesium).

The bond distances of the individual cations are listed in Table 30.

Table 30: Bond distances of MS_x coordination environments of the cations in $Li_{14}MgSi_2S_{12}$ at 448 K.

	Si	Li1/Zn1	Li2	Li3
S1	x	2.4566(5) Å	2.320(3) Å	x
S2	2.0934(5) Å	2.5345(5) Å	2.313(4) Å	2.4925(3) Å
S3	x	2.6083(5) Å	3.556(4) Å	2.2976(3) Å

5.3.3.7 Transport properties of $Li_{14}MgSi_2S_{12}$

Temperature dependent AC-impedance measurements were initially conducted on a cold pressed and gold sputtered pellet of $Li_{14}MgSi_2S_{12}$. Figure 111(a) shows the spectrum of the pristine cold pressed pellet after gold electrodes had been sputtered on the faces. The spectrum is difficult to interpret but a conductivity value of ~2 x 10^{-6} S cm^{-1} can be approximated. After the pellet has been heated to 503 K and cooled to 303 K the spectrum changes significantly as shown in Figure 111(b). The conductivity has dropped by ~2 orders of magnitude. Higher conductivity values were obtained for 323 K, 343 K, 363 K and 383 K during the first heating cycle compared to the cooling cycle.

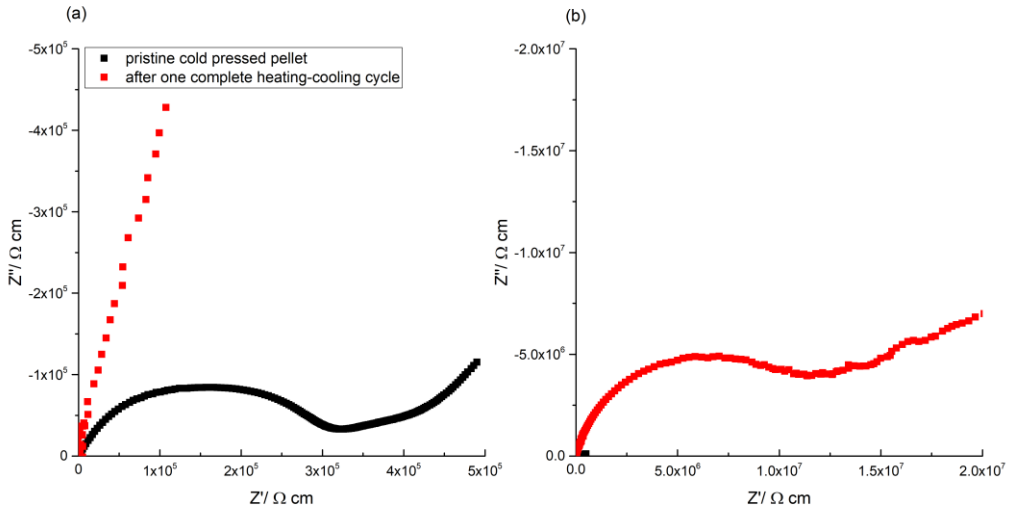

Figure 110: AC-impedance spectra of a cold pressed pellet of $Li_{14}MgSi_2S_{12}$ (a) spectrum of the pristine cold pressed sample (b) spectrum after one complete heating-cooling cycle.

In total the first heating regime gives significantly higher values compared to the consecutive cooling cycle up to the phase transition temperature at 398 K. Beyond the phase transition the discrepancy vanishes (compare to Figure 111 (a)). After the material has undergone the tetragonal-cubic phase transition for the first time the pellet can be cooled to ambient

temperature and reproducible low conductivity values are obtained in consecutive heating-cooling cycles.

Two regimes with distinctly different activation energies E_a can be differentiated after the first phase transition. At lower temperatures an activation barrier of 0.55(1) eV is calculated. After the tetragonal-cubic phase transition a lower activation energy of 0.43(1) eV is obtained.

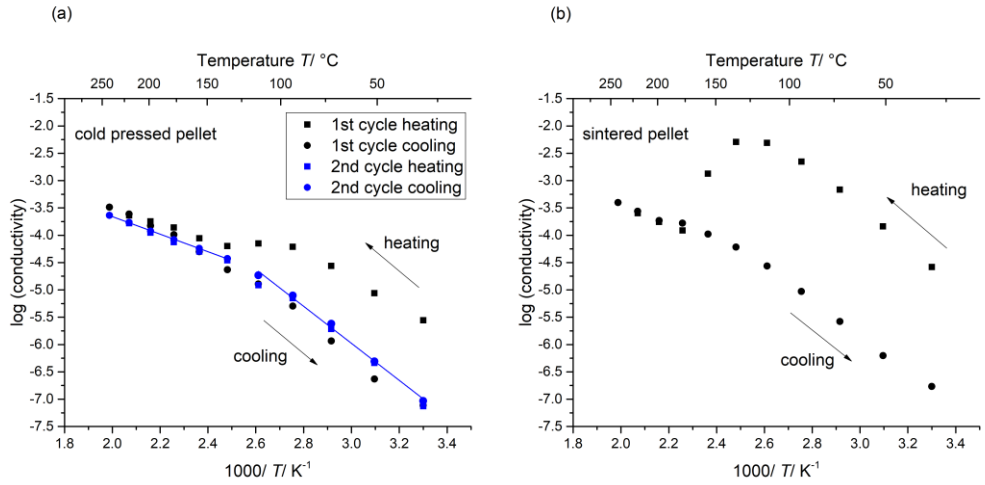

Figure 111: Arrhenius plot of AC-impedance measurements on (a) cold pressed pellet; (b) sintered pellet.

To investigate the irreversible behaviour of the temperature dependent conductivities further measurement was repeated on a pellet, which had been sintered at 923 K for 14 h; the results are plotted in Figure 111(b). Compared to the cold pressed pellet the first set of measurement on the heating series shows even higher conductivities. But the conductivity drops after the transition temperature and follows the trend seen in the cold pressed sample. This phenomenon has not been encountered before. The drop of conductivity with increasing temperature, as seen in the sintered pellet at temperatures between 403 K and 450 K, is counter-intuitive. In the temperature dependent SXRD experiment it had been observed that the tetragonal-to-cubic phase transition is not fully reversible in a helium atmosphere. The cooling conditions of the sample appears to have a significant impact on the conductivity. The synthesis of $Li_{14}MgSi_2S_2$ and sintering of the pellet takes place in evacuated quartz tubes, while the SXRD experiments and the AC-impedance experiments were conducted in a helium atmosphere. A second crucial parameter could be the cooling rate, as it could not be rigorously controlled during the synthesis. Different cooling conditions could lead to a loss of crystallinity, minor changes of the crystal structure and differences in the defect concentration. The not fully-reversible phase transition affects the conductivity of

the material significantly. But after the first heating-cooling cycle a reproducible conductivity of ~1x10^{-8} S cm^{-1} is obtained for both the cold pressed and the sintered pellet.

DC-polarization experiments can be used to determine the electronic contribution of the overall conductivity. A range of different DC voltages (0.01 V, 0.05 V, 0.1 V, 0.5 V, 1.0 V) was applied to a gold sputtered pellet and the resulting current was recorded as a function of time. Figure 112 shows the respective polarization curves.

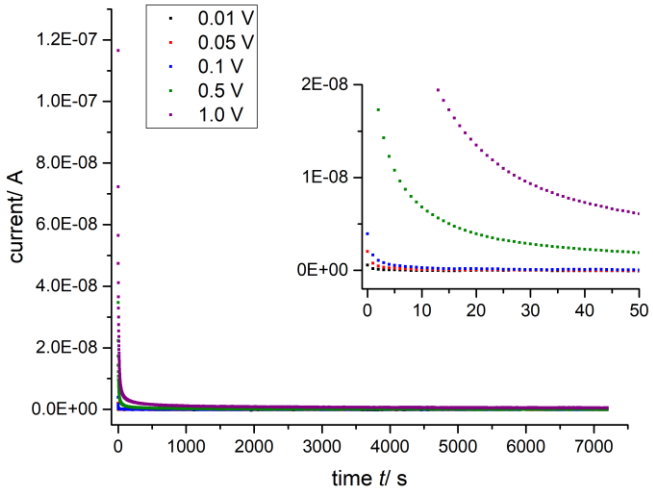

Figure 112: DC polarization experiment on $Li_{14}MgSi_2S_{12}$ with applied voltages of 0.01 V, 0.05 V, 0.1 V, 0.5V and 1.0 V respectively.

The polarization curve relaxes fully for all applied voltages. Electronic contributions of 7 %, 3 %, 1 %, 3 % and 0.4 % were calculated for applied voltages of 0.01 V, 0.05 V, 0.1 V, 0.5 V and 1.0 V respectively. This relaxation behaviour is different to $Li_{14}ZnSi_2S_{12}$, in which the material did not fully relax for applied voltages of 0.5 V and 1.0 V in the considered time scale.

5.3.3.8 Electrochemical stability

The cyclability and stability of $Li_{14}MgSi_2S_{12}$ was investigated against lithium metal electrodes at 323 K in a galvanostatic plating and stripping experiment. The results are plotted in Figure 113(a).

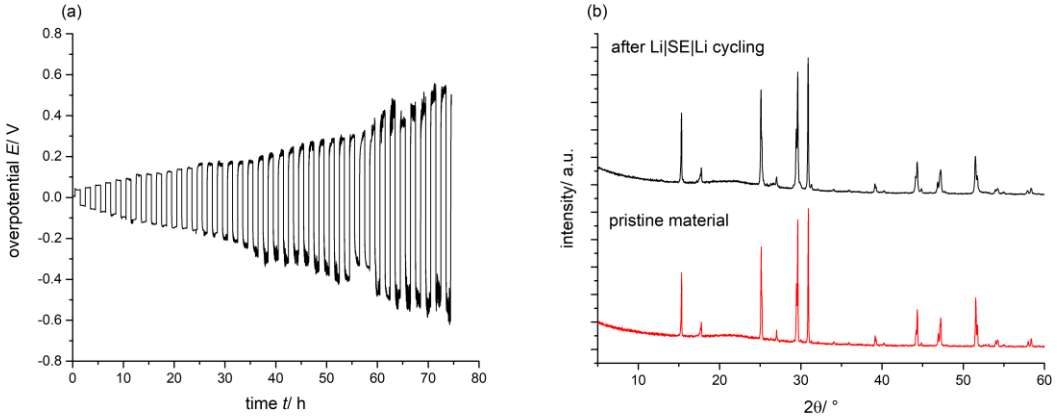

Figure 113: (a) Galvanostatic plating and stripping experiment in symmetric Li|$Li_{14}MgSi_2S_{12}$|Li cell obtained at 323 K at ± 0.01 mAcm^{-2} for 1 h per half-cycle. (b) PXRD patterns of pristine $Li_{14}MgSi_2S_{12}$ (red) and the material after cycling (black) (λ= 1.541 Å).

The overpotential *E* increases continuously over time. During the first 25 h relatively smooth plating and stripping plateaus are observed. These features are lost during the prolonged experiment and the signal fluctuates strongly. No stabilisation of the overpotential is achieved after 70 h, indicating significant reactions at the Li|SE interface. PXRD analysis of the ground pellet after the experiment does not show a change in the bulk material. The degradation reactions are restricted to the interface, which differs strongly with the $Li_{14}ZnSi_2S_{12}$ homologue where bulk degradation was observed.

5.3.4 Cation substitution in $Li_{14}MSi_2S_{12}$ (*M*= Zn^{2+}, Mg^{2+})

5.3.4.1 $Li_{14+x}MAl_xSi_{2-x}S_{12}$ (M= Zn^{2+}, Mg^{2+}): substitution of Si^{4+} for Al^{3+}

Cation substitution is a viable strategy to improve the conductivity of lithium conductivity of argyrodites. The first aluminium containing superionic lithium conductor, HT-$Li_{6.15}Al_{0.15}Si_{1.35}S_6$, was reported in 2018.[11] Quenching the reaction mixture from high temperatures (1273 K) resulted in the incorporation of Al^{3+} into the argyrodite structure. It was attempted to introduce Al^{3+} into the new $Li_{14}MSi_2S_{12}$ phase. Using the established synthetic procedure for $Li_{14}MSi_2S_{12}$ exploratory synthesis was carried along $Li_{14+x}MAl_xSi_{2-x}S_{12}$ (*M*= Zn^{2+}, Mg^{2+}) up to x= 0.8. Figure 114 shows the PXRD patterns along $Li_{14+x}ZnAl_xSi_{2-x}S_{12}$. At x= 0.2 the main phase consists of the tetragonal argyrodite, but already significant Li_4SiS_4/Li_5AlS_4 and Li_2S impurities are detectable (marked by * and # respectively). Li_4SiS_4 and

Li_5AlS_4 form a solid solution, making it impossible to unambiguously clarify the composition of the impurity phase.[40] For the sake of simplicity the impurity will be referred to as Li_4SiS_4. With increasing x this impurity content increases further. Interestingly the splitting of the reflection at 2θ= 29.5 ° decreases, which can best be seen for x= 0.4 in Figure 114(b). Furthermore, the large d-spacing supercell reflections are of zero or very low intensity. This indicates that a transition towards a more cubic structure is taking place as more aliovalent cations are introduced into the argyrodite structure. With increasing values of x, less argyrodite is formed and the reflections of Li_4SiS_4 and Li_2S overlap significantly with the argyrodite phase, making it impossible to follow the phase transition in the argyrodite further.

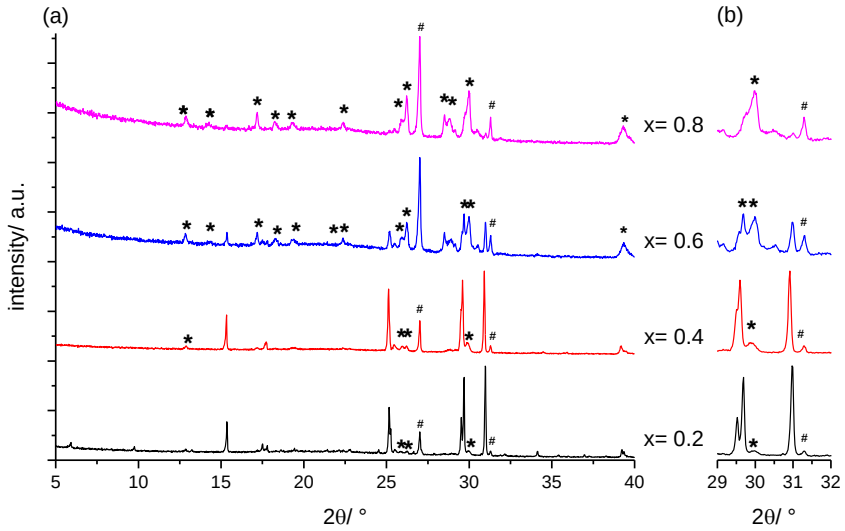

*Figure 114: PXRD patterns of the reactions $Li_{14+x}ZnAl_xSi_{2-x}S_{12}$ (#: Li_2S, *: Li_4SiS_4, λ= 1.541 Å).*

A similar trend can be found in $Li_{14+x}MgAl_xSi_{2-x}S_{12}$: Small amounts of Al^{3+} doping lead to a more cubic argyrodite related main phase. But with increasing Al^{3+} the impurity phases Li_2S and Li_4SiS_4 are becoming more dominant, as shown in Figure 115(a) and (b).

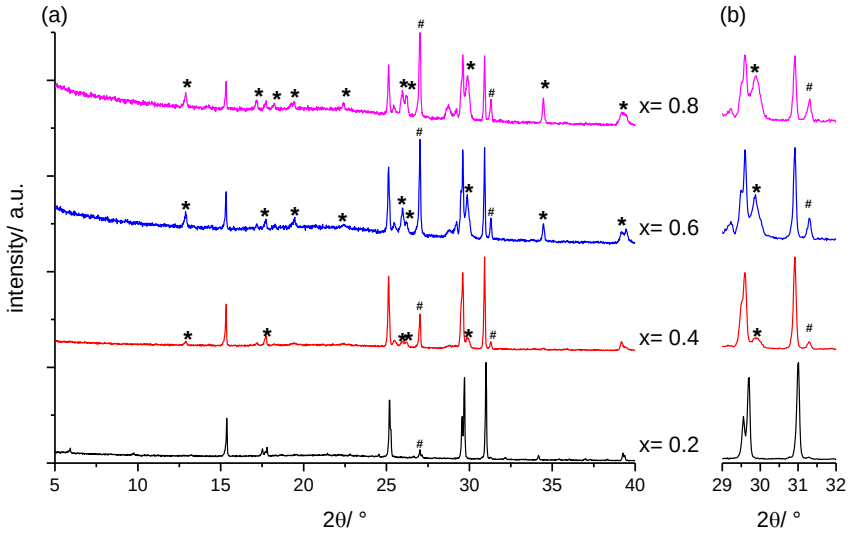

*Figure 115: PXRD patterns of the reactions $Li_{14+x}MgAl_xSi_{2-x}S_{12}$; (#: Li_2S, *: Li_4SiS_4, λ= 1.541 Å)).*

Al^{3+} doping into the Si^{4+} site in $Li_{14}MSi_2S_{12}$ (*M*= Zn^{2+}, Mg^{2+}) is not viable, as Al^{3+} cannot not be introduced into the structure in significant amounts. A similar result was obtained by Zhang *et al.* trying to incorporate trivalent metal cations into orthorhombic Li_7PS_6 according to $Li_{7+x}M^{3+}_xP_{1-x}S_6$.[18] They observed that no transition into the cubic structure took place with increasing values of x, which was corroborated by very low conductivities of the resulting materials. The first and only known aluminium containing argyrodite $Li_{6.15}Al_{0.15}Si_{1.35}S_6$ is thermodynamically stable only at very high temperatures and needs to be quenched in order not form compositions along the solid solution Li_4SiS_4-Li_5AlS_4.[11] Compared to known lithium argyrodites $Li_{14}MSi_2S_{12}$ is a cation rich argyrodite and the number of cations rises with increasing x in $Li_{14+x}MAl_xSi_{2-x}S_{12}$. But the number of energetically favourable tetrahedral sites is limited in argyrodites. Arguably the availability of energetically favourable sites restricts doping strategies which further increase the cation content.

5.3.4.2 $Li_{14-x}MSi_{2-x}P_xS_{12}$ (M= Zn^{2+}, Mg^{2+}): substitution of P^{5+} for Si^{4+}

Based on the attempts of doping Al^{3+} into $Li_{14}MSi_2S_{12}$ (*M*= Zn^{2+}, Mg^{2+}), it is logical to dope $Li_{14}MSi_2S_{12}$ with higher valent cations which reduce the total cation count. Phosphorous is a straightforward choice as most known lithium containing sulphide based argyrodites contain P^{5+} and one lithium is removed per introduced phosphorous cation.

Figure 116 shows the PXRD patterns of P^{5+} doped $Li_{14}ZnSi_2S_{12}$ (0 < x < 1.4). Samples with small P^{5+} content (x < 0.4) crystallise in the large tetragonal unit cell. But a transition towards a more cubic unit cell can be detected when inspecting carefully the small angle reflections (2 °< 2θ < 8 °). The intensity of these decreases significantly and reaches zero at x= 1.0 (Figure

116(b)). Similarly, the reflections in the region at 2θ= 13 ° - 16 ° is indicative of the phase transition. The initial split of the reflections is reduced and they completely overlap at x= 1.0. The patterns of x ≥ 1.0 can be indexed to the cubic $F\bar{4}3m$ space group. The Pawley fit of cubic $Li_{13}ZnSiPS_{12}$ in a $F\bar{4}3m$ unit cell (*a*= 9.9461(8) Å) is shown in panel (d).

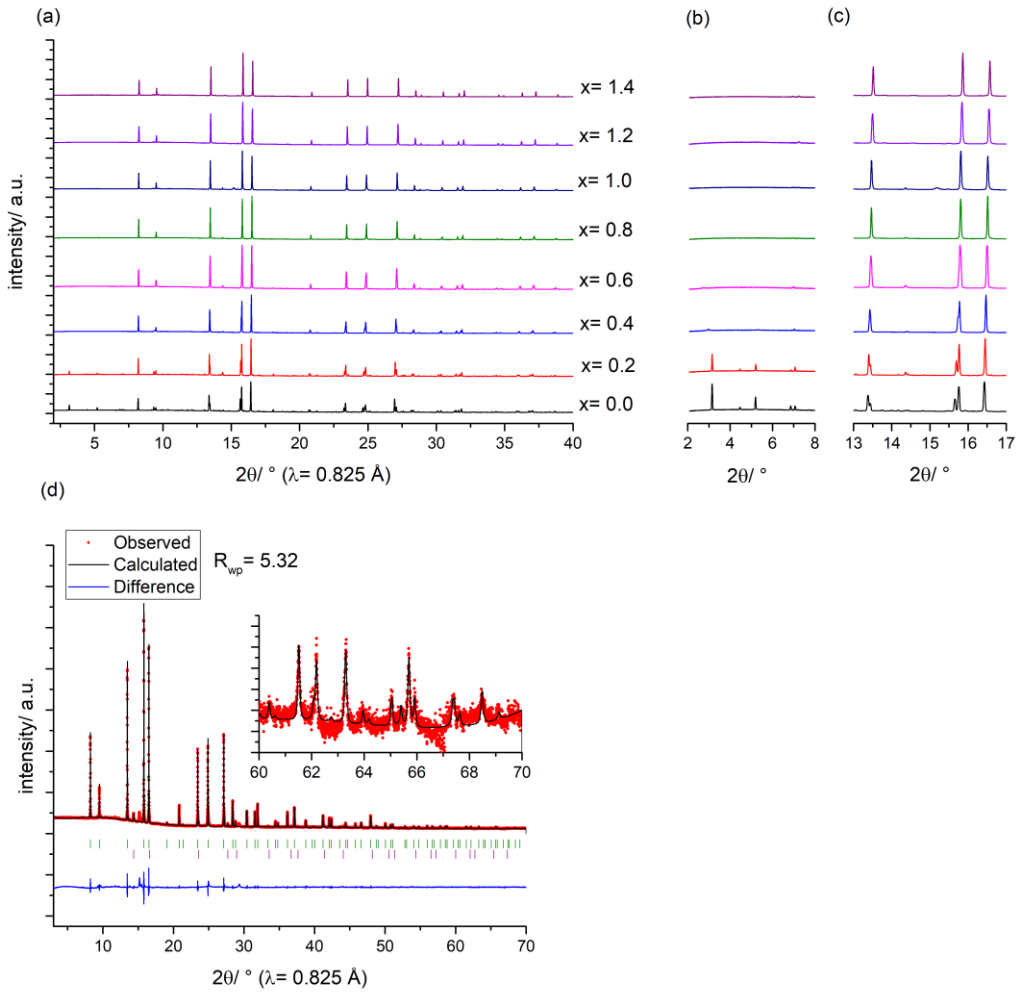

Figure 116: (a) PXRD patterns of $Li_{14-x}ZnSi_{2-x}P_xS_{12}$. (b) + (c) Upon increasing levels of x the tetragonalinity is reduced and full cubic structures are obtained at x > 1. (d) Pawley fit of $Li_{13}ZnSiPS_{12}$ in a cubic unit cell (space group: $F\bar{4}3m$, a= 9.9461(8) Å). The positions of calculated Bragg reflections are shown by tick marks (green: $Li_{13}ZnSiPS_{12}$, purple: Li_2S).

Various impurity phases start to form at x > 0.8 (which could not be indexed to known materials), as visible at 2θ= 15 ° in Figure 116(c). The lattice parameter *c* is plotted against x in Figure 117. Compositions indexed to the large tetragonal cell are shown as triangles, while cubic materials are depicted as squares. With increasing x the lattice parameter *c* decreases which can be related to the smaller ionic radius of P^{5+} compared to Si^{4+} (0.17 Å *vs* 0.26 Å).[37] A continued incorporation of P^{5+} into the argyrodite is confirmed. The slope does not strictly follow Vegard's law, as is not completely linear. This can be due to deviating stoichiometry of the crystalline main phase compared to the targeted composition. The formation of

crystalline by-phases and existence of amorphous impurities can result in significant change of the composition.

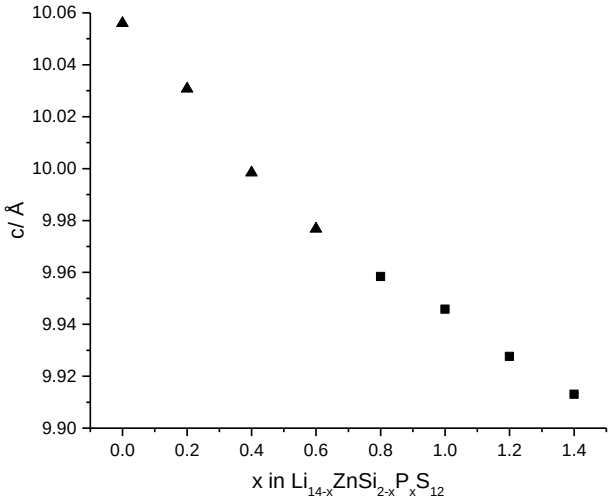

Figure 117: Lattice parameter c in $Li_{14-x}ZnSi_{2-x}P_xS_{12}$. Compositions which could be indexed to the large tetragonal cell are marked by triangles; cubic materials are marked by squares.

Similar results are obtained for the doping of P^{5+} into $Li_{14}MgSi_2S_{12}$. Upon increasing doping levels x, the materials become more cubic, until at $x \geq 0.8$ the patterns can be fully indexed to the cubic $F\bar{4}3m$ space group. Figure 118 shows the PXRD patterns of $Li_{14-x}MgSi_{2-x}P_xS_{12}$ in dependence of x.

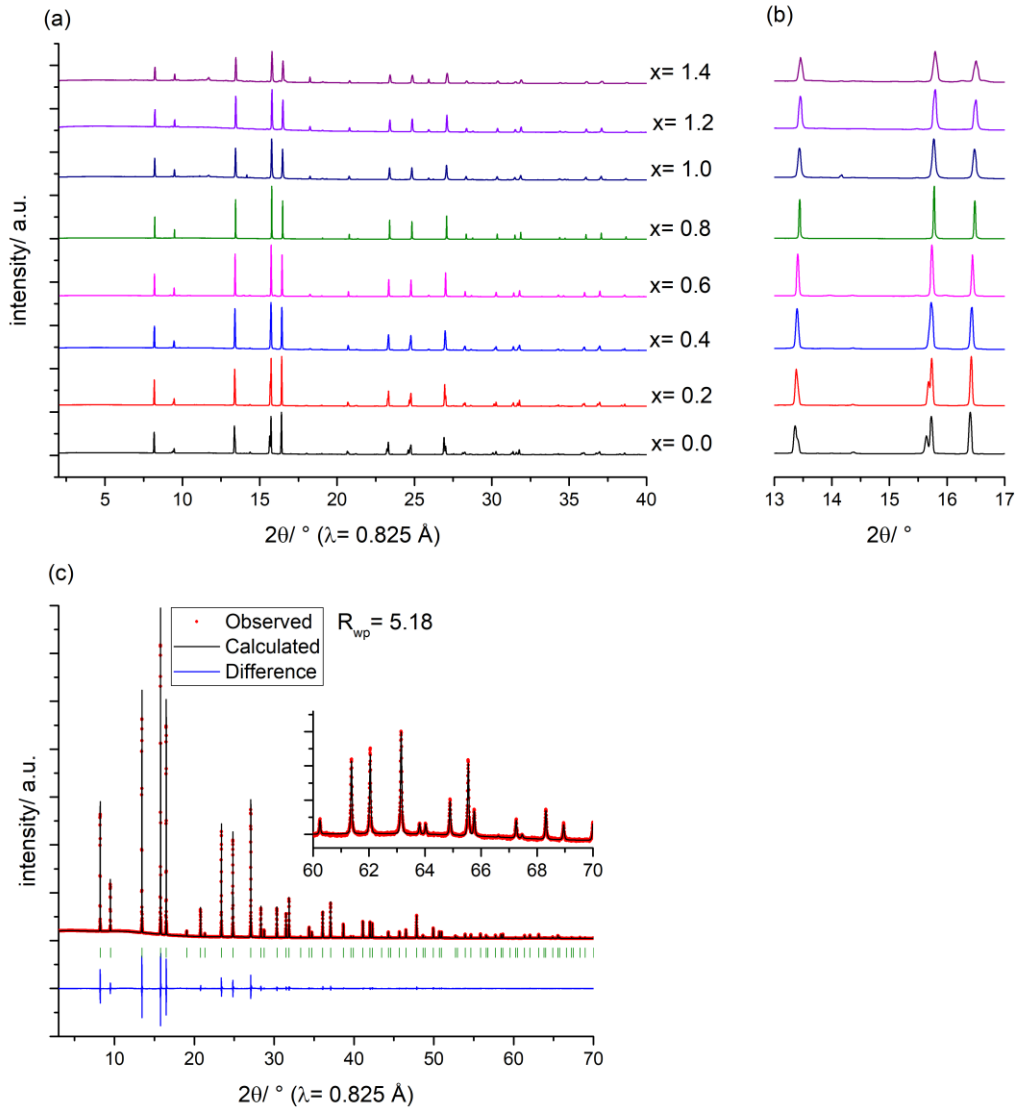

Figure 118: (a) PXRD patterns of $Li_{14-x}MgSi_{2-x}P_xS_{12}$. (b) Upon increasing levels of x the tetragonalinity is reduced and full cubic structures are obtained at x > 0.8.(c) Pawley fit of $Li_{13.2}MgSi_{1.2}P_{0.8}S_{12}$ in a cubic unit cell (space group: $F\bar{4}3m$, a= 9.9666(5) Å) The positions of calculated Bragg reflections are shown by tick marks (green: $Li_{13.2}ZnSi_{1.2}P_{0.8}S_{12}$).

Panel (c) shows a Pawley fit of $Li_{13.2}MgSi_{1.2}P_{0.8}S_{12}$ in a cubic unit cell (space group: $F\bar{4}3m$, a= 9.9666(5) Å). Remarkably no impurity reflections can be identified in this composition. Impurity phases start to form at x ≥ 1.0. This is reflected in the trend of the lattice parameter *c* plotted in Figure 119. A linear decrease of *c* is observed until x = 0.8, after which the values oscillate around *c*= 9.96 Å. An end of the solid solution $Li_{14-x}MgSi_2P_xS_{12}$ is reached around x = 0.8.

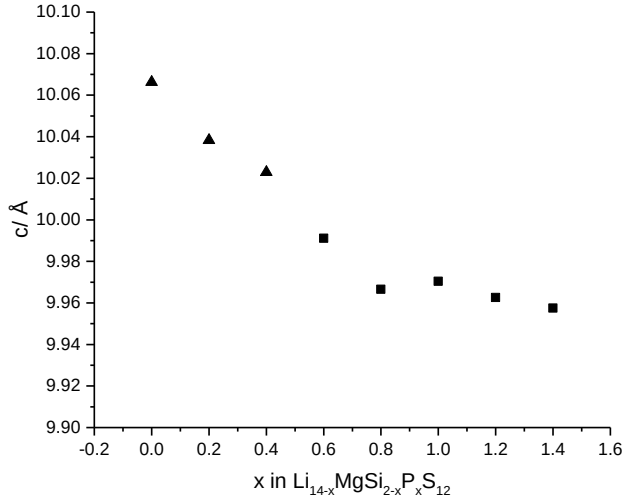

Figure 119: Lattice parameter c in $Li_{14-x}MgSi_{2-x}P_xS_{12}$. Compositions which could be indexed to the large tetragonal cell are marked by triangles; cubic materials are marked by squares.

5.3.4.3 Structure solution of $Li_{13}ZnSi_1P_1S_{12}$ and $Li_{13.2}MgSi_{1.2}P_{0.8}S_{12}$

The crystal structures of $Li_{13}ZnSiPS_{12}$ (x= 1.0) and $Li_{13.2}MgSi_{1.2}P_{0.8}S_{12}$ (x= 0.8) were solved by Rietveld refinement to investigate the role of P^{5+} in the structure. These samples showed the purest SXRD patterns while crystallising in a cubic $F\bar{4}3m$ unit cell. Rietveld refinements of the structural model were carried out against SXRD data using cubic Li_7PS_6 as a starting model. As only one set of data (SXRD, PSD detector) was available for each material the total compositions were fixed to $Li_{13}ZnSiPS_{12}$ and $Li_{13.2}MgSi_{1.2}P_{0.8}S_{12}$ respectively. Si^{4+} and P^{5+} are fixed on the same disordered 4*b* site with the formal ratio 1:1 ($Li_{13}ZnSiPS_{12}$) and 1.2:0.8 ($Li_{13.2}MgSi_{1.2}P_{0.8}S_{12}$). Based on the structures obtained for $Li_{14}ZnSi_2S_{12}$ and $Li_{14}MgSi_2S_{12}$ the divalent cations were fixed on the 48*h* site. The lithium occupation was refined on the 48*h* and 24*g* sites. The fractional coordinates of each site were refined where permitted by symmetry restrictions. Finally, the displacement parameters were refined for the three S sites, the silicon and the Li/*M* site. The refined structure and corresponding Rietveld fit for $Li_{13}ZnSiPS_{12}$ are shown in Figure 120:

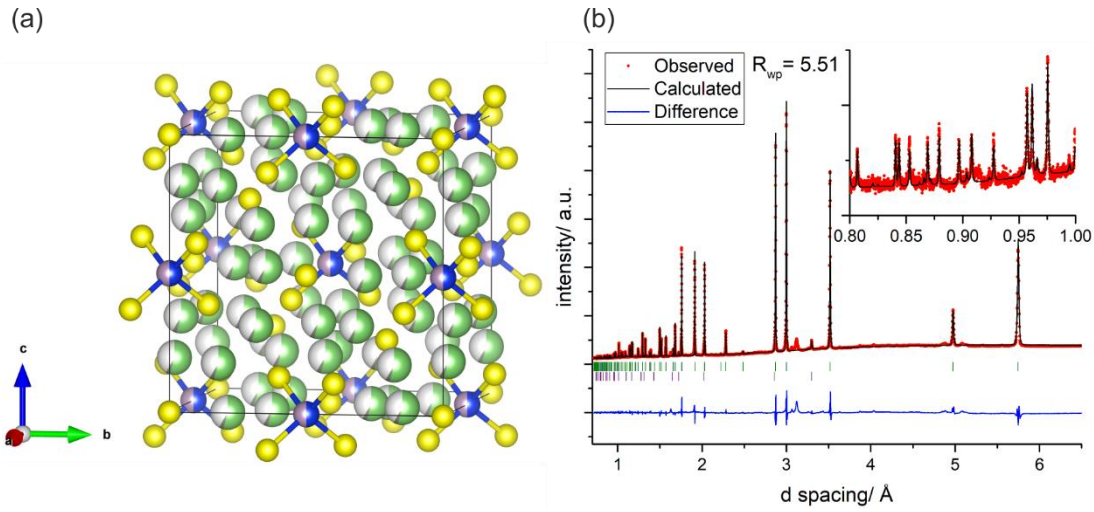

Figure 120: (a) Structure of $Li_{13}ZnSiPS_{12}$. All lithium cations can be found on the 48h site (yellow: sulphur, blue: silicon, grey: phosphorous, green: lithium, dark grey: zinc). (b) Rietveld refinement of $Li_{13.2}ZnSi_{1.2}P_{0.8}S_{12}$ against SXRD data, R_{wp}= 5.51. The positions of calculated Bragg reflections are shown by tick marks (green: $Li_{13.2}ZnSi_{1.2}P_{0.8}S_{12}$, purple: Li_2S).

In $Li_{13.2}ZnSiPS_{12}$ no electron density could be refined to the 24*g* site, while all lithium and zinc atoms are found on the 48*h* site. This results in an unphysical model, as the split 48*h* site would be occupied by 0.584 cations implicating very short cation-cation distances. Fourier difference maps (FDM) were calculated and inspected but no further sites of scattering density were identified. The sensitivity of X-ray diffraction techniques towards lithium is low and the experimental error could be quite significant, as seen in attempts to solve HT $Li_{14}ZnSi_2S_{12}$ structure. It is necessary to measure and analyse NPD data to unequivocally establish the crystal structures of lithium containing materials. The refined isotropic displacement parameters behave well and are found between 0.022(1) for S1 and 0.046(1) for the more mobile lithium on the 48*h* site (Li1). In total a good fit could be achieved up to low d spacings. The R_{wp} of the Rietveld refinement is slightly higher than the one obtained from the Pawley fit (5.32 vs 5.51). The full information of the Rietveld refinement of $Li_{13}ZnSiPS_{12}$ is given in Table 31.

Table 31: Structural parameters of $Li_{13}ZnSiPS_{12}$ from a Rietveld refinement at ambient temperature using SXRD data.

Atom	Wyckoff site	x	y	z	occupancy	$U_{iso}/Å^2$
S1	4*c*	0.75	0.25	0.75	1.0	0.022(1)
S2	16*e*	0.6211(1)	0.6211(1)	0.6211(1)	1.0	0.034(1)
S3	4*a*	0.5	0	0.5	1.0	0.048(1)
Si1	4*b*	0	0	0.5	0.6	0.027(1)
P1	4*b*	0	0	0.5	0.4	0.027(1)
Li1	48*h*	0.6818(4)	-0.0193(4)	0.3182(4)	0.542	0.046(1)
Zn1	48*h*	0.6818(4)	-0.0193(4)	0.3182(4)	0.042	0.046(1)

a= 9.9461(8) Å, Space group= $F\bar{4}3m$, R_{wp}= 5.51, χ^2= 132.9, impurity phases: Li_2S (1.5 wt %).

Bond distances were calculated and are given in Table 32. All bond distances compare well to bond distances from literature known cubic argyrodites (compare to Table 27).

Table 32: Bond distances of MS_4 tetrahedra of the cations in $Li_{13}ZnSiPS_{12}$ at ambient temperature.

	Li1/Zn1	Si1/P1
S1	2.544(3) Å	2.086(2) Å
S2	2.452(3) Å	x
S3	2.552(3) Å	x

Similar results were obtained for the Rietveld refinement of $Li_{13.2}MgSi_{1.2}P_{0.8}S_{12}$. In contrast to $Li_{13}ZnSiPS_{12}$ a significant occupation of the 24*g* site is calculated (occupation: 0.195(8)). This shows again how difficult it can be to fully refine a lithium containing material based on X-ray diffraction data only. An overall R_{wp} value of 5.43 was obtained which is slightly higher than the value obtained from the Pawley fit (5.18).

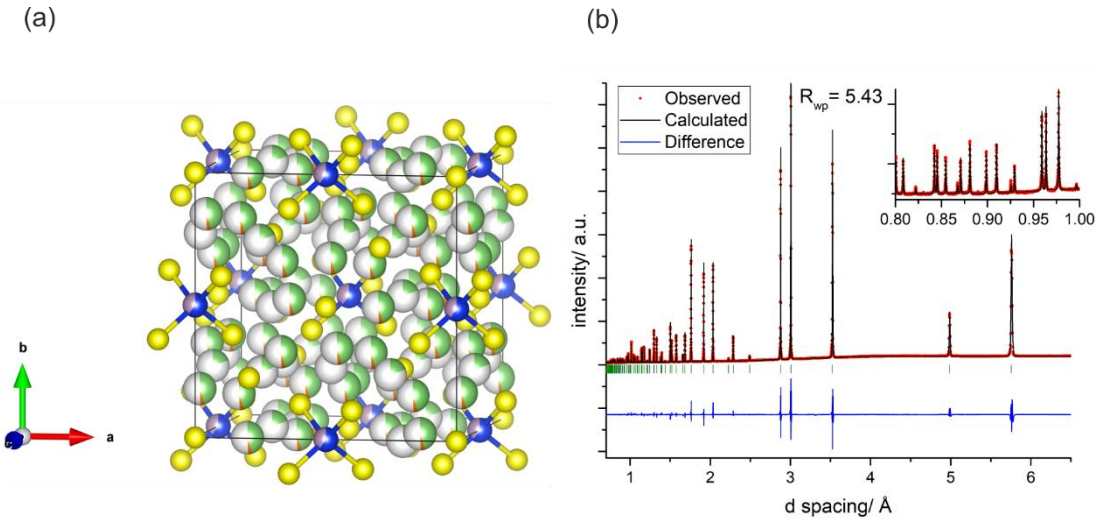

Figure 121: (a) Structure of $Li_{13.2}MgSi_{1.2}P_{0.8}S_{12}$ (yellow: sulphur, blue: silicon, grey: phosphorous, green: lithium, dark orange: magnesium) (b) Rietveld refinement of $Li_{13.2}MgSi_{1.2}P_{0.8}S_{12}$ against SXRD data, R_{wp}= 5.43. The positions of calculated Bragg reflections are shown by tick marks (green: $Li_{13.2}MgSi_{1.2}P_{0.8}S_{12}$).

The full crystallographic information of the Rietveld refinement of $Li_{13.2}MgSi_{1.2}P_{0.8}S_{12}$ is given in Table 33.

Table 33: Structural parameters of $Li_{13.2}MgSi_{1.2}P_{0.8}S_{12}$ from a Rietveld refinement at ambient temperature using SXRD data.

Atom	Wyckoff site	x	y	z	occupancy	U_{iso}/Å^2
S1	4*c*	0.75	0.25	0.75	1.0	0.021(1)
S2	16*e*	0.6206(1)	0.6206(1)	0.6206(1)	1.0	0.028(1)
S3	4*a*	0.5	0	0.5	1.0	0.037(1)
Si1	4*b*	0	0	0.5	0.6	0.020(1)
P1	4*b*	0	0	0.5	0.4	0.020(1)
Li1	48*h*	0.6698(4)	-0.0124(5)	0.3302(4)	0.453(3)	0.043(1)
Mg1	48*h*	0.6698(4)	-0.0124(5)	0.3302(4)	0.042	0.043(1)
Li2	24*g*	0.25	0.005(10)	0.75	0.195(8)	0.038

a= 9.96665(3) Å, Space group= $F\bar{4}3m$, R_{wp}= 5.43, χ^2= 58.1.

Table 34 gives the calculated bond distances of cations to their coordinating anions respectively. The bond distances are very similar to the bond distances obtained from the refinement of $Li_{14}ZnSi_2S_{12}$.

Table 34: Bond distances of MS_4 tetrahedra of the cations in $Li_{13.2}MgSi_{1.2}P_{0.8}S_{12}$ at ambient temperature.

	Li1/Mg1	Li2	Si1/P1
S1	2.584(2) Å	2.628(2) Å	2.091(2) Å
S2	2.498(3) Å	2.108(3) Å	x
S3	2.463(3) Å	3.526(3) Å	x

5.3.4.4 Transport properties of P^{5+} doped $Li_{14-x}MSi_{2-x}P_xS_{12}$

Temperature dependent AC-impedance measurements were carried out on cubic $Li_{14-x}MSi_{2-x}P_xS_{12}$ (M= Zn^{2+}, Mg^{2+}) for x= 1.0 and 1.4. The results are given in Figure 122 in an Arrhenius type plot.

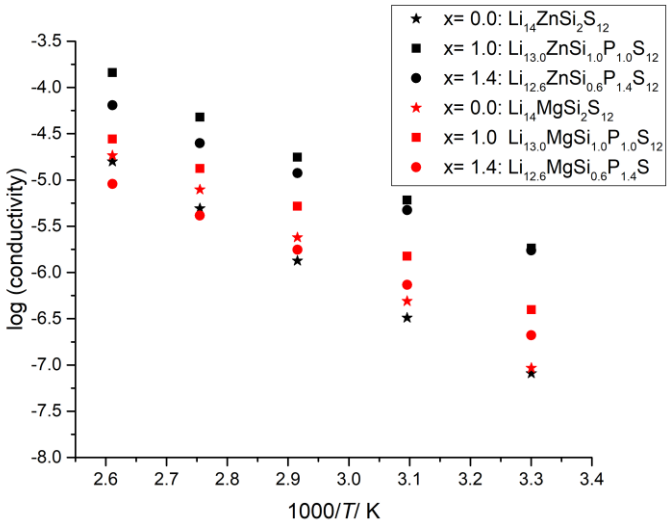

Figure 122: Arrhenius type plot for the AC-impedance measurement on cubic $Li_{14-x}MSi_{2-x}P_xS_{12}$ (M= Zn^{2+}, Mg^{2+}) for x= 0.0, 1.0 and 1.4.

Compared to the unsubstituted tetragonal parent structures an increased lithium conductivity can be observed for the cubic $Li_{14-x}MSi_{2-x}P_xS_{12}$ materials. An overview of measured conductivity values and corresponding activation energies is given in Table 35.

Table 35: Conductivity and corresponding activation energy values for $Li_{14-x}MSi_{2-x}P_xS_{12}$.

	Total conductivity σ_{total}/ S cm^{-1} at 303 K	Activation energy E_a/ eV
$Li_{14}ZnSi_2S_{12}$	2 x 10^{-7}	0.67(1) (LT) 0.35(1) (HT)
$Li_{13.0}ZnSi_{1.0}P_{1.0}S_{12}$	7 x 10^{-7}	0.54
$Li_{12.6}ZnSi_{0.6}P_{1.4}S_{12}$	2 x 10^{-6}	0.44
$Li_{14}MgSi_2S_{12}$	1 x 10^{-8}	0.55(1) (LT) 0.43(1) (HT)
$Li_{13.0}MgSi_{1.0}P_{1.0}S_{12}$	5 x 10^{-7}	0.54
$Li_{12.6}MgSi_{0.6}P_{1.4}S_{12}$	2 x 10^{-7}	0.46

But the overall ionic conductivity is still uncommonly low for cubic argyrodites. Only cubic Li_6PS_5I is reported to have a similarly low lithium mobility (10^{-6} S cm^{-1}). In $Li_{14-x}MSi_{1-x}P_xS_{12}$ (*M*= Zn^{2+}, Mg^{2+}) lithium and the divalent cation occupy the same crystallographic site. The combination of both cations is responsible for the AC-impedance response, as this method is insensitive towards the nature of the respective ions. In general, divalent cations have lower mobility in anionic frameworks compared to monovalent cations due to increased electrostatic interactions. This could explain how lithium pathways are blocked by the divalent cation with concomitant low overall ionic conductivity. But more experimental work is needed to unambiguously explain the low ionic conductivity.

5.3.5 Anion substitution in $Li_{14}MSi_2S_{12}$ (*M*= Zn^{2+}, Mg^{2+})

Substitution of sulphur for halides leads to a significant enhancement of the conductivity in Li_6PS_5X and $Li_{6-x}PS_{5-x}Cl_{1+x}$. Thus, halide doping was attempted into $Li_{12}MSi_2S_{10}X_2$ (*M*= Zn^{2+}, Mg^{2+} and *X*= Cl^-, Br^-, Cl^-) using the established synthetic conditions. It was observed that the firing temperature of 973 K was above the melting temperature of the halide substituted reaction mixtures. The PXRD patterns of $Li_{14-x}MSi_2S_{12-x}X_x$ (*M*= Zn^{2+}, Mg^{2+} and *X*= Cl^-, Br^-, I^-) are shown in Figure 123(a)-(b).

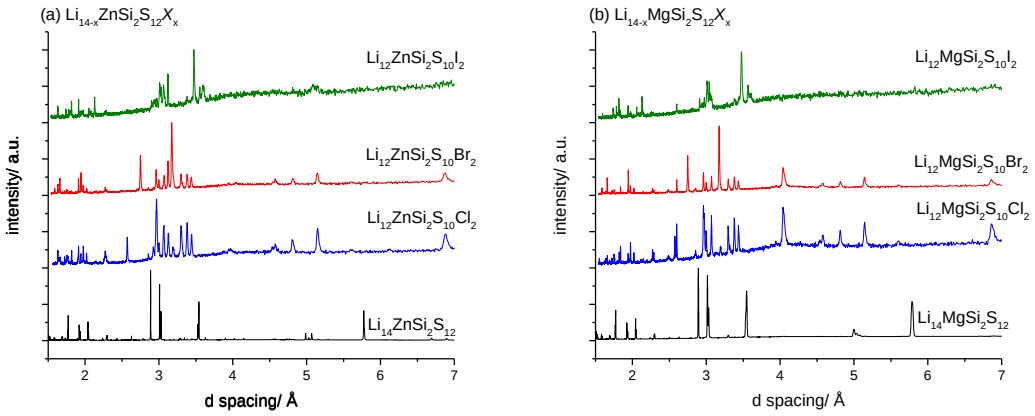

Figure 123: Anion substitution in $Li_{12}MSi_2S_{10}X_2$. (a) PXRD patterns of non-substituted $Li_{14}ZnSi_2S_{12}$ and halide substituted $Li_{12}ZnSi_2S_{10}X_2$. (b) PXRD patterns of non-substituted $Li_{14}MgSi_2S_{12}$ and halide substituted $Li_{12}MgSi_2S_{10}X_2$.

The PXRD patterns do not resemble the unsubstituted parent structures shown in black. The halide substituted materials could be indexed to mixtures of Li*X*, ZnS, MgS, Li_4SiS_4, Li_2S and SiI_4. The introduction of halides lowered the melting points of the reaction mixtures significantly, which might be responsible for decomposition of a potentially formed phase material. It might be possible to lower the synthesis temperature for the halide doped materials, even though experiments with undoped $Li_{14}ZnSi_2S_{12}$ showed that the synthesis temperature could not be lowered, as the phase did not form after repeated firing at 923 K.

5.4 Conclusion

Exploration of the pseudo-ternary $LiS_{0.5}$-ZnS-SiS_2 phase field led to the discovery of the new phase $Li_{14}ZnSi_2S_{12}$. Even though a full structure solution could not be carried out on ambient temperature SXRD and NPD data, DSC, Raman spectroscopy and temperature dependent SXRD analysis revealed the group-subgroup relationship with the cubic argyrodite structure. The ambient temperature polymorph crystallises in the body centred $I\bar{4}m2$ space group with an unusual large lattice parameter *a*= 21.1506(2) Å and *c*= 10.0564(2) Å. At ~423 K a reversible phase transition into the cubic structure is observed. The structure of the high temperature polymorph was solved by SXRD analysis and further refined using NPD data. HT $Li_{14}ZnSi_2S_{12}$ is isostructural to known cubic argyrodites, such as Li_7PS_6 or Li_6PS_5X (*X*= Cl^-, Br^-, I^-). S^{2-} and Si^{4+} ions form the framework structure. The mobile cations Li^+ and Zn^{2+} are found disordered on the same 48*h* site, with additional crystallographic sites occupied solely by lithium (24*g* and 16*e*). Various substitution reactions were attempted; full substitution of Zn^{2+} for Mg^{2+} is possible. Similarly to the Zn^{2+} homologue, $Li_{14}MgSi_2S_{12}$ crystallises in a tetragonal, low-temperature polymorph at room temperature and undergoes a phase transition to an isostructural cubic polymorph at ~398 K. The temperature dependent behaviour of $Li_{14}MgSi_2S_{12}$ could not be fully understood, as the phase transition is not fully reversible. Further studies will be needed to investigate this behaviour. Compared to other argyrodites the lithium mobility in both materials is low with values ~1 x 10^{-7} S cm^{-1} and ~1 x 10^{-8} S cm^{-1} respectively. $Li_{14}ZnSi_2S_{12}$ and $Li_{14}MgSi_2S_{12}$ degrade significantly different in contact with metallic lithium: The former shows signs of bulk degradation reactions, as the galvanostatic plating and stripping experiments result in cell failure after only 8 h and PXRD analysis confirms changes in the bulk material. The latter degrades only at the SE|Li interface, as a gradual increase of the overpotential in a galvanostatic plating and stripping experiment was observed and PXRD analysis did not show signs of bulk degradation. In total both materials are not promising solid electrolytes for solid-state batteries. But both materials can be doped to a considerable amount with P^{5+} for Si^4. A concomitant phase transition into a cubic room temperature structure is found for $Li_{14-x}MSi_{2-x}P_xS_{12}$ (*M*= Zn^{2+}, Mg^{2+}) starting at x= 0.8. Structural refinement based on SXRD data showed that the cubic polymorph is an argyrodite with disordered Si/P sites. But even though the doping resulted in a cubic argyrodite, the conductivity remains low. It is speculated that the mixing of Li^+ and M^{2+} on the same crystallographic sites leads to blocking of long-range diffusion pathways. Preliminary anion doping of $Li_{14-x}MSi_2S_{12-x}X_x$ did not result in the formation of stable

argyrodite-related phases. Further adjustment of the synthesis conditions might result in the formation of the targeted phase.

It would be very interesting to investigate the phase formation in compounds which are doped with halides with concomitant removal of the divalent cations, *e.g.* $Li_6SiS_4X_2$. Introduction of disorder of the anion site has been argued to be responsible for increased cation mobility.[41] Additionally this substitution strategy might unblock the diffusion pathways by removal of the divalent cation *M* and enable fast lithium mobility. Finally, the discovery of new argyrodites containing divalent cations opens the path towards novel zinc or magnesium conducting materials. Full substitution of lithium for M^{2+} according to $Li_0M_4SiS_6$ (*M*= Zn^{2+}, Mg^{2+}) might result in the formation of stabile argyrodite phases which would be promising cationic conductors.

5.5 References

1. Lim, H.; Kim, S. C.; Kim, J.; Kim, Y. I.; Kim, S. J., Structure of Li_5AlS_4 and comparison with other lithium-containing metal sulfides. *J. Solid State Chem.* **2018,** *257*, 19-25.
2. MacNeil, J. H.; Massi, D. M.; Zhang, J. H.; Rosmus, K. A.; Brunetta, C. D.; Gentile, T. A.; Aitken, J. A., Synthesis, structure, physicochemical characterization and electronic structure of thio-lithium super ionic conductors, Li_4GeS_4 and Li_4SnS_4. *J. Alloys Compd.* **2014,** *586*, 736-744.
3. Zhu, J. H.; Liu, C. T.; Pike, L. M.; Liaw, P. K., A thermodynamic interpretation of the size-ratio limits for laves phase formation. *Metall. Mater. Trans.* **1999,** *30* (5), 1449-1452.
4. Weisbach, A., Argyrodit, ein neues Silbererz. *Neues Jahrb. Mineral. Geol.* **1886,** *II*, 67-71.
5. Kuhs, W. F.; Nitsche, R.; Scheunemann, K., The argyrodites — A new family of tetrahedrally close-packed structures. *Mater. Res. Bull.* **1979,** *14* (2), 241-248.
6. Kraft, M. A.; Ohno, S.; Zinkevich, T.; Koerver, R.; Culver, S. P.; Fuchs, T.; Senyshyn, A.; Indris, S.; Morgan, B. J.; Zeier, W. G., Inducing High Ionic Conductivity in the Lithium Superionic Argyrodites $Li_{6+x}P_{1-x}Ge_xS_5I$ for All-Solid-State Batteries. *J. Am. Chem. Soc.* **2018,** *140* (47), 16330-16339.
7. Eulenberger, G., Die Kristallstruktur der Tieftemperaturmodifikation von Ag_8GeS_6. *Monatsh. Chem.* **1977,** *108* (4), 901-913.
8. Kong, S. T.; Deiseroth, H. J.; Reiner, C.; Gun, O.; Neumann, E.; Ritter, C.; Zahn, D., Lithium Argyrodites with Phosphorus and Arsenic: Order and Disorder of Lithium Atoms, Crystal Chemistry, and Phase Transitions. *Chem. Eur. J.* **2010,** *16* (7), 2198-2206.
9. Unterrichter Johanna, v.; Range, K.-J., Ag_8GeTe_6, ein Vertreter der Argyroditfamilie / Ag_8GeTe_6, a Representative of the Argyrodite Family. *Zeitschrift fur Naturforschung B* **1978,** *33* (8), 866-872.
10. Kraft, M. A.; Culver, S. P.; Calderon, M.; Böcher, F.; Krauskopf, T.; Senyshyn, A.; Dietrich, C.; Zevalkink, A.; Janek, J.; Zeier, W. G., Influence of Lattice Polarizability on the Ionic Conductivity in the Lithium Superionic Argyrodites Li_6PS_5X (X = Cl, Br, I). *J. Am. Chem. Soc.* **2017,** *139* (31), 10909-10918.
11. Huang, W. Z.; Yoshino, K.; Hori, S.; Suzuki, K.; Yonemura, M.; Hirayama, M.; Kanno, R., Superionic lithium conductor with a cubic argyrodite-type structure in the Li-Al-Si-S system. *J. Solid State Chem.* **2019,** *270*, 487-492.
12. Kong, S. T.; Gün, Ö.; Koch, B.; Deiseroth, H. J.; Eckert, H.; Reiner, C., Structural Characterisation of the Li Argyrodites Li_7PS_6 and Li_7PSe_6 and their Solid Solutions: Quantification of Site Preferences by MAS-NMR Spectroscopy. *Chem. Eur. J.* **2010,** *16* (17), 5138-5147.
13. Laqibi, M.; Cros, B.; Peytavin, S.; Ribes, M., New silver superionic conductors Ag_7XY_5Z (X = Si, Ge, Sn; Y = S, Se; Z = Cl, Br, I)-synthesis and electrical studies. *Solid State Ion.* **1987,** *23* (1), 21-26.
14. Deiseroth, H.-J.; Maier, J.; Weichert, K.; Nickel, V.; Kong, S.-T.; Reiner, C., Li_7PS_6 and Li_6PS_5X (X: Cl, Br, I): Possible Three-dimensional Diffusion Pathways for Lithium Ions and Temperature Dependence of the Ionic Conductivity by Impedance Measurements. *Z. anorg. allg. Chem.* **2011,** *637* (10), 1287-1294.
15. Deiseroth, H. J.; Kong, S. T.; Eckert, H.; Vannahme, J.; Reiner, C.; Zaiss, T.; Schlosser, M., Li_6PS_5X: A class of crystalline Li-rich solids with an unusually high Li^+ mobility. *Angew. Chem., Int. Edit.* **2008,** *47* (4), 755-758.
16. Epp, V.; Gün, Ö.; Deiseroth, H.-J.; Wilkening, M., Highly Mobile Ions: Low-Temperature NMR Directly Probes Extremely Fast Li^+ Hopping in Argyrodite-Type Li_6PS_5Br. *J. Phys. Chem. Lett.* **2013,** *4* (13), 2118-2123.

17. de Klerk, N. J. J.; Rosłoń, I.; Wagemaker, M., Diffusion Mechanism of Li Argyrodite Solid Electrolytes for Li-Ion Batteries and Prediction of Optimized Halogen Doping: The Effect of Li Vacancies, Halogens, and Halogen Disorder. *Chem. Mater.* **2016,** *28* (21), 7955-7963.
18. Zhang, Z.; Sun, Y.; Duan, X.; Peng, L.; Jia, H.; Zhang, Y.; Shan, B.; Xie, J., Design and synthesis of room temperature stable Li-argyrodite superionic conductors via cation doping. *J. Mater. Chem. A* **2019,** *7* (6), 2717-2722.
19. Minafra, N.; Culver, S. P.; Krauskopf, T.; Senyshyn, A.; Zeier, W. G., Effect of Si substitution on the structural and transport properties of superionic Li-argyrodites. *J. Mater. Chem. A* **2018,** *6* (2), 645-651.
20. Ohno, S.; Helm, B.; Fuchs, T.; Dewald, G.; Kraft, M. A.; Culver, S. P.; Senyshyn, A.; Zeier, W. G., Further Evidence for Energy Landscape Flattening in the Superionic Argyrodites $Li_{6+x}P_{1-x}M_xS_5I$ (M = Si, Ge, Sn). *Chem. Mater.* **2019**.
21. Wang, H.; Yu, C.; Ganapathy, S.; van Eck, E. R. H.; van Eijck, L.; Wagemaker, M., A lithium argyrodite $Li_6PS_5Cl_{0.5}Br_{0.5}$ electrolyte with improved bulk and interfacial conductivity. *J. Power Sources* **2019**, 29-36.
22. Adeli, P.; Bazak, J. D.; Park, K. H.; Kochetkov, I.; Huq, A.; Goward, G. R.; Nazar, L. F., Boosting Solid-State Diffusivity and Conductivity in Lithium Superionic Argyrodites by Halide Substitution. *Angew. Chem. Int. Ed. Engl.* **2019,** *58* (26), 8681-8686.
23. Xuan, M.; Xiao, W.; Xu, H.; Shen, Y.; Li, Z.; Zhang, S.; Wang, Z.; Shao, G., Ultrafast solid-state lithium ion conductor through alloying induced lattice softening of Li_6PS_5Cl. *J. Mater. Chem. A* **2018,** *6* (39), 19231-19240.
24. Wenzel, S.; Sedlmaier, S. J.; Dietrich, C.; Zeier, W. G.; Janek, J., Interfacial reactivity and interphase growth of argyrodite solid electrolytes at lithium metal electrodes. *Solid State Ion.* **2018,** *318*, 102-112.
25. Cheng, T.; Merinov, B. V.; Morozov, S.; Goddard, W. A., Quantum Mechanics Reactive Dynamics Study of Solid Li-Electrode/Li_6PS_5Cl-Electrolyte Interface. *ACS Energy Lett.* **2017,** *2* (6), 1454-1459.
26. Yu, C.; van Eijck, L.; Ganapathy, S.; Wagemaker, M., Synthesis, structure and electrochemical performance of the argyrodite Li_6PS_5Cl solid electrolyte for Li-ion solid state batteries. *Electrochim. Acta* **2016,** *215*, 93-99.
27. Li, G. M.; Chu, Y.; Zhou, Z. X., From $AgGaS_2$ to Li_2ZnSiS_4: Realizing Impressive High Laser Damage Threshold Together with Large Second-Harmonic Generation Response. *Chem. Mater.* **2018,** *30* (3), 602-606.
28. Boultif, A.; Louer, D., Powder pattern indexing with the dichotomy method. *J. Appl. Crystallogr.* **2004,** *37* (5), 724-731.
29. Wiles, D. B.; Young, R. A., A new computer program for Rietveld analysis of X-ray powder diffraction patterns. *J. Appl. Crystallogr.* **1981,** *14* (2), 149-151.
30. Petříček, V.; Dušek, M.; Palatinus, L., Crystallographic Computing System JANA2006: General features. *Z. Kristallogr. - Crystl. Mater.* **2014,** *229* (5), 345.
31. Kroumova, E.; Aroyo, M. I.; Perez-Mato, J. M.; Ivantchev, S.; Igartua, J. M.; Wondratschek, H., PSEUDO: a program for a pseudosymmetry search. *J. Appl. Crystallogr.* **2001,** *34* (6), 783-784.
32. Aroyo Mois, I.; Perez-Mato Juan, M.; Capillas, C.; Kroumova, E.; Ivantchev, S.; Madariaga, G.; Kirov, A.; Wondratschek, H., Bilbao Crystallographic Server: I. Databases and crystallographic computing programs. In *Z. Kristallogr. - Crystl. Mater.*, 2006; Vol. 221, p 15.
33. Ishii, M.; Onoda, M.; Shibata, K., Structure and vibrational spectra of argyrodite family compounds Cu_8SiX_6 (X = S, Se) and Cu_8GeS_6. *Solid State Ion.* **1999,** *121* (1-4), 11-18.
34. Yubuchi, S.; Teragawa, S.; Aso, K.; Tadanaga, K.; Hayashi, A.; Tatsumisago, M., Preparation of high lithium-ion conducting Li_6PS_5Cl solid electrolyte from ethanol solution for all-solid-state lithium batteries. *J. Power Sources* **2015,** *293*, 941-945.

35. Yubuchi, S.; Uematsu, M.; Deguchi, M.; Hayashi, A.; Tatsumisago, M., Lithium-Ion-Conducting Argyrodite-Type Li_6PS_5X (X = Cl, Br, I) Solid Electrolytes Prepared by a Liquid-Phase Technique Using Ethanol as a Solvent. *ACS Applied Energy Materials* **2018,** *1* (8), 3622-3629.
36. Altomare, A.; Cuocci, C.; Giacovazzo, C.; Moliterni, A.; Rizzi, R.; Corriero, N.; Falcicchio, A., EXPO2013: a kit of tools for phasing crystal structures from powder data. *J. Appl. Crystallogr.* **2013,** *46* (4), 1231-1235.
37. Shannon, R., Revised effective ionic radii and systematic studies of interatomic distances in halides and chalcogenides. *Acta Cryst. A* **1976,** *32* (5), 751-767.
38. Sears, V. F., Neutron scattering lengths and cross sections. *Neutron News* **1992,** *3* (3), 26-37.
39. Brandt, G.; Krämer, V., Phase investigations in the silver-gallium-sulphur system. *Mater. Res. Bull.* **1976,** *11* (11), 1381-1388.
40. Murayama, M.; Kanno, R.; Irie, M.; Ito, S.; Hata, T.; Sonoyama, N.; Kawamoto, Y., Synthesis of New Lithium Ionic Conductor Thio-LISICON—Lithium Silicon Sulfides System. *J. Solid State Chem.* **2002,** *168* (1), 140-148.
41. Strangmüller, S.; Eickhoff, H.; Müller, D.; Klein, W.; Raudaschl-Sieber, G.; Kirchhain, H.; Sedlmeier, C.; Baran, V.; Senyshyn, A.; Deringer, V. L.; van Wüllen, L.; Gasteiger, H. A.; Fässler, T. F., Fast Ionic Conductivity in the Most Lithium-Rich Phosphidosilicate $Li_{14}SiP_6$. *J. Am. Chem. Soc.* **2019,** *141* (36), 14200-14209.

5.6 Appendix

Table 36: Structural parameters of $Li_{14}ZnSi_2S_{12}$ from a preliminary Rietveld refinement using SXRD data measured at 448 K.

Atom	Wyckoff site	x	y	z	occupancy	$U_{iso}/Å^2$
S1	4*c*	0.75	0.25	0.75	1.0	0.031(1)
S2	16*e*	0.6216(5)	0.6216(5)	0.6216(5)	1.0	0.034(1)
S3	4*a*	0.5	0	0.5	1.0	0.056(1)
Si1	4*b*	0	0	0.5	0.986(2)	0.024(1)
Li1	48*h*	0.6818(2)	-0.0127(3)	0.3182(2)	0.583	0.075(1)
Zn1	48*h*	0.6818(2)	-0.0127(3)	0.3182(2)	0.037(1)	0.075(1)
Li2	24*g*	0.25	0.008(6)	0.75	0.069(6)	0.076

a= 10.0443(1) Å, Space group= $F\bar{4}3m$, R_{wp}= 3.50, χ^2= 3.89, impurity phases: Li_2S (0.8 wt %), Li_4SiS_4 (7.0 wt %)

Table 37: Structural parameters of $Li_{14}ZnSi_2S_{12}$ from a Rietveld refinement using NPD data measured at 448 K.

Atom	Wyckoff site	x	y	z	occupancy	$U_{aniso}/Å^2$
S1	4*c*	0.75	0.25	0.75	1.0	Table 38
S2	16*e*	0.6203(7)	0.6203(7)	0.6203(7)	1.0	Table 38
S3	4*a*	0.5	0	0.5	1.0	Table 38
Si1	4*b*	0	0	0.5	1.0	Table 38
Li1	48*h*	0.6828(3)	0.6828(3)	0.0246(3)	0.438(2)	Table 38
Zn1	48*h*	0.6828(3)	0.6828(3)	0.0246(3)	1/24	Table 38
Li2	24*g*	0.019(7)	0.25	0.75	0.076(3)	Table 38
Li3	16*e*	0.8679(4)	0.8679(4)	0.8679(4)	0.321(3)	Table 38

a= 10.0443(1) Å, Space group= $F\bar{4}3m$, R_{wp}= 1.62, χ^2= 3.22, impurity phases: Li_2S (0.8 wt %), Li_4SiS_4 (7.0 wt %)

Table 38: Anisotropic displacement parameters obtained from a Rietveld refinement using NPD data measured at 448 K.

	β_{11}	β_{22}	β_{33}	β_{12}	β_{13}	β_{23}
S1	0.028(1)	0.028(1)	0.028(1)	0.028(1)	0.028(1)	0.028(1)
S2	0.028(2)	0.028(2)	0.028(2)	-0.006(3)	-0.006(3)	-0.006(3)
S3	0.052(1)	0.052(1)	0.052(1)	0.052(1)	0.052(1)	0.052(1)
Si1	0.018(1)	0.018(1)	0.018(1)	0.018(1)	0.018(1)	0.018(1)
Li1	0.085(2)	0.085(2)	0.029(2)	-0.002(2)	-0.011(1)	-0.011(1)
Zn	0.085(2)	0.085(2)	0.029(2)	-0.002(2)	-0.011(1)	-0.011(1)
Li2	0.16(3)	0.16(3)	0.16(3)	0.16(3)	0.16(3)	0.16(3)
Li3	0.067(2	0.067(2	0.067(2	-0.012(2)	0.012(2)	0.012(2)

Table 39: Structural parameters of $Li_{14}MgSi_2S_{12}$ from a Rietveld refinement using NPD data measured at 448 K.

Atom	Wyckoff site	x	y	z	occupancy	$U_{aniso}/Å^2$
S1	4*c*	0.75	0.25	0.75	1.0	Table 40
S2	16*e*	0.6205(1)	0.6205(1)	0.6205(1)	1.0	Table 40
S3	4*a*	0.5	0	0.5	1.0	Table 40
Si1	4*b*	0	0	0.5	1.0	Table 40
Li1	48*h*	0.6885(3)	0.6885(3)	0.0207(3)	0.446(2)	Table 40
Mg1	48*h*	0.6885(3)	0.6885(3)	0.0207(3)	1/24	Table 40
Li2	24*g*	-0.025(2)	0.25	0.25	0.047(5)	Table 40
Li3	16*e*	0.8679(4)	0.8679(4)	0.8679(4)	0.340(3)	Table 40

a= 10.0608(3) Å, Space group= $F\bar{4}3m$, R_{wp}= 1.61, χ^2= 5.15, impurity phases: Li_2S (0.5 wt %), Li_4SiS_4 (1.7 wt %)

Table 40: Anisotropic displacement parameters obtained from a Rietveld refinement using NPD data measured at 448 K.

	β_{11}	β_{22}	β_{33}	β_{12}	β_{13}	β_{23}
S1	0.027(1)	0.027(1)	0.027(1)	0.027(1)	0.027(1)	0.027(1)
S2	0.027(3)	0.027(3)	0.027(3)	-0.005(3)	-0.005(3)	-0.005(3)
S3	0.040(1)	0.040(1)	0.040(1)	0.040(1)	0.040(1)	0.040(1)
Si1	0.014(4)	0.014(4)	0.014(4)	0.014(4)	0.014(4)	0.014(4)
Li1	0.092(2)	0.092(2)	0.020(2)	0.0196(2)	0.005(1)	0.005(1)
Mg	0.092(2)	0.092(2)	0.020(2)	0.0196(2)	0.005(1)	0.005(1)
Li2	0.3(3)	0.3(3)	0.3(3)	0.3(3)	0.3(3)	0.3(3)
Li3	0.082(2)	0.082(2)	0.082(2)	-0.006(2)	-0.006(2)	-0.006(2)

6 Summary and Conclusions

The discovery and characterisation of new materials remains a challenging undertaking. This thesis focuses on the exploratory synthesis in various chemical spaces/phase fields for the discovery new compounds which could potentially be used as lithium ion conductors in all-solid state batteries. In particular lithium containing metal sulphide phases were investigated, as these materials show the best lithium mobility up to date. The identification and characterisation of three novel classes of materials have been presented in this thesis.

Inspired by the report of a superconducting oxide based high entropy rock salt, $(MgCoNiCuZn)_{1-x-y}Ga_yLi_xO$, the concept of high entropy stabilised rock salts was expanded to sulphide-based phases for the first time. Experimental procedures were developed probing temperature, firing time, number of cations and suitability of reagents. Compositions containing binary reagents, which exhibit rock salt structures at ambient conditions (*e.g.* MgS), form disordered rock salts more easily than compositions which contain binary materials, which crystallise in other structure types at ambient conditions (*e.g.* ZnS). Quenching temperatures of ~1000 K are sufficient to stabilise phases, such as $LiBiMgMnCaS_5$, $LiYMgMnCaS_5$ or $LiBiMgCaS_4$. Application of higher firing temperatures leads to serious side-reactions with the reaction vessel (quartz tubes). The single phase material $LiBiMgCaS_4$ was investigated in detail regarding structure and lithium transport properties. SXRD and NPD experiments were carried out and a structural model was developed. $LiBiMgCaS_4$ crystallises with a rock salt type structure with complete disorder on the cation site. AC-impedance spectroscopy and solid state NMR were applied to probe the transport properties. No significant Li^+ mobility could be detected in either method. The AC-impedance spectrum hinted that the material might be electrically conducting instead of facilitating lithium mobility. The low lithium diffusivity was put into context to research on disordered rock salt phases. For low energy percolating pathways to be formed throughout the material, a lithium content threshold of ~ 0.55 $n_{Li}/n_{cations}$ must be met. $LiBiMgCaS_4$ ($n_{Li}/n_{cations}$ = 0.25) does not meet this requirement. The work presented in Chapter 1 shows that the application of high entropy stabilised phases is a viable route towards the discovery of new lithium containing sulphide phases. Careful selection of reagents and stoichiometries could finally lead to the discovery of materials which are not accessible by standard solid state procedures.

Many lithium containing metal sulphides (*e.g.* Li_5AlS_4, Li_4GeS_4, Li_3PS_4) are based on a hexagonal close packed S^{2-} sublattice with a distinct arrangement of non-lithium metal cations. The ternary materials do not exhibit high lithium ion conductivities, but solid

solutions between these have led to significant increased lithium mobility, for example in the thio-LISICONs. A particularly interesting material is the well-studied $Li_{10}GeP_2S_{12}$. The stoichiometry relates to the thio-LISICONs by placing it on the tie line Li_4GeS_4-Li_3PS_4. But the material exhibits a completely new structure type, based on a bcc related S^{2-} sublattice, which gives rise to the best solid state lithium mobility so far. In this work the identification of new materials was attempted, by expanding the chemical space to the pseudo-ternary Li_5AlS_4-Li_4GeS_4-Li_3PS_4 phase field. The idea was, that the similarity of the S^{2-} sublattice of the parent compounds, paired with distinctly different cation arrangements, might lead to formation of novel phases. Two new materials were discovered in this phase field: $Li_{4.4}Al_{0.4}Ge_{0.6}S_4$, crystallising in the trigonal space group $P\bar{3}m1$ with a novel structure type, and Ge^{4+}/P^{5+} doped Li_5AlS_4. The structure of $Li_{4.4}Al_{0.4}Ge_{0.6}S_4$ was solved using SXRD and NPD data. S^{2-} anions form a hcp sublattice with a layered cation motif, based on the distinct occupation of tetrahedral and octahedral sites: the tetrahedral layer, which is formed by a disordered Al^{3+}/Ge^{4+} site and a tetrahedrally coordinated lithium site. Alternatively stacked along the *c*-axis is a layer which is formed by octahedral coordination of lithium ions. Significant lithium disorder can be found in both layers. The tetrahedrally coordinated lithium is displaced statistically into a face-sharing tetrahedron. It is assumed that a single Li cation moves in-between those two sites. The octahedral lithium is moved off the centre of the octahedron and displaced towards the apices, which are related by a mirror plane. Those two related octahedral sites are occupied by only 0.9 Li, introducing disordered vacancies. The conductivity of this phase is 4.3(3) x 10^{-5} S cm^{-1} with an activation energy E_a= 0.38(1) eV. Computational calculations run on $Li_{4.4}Al_{0.4}Ge_{0.6}S_4$ by Dr Paul Sharp show that the disordered vacancies play an important role in the diffusion of lithium according to the direct-hopping mechanism. Substitution of the non-lithium cations for lighter and heavier homologues led to the discovery of the following structurally related materials: $Li_{4.4}Al_{0.4}Sn_{0.6}S_4$, $Li_{4.4}Ga_{0.4}Ge_{0.6}S_4$, $Li_{4.4}Ga_{0.4}Sn_{0.6}S_4$, $Li_{4.4}In_{0.4}Si_{0.6}S_4$, $Li_{4.4}In_{0.4}Ge_{0.6}S_4$ and $Li_{4.4}In_{0.4}Sn_{0.6}S_4$. The lithium ion conductivity of these materials ranges from 10^{-6} S cm^{-1} ($Li_{4.4}Al_{0.4}Sn_{0.6}S_4$) to 10^{-4} S cm^{-1} ($Li_{4.4}In_{0.4}Sn_{0.6}S_4$). Full structure solutions were carried out for $Li_{4.4}Al_{0.4}Ge_{0.6}S_4$, $Li_{4.4}Al_{0.4}Sn_{0.6}S_4$ and $Li_{4.4}In_{0.4}Sn_{0.6}S_4$ using SXRD and NPD data. No structural explanation could be found for the strongly differing lithium conductivities. Therefore relationships to various physical properties (atomic radii, ionic radii, Pauling electronegativity and polarizability) were investigated, but no satisfying correlations could be identified. The second material identified in the Li_5AlS_4-Li_4GeS_4-Li_3PS_4 phase field, $Li_{4.5}Al_{2/3}Ge_{1/6}P_{1/6}S_4$, adopts a structure based on layered Li_5AlS_4. Compared to Li_5AlS_4 the doped material has an increased lithium

conductivity of four orders of magnitude. This can be explained by the structure of the parent phase Li_5AlS_4. In Li_5AlS_4 all tetrahedral interstices in the tetrahedral layer and all octahedral interstices in the octahedral layer are occupied by Al^{3+}/Li^+ and Li^+ respectively. Introduction of tetra- and pentavalent germanium and phosphorous leads to the formation of Li-vacancies. These vacancies could facilitate long-range lithium diffusion in $Li_{4.5}Al_{2/3}Ge_{1/6}P_{1/6}S_4$ similar to lithium diffusion in $Li_{4.4}Al_{0.4}Ge_{0.6}S_4$. Further structural work, based on NPD experiments, is needed to elucidate the position and role of these vacancies in lithium transport through the material.

Finally, the discovery of a new argyrodite related $Li_{14}MSi_2S_{12}$ (*M*= Zn^{2+}, Mg^{2+}) phase was presented. Phosphorous based cubic argyrodites are known superionic lithium conductors and have been studied intensely regarding application in all solid-state batteries. Up to now their use has been hampered by the instability of thiophosphates against lithium metal anodes, as they are thermodynamically instable towards the formation of Li_3P. Exploratory synthesis in the $LiS_{0.5}$-ZnS-SiS_2 phase field led to the discovery of $Li_{14}ZnSi_2S_{12}$, which crystallises in the tetragonal $I\bar{4}m2$ space group. Partial solution of the crystal structure gave an anion sublattice which is related to the anion sublattice in argyrodites. Group-subgroup relationships directly link the cubic $F\bar{4}3m$ space group of cubic argyrodites to the tetragonal $I\bar{4}m2$ space group. Concomitantly the unusual large lattice vector *a*=21.1506(2) Å and *c*= 10.0564(2) Å can be related to the lattice parameters of cubic argyrodites, which are usually ~10 Å. Raman spectroscopy showed that similar phonon modes are present to those in cubic argyrodites, while DSC measurement showed that a reversible process takes place at 411 K. Variable temperature SXRD experiments confirmed that a reversible phase transition from the tetragonal structure into a cubic unit cell (space group: $F\bar{4}3m$) takes place at *T*~ 423 K. The structure of the cubic HT polymorph could be solved based on SXRD and NPD data. HT $Li_{14}ZnSi_2S_{12}$ crystallises in the argyrodite structure similar to Li_7PS_6 or Li_6PS_5I. Sulphur anions form a tetrahedral close packing, which is topologically equivalent to the packing of the positions of Cu and Mg in the Laves phase $MgCu_2$. The highly charged silicon Si^{4+} cations are distributed in tetrahedral interstices in a way, which maximises the distance between the SiS_4 building blocks. This fully ordered framework structure is accompanied by disordered Li^+ and Zn^{2+} cations on the crystallographic 48*h* and 24*g* sites. Additional Li density could be identified on the 16*e* crystallographic site. Based on the structure of the HT polymorph and the group-subgroup relationships between the HT and LT unit cells, it was concluded that LT $Li_{14}ZnSi_2S_{12}$ is a novel ordered argyrodite phase. Full crystal structure solution of the LT polymorph was not successful. The Li^+ ion transport properties were

assessed by AC-impedance spectroscopy and DC-polarization experiments, which gave low lithium conductivity of ~10^{-7} S cm^{-1} with negligible electronic contribution. Substitution reactions resulted in the synthesis of the Mg^{2+} polymorph $Li_{14}MgSi_2S_{12}$. Like $Li_{14}ZnSi_2S_{12}$ it crystallises in a large tetragonal unit cell (space group: $I\bar{4}m2$) at room temperature which dimensions are related to the argyrodite unit cell by group-subgroup relationships. During heating a tetragonal-cubic transition occurs at ~398 K, which can be measured by DSC and variable temperature SXRD experiments. Upon cooling the cubic-tetragonal transition showed hysteresis which affects the Li ion conductivity in the material. The crystal structure of the cubic HT polymorph was solved based on SXRD and NPD data and is isostructural to $Li_{14}ZnSi_2S_{12}$. The exchange of Zn^{2+} for Mg^{2+} does not result in improvement of lithium conductivity in the material. Both materials showed unstable behaviour against lithium metal, rendering them unsuitable for application in solid-state batteries. The modelling of the low temperature crystal structures of $Li_{14}MSi_2S_{12}$ (*M*= Zn^{2+}, Mg^{2+}) from powder diffraction data remains a challenging problem. The most elegant solution would be to simplify the problem by growing single crystals and attempt to solve the structures from single crystal diffraction data.

Various doping routes of the two materials were attempted. The formal parent structure Li_8SiS_6 could not be obtained using the established synthetic procedure. Arguably the anion sublattice does not exhibit enough low-energy tetrahedral interstices and can only be stabilised by substituting two Li^+ ions for one divalent Zn^{2+} cation. Similar to reports on Al^{3+} doped Li_7PS_6, introduction of trivalent metal cations into $Li_{14}MSi_2S_{12}$, according to $Li_{14+x}MAl_xSi_{2-x}S_{12}$, is not a viable doping strategy and results in the formation of significant impurity phases. Again, it can be argued that an increasing number of cations leads to destabilisation. In contrast doping pentavalent P^{5+} for Si^{4+} into $Li_{14-x}MSi_{2-x}P_xS_{12}$ decreases the total number of cations and argyrodite related phases can be synthesised. The materials crystallise in a single argyrodite related phase. Increased doping leads to a reduction in the tetragonal distortion and at x= 1.0 both the Zn^{2+} and the Mg^{2+} homologues crystallise in fully cubic structures. The structures of $Li_{13}ZnSiPS_{12}$ and $Li_{13.2}MgSi_{1.2}P_{0.8}S_{12}$ were exemplarily solved from SXRD data. Both materials exhibit the cubic argyrodite structure with mixed Si/P sites. AC-impedance measurements on these cubic argyrodites did not indicate significant improvement of lithium mobility at ambient temperature. It is speculated that divalent cations mixed on the same site as the lithium can block the diffusion pathways and impede lithium mobility.

Preliminary synthesis of halogen doped $Li_{12}MSi_2S_{10}X_2$ argyrodites did not result in formation of single phases. Melting of the reaction mixtures might have prevented the successful synthesis of the desired phase. Further work needs to be carried out on those stoichiometries using lower synthesis temperatures. Additionally, a reduction of M^{2+} in $Li_{14}M_{1-0.5x}Si_2S_{12-x}X_x$ (M= Zn^{2+} or Mg^{2+}) could enhance lithium mobility, while a full exchange of Li for divalent cations might result in solid state conductors for zinc and magnesium batteries.

Overall the field of lithium based metal sulphides remains underexplored. Difficulties in synthesis and sample handling make the exploration of these phase fields more challenging than oxide based phase fields. This thesis makes a significant contribution to the progress and understanding of sulphide based materials. Novel crystalline phases were synthesised, identified and characterised in respect to application as solid state conductors. This work encourages the continued exploration of difficult and unusual phase fields, as the outcomes are potentially rewarding.